Streamlined Gelator Discovery through the Analysis of Intermolecular Interactions in the Solid State

By

Kelsey King Carter

**A dissertation submitted in partial fulfillment
of the requirements for the degree of
Doctor of Philosophy
(Chemistry)
in the University of Michigan
2014**

Doctoral Committee

Associate Professor Anne J. McNeil (Chair)
Assistant Professor Kenichi Kuroda
Professor Adam J. Matzger
Associate Professor Nair Rodriguez-Hornedo

Dedication: To my family.

Acknowledgements

I would like to thank my advisor, Dr. Anne J. McNeil for all of her advice and encouragement over the years. I have learned so much from you that I could fill more pages than this document with examples.

Members of the McNeil lab throughout the duration of my Ph.D. have been instrumental in my success. I can attribute a lot of my current knowledge to desk-side conversations about chemistry (and of course other things, especially pets and food). All of you have a special place in my heart: Erica, Jonas, Cheryl, Jing, Yash, Se Ryeon, Danielle, Zack, Pete, Mitchell, Ariana, and now Kendra. Special thanks go out to the gel subgroup members. Jing, Cheryl and Yash were kind enough to bring me up to speed at the beginning, and Danielle who had to bear with me at the end. I also have to thank Halley and Sarah for their help on various projects and for generally being awesome people. I am so happy and proud to have had the chance to work with and get to know all of you.

I would also like to acknowledge my mentor, Dr. Charles Degenhardt, at Proctor and Gamble. Chuck took a chance on me for an internship and taught me a ton about life in industry.

Thank you to all of my friends in Ann Arbor (even if they've left already). You have helped me celebrate great times and make the bad times better.

I also would like to thank my family. It isn't possible to have had better parents. Thank you for teaching me not to quit, even when I wanted to, and for buying me all of those K'nex.

Finally, I have to thank my husband, Tyler. I could not have made it through graduate school without you. I am eternally grateful every minute we've spent together. I can't wait for what the future brings us. Also, thanks for lithiating my ligand that one time ;-).

Table of Contents

Dedication. ii
Acknowledgements iii
List of Figures v
List of Tables xiv
List of Schemes xvi
List of Charts xvii
List of Appendices xviii
Abstract xix
Chapter 1. Introduction 1
Chapter2. Streamlined Approach to a New Gelator: Inspiration From Solid-State Interactions for a Mercury-Induced Gelation 12
Chapter 3. Improving Hg-triggered Gelation via Structural Modifications 20
Chapter 4. A Strategy to Analyze Intermolecular Interactions and Target New Gelators Using Morphology Precition 33
Chapter 5. Conclusions and Future Directions 51
Appendices 57

List of Figures

Figure 1-1. A thiol non-gelling precursor is oxidized by TATP into a disulfide gelator ... 2
Figure 1-2. Schematric of the proposed self-assembly mechanism for fiber formation. The wavy lines represent solvent and the blue ellipses represent gelator molecules 5
Figure 1-3. Solubilities of pyridine-based gelators (red) and nongelators (blue) measured at room temperature 7
Figure 1-4. Enthalpy of dissolution for pyridine-based gelators (red) and nongelators (blue) 8
Figure 1-5. PXRD data for two gelators. The red line represents data for the gel form while the black represents the bulk solid from synthesis 8
Figure 2-1. Adding an aqueous solution of $Hg(OAc)_2$ to **1a** in hot MeOH (upper left) leads to gel formation (upper right). Control experiments show that simply adding an equivalent volume of H_2O (lower left) or cooling to rt (lower right) results in precipitation 14
Figure 2-2. Scanning electron micrograph of the in situ gel of **2a** (24 mM) in 90/10 MeOH/H_2O 15
Figure 2-3. Single crystal X-ray structure for **2a**. H-atoms were omitted for clarity 15
Figure 3-1. PXRD patterns for gelator **1a** under the following conditions: (A) gel formed in MeOH, (B) solid form after heating in EtOH, (C) solid form after heating in MeOH, (D) bulk form isolated from synthesis, (E) simulated pattern from crystal grown from MeOH/H_2O, (F) simulated pattern from crystal grown from DMSO/H_2O 25
Figure 3-2. Plots of the dissolution enthalpy (ΔH_{diss}, A and C) and entropy (ΔS_{diss}, B and D) versus compound number for **1–5** in MeOH (A/B) and EtOH (C/D). Grey shading denotes gelators 26

Figure 3-3. (A) Representative oscillating stress sweep for gelator **3a** in EtOH (15 mM). (B) Representative scanning electron micrograph for gelator **3a** in EtOH/HOAc (12.3 mM) 27
Figure 3-4. Gelation is observed when Hg^{2+}-contaminated water (0.2 mL, 48 mM) is added to a MeOH solution containing 7-bromoquinoxalin-2(1H)-one (0.8 mL, 20 mM) 28
Figure 3-5. Gel formation (with **3a** in EtOH) is observed when bottled water, tap water, and Huron River water containing $Hg(OAc)_2$ is added 29
Figure 4-1. Overlaid structures from the CIF files for (A) **1a** and (B) **2a**. Green represents the unoptimized molecular conformation (unopt.) while red shows the molecular conformation after optimization holding unit cell parameters constant (constrained opt.) and blue represents the fully optimized conformation (full opt.) 38
Figure 4-2. Electron density delocalization and multiple resonance structures after geometry optimization overlaid for (A) $\mathbf{1a_i}$ (red) and $\mathbf{1a_{ii}}$ (blue), (B) $\mathbf{3_i}$ (red), $\mathbf{3_{ii}}$ (green) and $\mathbf{3_{iii}}$ (blue) 40
Figure 4-3. Predicted morphologies for **1a** (A) and **2a** (B) resulting from crystal graphs calculated from an interaction radius of 1 (red), 1.5 (green), and 2 (blue) unit cell distances 42
Figure 4-4. Predicted morphologies for (A) **1a** and (B) **2a** with (red) and without (blue) a minimum energy filter of 0.596 kcal/mol 42
Figure 4-5. Predicted morphologies for **1a** (A) and **2a** (B) generated by the crystal graph (red) and Forcite (blue) energy methods 43
Figure 4-6. Predicted morphologies for **1a** (A) and **2a** (B). The morphology in red was predicted via AE theory and blue corresponds to the BFDH theory 45
Figure 4-7. A) Molecular structure for MOXZEF. B) Predicted morphologies for MOXZEF. The morphology in red was predicted via AE theory and blue corresponds to BFDH theory 45
Figure 4-8. (A) Scanning electron microscopy (SEM) images for **1d** (2.7 mM in acetone). (B) Rheology stress sweep of **1d** (7.18 mM in EtOAC). (C) SEM image of **2b** (13.9 mM in H_2O/EtOH, pH 11.) (D) Rheology stress sweep of **2b** (13.9 mM in H_2O/EtOH, pH 11.) 48

Figure 5-1. Aspect ratios are calculated by generating a crystal graph to assess relative intermolecular interaction in published crystal structures 53
Figure 5-2. Procedure for predicting new gelators developed for this thesis work..... 55
Figure S1-1. ^{1}H and ^{13}C NMR spectra of **2a**..... 63
Figure S1-2. ^{1}H and ^{13}C NMR spectra of **2b**. 64
Figure S1-3. ^{1}H and ^{13}C NMR spectra of **2c**. 65
Figure S1-4. ^{1}H and ^{13}C NMR spectra of **S1** 66
Figure S1-5. Gels of **2a** at their respective critical gel concentrations (cgc) in 1 mL of varying MeOH/H_2O ratios (See Tables S1-1 and S1-2.) 67
Figure S1-6. Selectivity test showing the results of adding aq. solutions of an array of metal acetate salts (0.2 mL, 0.157 M) to a solution of **1a** (10 mg, 0.068 mmol) in MeOH (0.8 mL)..... 68
Figure S1-7. The effect of a chloride source (Bu_4NCl) on **2a** in situ gel above cgc (20 mg/mL). Pictures depict gels 10 minutes after the addition of 0, 0.5, 1, and 2 equiv. of Bu_4NCl 68
Figure S1-8. Crystal structure of **2a.** The torsion angle between the quinoxalinone ligands is 4.41°. The Hg-N bond length is 2.04 Å and the N-Hg-N bond angle is 180.00°. The hydrogen atoms were omitted for clarity 69
Figure S1-9. Solid-state packing of **2a.** The aryl-aryl π stacking distance is 3.54 Å. The intramolecular Hg-O distance is 2.89 Å while the intermolecular Hg-O distance is 2.88 Å. The hydrogen atoms were omitted for clarity 69
Figure S1-10. Crystal structure of S1. The torsion angle between the quinoxalinone ligands is 14.47°. The Hg-N bond length is 2.74 Å and the N-Hg-N bond angle is 180.00°. The hydrogen atoms were omitted for clarity 70
Figure S1-11. Solid-state packing of **S1**. The Hg-Cl bond length is 2.34 Å the intermolecular distance between Hg-Cl atoms is 3.00 Å. The distance between offset aryl rings is 3.78 Å. The hydrogen atoms were omitted for clarity 70
Figure S1-12. SEM images of an in situ gel of **2a** (24 mM) in 90/10 MeOH/H_2O. The images on the right are at a higher magnification..... 71
Figure S1-13. SEM image of a gel of **2a** (complex) (25 mM) in 90/10 MeOH/H_2O. The images on the right are at a higher magnification..... 72

Figure S1-14. SEM image of a gel of **1a** (191 mM) in 90/10 MeOH/H_2O. The images on the right are at a higher magnification 72
Figure S1-15. Powder X-ray diffraction of (a) **2a** precipitated from MeOH, (b) a gel of **2a** (from isolated complex, 90/10 MeOH/H_2O),and (c) simulated from the crystal structure of **2a** 73
Figure S1-16. Powder X-ray diffraction patterns for gels of (a) **2a** (in situ) and (b) **2a** (isolated complex) 73
Figure S1-17. Powder X-ray diffraction patterns for (a) $Hg(OAc)_2$ and (b) **1a** simulated from the crystal structure 74
Figure S1-18. Frequency sweep data under a constant stress (0.2 Pa) for a gel of **2a** (20 mg/mL) in MeOH/H2O (90/10 v/v). The samples are viscoelastic, with the storage modulus (G') 5 times larger than loss modulus (G'') 75
Figure S1-19. Left: Strain sweep data for a gel of **2a** (20 mg/mL, 90/10 MeOH/H2O) acquired under constant frequency (1 Hz). The gel network completely breaks down above strain of 0.1%. Right: Oscillatory stress sweep measurements for a gel of 2a (20 mg/mL, 90/10 MeOH/H2O) under constant frequency (1 Hz). The gel network completely breaks down at a stress of 3.7 Pa 75
Figure S1-20. Calibration curve for ICP-OES detection of Hg^{2+} 76
Figure S2-1. ^{1}H and ^{13}C NMR spectra of **1a** 87
Figure S2-2. ^{1}H and ^{13}C NMR spectra of **S1** 88
Figure S2-3. ^{1}H and ^{13}C NMR spectra of **1b** 89
Figure S2-4. ^{1}H and ^{13}C NMR spectra of **S2** 90
Figure S2-5. ^{1}H and ^{13}C NMR spectra of **2a** 91
Figure S2-6. ^{1}H and ^{13}C NMR spectra of **S3** 92
Figure S2-7. ^{1}H and ^{13}C NMR spectra of **2b** 93
Figure S2-8. ^{1}H and ^{13}C NMR spectra of **S4** 94
Figure S2-9. ^{1}H and ^{13}C NMR spectra of **2c** 95
Figure S2-10. ^{1}H and ^{13}C NMR spectra of **S5** 96
Figure S2-11. ^{1}H and ^{13}C NMR spectra of **3a** 97
Figure S2-12. ^{1}H and ^{13}C NMR spectra of **S6** 98
Figure S2-13. ^{1}H and ^{13}C NMR spectra of **3b** 99

Figure S2-14. ^{1}H and ^{13}C NMR spectra of **S7** 100
Figure S2-15. ^{1}H and ^{13}C NMR spectra of **4** 101
Figure S2-16. ^{1}H and ^{13}C NMR spectra of **S8** 102
Figure S2-17. ^{1}H and ^{13}C NMR spectra of **5** 103
Figure S2-18. To a solution of **2c** (0.5 mL, 0.02 M, 1 equiv) in DMSO-d_6 in a J. Young NMR tube, o-fluorotoluene (4.2 µL, 1.5 equiv) and **S5** (0.5 mL, 0.04 M, 2 equiv) were added. The J. Young tube was sealed and heated at 100 ºC for 4 d. To determine quinoxalinone exchange, 19F NMR spectra were taken before and after the addition of **S5** and every 24 h 104
Figure S2-19. To a solution of **S4** (0.5 mL, 0.04 M, 2 equiv) in DMSO-d_6 in a J. Young NMR tube, o-fluorotoluene (4.2 µL, 1.5 equiv) and **3a** (0.5 mL, 0.019 M, 1 equiv) were added. The J. Young tube was sealed and heated at 100 ºC for 4 days. To determine quinoxalinone exchange, ^{19}F NMR spectra were taken before and after the addition of **3a** and after heating every 24 h. Manual integration to separate peaks was performed using MestReNova software for Windows 105
Figure S2-19. To a solution of **S4** (0.5 mL, 0.04 M, 2 equiv) in DMSO-d_6 in a J. Young NMR tube, o-fluorotoluene (4.2 µL, 1.5 equiv) and 3a (0.5 mL, 0.019 M, 1 equiv) were added. The J. Young tube was sealed and heated at 100 ºC for 4 days. To determine quinoxalinone exchange, ^{19}F NMR spectra were taken before and after the addition of 3a and after heating every 24 h. Manual integration to separate peaks was performed using MestReNova software for Windows 106
Figure S2-21. Representation of the crystal structure of S6 determined by single crystal X-ray diffraction (SCXRD) 107
Figure S2-22. Representation of a crystal structure of **1a** grown from slow diffusion of H_2O into DMSO. The simulated powder X-ray diffraction (PXRD) pattern can be found in Figure S24, F .....
..... 107
Figure S2-23. Representation of a crystal structure of **1a** grown by slow diffusion of MeOH into H_2O. The simulated PXRD pattern can be found in Figure S24, G 108
Figure S2-24. (I) Diagram showing how various forms of 1a were obtained. (II) PXRD patterns for **1a** (A) heated in MeOH, (B) heated in EtOH, (C) bulk from synthesis, (D)

dry gel, and (E) wet gel in MeOH. (III) Simulated PXRD patterns for crystal structures F and G, shown in Figures S22-23 109
Figure S2-25. (I) Diagram showing how various solid forms of **1b** were obtained. (II) PXRD patterns for 1b (A) heated in MeOH, (B) heated in EtOH, and (C) bulk from synthesis 110
Figure S2-26. (I) Diagram showing how various solid forms of 2a were obtained. (II) PXRD patterns for **2a** (A) heated in MeOH, (B) heated in EtOH, and (C) bulk from synthesis 110
Figure S2-27. (I) Diagram showing how various solid forms of **2b** were obtained. (II) PXRD patterns for **2b** (A) heated in MeOH, (B) heated in EtOH, (C) bulk from synthesis, (D) dry gel formed at cgc in EtOH/HOAc, and (E) wet gel in EtOH/HOAc 111
Figure S2-28. (I) Diagram showing how various solid forms of **2c** were obtained. (II) PXRD patterns for **2c** (A) heated in MeOH, (B) heated in EtOH, (C) bulk from synthesis, (D) dried gel formed at cgc in anhydrous EtOH, and (E) wet gel in anhydrous EtOH 111
Figure S2-29. (I) Diagram showing how various solid forms of **3a** were obtained. (II) PXRD patterns for **3a** (A) heated in MeOH, (B) heated in EtOH, (C) bulk from synthesis, (D) dried gel formed at cgc in EtOH, and (E) wet gel formed at cgc in EtOH 112
Figure S2-30. (I) Diagram showing how various forms of **3b** were obtained. (II) PXRD patterns for **3b** (A) heated in MeOH, (B) heated in EtOH, (C) bulk from synthesis, (D) dried gel formed at cgc in EtOH, and (E) wet gel formed at cgc in EtOH 112
Figure S2-31. (I) Diagram showing how various solid forms of **4** were obtained. (II) PXRD patterns for **4** (A) heated in MeOH, (B) heated in EtOH, and (C) bulk from synthesis 113
Figure S2-32. (I) Diagram showing how various solid forms of **5** were obtained. (II) PXRD patterns for **5** (A) heated in MeOH, (B) heated in EtOH, and (C) bulk from synthesis 113
Figure S2-33. Heat/cool/heat/cool DSC scans of the bulk form of **1a** from synthesis 114
Figure S2-34. Heat/cool/heat/cool DSC scans of **1a** that has been heated in EtOH for 48 h .....
..... 115

Figure S2-35. (A) Microscope images of a DSC pan before sample loading. (B) Microscope Image of the same pan after a suspension of **1a** in MeOH was added, left in air for MeOH to evaporate, then all material was removed and pan was washed with acetone 116
Figure S2-36. van't Hoff plots of (A) **1a**, (B) **1b**, (C) **2a**, and (D) **2b** in MeOH 120
Figure S2-37. van't Hoff plots for (A) **2c**, (B) **3a**, (C) **3b**, (D) **4**, and (E) **5** in MeOH... 121
Figure S2-38. van't Hoff plots for (A) **1a**, (B) **1b**, (C) **2a**, (D) **2b**, (E) **2c**, and (F) **3a** in EtOH .....
..... 122
Figure S2-39. van't Hoff plots for (A) **3b**, (B) **4**, and (C) **5** in EtOH..... 123
Figure S2-40. Plots of all compounds showing (A) ΔH_{diss} and (B) ΔS_{diss} in MeOH. Grey bars represent gelators in this solvent system, while nongelators are shown in white 124
Figure S2-41. Plots of all compounds showing (A) ΔH_{diss} and (B) ΔS_{diss} in EtOH. Grey bars represent gelators in this solvent system, while nongelators are shown in white 125
Figure S2-42. (A) Oscillating stress sweep and (B) frequency sweep of a gel of **2b** formed from the isolated complex (5.3 mM in EtOH/HOAc)..... 126
Figure S2-43. (A) Oscillating stress sweep and (B) frequency sweep of a gel of **2c** formed in situ (22.5 mM in EtOH)..... 127
Figure S2-44. (A) Oscillating stress sweep and (B) frequency sweep of a gel of **3a** formed in situ (15 mM in EtOH)..... 127
Figure S2-45. (A) Oscillating stress sweep and (B) frequency sweep of a gel of **3b** formed in situ (5.9 mM in EtOH)..... 128
Figure S2-46. SEM images of a gel at cgc of **1a** formed in situ in 1 mL of MeOH/H_2O (80/20 v/v) 129
Figure S2-47. SEM images of a gel at cgc of 2b formed from the isolated gelator in 1 mL of EtOH/HOAc..... 129
Figure S2-48. SEM images of a gel of **2c** at cgc formed in situ in 1 mL of EtOH 130
Figure S2-49. SEM images of a gel of **3a** at cgc formed in situ in 1 mL EtOH/HOAc 130
Figure S2-50. SEM images of a gel of **3b** at cgc formed in situ in 1 mL EtOH 130
Figure S2-51. Selectivity tests showing the results of adding solutions of an array of metal acetate salts 131

Figure S2-52. Tolerance tests showing the results of the addition of 0, 0.5, 1, and 2 equiv of NH_4Cl as a chloride source 132
Figure S2-53. Gels and control experiments formed in 80/20 (v/v) of solvent and H_2O where the water was sourced from A) bottled spring H_2O, B) tap H_2O, and C) H_2O from the Huron River in Ann Arbor, MI 133
Figure S2-54. Calibration curve for Hg^{2+} concentration for ICP-OES analysis 135
Figure S2-55. Cartoon of the procedure for the removal of solvent from gels of **1a**, **2c**, **3a**, and **3b**. (A) A gel was formed via the in situ method (Page S40). (B) A spatula was used to gently compress the fibers to release entrapped solvent. (C) Released solvent was removed using a syringe 136
Figure S2-56. Thermogravimetric analysis (TGA) of (A) the bulk form of **1a** (B) the heated form of **1a** in MeOH and (C) the heated form of 1a in EtOH..... 138
Figure S2-57. TGA data for (A) the bulk form of **2b**, (B) the heated form of **2b** in MeOH, and (C) the heated form of **2b** in EtOH..... 139
Figure S2-58. TGA data for (A) the bulk form of **2c** and (B) the heated form of **2c** in MeOH..... 140
Figure S2-59. TGA data for (A) the bulk form of **3a**, (B) the heated form of **3a** in MeOH, and (C) the heated form of **3a** in EtOH..... 141
Figure S3-1. ^{1}H and ^{13}C NMR spectra of **1a**..... 147
Figure S3-2. ^{1}H and ^{13}C NMR spectra of **1b**..... 148
Figure S3-3. ^{1}H and 13C NMR spectra of **1c** 149
Figure S3-4. ^{1}H and ^{13}C NMR spectra of **1d**..... 150
Figure S3-5. ^{1}H and ^{13}C NMR spectra of **2a**..... 151
Figure S3-6. ^{1}H and ^{13}C NMR spectra of **2b**..... 152
Figure S3-7. Predicted aspect ratios for CIF files included in calculations. BFDH theory values are plotted in red and AE theory values are in blue 173
Figure S3-8. Predicted aspect ratios for CIF files included in calculations. BFDH theory values are plotted in red and AE theory values are in blue 174
Figure S3-9. Molecular diagram and predicted morphology for KUQFAE01 180
Figure S3-11. Molecular diagram and predicted morphology for CIJQOC 180

Figure S3-12. Molecular diagram and predicted morphology for AJOGOW 181
Figure S3-13. Molecular diagram and predicted morphology for NUNXOK..... 181
Figure S3-14. Molecular diagram and predicted morphology for WACCUA 181
Figure S3-15. Molecular diagram and predicted morphology for NAYNUW01 181
Figure S3-16. Molecular diagram and predicted morphology for EFOZUV 182
Figure S3-17. Molecular diagram and predicted morphology for MOXZEF 182
Figure S3-18. Molecular diagram and predicted morphology for ETUJOT. 183
Figure S3-19. Resonance structures of 3 used in morphology calculations. Structures **3**$_{i}$, **3**$_{ii}$, and **3**$_{iii}$ were used to predict morphologies in Error! Reference source not found.. 184
Figure S3-20. Predicted morphologies for resonance structures **3**$_{i}$ (red), **3**$_{ii}$ (green), and **3**$_{iii}$ (blue). 184
Figure S3-21. Resonance structures for **1a** used in morphology calculations. Resonance structures **1a**$_{i}$ and **1a**$_{ii}$ correspond to predicted morphologies in Figure S3-22. 185
Figure S3-22. Predicted morphologies for resonance structures **1a**$_{i}$ (red) and **1a**$_{ii}$ (blue) 185
Figure S3-23. (A) Frequency sweep and (B) oscillating stress sweep of a gel of **1d** (7.18 mM in EtOAc). 187
Figure S3-24. (A) Frequency sweep and (B) oscillating stress sweep of a gel of **2b** (13.9 mM in H_2O/EtOH solution, pH=11). 188
Figure S3-25. SEM image of **1a** (2.7 mM) in acetone..... 189
Figure S3-26. SEM image of **2b** (13.9 mM) in a H_2O/EtOH solution, pH=11. 189

List of Tables

Table 2-1. Critical gel concentrations for **1a** and **2a**. 14
Table 3-2. Critical gel concentrations (cgcs) in select solvents. 23
Table 4-3. Bond lengths and angles for **1a**. 38
Table 4-4. Bond lengths and angles for **2a**. 39
Table 4-5. Optimized and unoptimized bond lengths for the forms of **1a** found in Chart 4-5. 41
Table 4-6. Optimized and unoptimized bond lengths for the forms of **3** found in Chart 4-5. 41
Table 4-5. Data on the predicted morphology of **1a** calculated in via the crystal graph and Forcite energy methods 43
Table 4-7. Data on the predicted morphology of **2a** calculated in via the crystal graph and Forcite energy methods. 44
Table 4-7. Data for the predicted morphologies in the top 5% of aspect ratios, including normalized lattice energies, aspect ratio, and the attachment energies of the smallest and largest faces 46
Table 4-8. Critical gelation concentration data for **1d** and **2b**. 47
Table S1-1. Cgcs of **2a** (complex) in 1 mL of varying MeOH/H_2O ratios at 25 °C. 67
Table S1-2. Cgcs of **2a** (in situ) in 1 mL of varying MeOH/H_2O ratios at 25 °C. The molarities were calculated assuming quantitative formation of **2a**. 67
Table S1-3. Cgcs of **1a** in 1 mL of varying MeOH/H_2O ratios at 25 °C 68
Table S1-4. ICP-OES data of the mercury concentration remaining after gelation. 76
Table S2-1. Summary of cgcs for all gels. The solvent marked EtOH/HOAc refers to 1 mL of EtOH with 10 µL of HOAc added to increase gelator solubility. 117
Table S2-2. Summary of all solvents used in screening for gels of **1a** identified using HSPiP software. The solvents used to generate the sphere are indicated below with either (+) for those marked as soluble and (-) for those marked as insoluble. The

solution parameters are listed, as well as the RED. 118
Table S2-3. Summary of dissolution enthalpies and entropies for complexes **1**–**5**. ... 123
Table S2-4. Data for the in situ gel formation for **3a** with three different water sources. Controls were performed in identical conditions without additional $Hg(OAc)_2$ but are not included in the data below. 133
Table S2-5. Data for the in situ gel formation for **1a** with three different water sources. Controls were performed in identical conditions without additional $Hg(OAc)_2$ but are not included in the data below. 134
Table S2-6. Summary of data for ICP-OES analysis. The notation, $[Hg^{2+}]_d$, is the detected concentration of Hg^{2+} by the instrument, and $[Hg^{2+}]_a$ is the concentration of Hg^{2+} calculated for the entire sample. 137
Table S3-9. Unit cell parameters before and after full, unconstrained Forcite calculations. 166
Table S3-10. Data for interactions present in compounds that showed a 75% or larger change in aspect ratio when calculated by the AE method compared to the BFDH method. 174
Table S3-11. Predict BFDH aspect ratios (BFDH AR), as well as energy of crystallization (Elatt) and attachment energy aspect ratios (AE AR) for all CIF files after a constrained (Const.) and unconstrained (Unconst.) geometry optimization. Also contains predicted AE AR with partial bonding to represent electron delocialization after an unconstrained geometry optimization. 175
Table S3-12 Predicted aspect ratios and lattice energies for the highest 5% of predicted aspect ratios, sorted smallest to largest. Normalized E_{latt} is the energy per molecule in the unit cell. 180
Table S3-13. Bond length data and predicted aspect ratios for structures unoptimized 1a (from CIF file), and optimized $\mathbf{3}_{i}$, $\mathbf{3}_{ii}$, and $\mathbf{3}_{iii}$. 184
Table S3-14. Bond length data and predicted aspect ratios for unoptimized **1a** (from CIF file), and optimized $\mathbf{1a}_{i}$ and $\mathbf{1a}_{ii}$. 185
Table S3-15. Cgcs for gelators **1d** and **2b** in various solvent conditions. 186

List of Schemes

Scheme 1-1. 4
Scheme 1-2. 4
Scheme 1-3. 6
Scheme 2-3. 13
Scheme 5-4. 54

List of Charts

Chart 1-1. 3
Chart 1-2. 3
Chart 3-3 21
Chart 4-4 38
Chart 4-5 40
Chart 4-6 47
Chart 5-7 51
Chart 5-8 52
Chart 5-9 54

List of Appendices

Appendix 1. Supporting Information for Chapter 2 57

Appendix 2. Supporting Information for Chapter 3 78

Appendix 3. Supporting Information for Chapter 4 144

Abstract

Low molecular weight gels are self-assembled materials comprised of a fiberous structure that is able to immobilize a liquid phase. Gels can be triggered by an external stimulus, which gives rise to proposed applications such as sensing. The causes for gelation are not well understood. It is hypothesized that one dimensional (1D) intermolecular interactions cause aggregation into a fiber-like structure. This thesis details our efforts to understand how intermolecular interactions in the solid state can be used to predict new gelators and how those gels can be used for practical applications.

Chapter 2 describes the discovery of a new Hg-containing gelator (Hg(2-(1H)-quinoxalinone)$_2$) by identifying prominent 1D intermolecular interactions in solid state packing structures accessed from Cambridge Structural Database. This gelator has potential for application in sensing and environmental remediation. The gel can be triggered selectively by the addition of mercury ions, but is unstable to chloride.

Chapter 3 details a structure-property relationship study on five gelators and four nongelators obtained by structural modification of Hg(2-(1H)-quinoxalinone)$_2$,. These compounds exhibit multiple solid-state forms. It has been demonstrated that dissolution enthalpies are higher for gelators than nongelators. The influence of multiple forms on dissolution enthalpy was investigated, but we concluded that dissolution enthalpies must be measured on forms matching the gel to have meaningful results. Nevertheless, a new chloride-tolerant gelator was discovered that gelled a solution of river water.

Chapter 4 illustrates the development of a widely-applicable method to identify new gelators using information in solid-state packing structures. Morphologies of Pb^{2+}-containing CIF files were predicted using the attachment energy theory. We hypothesized that high predicted aspect ratios would be the result of 1D intermolecular interactions and could lead to classes of molecules that contain gelators. Two gelators were identified from the top 5% of aspect ratios. The influence geometry optimization parameters and other factors on the computational model were thoroughly investigated.

This work represents an investigation of how intermolecular interactions direct self-assembly and how this information can be used to identify new gelators.

Chapter 1. Introduction.

Low molecular weight (LMW) gels are formed by the self-assembly[1] of small molecules into a fibrous network that is able to entrap and immobilize solvent.[2,3] This process creates a unique, biphasic, reversible material that has been considered for use in a variety of applications, such as crystallization media and catalysis.[4,5] Interestingly, the self-assembly process can be induced by an external stimulus, such as ion addition[6,7] or a change in pH or temperature.[8–10] This ability has inspired our group[11–13] and others[14] to investigate the use of gels for sensors and environmental remediation materials.

Sensing is an important tool for maintaining healthy food and drinking water. Instrumental analysis is the state of the art for environmental sensing. Extremely sensitive techniques have been developed to sense for a variety of analytes. For example, cold-vapor atomic absorption can sense mercury in water on a parts per quadrillion level. The downside to these techniques is that instrumentation is often expensive, large, and requires a trained operator, which limit the use of these techniques in the field. To address this issue, attempts have been made to develop chemical-based sensors that are portable, inexpensive, sensitive, and selective.[15–17] Many of these methods rely on a colorimetric or fluorescent response, but samples with background color or fluorescence could interfere with data interpretation. Gels have the advantage of being portable for use in the field, relatively cheap, and easy to use, unlike instrumental analysis. Gels also provide a distinct positive signal even for an analyte that has background fluorescence or is highly colored, unlike colorimetric or fluorescent sensors. In the example of analyte-triggered gelation for use in a gel-based sensor that can be seen in Figure 1-1, a thiol non-gelling precursor is oxidized by an explosive,

triacetone triperoxide (TATP), into a disulfide gelator. The gelator molecules can then assemble into a gel, providing an unambiguous positive readout.

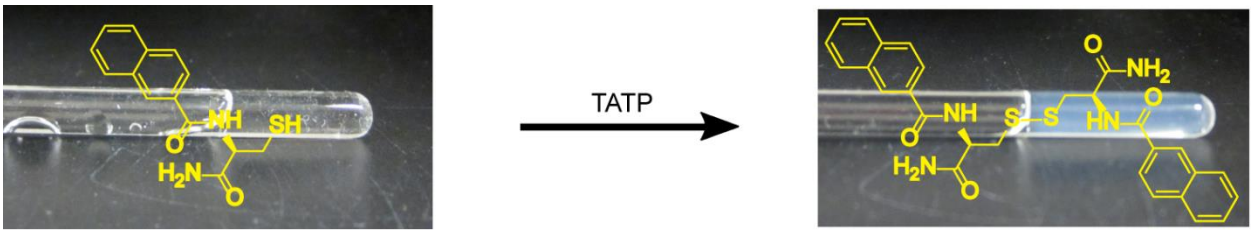

Figure 1-1. A thiol non-gelling precursor is oxidized by TATP into a disulfide gelator.[13]

Gelators have been identified for a variety of molecular scaffolds. A small sampling of some of the architectures that have been published in the literature can be seen in Chart 1-1.[11,18–24] Gel formation cannot be attributed to a specific molecular structure or functional group. The large variety of molecular structure means that LMW gelators can be tuned to a number of different applications. It also means that discovering these materials can be difficult, which limits their utility. A priori design of gelators remains the biggest challenge in the field and most gelators are discovered serendipitously. Small, seemingly insignificant changes to a molecular structure can have a drastic effect on the ability of a molecule to gel.[25,26] This observation is important because many examples of developing “libraries” of gelators related by structure are produced in this way. Because it is not understood why certain changes lead to gelators while others do not, this process is wasteful and time-consuming. The example pictured in Chart 1-2 illustrates the complicated relationship between gelators and nongelators. Moving the chloro-group from position 6 to position 7 on the quinoxalinone ligand results in a different gelator, but if a bromo-substituent is used instead of the chloro-substituent, the same trend is not observed.[27] An understanding of the differences between gelators and nongelators is necessary to tune and design these materials for future applications.

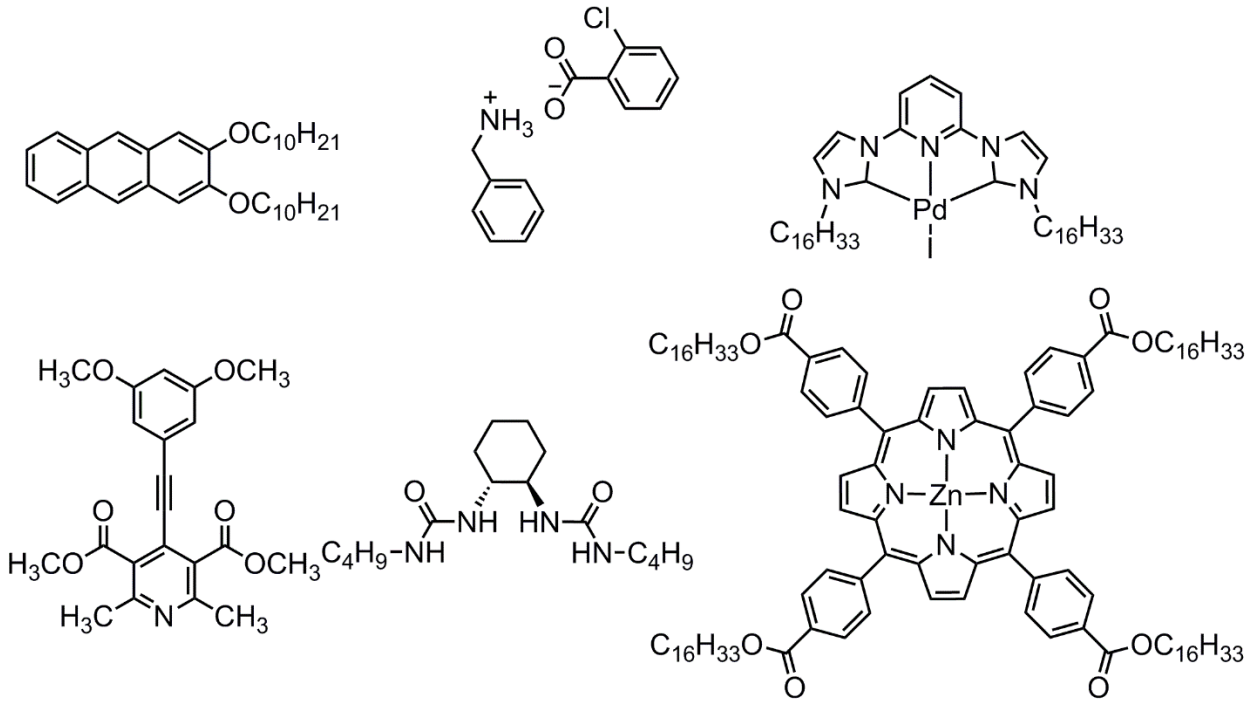

Chart 1-1.

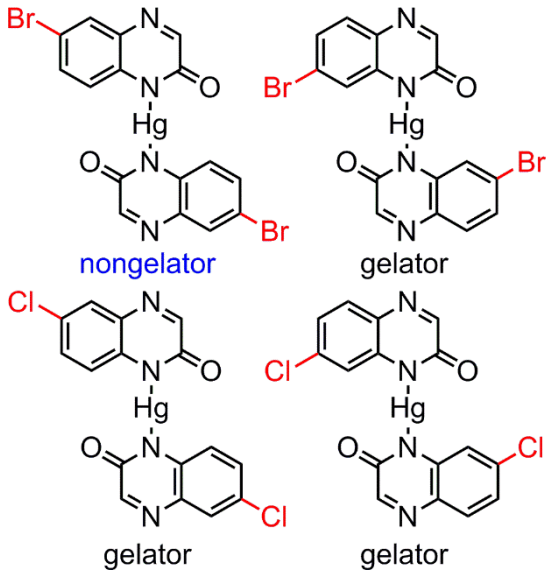

Chart 1-2.

Other attempts at designing these materials generally follow one of two methods: appending a known gelator unit or designing systems with a high likelihood of possessing 1D intermolecular interactions. As cholesterol is a known gelator, it has been commonly utilized in the first approach (Scheme 1-1).[28] Cholesterol has been

appended to many structures, such as metalloenes,[29] aromatics,[30] and salts,[31] among others,[32] to create new gelators. Even so, this method does not always lead to gelation.

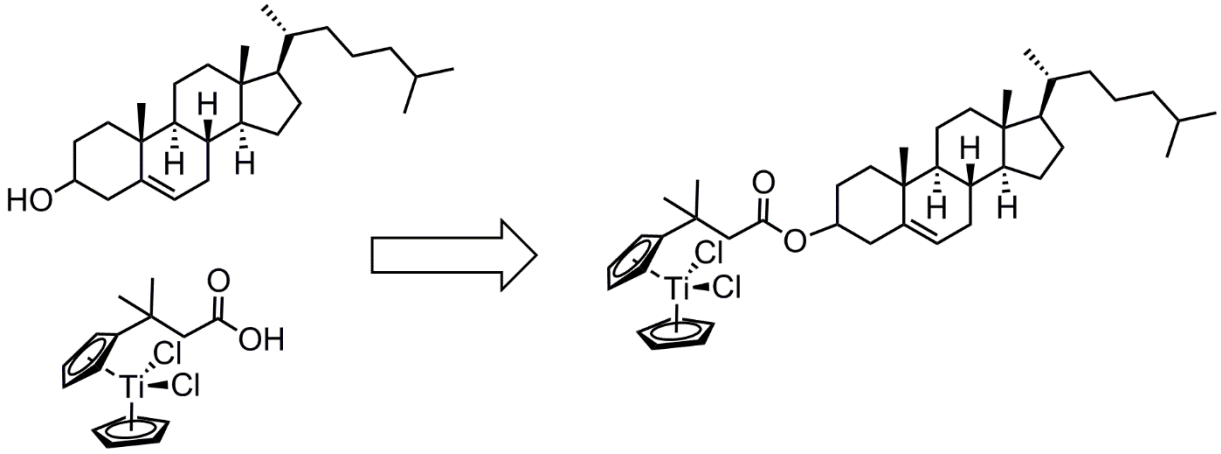

Scheme 1-1.

The second method has been termed the “crystal engineering” approach because it uses building blocks that have been demonstrated to exhibit a specific intermolecular interaction, called supramolecular synthons. Dastidar and coworkers[20,33] have primarily focused on a relatively strong ionic interaction by mixing carboxylic acids and amines (Scheme 1-2). By focusing on this interaction, a large library of salts has been developed, but gelation is only observed approximately 30% of the time.[33]

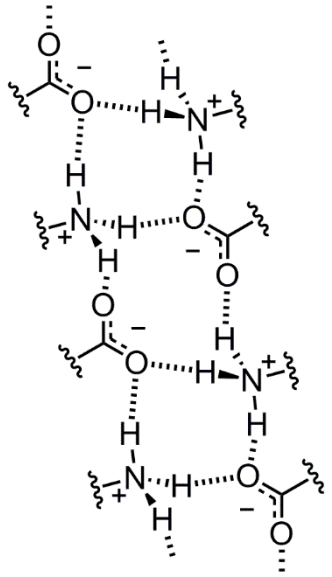

Scheme 1-2. Ionic interactions observed in some salt-based gelators.[33]

Before gelator design can truly be reproducible and controlled, it is necessary to understand how and why gels form. Crystallization and gelation are precipitation-based processes. In both cases, supersaturation forces molecules into contact until aggregation begins to occur.[34,35] Figure 1-2 shows the proposed mechanism of self-assembly to form a fiber-network often observed in gels.[2] The major hypothesis in the field of gelation, proposed by Hanabusa and coworkers, states that molecules that form gels possess anisotropic intermolecular interactions, which direct molecules to assemble primarily along one axis to produce fiber-like aggregates.[36,37] These anisotropic intermolecular interactions are referred to as one-dimensional or 1D. Understanding how discrete, unconnected molecules self-assemble into a fiber-like aggregate could hold the key to designing gelators.

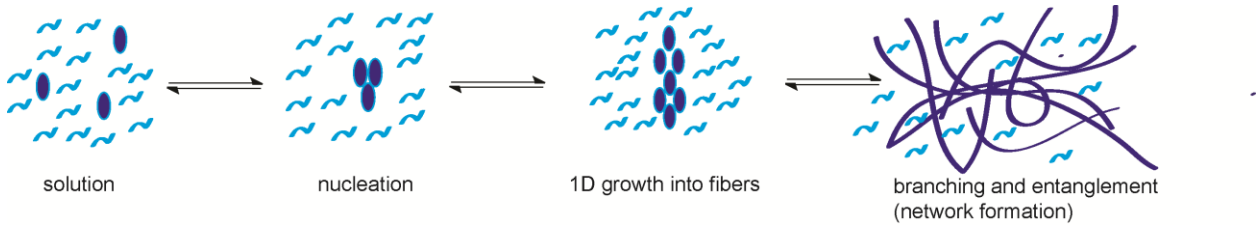

Figure 1-2. Proposed self-assembly mechanism for fiber formation. The wavy lines represent solvent and the blue ellipses represent gelator molecules.[2,34]

We propose that the relationship between crystallization and gelation can benefit the gel discovery process.[33,38,39] By identifying and targeting compounds that possess prominent 1D interactions in the solid state, we hypothesize that gelators can be identified more quickly. To investigate this idea, we proposed to start with known, published crystal structures accessed from the Cambridge Structural Database (CSD). Crystal structures were examined by two methods for promising intermolecular interactions to select targets, as will be discussed in the second and fourth chapters of this dissertation.

The differences between gelators and nongelators can be extremely subtle and few structure-gelation relationship investigations can be applied universally.[40] Weiss and coworkers[41–46] endeavored to study gels on a molecular level by focusing on a structurally simple gelator, hydroxystearic acid (HSA). By changing the position of the secondary hydroxy-group, they observed five gelators (positions 6, 8, 10, 12 and 14) and two nongelators (positions 2 and 3). They demonstrated packing arrangements

supported by FT-IR and X-ray diffraction data, in which the gelators were able to form an extended 1D intramolecular hydrogen-bonding network and the nongelators do not.[43] Scheme 1-3 shows the packing arrangements for 2HSA (a nongelator) and 6HSA (a gelator). While understanding simple systems on a molecular level can provide valuable information about gel self-assembly, there is always a risk that competing factors introduced with increased complexity could change the system.

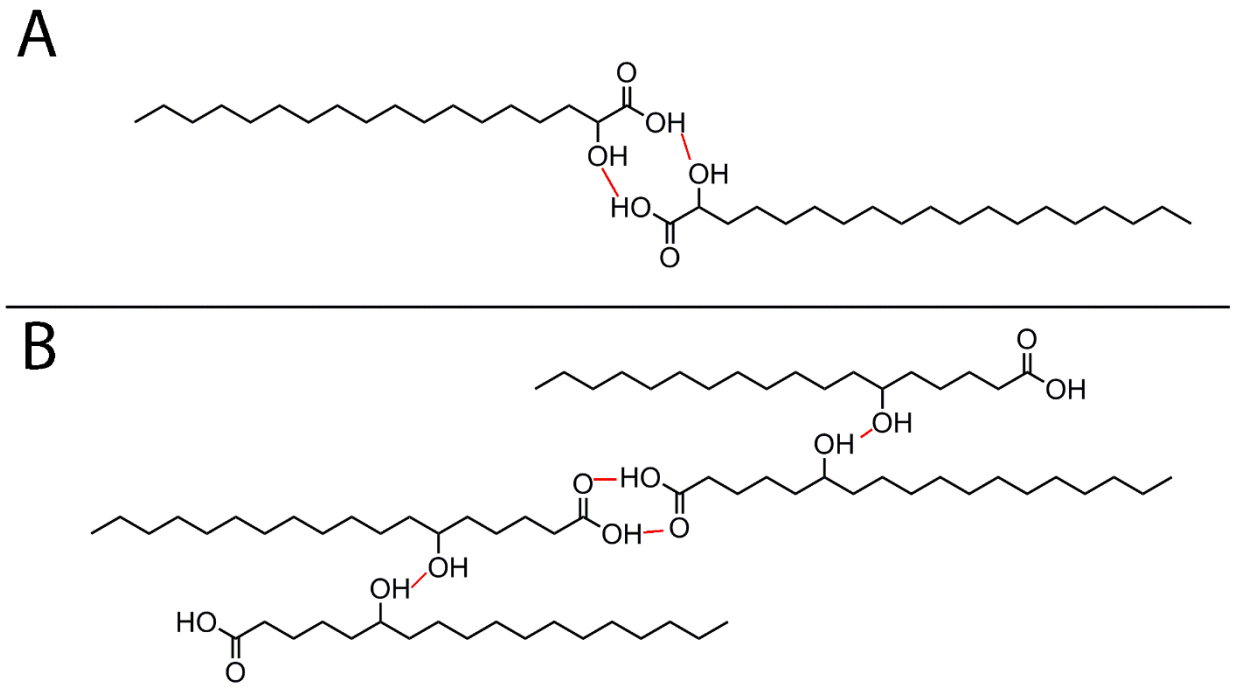

Scheme 1-3.

As gelation is a precipitation process, many researchers point to the moderate solubility of gelators in certain solvents as a major influence over a molecule's ability to form a gel. It is argued that because most gelators are only moderately soluble, the rate of nucleation and precipitation is altered to favor the kinetically trapped, metastable gel form instead of the thermodynamically favored crystal.[47] Evidence from our group shows that solubility is not the only factor at play in this scenerio. For a family of pyridine-based molecules containing gelators and nongelators, the solubilities were measured at room temperature. As seen in Figure 1-3, the values are similar for both gelators and nongelators, implying that solubility alone is not enough to distinguish gelators from nongelators.[48]

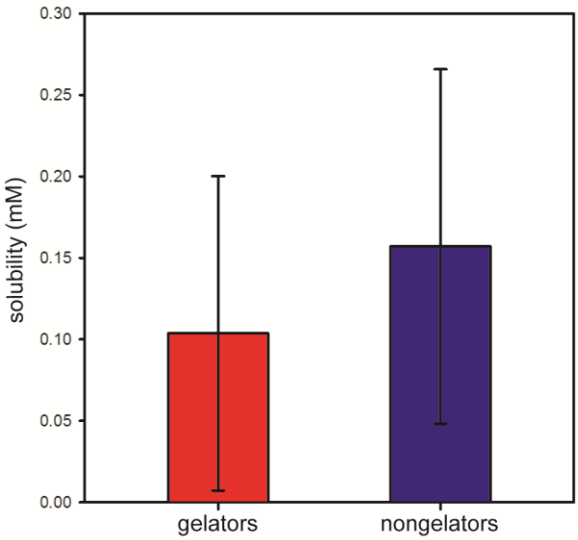

Figure 1-3. Average solubility (mM) of pyridine-based gelators (red) and nongelators (blue) measured at room temperature.

Similar investigations were performed for other attributes that could potentially play a role in gelation, such as π-stacking distance, and comparisons of Hirshfield surfaces, but no distinction could be found between gelators and nongelators. The only significant identifying feature was found by measuring the solubility of each pyridine at various temperatures, then using van't Hoff analysis to determine the thermodynamics of dissolution. Average dissolution enthalpies for gelators were statiscally significantly higher on average than nongelators (Figure 1-4). It was proposed that solid-solid gelator interactions molecules are stronger and/or solute-solvent gelator are weaker than the analogous interactions involving nongelators.[48] This observation represents the first definitive difference identified to distinguish gelators and nongelators. It was established for not only the family of pyridine-based gelators and nongelators, but also for a structurally different class of dipeptide-based molecules, both in two separate solvent systems. The only limitation identified was that in all of these cases, the solid-state packing structures, as identified by powder X-ray diffraction (PXRD), of the bulk material and the gel matched in every case. As this condition is not always observed in gels, as shown in Figure 1-5, further work was necessary to investigate the limits of this new trend, which will be discussed in the third chapter of this dissertation. Knowledge of the limitations of a method to distinguish potential gelators from nongelators will be useful for future attempts to identify new gelators.

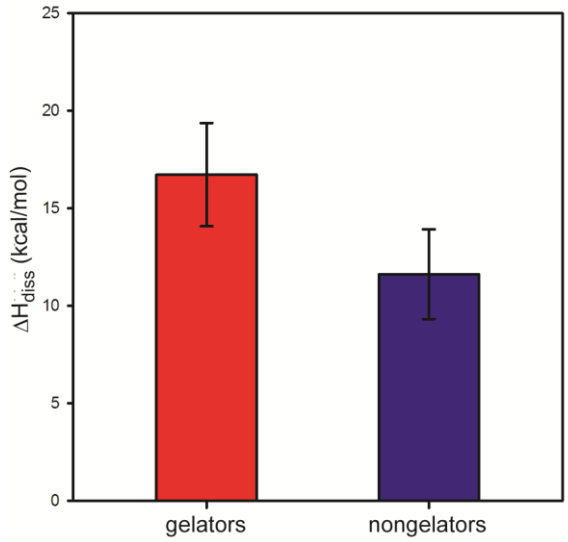

Figure 1-4. Enthalpy of dissolution (ΔH_{diss}) for pyridine-based gelators (red) and nongelators (blue). A T-Test determined that the average dissolution enthalpy for gelators were statistically different from that of nongelators.

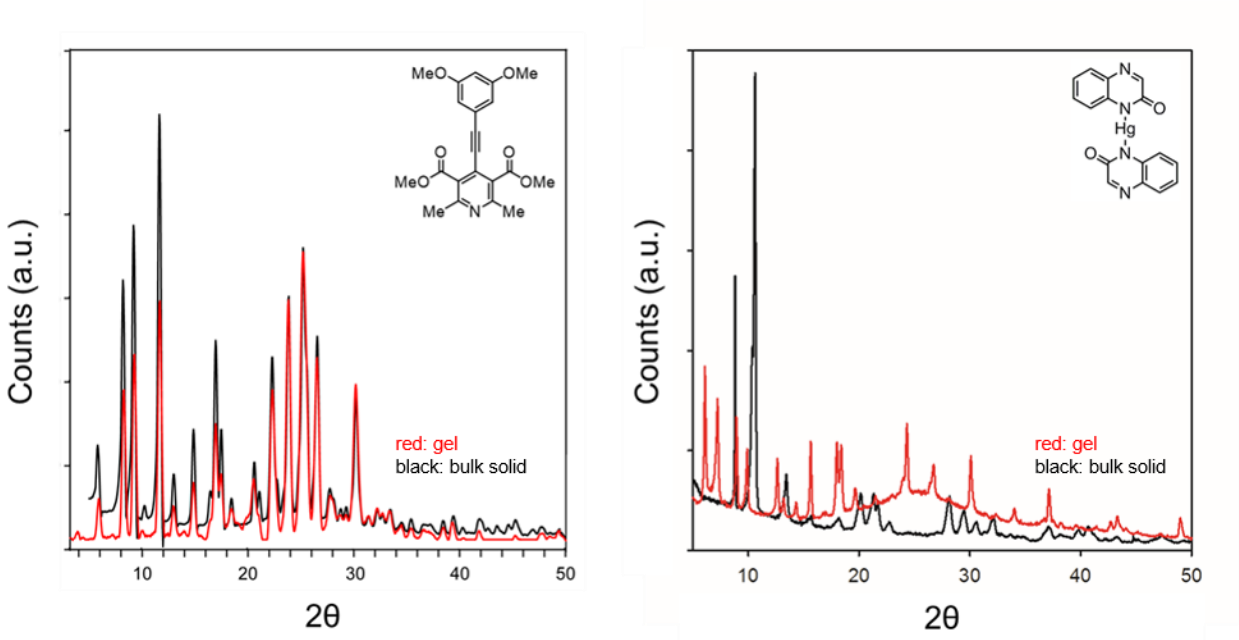

Figure 1-5. PXRD data for two gelators. The red line represents data for the gel form, while the black represents the bulk solid from synthesis.

Conclusions

This dissertation details my work on the discovery and application of new, metal-containing LMW gels. Our efforts capitalize on the relationship between gelation and crystallization. We hypothesized that one dimensional intermolecular interactions in the

solid state could be used to direct screening to increase the likelihood of discovering new gelators. To demonstrate this idea, we approached it in two different ways: by examination of intermolecular interactions both visually and computationally from previously-published crystal structures. The computational approach utilizes Materials Studio, a common commercially available software program, and shows the potential to be the first-ever universal method to identify new gelators. We also investigated structure-property relationships between structurally related gelators and nongelators, specifically the observed tend that the dissolution enthalpy for gelators is greater than that of nongelators. We sought to gain an understanding of what makes gelators different from nongelators, which could aid in designing these materials in the future. Finally, we applied these materials as environmental remediation devices and sensors due to their stimulus-responsive properties. The gel-based sensors and remediators showed the potential to be selective, portable devices with many advantages compared to instrumental analysis.

---

[1] Whitesides, G. M.; Grzybowski, B. *Science* **2002**, *295*, 2418–2415.

[2] Caran, K. L.; Lee, D.-C.; Weiss, R. G. In Soft Fibrillar Materials: fabrication and applications; Liu, X.-Y., Li, J.-L., Eds.; Wiley-VCH Verlag: Weinheim, 2013.

[3] de Loos, M.; Feringa, B. L.; van Esch, J. H. *Eur. J. Org. Chem.* **2005**, 3615–3631.

[4] Steed, J. W. *Chem. Commun.* **2011**, *47*, 1379–1383.

[5] Garner, C. M.; Terech, P.; Allegraud, J.-J.; Mistrot, B.; Nguyen, P.; de Geyer, A.; Rivera, D. *J. Chem. Soc., Faraday Trans.* **1998**, *94*, 2173–2179.

[6] Maeda, H. *Chem. Eur. J.* **2008**, *14*, 11274–11282.

[7] Piepenbrock, M.-O. M., Lloyd, G. O.; Clarke, N.; Steed, J. W. *Chem. Rev.* **2010**, *110*, 1960–2004.

[8] Yang, X.; Zhang, G.; Zhang, D. *J. Mater. Chem.* **2012,** *22*, 38–50.

[9] Banerjee, S.; Das, R. K.; Maitra, U. *J. Mater. Chem.* **2009**, *19*, 6649–6687.

[10] Hirst, A. R.; Escuder, B.; Miravet, J. F.; Smith, D. K. *Angew. Chem. Int. Ed.* **2008**, *47*, 8002–8018.

[11] Chen, J; McNeil, A. J. *J. Am. Chem. Soc.* **2008**, *46,* 16496–16497.

[12] Bremmer, S. C.; McNeil, A. J.; Soellner, M. B. *Chem. Commun.* **2014**, *50*, 1691–1693.

[13] Chen, J.; Wu, W.; McNeil, A. J. *Chem. Commun.* **2012**, *48*, 7310-7312.

[14] Hemamalini, A.; Das, T. M. *New J. Chem.* **2013**, *37*, 2419–2425.

[15] Askim, J. R.; Mahmoudi, M.; Suslick, K. S. *Chem. Soc. Rev.* **2013**, *42*, 8649–8682.

[16] Zhang, X.; Yin, J.; Yoon, J. *Chem. Rev.* **2014**, *114*, 4918–4959.

[17] Kim, H. N.; Ren, W. X.; Kim, J. S.; Yoon, J. *Chem. Soc. Rev.* **2012**, *41*, 3210–3244.

[18] Kiyonaka, S.; Shinkai, S.; Hamachi, I. *Chem. Eur. J.* **2003**, *9*, 976–983.

[19] Placin, F.; Colomes, M.; Desvergne, J.-P. *Tetrahedron Lett.* **1997**, *38,* 2665-2668.

[20] Das, U. K.; Trivedi, D. R.; Ardarsh, N. N.; Dastidar, P. *J. Org. Chem.* **2009**, *74,* 7111–7121.

[21] Terech, P; Gebel, G; Ramasseul, R. *Langmuir* **1996**, *12*, 4321–4323.

[22] Yang, Z. M.; Xu, B. *J. Mater. Chem.* **2007**, 1*7,* 850–854.

[23] Tu, T.; Assenmacher, W.; Peterlik, H.: Weisbarth, R.; Niger, M.; Dotz, K.H. *Angew. Chem. Int. Ed.* **2007**, *46*, 6368–6371.

[24] Van Esch, J.; Schoonbeek, F.; de Loos, M.; Kooijman, H.; Spek, A. L.; Kellogg, R. M.; Feringa, B. L. *Chem. Eur. J.* **1999**, *5*, 937–950.

[25] Chen, L.; Revel, S.; Morris, K.; Serpell, L. C.; Adams, D. J. *Langmuir* **2010**, *26*, 13466–13471.

[26] Kumar, K. K.; Elango, M.; Subramanian, V.; Das, T. M. *New. J. Chem.* **2009**, *33*, 1570–1577.

[27] Carter, K. C.; Rycenga, H. B.; McNeil, A. J. *Langmuir* **2014**, *30*, 3522–3527.

[28] Klawonn, T.; Gansauer, A.; Winkler, I.; Lauterbach, T.; Franke, K.; Nolte, R. J. M.; Feiters, M. C.; Broner, H.; Hentschel, J.; Dotz, K. H. *Chem. Commun.* **2007**, 1894–1895.

[29] He, Panli; Liu, J.; Liu, K.; Ding, L; Yan, J.; Gao, D.; Fang, Y. *Coll. Surf. A: Physiochem. Eng. Aspects* **2010**, *362*, 127–134.

[30] Yu, C.; Xue, M.; Liu, K.; Wang, G.; Fang, Y. *Langmuir* **2014**, *30*, 1257–1265.

[31] Lu, L.; Weiss, R. G. *Langmuir* **1995**, *11*, 3630–3632.

[32] van Herpt, J. T.; Areenphong, J.; Stuart, M. C. A.; Browne, W. R.; Feringa, B. L. *Chem. Eur. J.* **2014**, *20*, 1737–1742.

[33] Adaldar, T. K.; Dastidar, P. *Cryst. Growth Des.* **2014**, *14*, 2254–2262.

[34] Weiss, R. G. *J. Am. Chem. Soc.* **2014**, *136*, 7519–7530.

[35] Gelation is extremely solvent dependent. Recent work in the literature has shown that gelators will gel solvents with similar parameters. For information on this topic, please see: Lan, Y. L.; Corradini, M. G.; Liu, X.; May, T. E.; Borondics, F.; Weiss, R. G. *Langmuir* **2014**, ASAP.

[36] Hanabusa, K.; Yamada, M.; Kimura, M.; Shirai, H. *Angew. Chem.* **1996**, *35*, 1949–1951.

[37] Shirakawa, M.; Fujita, N. Shinkai, S. *J. Am. Chem. Soc.* **2005**, *127*, 4162–4163.

[38] Das, U. K.; Trivedi, D. R.; Adarsh, N. N.; Dastidar, P. *J. Org. Chem.* **2009**, *74*, 7111–7121.

[39] Sahoo, P.; Kumar, D. K.; Trivedi, D. R.; Dastidar, P. *Tetrahedron. Lett.* **2008**, *49*, 3052–3055.

[40] de Loos, M.; van Esch, J. H.; Kellogg, R. M.; Feringa, B. L. *Tetrahedron* **2007**, *63*, 7285–7301.

[41] Mallia, V. A.; Weiss, R. G. *J. Pys. Org. Chem.* **2014**, *27*, 310–314.

[42] Toro-Vazquez, J. F.; Morales, Rueda, J.; Torres-Martinez, A.; Charo-Alonso, M. A.; Mallia, V. J.; Weiss, R. G. *Langmuir* **2013**, *29*, 7642–7654.

[43] Shibu, A.; Lan, Y.; Lam, R. S. H.; Grahame, D. A. S.; Kim, J. J. H.; Weiss, R. G.; Rogers, M. A. *Langmuir* **2012**, *28*, 4955–4964.

[44] Grahame, D. A. S.; Olauson, C.; Lam, R. S. H.; Pederson, T.; Borondics, F.; Abraham, S.; Weiss, R. G.; Rogers, M. A. *Soft Mater.* **2011**, *7*, 7359–7365.

[45] Mallia, V. A.; George, M.; Blair, D. L.; Weiss, R. G. *Langmuir* **2009**, *25*, 8615–8625.

[46] Huang, X.; Weiss, R. G. *Tetrahedron* **2007**, *63*, 7375–7385.

[47] Hirst, A. R.; Coats, I. A.; Boucheteau, T. R.; Miravet, J. F.; Escuder, B.; Castelletto, V.; Hamley, I. W.; Smith, D. K. *J. Am. Chem. Soc.* **2008**, *130*, 9113–9121.

[48] Chen, J.; Kampf, J. W.; McNeil, A. J. *Langmuir* **2010**, *26*, 13076–13080.

Chapter 2: Streamlined Approach to a New Gelator: Inspiration From Solid-State Interactions for a Mercury-Induced Gelation[a,b]

Molecular gels are a class of organic materials that exhibit solid-like rheological properties despite being mostly composed of liquid.[1–9] These properties originate from their continuous microscopic structure that is formed by non-covalent self-assembly of small molecules. Molecular gels are being widely investigated for diverse applications such as sensing,[10–12,] regenerative medicine,[13–15] and environmental remediation.[16–18] Despite intense research on these materials, the relationship between molecular structure and gelation ability is still poorly understood.[19–21] As a result, designing new gelators remains a significant challenge.

To date, the most successful strategy for creating new gelators has been to modify known gelator scaffolds. In contrast, several de novo design strategies have been proposed by us[10] and others.[20–23] These strategies are based on an early hypothesis by Hanabusa et al.[24] in which it is suggested that an important criterion for developing gelators is to have "intermolecular interactions for building up macromolecule-like aggregates." The implication is that unidirectional (or 1D) interactions should promote 1D self-assembly, leading to the fiber-like morphologies typically observed in molecular gels. This hypothesis has been supported in several cases where predominant 1D interactions observed in gelator single-crystal X-ray structures have been shown to be maintained in the gel fibers by powder X-ray diffraction.[10–29] Yet predicting which molecules will exhibit these interactions remains a significant challenge. We believe that the discovery of new gelators can be streamlined by using the Cambridge Structural Database (CSD)[30] to identify

[a] Reproduced with permission from King, K. N.; McNeil, A. J. "Streamlined Approach to a New Gelator: Inspiration From Solid-State Interactions for a Mercury-Induced Gelation" *Chem. Commun.* **2010**, *46*, 3511-3513. Copyright 2010 Royal Society of Chemistry.

[b] K. N. K. acknowledges Dr. Jeff Kampf for performing X-ray crystallography and Dr. Jing Chen for performing rheology. All other work was performed by K. N. K.

molecular scaffolds which show predominant 1D intermolecular interactions and are easily synthetically modified. As evidence, we describe herein the successful discovery of a new gelator using this approach.

We postulated that Hg^{2+} ions could promote 1D self-assembly and gelation of an aromatic molecule via cation-π interactions. The CSD was searched for molecules that exhibit this interaction and the search led to compound **2c**, reported by Goodgame and co-workers in 1992.[31] The solid-state packing of planar **2c** exhibited 1D aryl-Hg-aryl (π-cation-π) interactions. Based on these predominant 1D interactions, we predicted that either this Hg^{2+} complex or structurally related derivatives may be gelators. In addition, because these cation-π interactions are only available when Hg^{2+} is present, we predicted that the precursor (**1**) would not form gels under the same conditions as **2**.[32–44]

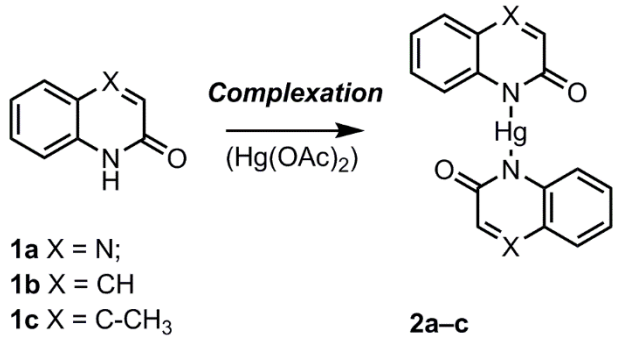

1a X = N;
1b X = CH
1c X = C-CH_3

2a–c

Scheme 2-1. Synthesis of Hg-quinolinones complexes.

Complexes **2a–c** were prepared in high yields (> 80%) from commercially available quinoxalinone **1a** or quinolinones **1b**-**c** and $Hg(OAc)_2$ (Appendix 1).[31] Complex **2a** formed gels in several different MeOH/H_2O mixtures. On the other hand, complexes **2b** and **2c** did not form gels in any of the organic solvent/water mixtures examined. The critical gel concentration (cgc) of **2a** is 25 mM (1.6 wt %) in 90/10 MeOH/H_2O at 25 °C. Gelator **2a** did not form stable gels in mixtures of water with any other organic solvent tested (e.g., DMSO, DMF, acetone, or THF). Although **1a** did form gels in MeOH/H_2O, the cgc was much higher, suggesting that the Hg^{2+} ion is playing an important role in the gelation of **2a** (Table 2-1).

Gelation can be triggered by adding $Hg(OAc)_2$ to **1a** in situ. For example, adding an aqueous solution of $Hg(OAc)_2$ to a hot solution of **1a** in MeOH led to a stable gel

within 10 min (Figure 2-1). A control experiment confirmed that simply adding an equivalent volume of water to **1a** led to precipitation. Comparing the cgc for gels prepared in situ versus those formed with isolated **2a** indicates that the released HOAc has a negligble effect (Table 2-1). The metal-ion induced gelation appears to be specific to Hg^{2+}; independently adding aqueous solutions containing $Co(OAc)_2$, $Ni(OAc)_2$, $Cd(OAc)_2$, $Ba(OAc)_2$, $Cu(OAc)_2$, $Zn(OAc)_2$, or AgOAc to **1a** in MeOH led to precipitation (Appendix 1). Though this Hg-selective gelation could function as a sensor, the sensitivity is too low to be practical (~ 4000 ppm).

Table 2-1. Critical gel concentrations for **1a** and **2a**.[a]

MeOH/H_2O (v/v)	**1a** (mM)	**2a** isolated (mM)	**2a** in situ (mM)
90/10	191 ± 6	25 ± 1	23 ± 2
80/20	162 ± 4	24 ± 2	24 ± 0
70/30	155 ± 4	26 ± 0	22 ± 2
60/40	--	--	21 ± 0

[a] Reported cgcs represent an average of three runs (ESI).

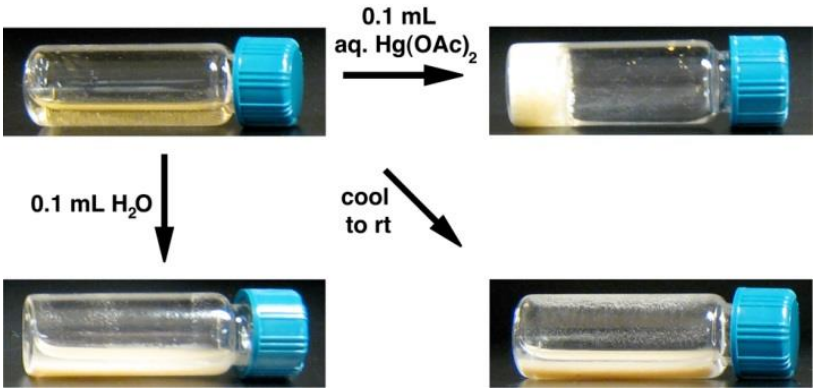

Figure 2-1. Adding an aqueous solution of $Hg(OAc)_2$ to **1a** in hot MeOH (upper left) leads to gel formation (upper right). Control experiments show that simply adding an equivalent volume of H_2O (lower left) or cooling to rt (lower right) results in precipitation.

The gel microstructure consists of bundles of high-aspect-ratio fibers as shown via scanning electron microscopy (Figure 2-2). Rheological measurements confirmed that **2a** forms a viscoelastic gel-like material (Appendix 1). X-ray quality single-crystals of **2a** were obtained from DMSO/H_2O solutions. Surprisingly, X-ray diffraction analysis revealed that the predominant intermolecular interactions were π-

stacking between the quinoxalinones (3.54 Å) and not the cation-π interactions as anticipated (Figure 2-3). An intermolecular carbonyl-Hg-carbonyl interaction (2.88 Å) was also observed. Powder X-ray diffraction studies revealed that the solid-state packing in the single-crystal (obtained from DMSO/H_2O) is different than the gel fibers (in MeOH/H_2O, see Appendix 1). Thus, cation-π interactions may still be involved in the Hg^{2+}-induced gelation.

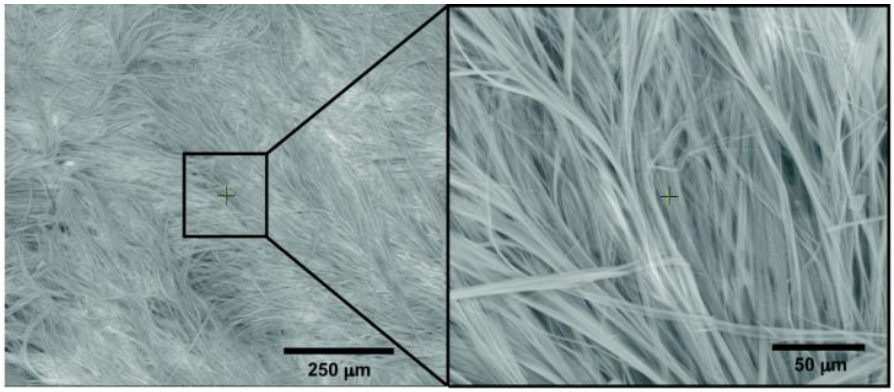

Figure 2-2. Scanning electron micrograph of the in situ gel of **2a** (24 mM) in 90/10 MeOH/H_2O.

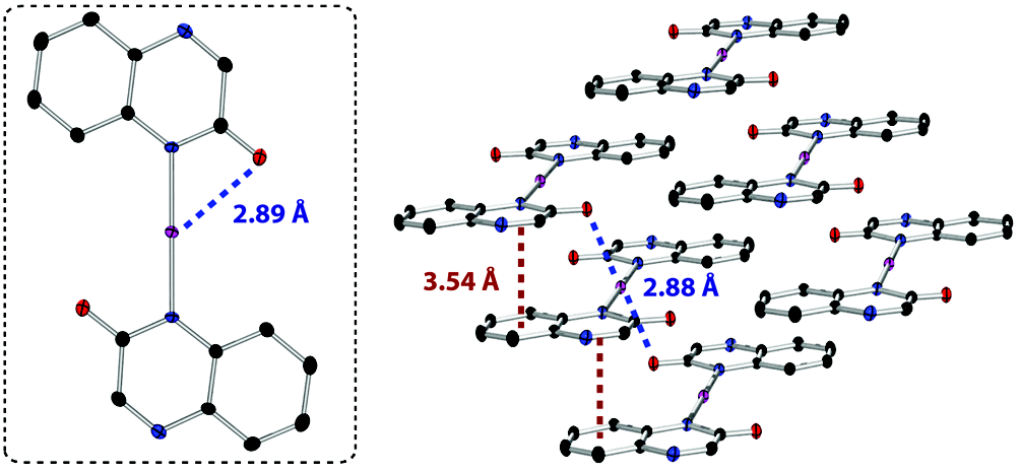

Figure 2-3. Single crystal X-ray structure for **2a**. H-atoms were omitted for clarity.

The role of the counterion was probed by adding an aqueous solution of $HgCl_2$ to **1a** in MeOH. Single-crystal X-ray diffraction analysis on the product revealed that $HgCl_2$ was ligated by two quinoxalinones (Appendix 1). The selective formation of this complex can be understood based on the stronger binding strength of Cl^- than OAc^- to cationic mercury.[45,46] A screen of solvent mixtures and concentrations

revealed that this complex does not form gels under any conditions tested. Interestingly, adding 1 equiv Bu_4NCl to a gel of **2a** resulted in complete breakdown of the gel network (Appendix 1). Such anion-dependent gelations have been observed with other metal complexes.[47–50]

Because molecular gels are mostly composed of liquid, these materials can be utilized to extract pollutants into the solid-phase and a subsequent filtration can recover the liquid.[51,52] Inductively coupled plasma-optical emission spectroscopy was used to determine whether Hg^{2+} can be effectively removed from aqueous solutions with this in situ gelation. Mercury ions are highly toxic, persistant pollutants in several water sources[53] and methods for effectively removing mercury are still needed.[54] Indeed, an impressive reduction in mercury was observed (Appendix 1). For example, a 3800 ppm Hg^{2+}-contaminated water sample was used to form a gel in situ. ICP-OES analysis revealed that 289 ppm Hg^{2+} remained in solution, suggesting that this gel can effectively remove significant quantities of mercury from contaminated water sources.

In summary, a new gelator was discovered via a straightforward method which involves identifying molecular scaffolds that show predominant 1D intermolecular interactions in the solid-state, synthesizing derivatives, and testing for gelation ability. Importantly, this approach should prove general for a variety of intermolecular interactions and greatly accelerate the discovery of new classes of gelators. Our current efforts are focused on determining the generality of this method.

References:

[1] *Molecular Gels: Materials with Self-Assembled Fibrillar Networks*, ed. R. G. Weiss and P. Terech, Springer, Dordrecht, The Netherlands, 2006

[2]D. K. Smith, *Molecular Gels - Nanostructured Soft Materials in Organic Nanostructures*, ed. J. W. Steed and J. L. Atwood, Wiley-VCH, Weinheim, 2008

[3] *Low Molecular Mass Gelator*, Topics in Current Chemistry, Vol. 256, Springer Berlin, Heidelberg, 2005

[4] Banerjee, S.; Das, R. K.; Maitra, U. *J. Mater. Chem*. **2009**, *19*, 6649–6687.

[5] Hirst, A. R.; Escuder, B.; Miravet, J. F.; Smith, D. K. *Angew. Chem. Int. Ed.* **2008**, *47*, 8002–8018.

[6] Sangeetha, N. M.; Maitra, J. *Chem. Soc. Rev.* **2005**, *34*, 821–836.

[7] de Loos, M.; Feringa, B. L.; van Esch, J. H. *Eur. J. Org. Chem.* **2005**, 3615–3631.

[8] Estroff, L. A.; Hamilton, A. D. *Chem. Rev.* **2004**, *104*, 1201–1217.

[9] Terech, P.; Weiss, R. G. *Chem. Rev*. **1997**, *97*, 3133–3159.

[10] Chen, J.; McNeil, A. J. *J. Am. Chem. Soc.,* 2008, **130**, 16496–16497.

[11] Yang, Z.; Ho, P.-L.; Liang, G.; Chow, K. H.; Wang, Q.; Cao, Y.; Guo, Z.; Xu, B. *J. Am. Chem. Soc.* **2007**, *129*, 266–267.

[12] Bhuniya, S.; Kim, B. H. *Chem. Commun.* **2006**, 1842–1844.

[13] Xu, B. *Langmuir* **2009**, *25*, 8375–8377.

[14] Webber, M. J.; Kessler, J. A.; Stupp, S. I., *J. Intern. Med.* **2010**, *267*, 71–88.

[15] Webber, M. J.; Tongers, J.; Renault, M.-A.; Roncalli, J. G.; Losordo, D. W.; Stupp, S. I. *Acta Biomaterialia* **2010**, *6*, 3–11.

[16] Bardelang, D.; Camerel, F.; Margeson, J. C.; Leek, D. M.; Schmutz, M.; Zaman, M. B.; Yu, K.; Soldatov, D. V.; Ziessel, R.; Ratcliffe, C. I.; Ripmeester, J. A. *J. Am. Chem. Soc.* **2008**, *130*, 3313–3315.

[17] Ballabh, A.; Trivedi, D. R.; Dastidar, P. *Chem. Mater.* **2006**, *18*, 3795–3800.

[18] Battacharya, S.; Krishnan-Ghosh, Y. *Chem. Commun*. **2001**, 185–186.

[19] van Esch, J. H. *Langmuir* **2009**, *25*, 8392–8394.

[20] Dastidar, P. *Chem. Soc. Rev.* **2008**, *37*, 2699–2715.

[21] van Esch, J. H.; Feringa, B. L. *Angew. Chem. Int. Ed.* **2000**, *39*, 2263–2266.

[22] The crystal engineering approach has been used by Dastidar et al. to identify new organic salt-based gelators. This approach appends supramolecular synthons (e.g., ammonium dicarboxylates) to organic molecules to enhance 1D interactions. For a

recent example, see: Das, U. K.; Trivedi, D. R.; Adarsh, N. N.; Dastidar, P. *J. Org. Chem*. **2009**, *74*, 7111–7121.

[23] For a review on crystal engineering, see: Desiraju, G. R. *Angew. Chem. Int. Ed.* **2007**, *46*, 8342–8356.

[24] Hanabusa, K.; Yamada, M.; Kimura, M.; Shirai, H. *Angew. Chem. Int. Ed. Engl.,* **1996**, *35*, 1949–1951.

[25] Ballabh, A.; Adalder, T. K.; Dastidar, P. *Cryst. Growth Des.* **2008**, *8*, 4144–4149.

[26] Basit, H.; Pal, A.; Sen, S.; Bhattacharya, S. *Chem. Eur. J*. **2008**, *14*, 6534–6545.

[27] Trivedi, D. R.; Ballabh, A.; Dastidar, P. *J. Mater. Chem.* **2005**, *15*, 2606–2614.

[28] Makarević, J.; Jokić, M.; Raza, Z.; Štefanić, Z.; Kojić-Prodić, B.; Žinić, M. *Chem. Eur. J.* **2003**, *9*, 5567–5580.

[29] Shirakawa, M.; Kawano, S.; Fujita, N.; Sada, K.; Shinkai, S. *J. Org. Chem.* **2003**, *68*, 5037–5044.

[30] For more information, see: www.ccdc.cam.ac.uk/products/csd.

[31] Goodgame, D. M. L.; Hill, S. P. W.; Williams, D. J. *Polyhedron* **1992**, *11*, 1507–1512.

[32] Hirst, A. R.; Smith, D. K. *Chem. Eur. J.* **2005**, *11*, 5496–5508.

[33] Taira, T.; Suzaki, Y.; Osakada, K. *Chem. Commun*. **2009**, 7027–7029.

[34] Mahesh, S.; Thirumalai, R.; Yagai, S.; Kitamura, A.; Ajayaghosh, A. *Chem. Commun.* **2009**, 5984–5986.

[35] Hirst, A. R.; Miravet, J. F.; Escuder, B.; Noirez, L.; Castelletto, V.; Hamley, I. W.; Smith, D. K. *Chem. Eur. J*. **2009**, *15*, 372–379.

[36] Piepenbrock, M.-O. M.; Lloyd, G. O.; Clarke, N.; Steed, J. W. *Chem. Rev*. **2010**, *110*, 1960–2004.

[37] Joshi, S. A.; Kulkarni, N. D. *Chem. Commun*. **2009**, 2341–2343.

[38] Tam, A. Y. Y.; Wong, K. M. C.; Yam, V. W. W. *J. Am. Chem. Soc.* **2009**, *131*, 6253–6260.

[39] Gansäuer, A.; Winkler, I.; Klawonn, T.; Nolte, R. J. M.; Feiters, M. C.; Börner, H. G.; Hentschel, J.; Dötz, K. H. *Organometallics* **2009**, *28*, 1377–1382.

[40] Fages, F. *Angew. Chem. Int. Ed*. **2006**, *45*, 1680–1682.

[41] Cardolaccia, T.; Li, Y.; Schanze, K. S. *J. Am. Chem. Soc.* **2008**, *130*, 2535–2545.

[42] Shirakawa, M.; Fujita, N.; Tani, T.; Kaneko, K.; Ojima, M.; Fujii, A.; Ozaki, M.; Shinkai, S. *Chem. Eur. J.* **2007**, *13*, 4155–4162.

[43] Hahn, U.; Hirst, A. R.; Delgado, J. L.; Kaeser, A.; Delavaux-Nicot, B.; Nierengarten, J.-F.; Smith, D. K. *Chem. Commun.* **2007**, 4943–4945.

[44] Tam, A. Y.-Y.; Wong, K. M.-C.; Wang, G.; Yam, V. W.-W. *Chem. Commun*. **2007**, 2028–2030.

[45] Martin, R. B. *Inorg. Chim. Acta* **2002**, *339*, 27–33.

[46] Schwarzenbach, G.; Schellenberg, M. *Helv. Chim. Acta* **1965**, *48*, 28–46.

[47] Lloyd, G. O.; Steed, J. W. *Nature Chem.* **2009**, *1*, 437–442.

[48] Maeda, H. *Chem. Eur. J.* **2008**, *14*, 11274–11282.

[49] Piepenbrock, M.-O. M.; Clarke, N.; Steed, J. W. *Langmuir* **2009**, *25*, 8451–8456.

[50] Tam, A. Y. Y.; Wong, K. M. C.; Yam, V. W. W. *Chem. Eur. J*., **2009**, *15*, 4775–4778.

[51] Adhikari, B.; Palui, G.; Banerjee, A. *Soft Matter* **2009**, *5*, 3452–3460.

[52] Kar, T.; Debnath, S.; Das, D.; Shome, A.; Das, P. K. *Langmuir* **2009**, *25*, 8639–8648.

[53] For a recent review, see: Selin, N. E. *Annu. Rev. Environ. Resour.* **2009**, *34*, 43–63.

[54] For a recent review, see: Wang, Q.; Kim, D.; Dionysiou, D. D.; Sorial, G. A.; Timberlake, D. *Environ. Pollut.* **2004**, *131*, 323–336.

Chapter 3. Improving Hg-triggered Gelation via Structural Modifications.[a,b]

Molecular gels are a class of organic materials that are garnering interest due to their stimuli-responsive behavior.[1–8] As an example, molecular gel-based materials that respond to the presence of metal ions,[9–11] reductants,[12,13] oxidants,[14,15] and enzymes,[16,17,18] have been developed. Despite extensive research in this field, predicting which molecules will form gels remains a major challenge.[19–23] One hypothesis is that the presence of one-dimensional (1D) intermolecular interactions leads to the preferential 1D growth of gel fibers.[24] Based on this hypothesis, we introduced a new approach for discovering gelators that utilizes the Cambridge Structural Database (CSD) to identify molecules that exhibit these 1D interactions in the solid-state.[25] In short, the CSD was searched for molecules with intermolecular Hg-arene interactions, from which a Hg(quinolinone)$_2$ compound was identified as the lead structure.[26] Three derivatives of this scaffold were then synthesized and screened for gelation. Excitingly, one of these compounds (**1a**) formed gels in water/organic solvent mixtures. This compound served as a remediation agent, removing >90% of Hg^{2+} ions from water samples via gel formation. There were some limitations, however, including the need for an organic co-solvent, the high concentration of gelator needed to form a gel, and the rapid dissolution of the gel in the presence of Cl^- ions.

With the aim of improving this gel-based material, we now report several alternative structures (Chart 3-1, **1b–5**). Because the intermolecular interactions and solid-state packing of the gel form of **1a** were unknown, several different functional groups were examined. Halogens and extended aromatic systems were chosen because of their demonstrated ability to improve gelation of aromatic peptides in water.[17,27–29] We describe herein the synthesis and gel screening of eight new Hg-containing compounds. Four of these compounds were discovered to form gels and their gel properties are reported. Comparing the gelators and nongelators revealed a

[a] Reproduced with permission from Carter, K. C.; Rycenga, H. B.; McNeil, A. J. "Improving Hg-triggered Gelation via Structural Modifications." *Langmuir* **2014**, *30*, 3522-3527. Copyright American Chemical Society 2014.

[b] K. K. C. gratefully acknowledges the contribution of coauthor H. B. R, who contributed the ICP studies and determined cgcs. All other work was performed by K. K. C.

complex set of solid-state structures, which varied based on the preparation method, solvent, and temperature. One of the gelators (**3a**) exhibited marked improvement in Hg^{2+} remediation, removing >99% of Hg^{2+} from water samples at lower concentrations, while remaining insensitive to Cl^- ions. Overall, these studies highlight the complex interplay between chemical structure, gelation ability, and gel properties.

Chart 3-1.

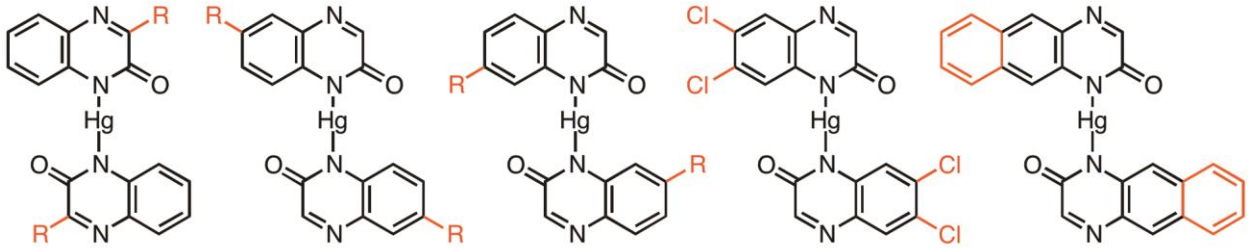

1a R = H;
1b R = CH_3;

2a R = Br;
2b R = Cl;
2c R = F;

3a R = Br;
3b R = Cl;

4

5

Experimental Methods

Gel Screening and Critical Gel Concentration (cgc) Procedure. The cgc was determined by adding a known amount of compounds **1–5** (~1–10 mg) into an 8 mL vial containing 1 mL of solvent. The vial was capped, heated to dissolve the solid, and allowed to cool with approximately 20 s of sonication in a water bath (near ambient temperature). If the resulting gel was stable to inversion, then 0.1 mL of solvent was added and the procedure was repeated until the gel was no longer stable to inversion. If no gel formed initially, then additional Hg(quinoxalinone)$_2$ was added and the procedure was repeated until the solubility limit was reached.

Procedure for Measuring Equilibrium Solubilities. Compounds **1–5** (10 mg x 3 vials per compound) and ~7.5 mL of solvent (EtOH or MeOH) were each added to an 8 mL vial and heated at 45 °C for 7 d. PXRD analysis was used to identify the solid form that was present before and after heating. (Samples were prepared for PXRD by pipetting the mixture onto a microscope slide and allowing the solvent to evaporate prior to analysis.) The solvent was then evaporated from the vials by heating at 45 °C for 5 h with the caps removed. PXRD analysis was again performed to verify that the solid form

remained unchanged after evaporation. New solvent (~6-7 mL of EtOH or MeOH) was added to the vials and the mixtures were equilibrated for 48 h at 25, 30, 40, and 50 °C. Aliquots (200 μL) were taken at each temperature and diluted with a known amount of solvent (~3-4 mL). The solution concentration was determined using UV-vis spectroscopy and a calibration curve. To minimize sampling error, the solubility was determined by averaging the results of three aliquots from each vial (9 aliquots total) at each temperature. van′t Hoff plots (ln(*x*) versus 1/T, where *x* is the mole fraction solubility) were employed to determine the dissolution enthalpies (ΔH_{diss}) and entropies (ΔS_{diss}) using eq 1. The error bars reported at each point on the van′t Hoff plots were calculated as the relative error ($\Delta x/x$).

$$\ln(x) = -\frac{\Delta H_{diss}}{RT} + \frac{\Delta S_{diss}}{R} \quad (1)$$

Representative Procedure for Hg^{2+} Remediation. A gel of **1a** was prepared by mixing quinoxalin-2(1H)-one (9.4 mg, 0.064 mmol) and $Hg(OAc)_2$ (9.6 mg, 0.030 mmol) in MeOH/H_2O (1 mL, 70/30 v/v). A spatula was used to gently compress the gel and release the entrapped solvent. An aliquot (~20 μL) was taken and the solvent was removed in vacuo. Then, 2.8 mL HNO_3/H_2O (5/95 v/v) and an yttrium standard (0.140 μL of a 100 ppm stock solution) were added to the vial. The solutions were diluted to 14 mL with deionized H_2O. Inductively coupled plasma-optical emission spectroscopy (ICP-OES) measurements were taken on a Perkin-Elmer Optima 2000 DV. The detection limit for Hg^{2+} was approximately 10 ppb and was analyzed with a wavelength of 194.167 nm. Yttrium was used as an internal standard and detected with a wavelength of 371.029 nm. To minimize sampling error, the experiment was repeated three times for each gel and each sample was analyzed by ICP-OES in triplicate.

Results and Discussion

Synthesis and Gel Screening. Nine mercury-containing compounds were synthesized and screened for gelation (Chart 3-1 and Appendix 2). Most of the quinoxalinone ligands were synthesized in one step by condensation of a commercially available aryl diamine and glyoxylic or pyruvic acid.[30] Subsequent reaction with $Hg(OAc)_2$ generated the target compounds in moderate yields.[26] Full characterization

data for these compounds can be found in Appendix 2. Compounds **1–5** were screened for gel formation using the heat/cool method with sonication during the cooling phase. Initial gel screening revealed that five compounds (**1a**, **2b**, **2c**, **3a**, and **3b**) formed gels in at least one solvent system (Table 3-1and Table S2-1 in Appendix 2). Gelation was found to be highly sensitive to both the solvent composition and structure. As an example, while gelator **3b** formed gels in MeOH, EtOH, and EtOH/HOAc, its regioisomer, **2b**, only formed gels in EtOH/HOAc. Similarly, compound **3a** forms gels in EtOH and EtOH/HOAc whereas its regioisomer, **2a**, does not form gels in any of the solvents examined. These results lead to the conclusion that the gel formation is largely dictated by the position and nature of the substituents, rather than being dominated by the quinoxalinone framework.[31,32]

Table 3-1. Critical gel concentrations (cgcs) in select solvents.

Gelator	MeOH (mM)	EtOH (mM)	EtOH/HOAc[a] (mM)
1a	30 ± 1	precip.	precip.
2b	precip.	precip.	3.5 ± 0.4
2c	precip.	15 ± 0	precip.
3a	precip.	10.2 ± 0.3	5.0 ± 0.0
3b	3.5 ± 0.1	3.9 ± 0.2	7.1 ± 0.3

[a]10 µL of HOAc in 1 mL EtOH.

Solubility and Dissolution Parameters. We previously reported that gelators exhibited (on average) higher dissolution enthalpies (ΔH_{diss}) and entropies (ΔS_{diss}) than the nongelators.[22,23] This result suggests that gelators have stronger solid-state interactions and/or weaker solvent-solute interactions than the nongelators. To determine whether this correlation is general, we initiated solubility studies on compounds **1–5**. Because dissolution parameters are solvent-dependent, a single solvent system wherein all gelators form stable gels is desired. As evident in Table 3-1, our initial gel screening did not reveal any common solvents for all five gelators. As a

result, we identified potential alternatives using a program centered on the Hansen solubility parameters (HSPiP).[33] Although these parameters are typically used to identify solvents that will solubilize compounds, several groups have successfully extended this type of analysis to gel formation.[19–21,34–37] Compound **1a** was selected for this analysis based on its facile synthesis from commercially available reagents. On the basis of the solubility of **1a** in eight different solvents, the HSPiP program generated a list of approximately 1200 potential solvents. Solvents with a "relative energy difference"[38] of less than or equal to 1 were selected for further exploration, generating a more manageable list of approximately 300 solvents. This list was further narrowed to nine solvents, by taking into account boiling points, the nature of functional groups, and accessibility (Table S2-2 in Appendix 2). Some representative examples include 2-pentanol, 3-methoxypropanol, and 2,2,2-trifluoroethanol. Of these, compound **1a** was only able to form gels in 2,2,2-trifluoroethanol, and further screening revealed that none of other compounds formed gels in this solvent (Table S2-1 in Appendix 2). As a consequence, there were still no solvent systems wherein more than 3 of the 5 compounds formed gels. Nevertheless, we reasoned that comparisons across solvents might prove valuable and proceeded with the variable-temperature solubility measurements for **1**–**5** in both MeOH and EtOH.

In our previous work, the solubility measurements were performed on the bulk solid obtained directly from synthesis. Powder X-ray diffraction (PXRD) analysis was used to determine whether the bulk solid was representative of the gel form. If the solid-state packing was different between these two forms, the equilibrium solubilities were not measured.[22,23] For all gelators described herein, the solid-state packing in the bulk solid did not match the gel form (Figures S2-24–S2-32 in Appendix 2). Further PXRD analysis revealed that all nine compounds underwent a solid-solid transformation (bulk form → new form) in MeOH and some did in EtOH as well. As a representative example, the complex polymorphism exhibited by compound **1a** is highlighted in Figure 3-1. We observed a total of five different forms, including the gel form, bulk form, heated in EtOH form, and two single-crystal structures (see also Figures S2-21–S2-23 in Appendix 2). We suspected that some of these forms are solvates. Indeed differential scanning calorimetry studies confirmed that there are no obvious transitions that

interconvert these forms in the solid state (Figures S2-33–S2-35 in Appendix 2). In addition, thermogravimetric analysis revealed an initial solvent loss upon heating for some (but not all) of the gelator forms examined, which suggests that these compounds exhibit both solvates and polymorphs (Figures S2-56–S2-59 in Appendix 2). Overall, of the >20 different solid forms observed for compounds **1**–**5** in these experiments, only one matched the gel form (i.e., heated form of **1a** in MeOH). Because it was unclear to what extent these differences in the solid-state structure will influence the relative discrimination of gelators and nongelators, we proceeded with the variable-temperature solubility measurements. Note that the most stable (heated) form was used in the solubility measurements. The results of these solubility studies are highlighted in Figure 3-2.

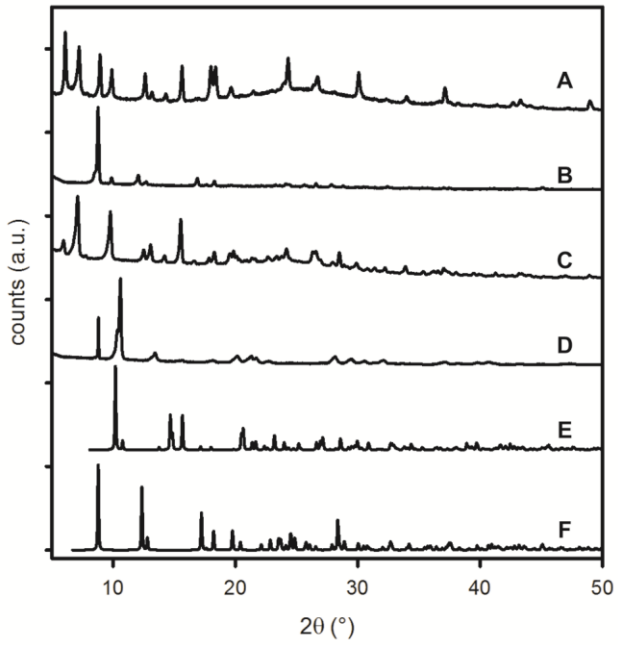

Figure 3-1. PXRD patterns for gelator **1a** under the following conditions: (A) gel formed in MeOH, (B) solid form after heating in EtOH, (C) solid form after heating in MeOH, (D) bulk form isolated from synthesis, (E) simulated pattern from crystal grown from MeOH/H_2O, (F) simulated pattern from crystal grown from DMSO/H_2O.

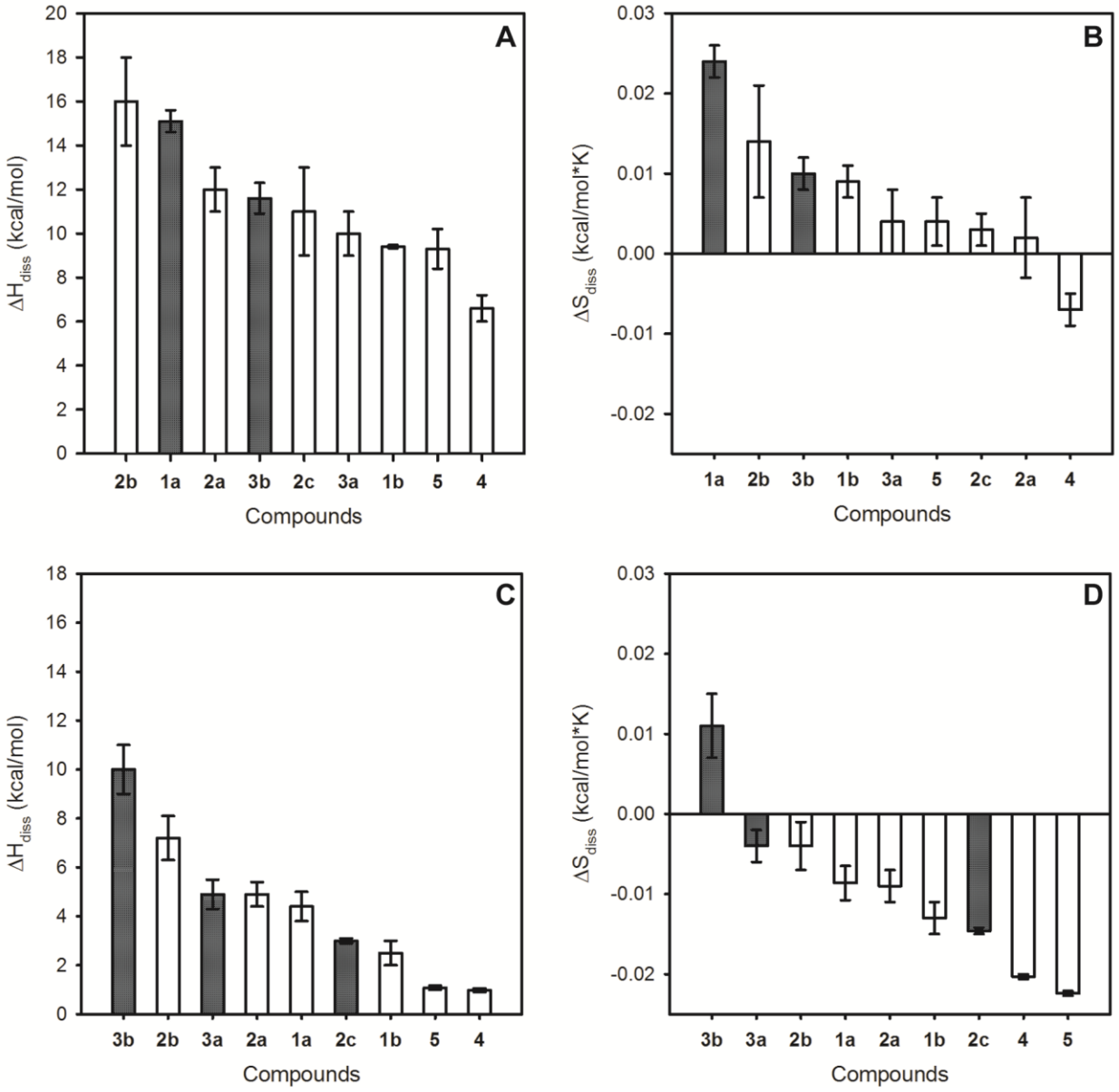

Figure 3-2. Plots of the dissolution enthalpy (ΔH_{diss}, A and C) and entropy (ΔS_{diss}, B and D) versus compound number for **1–5** in MeOH (A/B) and EtOH (C/D). Grey shading denotes gelators.

Overall, the conclusions are tenuous given that (i) the solid forms do not exhibit the same molecular packing as the gel form, and (ii) the limited data set for each solvent system. Nevertheless, useful comparisons can be made. For example, for all nine compounds, the ΔH_{diss} is higher in MeOH than EtOH by ~5–10 kcal/mol. This result can be attributed to the different solid forms, which would reflect a change in the solid-state interactions, or to the different solvent properties (e.g., hydrophobicity), which would

reflect a change in the solvent-solute interactions. Overall, these studies revealed that comparisons amongst structurally similar gelators and nongelators can be challenging if the compounds do not all gel in the same solvent system, and are polymorphic under the conditions used in the analysis.

Gel Properties. The critical gel concentrations ranged from 3.5–30 mM, depending on both chemical structure and solvent composition (Table 3-1). For example, while the addition of HOAc lowered the cgc of compound **3a**, it increased the cgc of compound **3b**. All gels displayed characteristic viscoelastic behavior, with an elastic modulus to storage modulus ratio (G′/G″) of greater than 10 (Figure 3 and Figures S2-42–S2-45 in Appendix 2). In addition, the gels were robust, exhibiting a breaking stress near 100 Pa. These values are similar to other metal-containing molecular gelators.[9,12] Scanning electron microscopy revealed a dense network of fibers for all gels, although the fiber diameters varied among the gelators (0.1–1.5 μm, Figure 3-3 and Figures S2-46–S2-50 in Appendix 2).

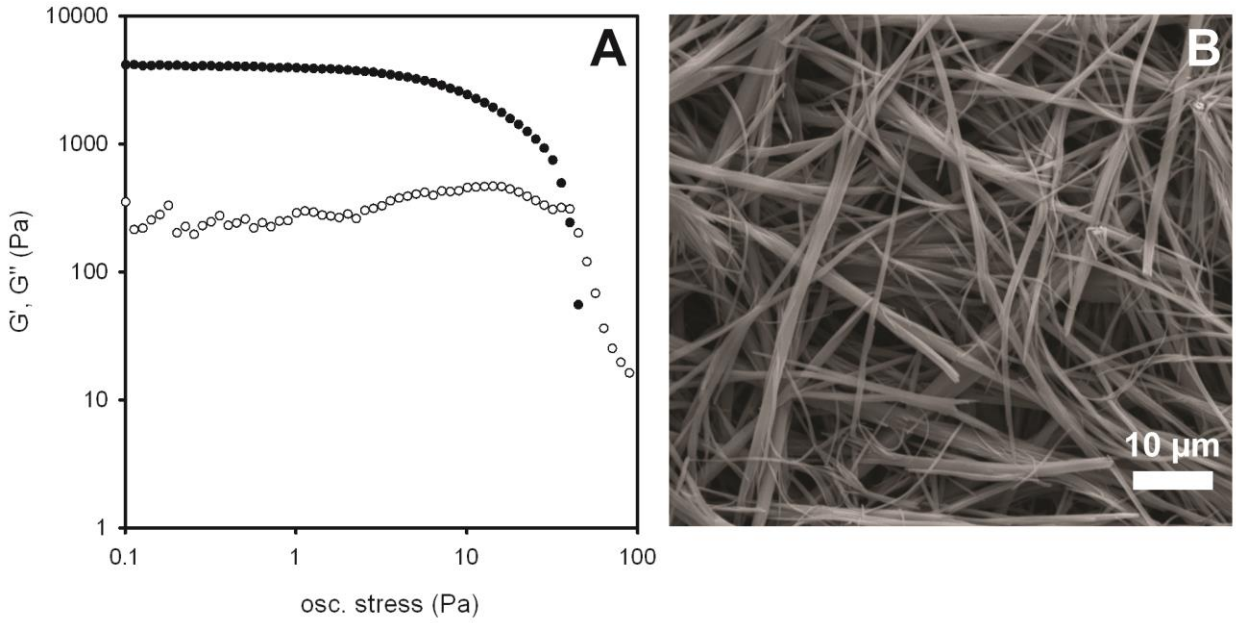

Figure 3-3. (A) Representative oscillating stress sweep for gelator **3a** in EtOH (15 mM). (B) Representative scanning electron micrograph for gelator **3a** in EtOH/HOAc (12.3 mM).

Hg^{2+} Remediation. Stimuli-responsive gelation represents an appealing platform for both detecting environmental contaminants and removing them. In 2010, we reported that **1a** can be used to effectively remove >90% of Hg^{2+} ions from an aqueous solution via gelation.[25] However, its practical utility was limited by the relatively high cgc and ready dissolution on adding Cl^- ions. As a consequence, we investigated the remediation potential of four gelators (**1a**, **2c**, **3a** and **3b**).[39] Gel formation was instantaneously observed when Hg-contaminated water was added to a MeOH solution containing each of the quinoxalinones at the appropriate concentration (Figure 3-4). The gelators exhibited similarly high remediation abilities (>98% Hg^{2+} removed, Table S2-6 in Appendix 2). The improved performance for **1a**, compared to our earlier work,[25] is due to the super-stoichiometric amounts of quinoxalinone used herein. Gel formation was found to be remarkably selective for Hg^{2+} over other metal ions (Figure S2-51 in Appendix 2), possibly be due to the linear geometry of these complexes, which would facilitate 1D intermolecular interactions.

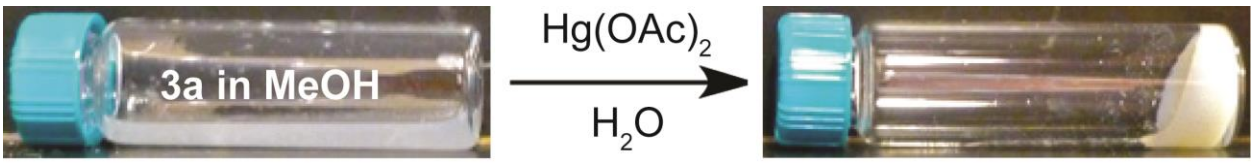

Figure 3-4. Gelation is observed when Hg^{2+}-contaminated water (0.2 mL, 48 mM) is added to a MeOH solution containing 7-bromoquinoxalin-2(1H)-one (0.8 mL, 20 mM).

The chloride ion tolerance of the gels was also examined because we previously reported that gels of **1a** dissolved with added NBu_4Cl,[25] limiting its practical application. Remarkably, gels of **3a** were completely resistant to chloride treatment and remained stable for months (Figure S2-52 in Appendix 2). This stability to Cl^- ions was not observed with the other gelators. We hypothesized that these results reflect the relative stabilities of the various complexes ($HgCl_2$ versus $Hg(quinoxalinone)_2$) rather than a kinetic phenomenon. To test this hypothesis, we performed a series of ligand displacement experiments using 7-bromoquinoxalin-2(1H)-one (from **3a**) and the 6-fluoroquinoxalin-2(1H)-one (from **2c**) and monitored the reactions using ^{19}F NMR spectroscopy (Figures S2-18–S2-20 in Appendix 2). These studies revealed that rapid exchange of the quinoxalinone ligands occurs during mixing. When both quinoxalinones were present in equal concentrations and were competing for a substoichiometric

amount of Hg^{2+} ions, complex **3a** formed preferentially over **2c**, indicating that the relative binding affinities of the two quinoxalinones are different.[40] This stronger binding affinity of the 7-bromoquinoxalin-2(1H)-one might explain why complex **3a** is more resistant than **2c** to ligand exchange by Cl^- ions.

To probe the robustness of this sensing platform, environmentally relevant water sources (bottled water, tap water, and Huron River water) were also examined. Because the Hg^{2+} concentration in these natural samples are low, $Hg(OAc)_2$ was added to the water prior to analysis. Gelation of **3a** was observed when these water samples were added to an EtOH solution containing 7-bromoquinoxalin-2(1H)-one with brief sonication. A control experiment confirmed that no gels formed when the unaltered water samples (e.g., no $Hg(OAc)_2$) were used, consistent with a Hg-triggered gel formation (Figure 3-5).

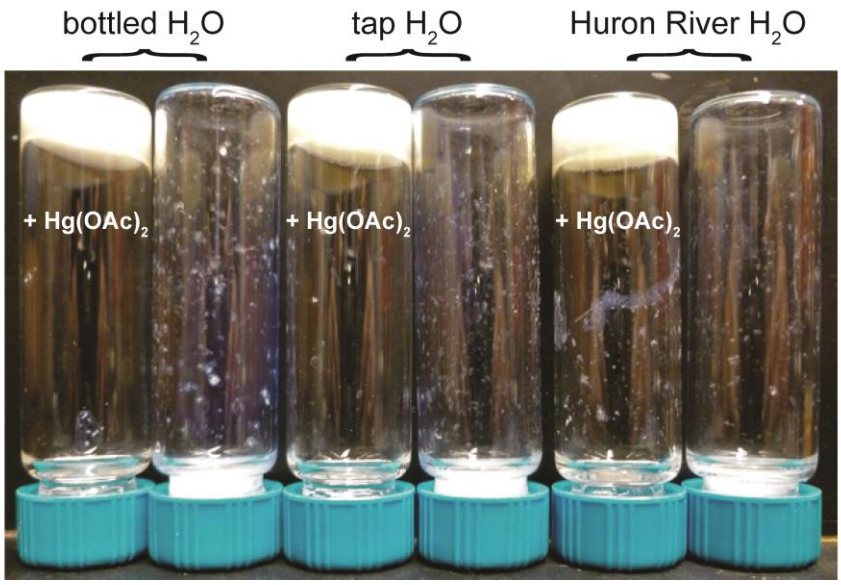

Figure 3-5. Gel formation (with **3a** in EtOH) is observed when bottled water, tap water, and Huron River water containing $Hg(OAc)_2$ is added.

Conclusions

The synthesis and evaluation of nine Hg-containing compounds was described. Five of these compounds formed gels in organic solvent/water solvent systems. Comparing the gelators and nongelators based on dissolution enthalpies and entropies was complicated by the lack of a common solvent system for gelation and the large variety

of accessible solid forms. The gels were all composed of dense networks of fibers, although the fiber diameters varied among the gelators. Despite these differences, the gelators all exhibited similar rheological properties near their critical gel concentrations. We also demonstrated that these Hg-triggered gelations can effectively remove >98% of the Hg^{2+} in aqueous solutions, and are able to form gels in complex samples (e.g., river water), suggesting that a promising application of these stimuli-responsive materials is in environmental remediation.

References

[1] Segarra-Maset, M. D.; Nebot, V. J.; Miravet, J. F.; Escuder, B. *Chem. Soc. Rev.* **2013**, *42*, 7086–7098.

[2] Babu, S. S.; Prasanthkuma, S.; Ajayaghosh, A. *Angew. Chem. Int. Ed.* **2012**, *51*, 1766–1776.

[3] Buerkle, L. E.; Rowan, S. J. *Chem. Soc. Rev.* **2012**, *41*, 6089–6102.

[4] Yang, X.; Zhang, G.: Zhang, D. *J. Mater. Chem.* **2012**, *22*, 38–50.

[5] Dawn, A.; Shiraki, T.; Haraguchi, S.; Tamaru, S.; Shinkai, *Chem.—Asian J.* **2011**, *6*, 266–282.

[6] Díaz Díaz, D.; Kühbeck D.; Koopmans, R. J. *Chem. Soc. Rev.* **2011**, *40*, 427–448.

[7] Banerjee, S.; Das, R. K.; Maitra, U. *J. Mater. Chem.* **2009**, *19*, 6649–6687.

[8] Hirst, A. R.; Escuder, B.; Miravet, J. F.; Smith, D. K. *Angew. Chem. Int. Ed.* **2008**, *47*, 8002–8018.

[9] Piepenbrock, M.-O. M.; Lloyd, G. O.; Clarke, N.; Steed, J. W. *Chem. Rev.* **2010**, *110,* 1960–2004.

[10] Hemamalini, A.; Das, T. M. *New J. Chem*. **2013**, *37*, 2419–2425.

[11] Bachman, R. E.; Zucchero, A. J.; Robinson, J. L. *Langmuir* **2012**, *28*, 27–30.

[12] Yang, X.; Zhang, G.; Li, L.; Zhang, D.; Chi, L.; Zhu, D. *Small* **2012**, *8*, 578–584.

[13] Ren, C.; Song, Z.; Zheng, W.; Chen, X.; Wang, L.; Kong, D.; Yang, Z. *Chem. Commun.* **2011**, *47*, 1619–1621.

[14] Chen, J.; Wu, W.; McNeil, A. J. **2012**, *48*, 7310–7312.

[15] Krieg, E.; Shirman, E.; Weissman, H.; Shimoni, E.; Wolf, S. G.; Pinkas, I.; Rybtchinski, B. *J. Am. Chem. Soc.* **2009**, *131*, 14365–14373.

[16] Bremmer, S. C.; Chen, J.; McNeil, A. J. *Chem. Commun.* **2012**, *48*, 7310–7312.

[17] Zhang, Y.; Kuang, Y.; Gao, Y.; Xu, B. *Langmuir* **2011**, *27*, 529–537.

[18] Gao, Y.; Yang, Z.; Kuang, Y.; Ma, M.-L.; Li, J.; Zhao, F.; Xu, B. *Biopolymers* **2010**, *94*, 19–31.

[19] Xu, H.; Song, J.; Tian, T.; Feng, R. *Soft Matter* **2012**, *8*, 3478–3486.

[20] Raynal, M.; Bouteiller, L. *Chem. Commun.* **2011**, *47*, 8271–8273.

[21] Hirst, A. R.; Smith, D. K. *Langmuir*, **2004**, *20*, 10851–10857.

[22] Muro-Small, M. L.; Chen, J.; McNeil, A. J. *Langmuir* **2011**, *27*, 13248–13253.

[23] Chen, J.; Kampf, J. W.; McNeil, A. J. *Langmuir* **2010**, *26*, 13076–13080.

[24] Hanabusa, K.; Yamada, M.; Kimura, M.; Shirai, H. *Angew. Chem. Int. Ed.* **1996**, *35*, 1949–1951.

[25] King, K. N.; McNeil, A. J. *Chem. Commun.* **2010**, *46*, 3511–3513.

[26] Goodgame, D. M. L.; Hill, S. P. W.; Williams, D. J. *Polyhedron* **1992**, *11*, 1507–1512.

[27] Ryan, D. M.; Anderson, S. B.; Nilsson, B. L. *Soft Matter* **2010**, *6*, 3220–3231.

[28] Ryan, D. M.; Anderson, S. B.; Senguen, F. T.; Youngman, R. E.; Nilsson, B. L. *Soft Matter* **2010**, *6*, 475–479.

[29] Ma, M.; Kuang, Y.; Gao, Y.; Zhang, Y.; Gao, P.; Xu, B. *J. Am. Chem. Soc.* **2010**, *132*, 2719–2728.

[30] Lumma, W. C. Jr.; Hartman, R. D.; Saari, W. S.; Engelhardt, E. L.; Lotti, V. J.; Stone, C. A. *J. Med. Chem.* **1981**, *24*, 93–101.

[31] Recent theoretical studies have suggested that the interactions between substituents and π-systems can dominate the molecular orientation and packing. For leading references, see: Wheeler, S. E. *CrystEngComm* **2012**, *14*, 6140–6145.

[32] Raju, R. K.; Bloom, J. W. G.; An, Y.; Wheeler, S. E. *ChemPhysChem* **2011**, *12*, 3116–3130.

[33] Abbott, S.; Hansen, C. M.; Yamamoto, H. Hansen Solubility Parameters in Practice (HSPiP). For reference, see: http://www.hansen-solubility.com

[34] Gao, J.; Wu, S.; Rogers, M. A. *J. Mater. Chem.* **2012**, *22*, 12651–12658.

[35] Wu, S.; Gao, J.; Emge, T. J.; Rogers, M. A. *Soft Matter*, **2013**, *9*, 5942–5950.

[36] Pal, A.; Abraham, S.; Rogers, M. A.; Dey, J.; Weiss, R. G. *Langmuir* **2013**, *29*, 6467–6475.

[37] Hanabusa, K.; Matsumoto, M.; Kimura, M.; Kakehi, A.; Shirai, H.. *J. Colloid Interface Sci.* **2000**, *224*, 231–244.

[38] Relative energy difference (RED) refers to the distance from the center of the solvent "sphere" divided by the radius (see Appendix 2).

[39] These remediation experiments were not performed with gelator **2b** because it does not form gels in situ.

[40] We note that the "mixed" complex, containing both ligands, is formed in the highest concentration (see Appendix 2).

Chapter 4. A strategy to analyze intermolecular interactions and target new gelators using morphology prediction.

Despite decades of active research, most new gelators are still identified serendipitously,[1-3] because the principles of gelation are not understood, which makes predicting and designing new gelators difficult and limits utility in practical applications.[4] Only a few systematic attempts at predicting new gelators have been successful, most of which have been focused on the theory that unidirectional (1D) intermolecular interactions direct self-assembly to occur along one axis, promoting the formation of fibers.[5–11] For example, Dastidar and coworkers have attempted to predict new gelators by focusing on functional groups with well-studied interaction patterns. They call these functional groups synthons to draw a connection to the similar approach taken in crystal engineering. Specifically, they focus on hydrogen bond acceptor/donor pairs such as amines and carboxylic acids which associate through proton transfer and a subsequent ionic association. Dastidar and coworkers have developed a large library of these salt pairs. Gels have been identified approximately 30% of the time and in many cases, the existence of 1D intermolecular interactions has been confirmed by X-ray crystal packing structures that correspond to the gel form. Although this method is promising, it is limited by the need to identify synthons. While Dastidar and co-workers, as well as many others, have confirmed hydrogen bonding in crystal packing structures, many other, relatively weaker interactions have also been associated with gelation that may not be easy to identify or classify as synthons.

Our group has also attempted to systematically predict new gelators. In previously published work, we proposed using known crystal structures as a starting point for identifying new gelators. Using the Cambridge Structural Database (CSD), we to identify non-covalent 1D intermolecular interactions other than hydrogen bonding that would lead to gelation. Work previously published in our group described an effort to

predict new gelators by examining solid-state packing structures for prominent 1D intermolecular interactions.[12,13] A new Hg-containing gelator was identified by first searching the CSD for molecules involved in 1D Hg-π interactions. Although this method was successful in identifying a new gelator with minimal screening, the selection was time consuming because it involved the visual examination of more than a thousand CIF files. Criteria for target selection were subjective because there was no way to quantify the relative strengths of the intermolecular interactions. An objective index to identify 1D intermolecular interactions in the solid state is required before this method can be widely applied.

We turned to the crystallization and self-assembly literature to improve on our previous method. The relationship between crystalline shapes and molecular structure has long been a subject of scientific interest.[14–18] A crystal's morphology has an effect on its bioactivity and processiblity and as such remains an area of interest in modern times.[19,20] The first attempt to predict a crystal's morphology from its structure was developed at the turn of the 20th century, and became known as the Bravais,[21] Friedel,[22] Donnay, and Harker[23] (BFDH) theory. This theory focuses on geometric aspects in the crystal lattice to predict morphology. It was posited that the largest crystal faces, referred to as the most morphologically important (MI) faces, would have the largest lattice spacing ($d_{hkl} \propto$ MI). This method has been verified in some cases, but focusing only on geometric aspects and ignoring all chemical interactions has serious limitations.

Hartman and Perdok in the 1950s[24,25] and later Harman and Benema expanded on the BFDH theory and introduced a way to include the intermolecular interactions in morphology prediction. This theory became known as the Attachment Energy (AE) theory. The major assumption of the AE theory is that the energy released new molecules attach to a growing face of a crystal is proportional to the rate of growth of that face, which means that faces that release the most energy grow fastest. The total energy of crystallization can be calculated using a crystal graph, which is a representation of the interactions between molecules in the solid state. The morphological importance (or size) of a face is inversely proportional to its growth rate, causing the fastest growing faces to be the smallest.

As a result, predicted morphologies offer a visual representation of the relative strength of intermolecular interactions in the solid state. If a crystal structure has anisotropic, 1D intermolecular interactions, its predicted morphology will be an anisotropic, 1D structure. We propose that the same intermolecular interactions that are responsible for the self-assembly of molecules into a high aspect ratio, needle-like crystal could also lead to fiber formation. We therefore hypothesized that the gelator discovery process can be streamlined by targeting crystal structures that are predicted to have high aspect ratio morphologies.

In this chapter, we report on our efforts to identify new LMW gelators through a systematic, objective process and expand our understanding of how intermolecular interactions affect self-assembly. Specifically, our proposed method uses Materials Studio, a widely-available computer software program, to predict morphologies from crystal structures. This process will provide summary of the intermolecular interactions between molecules in the unit cell. Hence, we were able to reduce reliance on serendipity, which in turn increases the efficiency and reduces waste in the gelator discovery process. Using the method described in this chapter, we identified two novel Pb^{2+} gelators. Excitingly, this method, with further verification, shows potential to be used as the first-ever universal tool for new LMW gelator discovery.

Experimental

CSD Search Criteria

All crystal structures discussed in this paper were previously published and accessed as CIF files through the Cambridge Structural Database (CSD). As the CSD contains over 700,000 crystal structures, criteria were required to narrow the search parameters to a manageable sample set. For our purposes, we focused on toxic metal-containing compounds (specifically Pb) because we are ultimately interested in using them for environmental remediation and sensing applications.

The CSD search was performed using the “draw” query tool by searching for Pb, with the R factor set at >0.05 and “organometallics only,” as well as filters selected for “not disordered,” “no errors,” “not polymeric,” and “no ions.” These filters were

necessary to eliminate CIF files that were unsuitable for the selected computational method. For example, disordered or structures with errors need additional manual preparation to calculate the crystal graph, which would deviate from the experimental crystal structures. For simplification in an initial investigation, ionic compounds[26,27] were excluded due to the strength and lack of directionality of the interaction, which would predominate the calculated morphology.

Using the combine queries tool, all other metals and metalloid-containing structures were excluded. These CIF files were excluded to reduce the complexity of the molecules as a benefit to both the calculations and the practicality of the gelators for use in potential applications. Finally, solvate crystal structures were manually eliminated from the target pool. It was proposed that solvent within a crystal structure could dominate intermolecular interactions. Solvates also introduce additionally challenges with stability during the storage and gel screening process. We chose to exclude solvates from the initial data set, but believe that this could be an interesting subject for further investigation. The search resulted in a total of 354 Pb(II) and Pb(IV) complexes. A full list of CIF files included in this study and CSD search criteria can be found in Appendix 3.

Geometry Optimization

Morphology prediction was performed with Morphology in Materials Studio by Accelrys.[28] Structures were prepared for calculations by importing CIF files into Materials Studio, calculating bonds according to the van der Waals radii of the atoms, and normalizing hydrogens. Geometry optimization was performed using Forcite (a module within Materials Studio that performs molecular dynamics optimizations) to ensure that calculations were being performed on the lowest energy form. As crystallography tends to systematically underestimate the bond lengths involving hydrogens, geometry optimization is necessary to obtain more realistic values.[29]

The force field selected for the calculations was the Universal Force Field (UFF)[30] because it was the only force field in Materials Studio that would accommodate Pb. If this method were applied to the discovery of a different molecular scaffold (e.g.,

organics only), then another force field could more accurately model that system. Force fields are commonly evaluated by performing an unconstrained geometry optimization and comparing the optimized structure to the experimentally determined CIF file. If the values are in good agreement (i.e. lattice parameters change less than 5%) then the force field can adequately model the structure. The charges were assigned with the Qeq model, which is appropriate for periodic systems. Because the UFF only recognizes tetrahedral lead coordination geometry, all Pb(IV) and Pb(II) sandwich compounds failed the geometry optimization calculation.[30] Compounds containing Pb(IV) tend to display square planer coordination geometry and Pb(II)-sandwich compounds show linear coordination geometry. For initial investigation into using morphology prediction to discover new gelators, we decided to exclude Pb(IV), but if a Pb(IV)-containing gelator is desired, the force field would have to be modified. The removal of Pb(IV) and Pb(II)-sandwich compounds from the data set brought the number of compounds to 186.

Because the CIF files represent experimentally-obtained data, it offered an opportunity to investigate the effect of geometry optimization on the crystal structures. The geometry optimization was performed in two ways: allowing the unit cell parameters to change during the optimization, as well as holding them constant. It was observed that major changes occurred to the unit cell parameters when they were allowed to fluctuate (Appendix 3), which could result in an inaccurate description of the intermolecular interactions in a given structure. Chart 4-1 provides the structure and CSD 6-letter labels for two example compounds, **1a** and **2a**. As can be seen in Figure 4-1A, the two optimized conformations are in fairly good agreement with each other as well as the unoptimized, experimentally-obtained structure, only differing in lead coordination bond lengths (Table 4-1). In This case, whether or not the unit cell is allowed to change during the optimization had little effect on the molecular confirmation. On the other hand, **2a** (Figure 4-1B) represents the majority case. Significant changes from the unoptimized structure (shown in green) were observed, especially from the case (in blue) when the unit cell was allowed to change. The optimization where the unit cell parameters were constrained showed similar bond angles around the lead center and bond length differences, but the basic shape of the molecule was maintained. These data are summarized in Table 4-2**.**

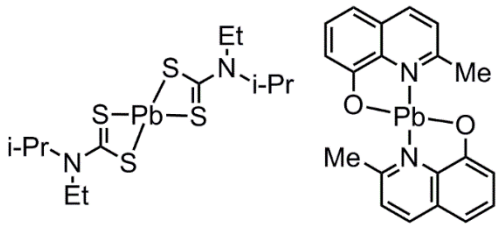

1a
NAYNUW01

2a
NUNXOK

Chart 4-1.

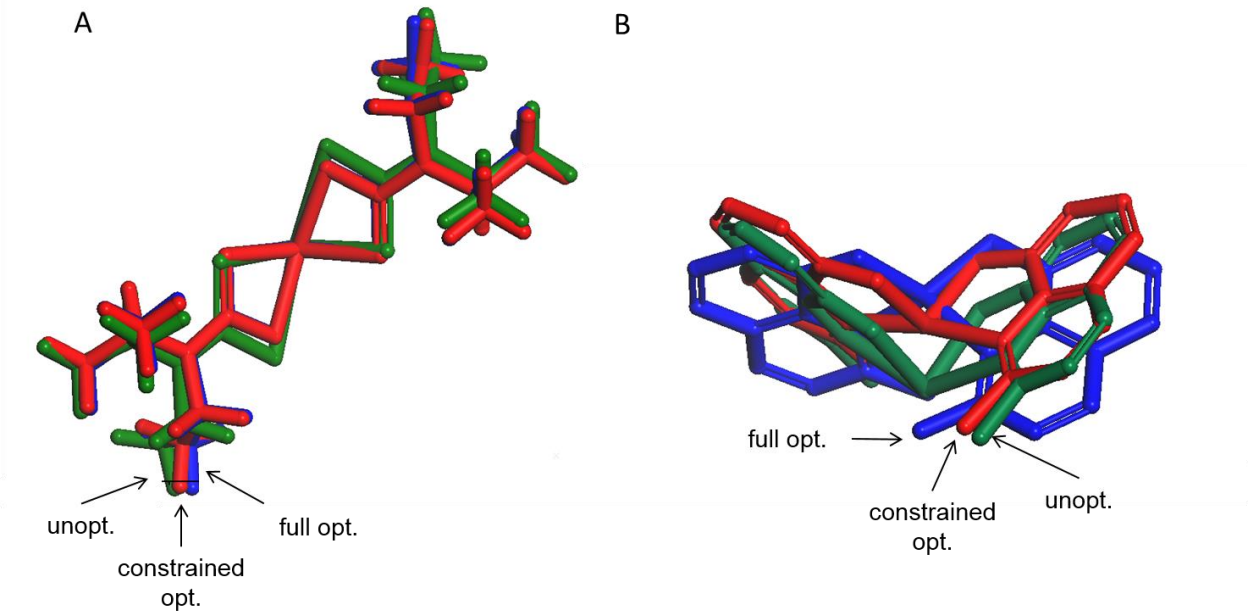

Figure 4-1. Overlaid structures from the CIF files for (A) **1a** and (B) **2a**. Green represents the unoptimized molecular conformation (unopt.) while red shows the molecular conformation after optimization holding unit cell parameters constant (constrained opt.) and blue represents the fully optimized conformation (full opt.).

Table 4-1. Bond lengths and angles for **1a**.

Optimization Type	**Angle (S_1-Pb-S_1',˚)**	**Length (S-Pb, Å)**
unoptimized	138.744	2.837
constrained unit cell	115.83	2.245
unconstrained unit cell	113.986	2.234

Table 4-2. Bond lengths and angles for **2a.**

Optimization Type	Angle (O-Pb-O′,˚)	Length (O-Pb, Å)
unoptimized	93.609	2.262
constrained unit cell	106.614	2.033
unconstrained unit cell	118.456	2.012

Overall, the changes in unit cell parameters and molecular conformations were large as a result of an unconstrained geometry optimization using the UFF force field. We concluded that the force field is not accurately modeling the CIF files. As UFF is the only force field supported by Materials Studio that will describe lead, choosing a different force field was not an option. Based on work by Matzger and coworkers, relative energy differences between pairs of polymorphs were most accurately described in a system where atomic positions were optimized, but unit cell parameters were held constant.[29] A constrained geometry allows the periodic systems represented in CIF files to equilibrate, but not completely change the interactions represented in the experimentally obtained crystal structure.

Conjugated systems are known to have delocalized electron density, but are often represented as localized within a structure for simplicity. To investigate the influence of delocalized electron density on the crystal structures in the data set on intermolecular interactions in the solid state, morphology prediction calculations were performed on CIF files prepared by two methods: (1) bonds were calculated according to Material's Studio's default algorithm for van der Waals radii or (2) electron delocalization was accommodated by manually modifying effected bonds to partial double bonds. These two methods for representing electron density are illustrated in Chart 4-2 using compounds 1a and 3[31] as examples and the results of the input changes can be compared in Figure 4-2. The three input structures used for **3** included the structure as determined experimentally by X-ray diffraction (**3**$_{i}$), a resonance structure where the O-Pb bond is X-type bond and the S-Pb bond is L-type (**3**$_{ii}$), and a structure where delocalized electrons are represented by partial double bonds (**3**$_{iii}$). As seen in Table 4-4 the bond lengths in **3**$_{i}$ after optimization most closely match those from the unoptimized, experimentally determined structure. Bond lengths in the partially

bonded structure are intermediate between the two resonance structures. Compound **1a** was also prepared using two input structures but is more symmetric than **3** (Chart 4-1). Bond lengths did not change after optimization regardless of the way bonding is represented in the calculation and is shown in Table 4-3. We were convinced by both examples that the force field is adequately describing electron density delocalization and it is not necessary to modify the structures.

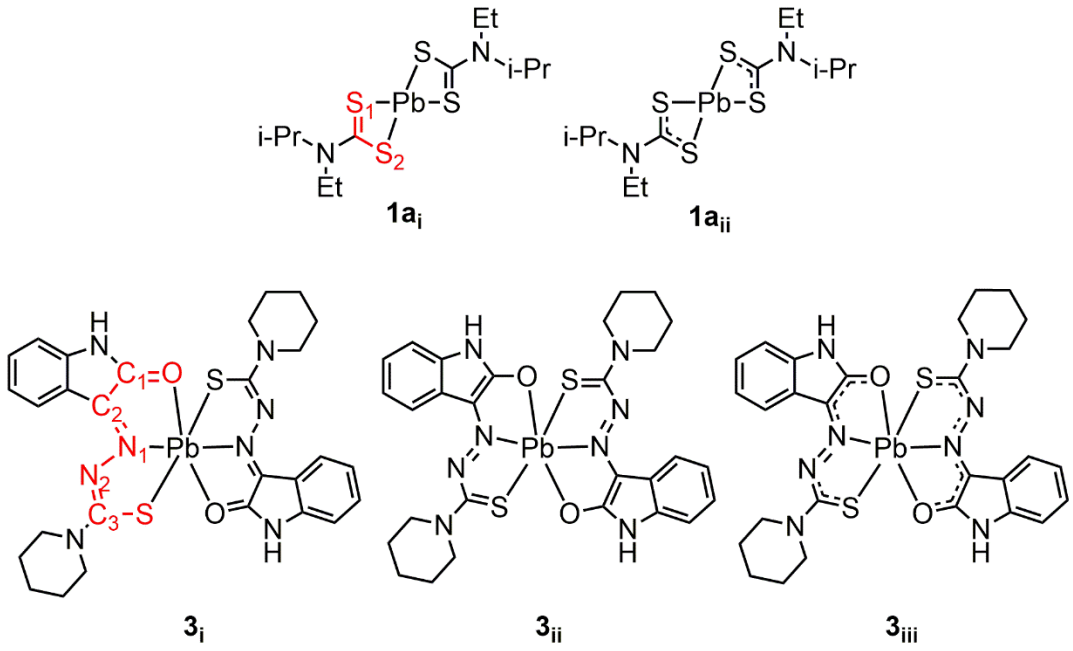

Chart 4-2.

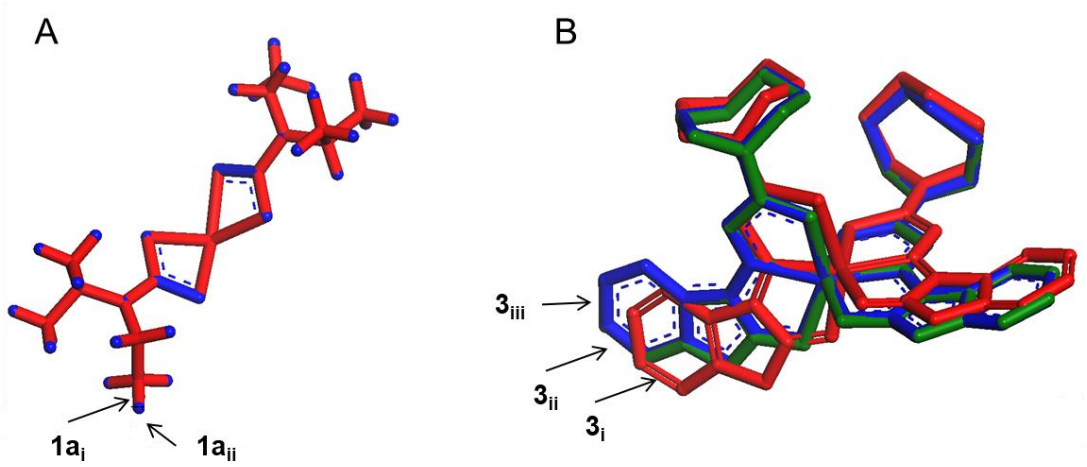

Figure 4-2. Electron density delocalization and multiple resonance structures after geometry optimization overlaid for (A) **1a**$_i$ (red) and **1a**$_{ii}$ (blue), (B) **3**$_i$ (red), **3**$_{ii}$ (green) and **3**$_{iii}$ (blue).

Table 4-3. Optimized and unoptimized bond lengths for the forms of **1a** found in Chart 4-2.

	S1-C (Å)	C-S_2 (Å)	Aspect Ratio
unoptimized **1a**	1.720	1.728	n/a
1a$_i$	1.507	1.506	4.672
1a$_{ii}$	1.507	1.506	4.672
1a$_{iii}$	1.507	1.506	4.672

Table 4-4. Optimized and unoptimized bond lengths for the forms of **3** found in Chart 4-2.

	O-C_1 (Å)	C_1-C_2 (Å)	C_2-N_1 (Å)	N_1-N_2 (Å)	N_2-C_3 (Å)	C_3-S (Å)	Aspect Ratio
unoptimized **3**	1.211	1.488	1.300	1.347	1.355	1.726	n/a
3$_i$	1.218	1.429	1.279	1.391	1.289	1.806	3.619
3$_{ii}$	1.393	1.362	1.403	1.269	1.419	1.429	3.607
3$_{iii}$	1.273	1.352	1.324	1.318	1.339	1.491	2.505

Crystal Graph Generation

After the Forcite geometry optimization, a crystal graph was generated of the crystal structure using UFF and Qeq as the charge assignment. The crystal graph describes the energy of interaction between the center of mass of a molecule and all molecules in a given sphere. The calculation sphere is defined by a radius (i.e., the distance of one or more unit cells) that is set by the user. A crystal graph provides insight into the relative importance of the intermolecular interactions in the solid state. We investigated the effect of varying the size of the calculation radius on predicted morphology for **1a** and **2a,** and the data are summarized in Table 4-5 and Table 4-6. The smallest calculation radius (1 unit cell distance from center of mass) resulted in the largest aspect ratio and lowest lattice energy for both **1a** and **2a**, but the differences between calculation radii had very little effect on the faces and shape of the predicted morphology. The same morphology was predicted regardless of the size of the interaction sphere Figure 4-3). For both examples, the change in aspect ratio or lattice energy was less than 10%. We proceeded with the calculation radius set at one unit cell distance because it places an emphasis on the shorter range, directional intermolecular interactions that are the focus of our hypothesis. Further comparisons in this

dissertation are made in reference to the predicted morphology generated from a one unit cell calculation sphere crystal graph.

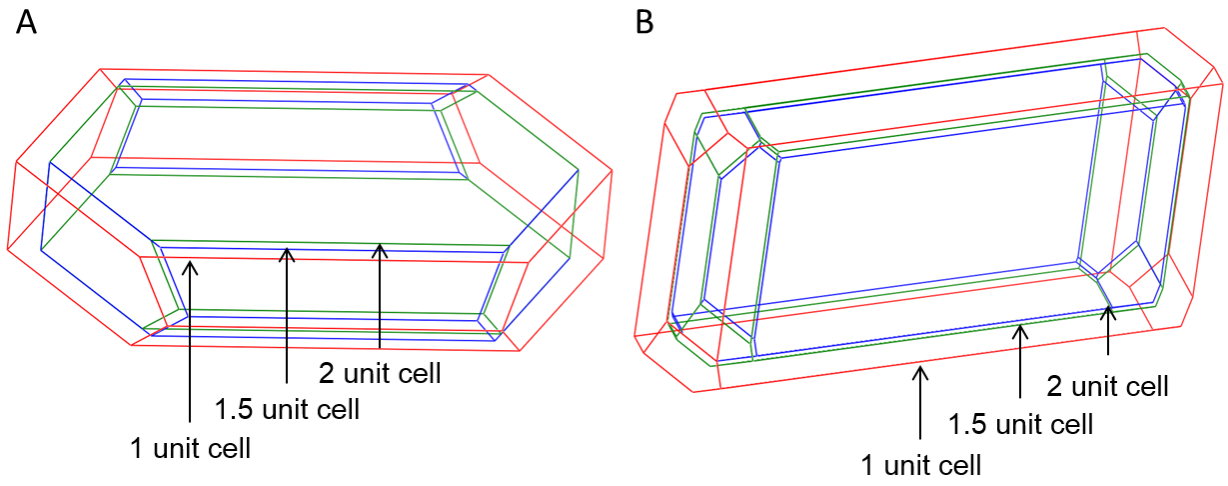

Figure 4-3. Predicted morphologies for (A) **1a** and (B) **2a** resulting from crystal graphs calculated from an interaction radius of 1 (red), 1.5 (green), and 2 (blue) unit cells.

A minimum energy filter of -0.596 kcal/mol was applied on the recommendation of Materials Studio as interactions less than that value do not exist at room temperature. Nevertheless, the effect of the minimum energy filter on the predicted morphology was investigated. As can be seen in Figure 4-4 and Table 4-6, the aspect ratio, morphology, and lattice energy are very similar with and without the minimum energy filter.

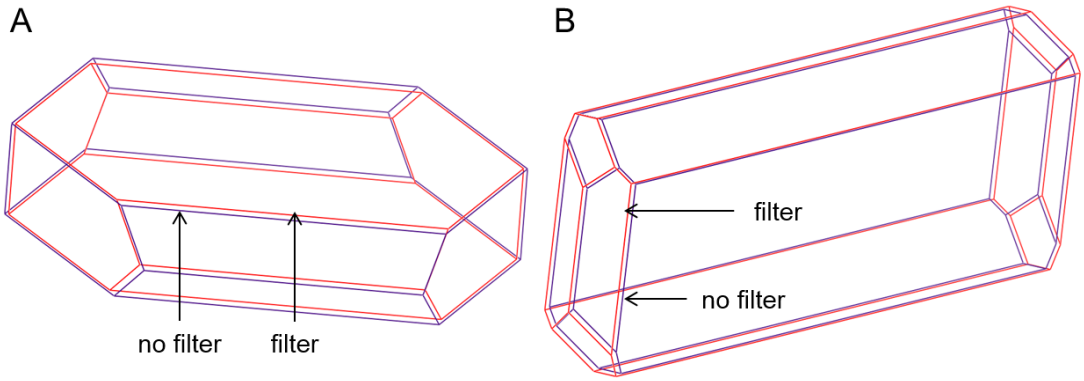

Figure 4-4. Predicted morphologies for (A) **1a** and (B) **2a** with (red) and without (blue) a minimum energy filter of -0.596 kcal/mol.

Morphology Prediction

The morphology prediction calculation performed was Growth Morphology, which is Materials Studio's version of AE Theory. Generation of the predicted morphology is available in two ways: via the crystal graph or using the molecular dynamics model, Forcite. Calculations were performed from the previously generated crystal graph at the highest level of quality. The primary advantage of predicting the morphology from the crystal graph is that it allows the user to visualize the relative strengths of intermolecular interactions in the solid state.[32] Additionally, the crystal graph energy method was less computationally intense than Forcite and resulted in only minor changes in the predicted morphology, as is depicted in Figure 4-5. The differences in morphologies can most likely be attributed to the influence of longer range interactions.

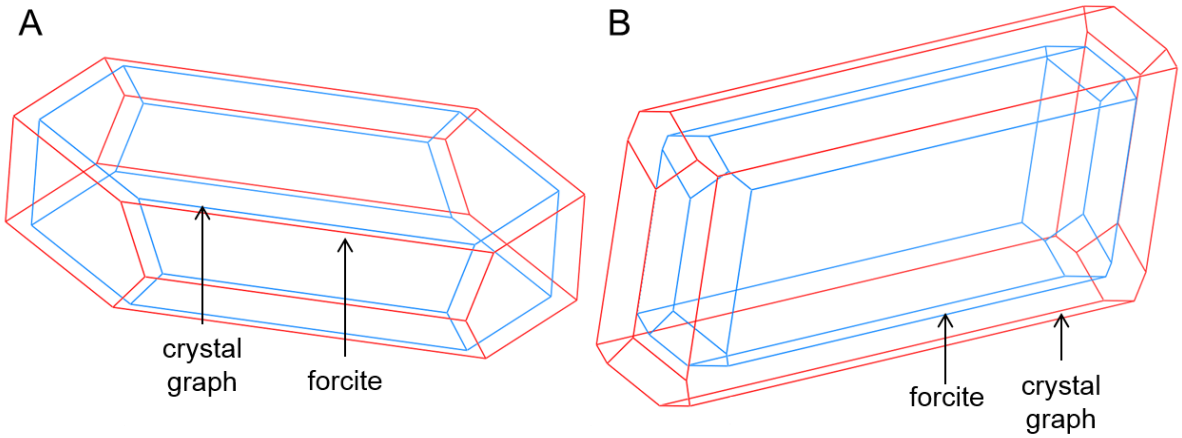

Figure 4-5. Predicted morphologies for (A) **1a** and (B) **2a** generated by the crystal graph (red) and Forcite (blue) energy methods.

Table 4-5. Data on the predicted morphology of **1a** calculated in via the crystal graph and Forcite energy methods.

calc. radius (unit cell)	minimum energy limit (kcal/mol)	energy method	AR
1	-0.596	crystal graph	4.672
1.5	-0.596	crystal graph	4.19
2	-0.596	crystal graph	4.191
1	None	crystal graph	4.738
n/a	n/a	Forcite	4.284

Table 4-6. Data on the predicted morphology of **2a** calculated in via the crystal graph and Forcite energy methods.

calc. radius (unit cell)	minimum energy limit (kcal/mol)	energy method	AR
1	-0.596	crystal graph	4.489
1.5	-0.596	crystal graph	3.957
2	-0.596	crystal graph	3.864
1	none	crystal graph	4.392
n/a	n/a	Forcite	3.777

Morphologies were also calculated for all CIF files in the data set using the BFDH theory. Since the BFDH theory is purely geometric, no force field is needed for the calculations and it was proposed that it could be used to check the validity of the morphologies calculated using UFF. The data for these calculations can be found in Appendix 3 for all of the CIF files. In many cases, the morphologies predicted via the BFDH theory were very similar to those calculated via the AE theory. That is, both theories generally predicted the same faces but in different proportions. No correlation was observed between aspect ratios calculated via the AE or BFDH theory (Appendix 3).

In some cases, the aspect ratio calculated by the AE theory was much higher than that of the BFDH theory. It was hypothesized this difference is due to the influence of intermolecular interactions. Specifically, higher aspect ratios are believed to be the result of 1D intermolecular interactions. To test this hypothesis, CIF files in which predicted AE aspect ratios were more than 80% larger than their BFDH counterparts were investigated. Both **1a** and **2a** supported this hypothesis and 1D intermolecular interactions were identified perpendicular the smallest, fastest growing faces (Figure 4-6). A few of the structures predicted to have high aspect ratios were had interactions that extended in two dimensions. The AE predicted morphologies in those cases were more plate-like than those displaying 1D interactions. The CIF files MOXZEF, which showed perpendicular hydrogen bonding and π-π stacking interactions, is displayed as an example (Figure 4-7). We concluded that the differences are indeed due to intermolecular interactions and are being adequately described by the force field.

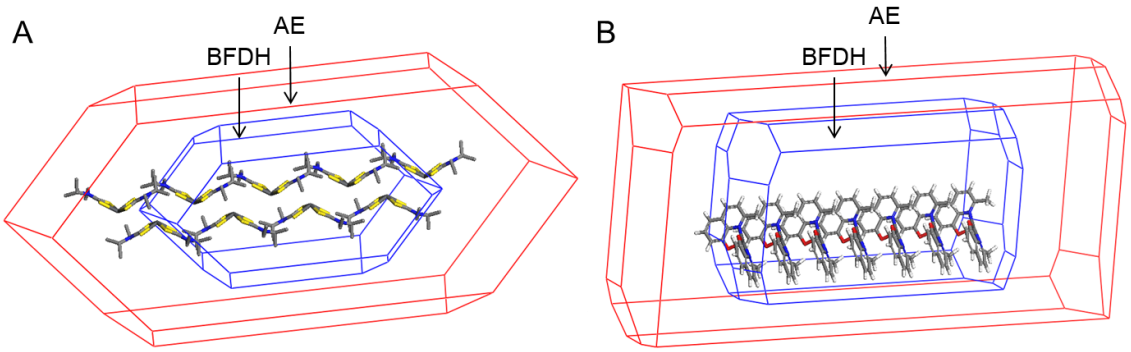

Figure 4-6. Predicted morphologies for (A) **1a** and (B) **2a**. The morphology in red was predicted via AE theory and blue corresponds to BFDH theory.

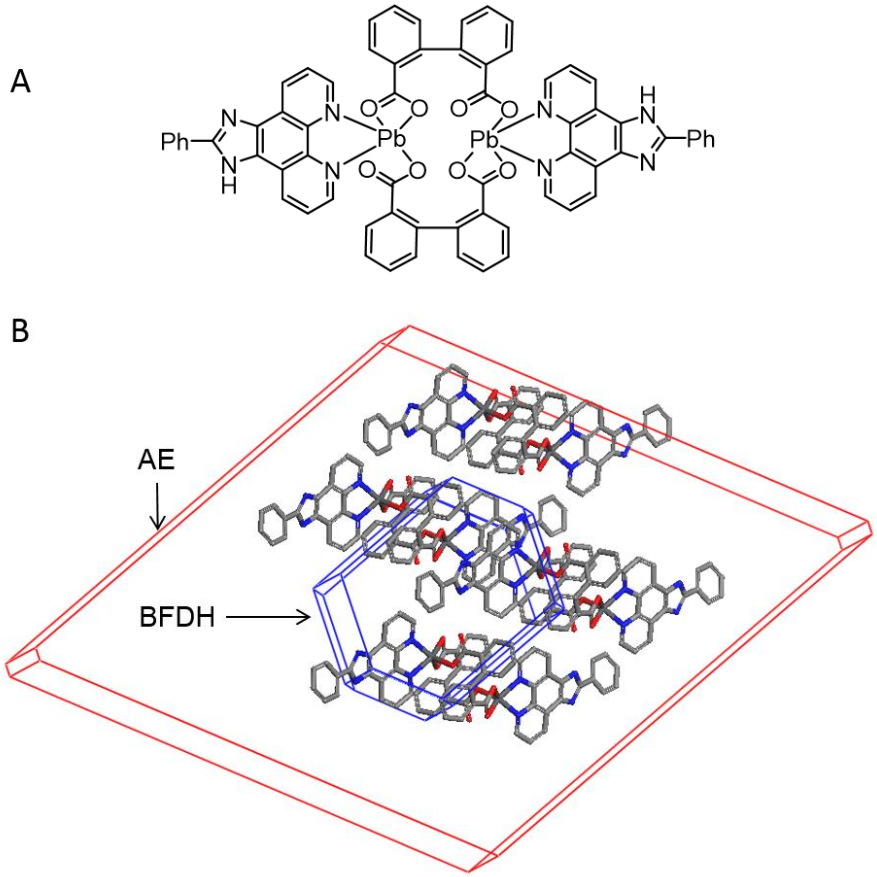

Figure 4-7. (A) Molecular structure for MOXZEF. (B) Predicted morphologies for MOXFEF. The morphology in red was predicted via AE theory and blue corresponds to BFDH theory.

Target Selection and Gelator Discovery.

Potential targets were analyzed using primarily the predicted aspect ratio. Details on the predicted aspect ratio and energy of crystallization can be found for each compound in Appendix 3. Target compounds for synthesis and gel screening were selected from the top 5% of predicted aspect ratios. For practical reasons, only air and moisture tolerant complexes were selected for initial synthesis and gel screening. The nine CIF files in the top 5% are shown in Table 4-7. Visual representations of all predicted morphologies for all of the Pb(II) compounds in the top 5% aspect ratio group can be found in Appendix 3.

Table 4-7. Data for the predicted morphologies in the top 5% of aspect ratios, including normalized lattice energies, aspect ratio, and the attachment energies of the smallest and largest faces.

CIF	normalized E_{latt}	AR	AE smallest face (kcal/mol)	AE largest face (kcal/mol)
AJOGOW	-142.885	3.833	-125.997	-71.703
KUQFAE01	-29.706	3.967	-84.308	-24.667
CIJQOC	-59.459	4.088	-99.244	-42.581
PASBAM	-12.505	1.918	-143.019	-78.875
NUNXOK	-33.202	4.489	-149.674	-35.186
WACCUA	-44.357	4.536	-67.643	-16.099
NAYNUW01	-30.662	4.672	-105.712	-32.650
EFOZUV	-60.678	4.796	-73.338	-16.416
MOXZEF	-23.195	5.540	-83.589	-15.809
ETUJOT	-26.866	7.125	-281.629	-27.367

Compounds **1a**[33] and **2a**[34] were chosen as the initial test cases for gelator discovery. The Pb-dithiocarbamate structure (**1a**) shows Pb-S interactions in the solid state which we propose as the “fiber-forming” interaction. The Pb-hydroxyquinoline complex (**2a**) displays an analogous Pb-O interaction as well as π-π stacking. Both complexes show a semi-hemispheric coordination geometry pattern often seen in lead complexes.[35,36] Both compounds can be synthesized in a robust, one-pot reaction that can be modified to allow the synthesis of analogs. Detailed synthetic procedures can be found in the Appendix 3. Derivatives **1a–d** and **2a–b** can be seen in Chart 4-3. Gel

screening was performed on the as-synthesized derivatives in a variety of solvents (polar and nonpolar, protic and aprotic) by heating a sealed vial containing the compound and solvent to dissolve, then allowing it to cool with ~20 s of sonication to speed aggregation. Compounds **1d** and **2b** were identified as gelators (Appendix 3). Compound **1d** gels in a several solvents and **2b** gels in a basic water solution (Table 4-8). Rheological studies revealed that, for both gelators, the elastic modulus (G′) was higher than the storage modulus (G″) by about an order of magnitude in both a stress and frequency sweep, as is expected for a gel. LMW gels form a fibrous network with fibers 1-3 μm in diameter (Figure 4-8).

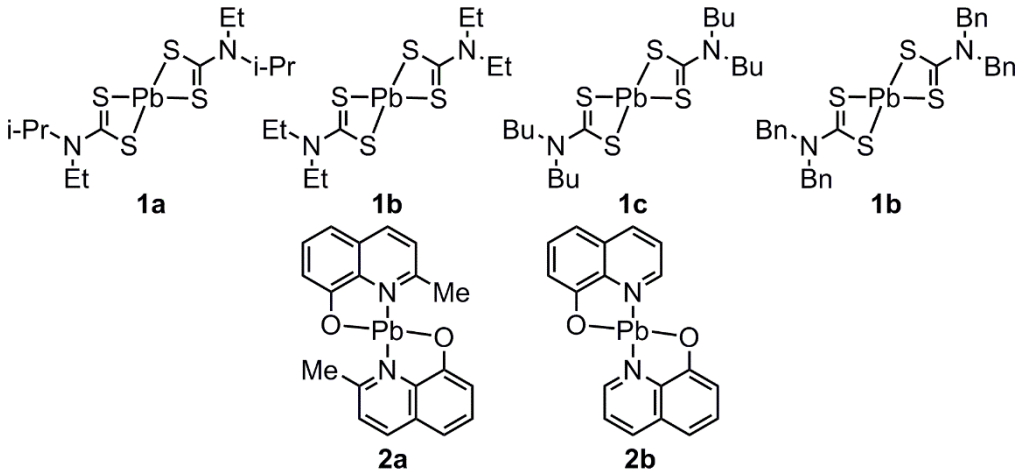

Chart 4-3.

Table 4-8. Critical gelation concentration data for **1d** and **2b**.

compound	Acetone	EtOAc	H_2O/EtOH (pH 12)[a]
1d	1.99 ± 0.00 mM	1.46 ± 0.01 mM	--
2b	--	--	13.9 ± 0.3

[a] detailed solvent conditions can be found in Appendix 3

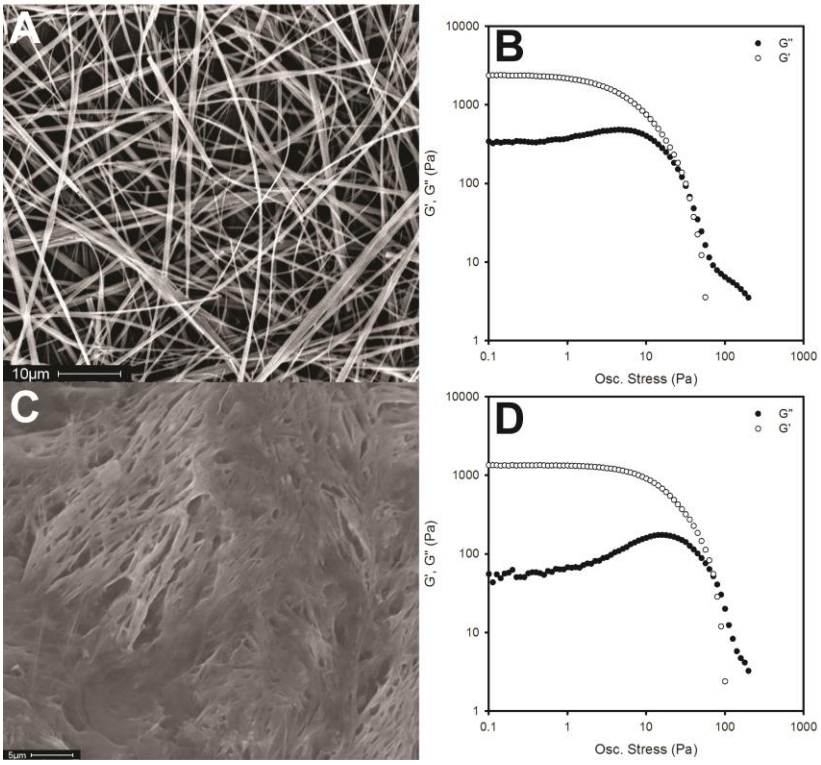

Figure 4-8. (A) Scanning electron microscopy (SEM) image of **1d** (2.7 mM in acetone), (B) Rheology stress sweep of **1d** (7.18 mM in EtOAc), (C) SEM image of **2b** (13.9 mM in H_2O/EtOH, pH 11), (D) Rheology stress sweep of **2b** (13.9 mM in H_2O/EtOH, pH 11).

Conclusions.

The method described in this chapter represents the first systematic route for gelator discovery and has the potential to be widely applied. Predicting gelators accurately should prove an important step towards a priori design. We have demonstrated that families of molecules that contain gels have high predicted aspect ratios due to 1D intermolecular interactions. Starting with published crystal structures in the Cambridge Structural Database, we identified CIF files that displayed 1D intermolecular interactions by selecting predicted morphologies with the highest aspect ratios. Influencing factors on the computational model, such as preparing CIF files for calculation, geometry optimization, and crystal graph generation, were investigated. Targets for gel screening were selected from the top 5% highest aspect ratios,

synthesized, and two new gelators were found. This method could be adapted to any crystal structure simply by selecting an appropriate force field.

---

[1] Feringa, B. L. Controlling Self-Assembly in Time and Space. In *From Non-Covalent Assemblies to Molecular Machines*; Sauvage, J.-P., Gaspard, P., Eds.; Wiley-VCH Verlag GmbH & Co. KGaA: Weinheim, Germay, 2010; pp 453–461.

[2] Dastidar, P. *Chem. Soc. Rev.* **2008**, *37*, 2699–2715.

[3] Weiss, R. G. *J. Am. Chem. Soc.* **2014**, *136*, 7519–7530.

[4] van Esch, J. H. *Langmuir* **2009**, *25*, 8392–8394.

[5] Hanabusa, K.; Yamada, M.; Kimura, M.; Shirai, H. *Angew. Chem., Int. Ed.* **1996**, *35*, 1949–1951.

[6] Muro-Small, M. L.; Chen, J.; McNeil, A. J. *Langmuir* **2011**, *27*, 13248–13253.

[7] X, P.; Chu, X.; Li, S.; Ma, M.; Hao, A. *ChemPhysChem* **2014**, 2377–2385.

[8] Das, U. K.; Trivedi, D. R.; Adarsh, N. N.; Dastidar, P. *J. Org. Chem.* **2009**, *74*, 7111–7121.

[9] Yan, N.; Xu, Z.; Diehn, K. K.; Raghavan, S. R.; Fang, Y.; Weiss, R. G. *Langmuir* **2013**, *29*, 793–805.

[10] Yamanaka, M. *J. Incl. Phenom. Macrocycl. Chem.* **2013**, *77*, 33–48.

[11] Caran, K. L.; Lee, D.-C.; Weiss, R. G. Molecular Gels and their Fibrillar Networks. In *Soft Fibrillar Materials: Fabrication and Applications*; Liu, X. Y., Li, J.-L., Eds.; Wiley-VCH Verlag GmbH & Co. KGaA: Weinheim, Germany, 2013, pp 3–75.

[12] King, K. N.; McNeil, A. J. *Chem. Commun.* **2010**, *46*, 3511–3513.

[13] Carter, K. K.; Rycenga, H. B.; McNeil, A. J. *Langmuir* **2014**, *30*, 3522–3527.

[14] Schmidt, C.; Ulrich, J. *J. Cryst. Growth* **2012**, *353*, 168–173.

[15] Winn, D.; Doherty, M. F. *Am. Inst. Chem. Eng.* **2000**, *46*, 1348–1367.

[16] Docherty, R.; Clydesdale, G.; Roberts, K. J.; Benema, P. *J. Phys. D: Appl. Phys.* **1991**, *24*, 89–99.

[17] Woensdregt, C. F. *Faraday Discuss.* **1993**, *95*, 97–107.

[18] Yellin-Berkovitch, Z. *J. Am. Chem. Soc.* **1985**, *107*, 8239–8253.

[19] Buller, R.; Peterson, M. L.; Almarsson, O.; Leiserowitz, L. *Cryst. Growth Des.* **2002**, *2*, 553–562.

[20] Poloni, L. N.; Ward, M. D. *Chem. Mater.* **2014**, *26*, 447–495.

[21] Bravais, A. *Etudes Crystallographiques*. Acadamie Des Sciences, Paris, 1913.

[22] Friedel, G. *Bull. Soc. Fr. Miner.* **1907**, *30*, 326–455.

[23] Donnay, J. D. H.; Harker, D. *J. Amer. Minerologist* **1937**, *22*, 436–444.

[24] Hartman, P.; Perdok, W. G. *Acta Cryst.* **1955**, *8*, 521–524.

[25] Hartman, P.; Perdok, W. G. *Acta Cryst.* **1955**, *8*, 525–529.

[26] Stoltzberg, L. J.; Madden, E. *Acta Cryst.* **1999**, *B55*, 882–885.

[27] Alfredsson, M.; Cora, F. Brodholt, J. P.; Parker, S. C.; Price, G. D. *Phys. Chem. Miner.* **2005**, *32*, 379–385.

[28] Accelrys Software Inc., Discovery Studio Modeling Environment, Release 4.0, San Diego: Accelrys Software Inc., 2013.

[29] Mitchell-Koch, K. R.; Matzger, A. J. *J. Pharm. Sci.* **2008**, *97*, 2121–2129.

[30] Rappe, A. K.; Casewit, C. J.; Colwell, K. S.; Goddard, W. A. III.; Skiff, W. M. *J. Am. Chem. Soc.* **1992**, *114*, 10024-10035.

[31] Labisbal, E.; Sousa, A.; Castineiras, A.; Garcia, Vasques, J. A.; Romero, J. West, D. X. *Polyhedron* **2000**, *19*, 1255–1262.

[32] Punzo, F. *J. Mol. Struct.* **2013**, *1032*, 147–154.

[33] Trindade, T.; O'Brien, P.; Zheng, X.-M.; Motevalli, M. *J. Mater. Chem.* **1997**, *7*, 1011–1016.

[34] Mohammadnezhad, G.; Ghanbarpour, A. R.; Amini, M. M.; Ng, S. W. *Acta Cryst.* **2010**, *E66*, m529.

[35] Golden, M. L.; Reibenspies, J. H.; Darensbourg, M. Y. *Inorg. Chem.* **2004**, *43*, 5798–5800.

[36] Shimoni-Livny, S.; Glusker, J. P.; Bock, C. W. *Inorg. Chem.* **1998**, *37*, 1853–1867.

Chapter 5. Conclusions and Future Directions

In 2013, more than four thousand articles were published on the topic of low molecular weight gelators, which is good evidence of the scientific community's interest in these materials.[1] A multitude of applications have been proposed low molecular weight gels, such as sensing, environmental remediation, neuron growth media, and catalysis.[2–5] Many challenges still must be overcome before these materials can gain commercial purchase, but some understanding of how and why these materials form is beginning to take shape.[6,7] An understanding of how and why gels form is necessary to predict and eventually design molecules with this property.[8–10]

We have demonstrated the ability to predict what classes of molecules will contain gelators in three distinct cases (Chart 5-1). This work was initially embarked upon by manual examination of crystal structures accessed through the Cambridge Structural Database (CSD). By measuring the distances of intermolecular interactions and chemical intuition, we were able to identify a new mercury-containing gelator. In this case, gelation can selectively be induced by the addition of $Hg(OAc)_2$ to a solution of a non-gelling precursor, which gives this material potential to be used in sensing. Because the mercury ions are incorporated into the fibers themselves during gelation, the solvent removed from the gel showed a significant reduction in the concentration of mercury, signifying the potential to be used in environmental remediation. Intolerance to chloride and low sensitivity detracted from the materials' usefulness.[11,12]

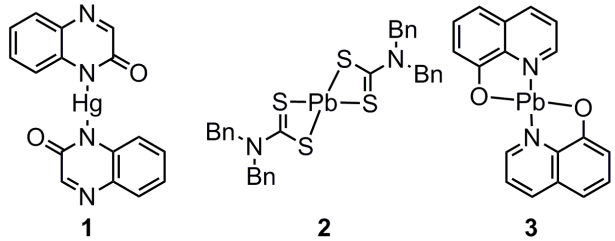

1 **2** **3**

Chart 5-1.

Derivatization of the mercury-containing gelator resulted in a library of related gelators and nongelators (Chart 5-2). The trend that gelators tend to show higher dissolution enthalpies than non-gelators has been observed in other systems. To investigate whether the same observation could be made for this system, the dissolution enthalpies were measured on the compounds in this library. Due to the lack of a common gelling solvent and the identification of several solid forms for each Hg-complex, we concluded that there was no way to compare these compounds. Although this result was unfortunate, we determined that it is necessary to measure dissolution enthalpies on a form that matches the gel. Derivatization led to a Hg-containing gelator (Hg(7-bromoquinoxalinone)$_2$) that showed complete tolerance to chloride, which was shown to be due to the increased binding affinity of Hg to that particular ligand. This gelator even gelled solutions containing river water. Derivatization also led to lower concentrations of mercury necessary to form a gel, but not to the extent necessary to approach the EPA's maximum consumption limit for mercury in drinking water.[13]

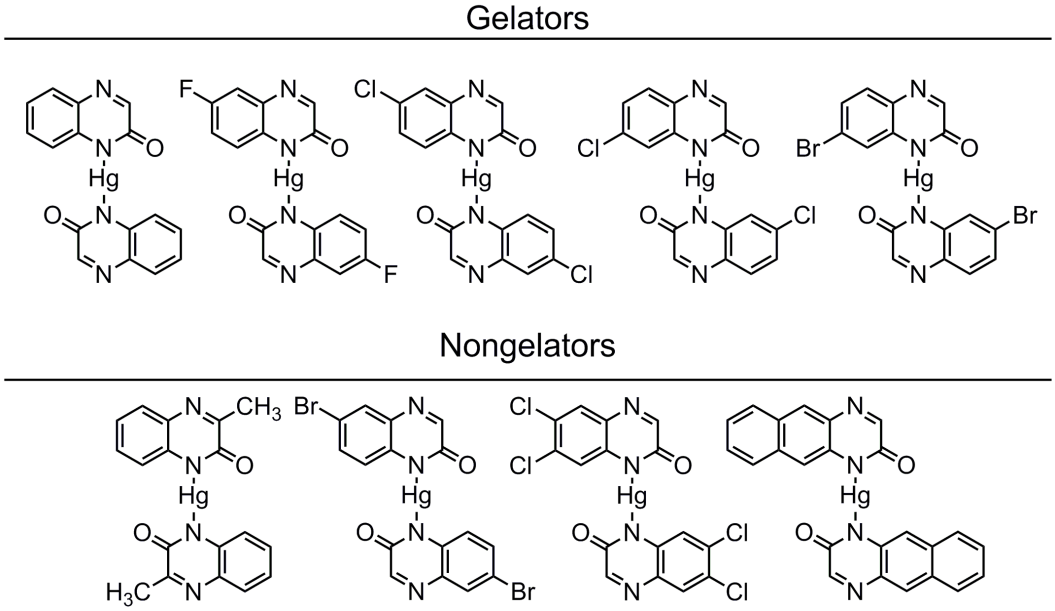

Chart 5-2.

We approached identifying new gelators in a less subjective manner by developing a computational tool to aid in target selection. Based on the predicted morphologies (generated by Materials Studio[14]) of crystal structures accessed from the CSD, we were able to streamline the gelator discovery process. Intermolecular

interactions in a crystal structure are calculated by generating a crystal graph, which is then used to predict the morphology (Figure 5-1). A thorough investigation of the computational model was performed by looking at factors such as preparing CIF files for calculation, geometry optimization, and crystal graph generation. By targeting the top 5% of predicted aspect ratios, we identified two new Pb-containing gelators with minimal derivatization and gelation (Chart 5-1).

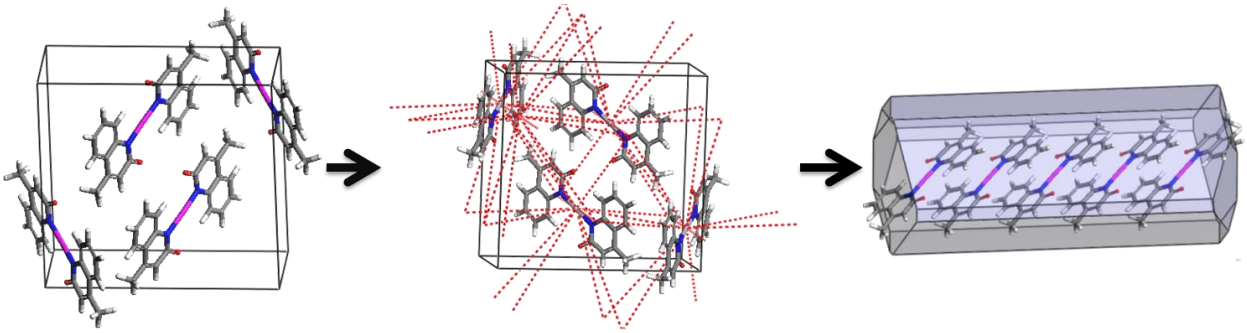

Figure 5-1. Aspect ratios are calculated by generating a crystal graph to assess relative intermolecular interactions in published crystal structures

During the process of developing the computational model, we encountered a question the ability of the force field to describe Pb-containing compounds. Because an initial study was performed on CIF files that contained Pb^{2+}, we were limited in our force field selection. Only the broadly-applicable but less accurate Universal force field was able to describe Pb compounds. We envision future studies of this nature on purely organic compounds would lead to a variety of force fields available for calculation, such as COMPASS and the Drieding model, which are often used to describe organic molecules. We propose to further validate our method by using phenazine as our target. An initial search of the CSD reveals over thirty crystal structures containing this scaffold. A few examples of these structures can be found in Chart 5-3. As this molecule contains no metals or metalloids, a number of force fields supported by Materials Studio could be employed. Phenazine can be prepared by the oxidation of 5,10-dihydrophenazine. If 5,10-dihydrophenazine is determined to be a non-gelator, this reaction could be developed into stimuli-responsive gelator. We propose that the oxidation could be triggered by a Cr(VI) compound, which is known to be a good oxidant. A similar, stoichiometric oxidation of 5,14-dihydro-5,14-diazapentacene by potassium

dichromate[15] was shown in the literature (Scheme 5-1). Hexavalent chromium is extremely toxic and it is necessary to detect trace amounts of it in drinking water.[16,17]

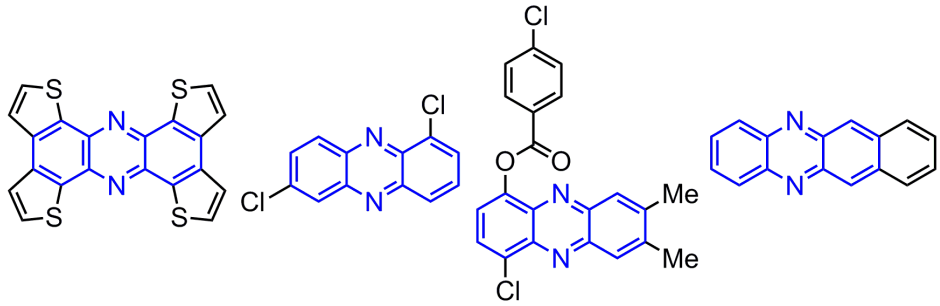

Chart 5-3.

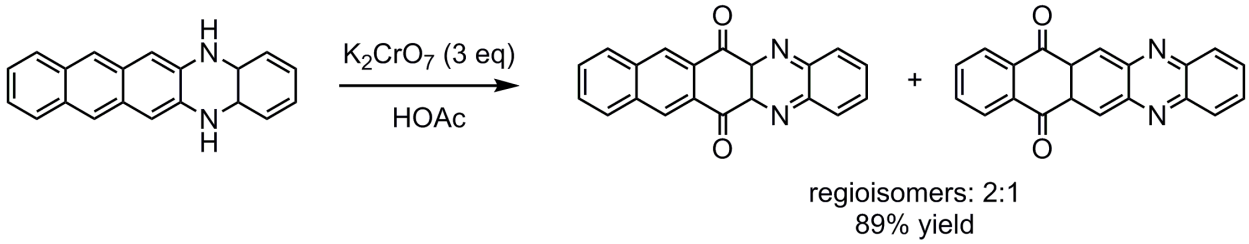

Scheme 5-1. The oxidation of 5,14-dihydro-5,14-diazapentacene into 5,14-Diaza-6,13-pentacenequinone and 7,12-diaza-5,14-pentacenequinone by potassium dichromate in acetic acid.

In the future, lead gelators described in this dissertation will be investigated for practical applications. Lead has been historically used in a variety of applications, such as an engine anti-knocking agent, solder, and as an additive to paint. As it is highly toxic, the use of lead in these applications has been prohibited, but many older homes still contain lead paint, which can be dangerous to human inhabitants, as well of costly to dispose of safely.[18] A selective, inexpensive, user-friendly sensor is necessary to identify lead paint.

Detecting lead in paint offers unique challenges. Currently, a colorimetric lead sensor for paint is available in hardware stores produced by 3M.[19] It has the advantage of being inexpensive and easy to use, but it is too sensitive for the 5 ppt detection target set by the EPA and relies on a color change to a bright pink in the presence of lead, which could easily be distorted by a highly colored paint. We envision a system where a standard-sized paint chip is added to a solution of a non-gelling precursor. The solvent

would dissolve the paint chip, facilitating coordination to lead to trigger gelation. A gel-based sensor for lead in paint would be independent of color and tunable in terms of concentration based on solvent and volume selection.

Solvent and sample size conditions need to be determined to trigger gelation at the detection target of 5 ppt set by the EPA.[20] Gel conditions are paramount for this sensor to be a commercially viable option. Gelation is required to reliably occur without the aid of equipment not commonly found in a hardware store. The stability of the sodium *N*,*N*-dibenzyldithiocarbamate under non-ideal conditions (e.g. heat or moisture) would need to be investigated. Finally, **3** was the first Pb-dithiocarbamate structure to be identified as a gelator, but potentially others exist within the class that could have advantageous properties, such as increased stability or a more ideal critical gelation concentration. Further derivatization is necessary to identify other gelators within this class of materials, which would allow us to perform structure-property relationship studies on these materials.

The method described in Chapter 4 is the first generalizable approach to new gelator discovery. It should prove to be an important tool in understanding these complicated and unique materials. Predicting these materials reliably would represent a big advance in the field of low molecular weight gelation. We will continue investigating this method because further examples of accurately predicted gelators will encourage other researchers to follow our example and continue to enrich the general understanding of the underlying principles of self-assembly and gelation.

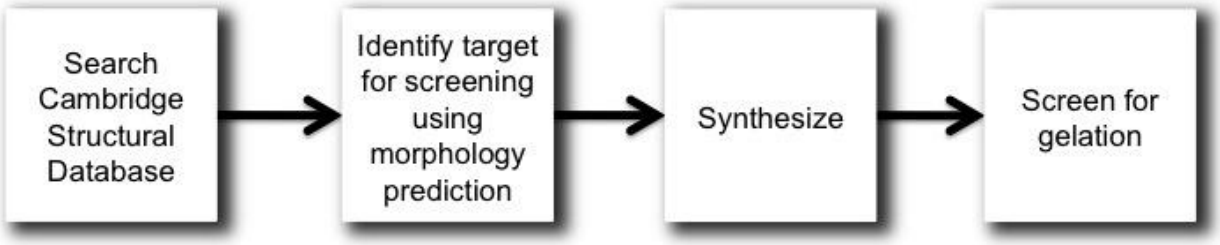

Figure 5-2. Procedure for predicting new gelators developed for this thesis work.

---

[1] Weiss, R. G. *J. Am. Chem. Soc.* **2014**, *136*, 7519-7530.

[2] Hirst, A. R.; Escuder, B.; Miravet, J. F.; Smith, D. K. *Angew. Chem. Int. Ed.* **2008**, *42*, 8002-8018.

[3] Banerjee, S.; Das, R. K.; Maitra, U. *J. Mater. Chem.* **2009**, *19*, 6649–6687.

[4] Sangeetha, N. M.; Maitra, U. *Chem. Soc. Rev.* **2005**, *34*, 821–836.

[5] Dawn, A.; Shiraki, T.; Haraguchi, S.; Tamaru, S.; Shinkai, S. *Chem. Asian J.* **2011**, *6*, 266–282.

[6] Fages, F. Ed. *Low Molecular Mass Gelators: Design, Self-Assembly, Function*; Topics in Current Chemistry 256; Springer-Verlag: Berlin, 2005.

[7] Terech, P.; Weiss, R. G., Eds. *Molecular Gels, Materials with Self-Assembled Fibrillar Networks*; Springer: Dordrect, 2006.

[8] Tam, A. Y.-Y.; Yam, V. W.-W. *Chem. Soc. Rev.* **2013**, *42*, 1540-1567.

[9] Van Esch, J. H. *Langmuir* **2009,** *25,* 8392-8394.

[10] Dastidar, P. *Chem. Rev. Soc.* **2008**, *37*, 2699-2715.

[11] King, K. N.; McNeil, A. J. *Chem. Commun*. **2010**, *46*, 3511-3513.

[12] Environmental Protection Agency: Mercury. www.epa.gov/mercury/ (Accessed July 2, 2014).

[13] Carter, K. C.; Rycenga, H. B.; McNeil, A. J. *Langmuir* **2014**, *30*, 3522-3527.

[14] *Accelrys Software Inc., Discovery Studio Modeling Environment, Release 4.0, San Diego: Accelrys Software Inc., 2013.*

[15] Liang, Z.; Tang, Q.; Liu, J.; Li, J.; Yan, F.; Miao, Q. *Chem. Mater.* **2010**, *22*, 6438-6443.

[16] U. S. Environmental Protection Agency. Water: Chromium in Drinking Water. http://water.epa.gov/drink/info/chromium/guidance.cfm (Accessed July 6, 2014).

[17] Velma, V.; Vutukuru, S. S.; Tchounwou, P. B. *Rev. Environ. Health* **2009**, *4*, 129-145.

[18] U. S. Environmental Protection Agency: Lead. www2.epa.gov/lead (Accessed July 2, 2014).

[19] 3M LeadCheckTM Swabs. http://leadcheck.com/?WT.srch=1&WT.mc_id=SE_lcheck_lead-test-swabs (accessed July 2, 2014).

[20] U.S. Environmental Protection Agency: Renovation, Repair and Painting Program. www.epa.gov/lead/renovation-repair-and-painting-program (Accessed July 2, 2014).

Appendix 1
Supporting Information for Chapter 2
Streamlined Approach to a New Gelator:
From Solid-State Interactions to Mercury-induced Gelation

Contents

I. Materials 57
II. General Experimental 57
III. Synthetic Procedures 61
IV. NMR Spectra 63
V. Gelation Tests 67
VI. X-ray Crystal Structures 69
VII. SEM Images 71
VIII. Powder X-ray Diffraction Data 73
IX. Rheological Data 75
X. ICP-OES Data 76
References 77

I. Materials

All reagent grade materials and solvents were purchased from Sigma-Aldrich, Acros, or TCI and used without further purification.

II. General Experimental

Complex Gel Formation – An 8 mL vial was charged with **2a** (13 mg, 0.026 mmol) and a MeOH/H_2O (90/10 v/v, 1 mL) solution. The vial was sealed and the mixture was heated until homogeneous and then cooled to rt to form a gel.

In Situ Gel Formation – An 8 mL vial was charged with **1a** (7 mg, 0.05 mmol) and MeOH (0.9 mL) and heated to dissolve. An aq. $Hg(OAc)_2$ solution (0.1 mL, 0.157 M) was then added. The vial was sealed and the mixture was heated until homogeneous and then cooled to rt to form a gel.

Gelation Selectivity Tests – Six 12 mL vials were charged with **1a** (10 mg, 0.068 mmol) in MeOH (0.8 mL) and heated to dissolve. One of an array of aq. solutions of metal acetate salts (AgOAc, $Ba(OAc)_2$, $Cd(OAc)_2$, $Co(OAc)_2$, $Cu(OAc)_2$, $Ni(OAc)_2$; 0.2 mL, 0.157 M) were added to each vial. The vials were sealed, the mixtures were heated until homogeneous, and then cooled to rt. No gels were observed.

Counter Ion Effect Test – In situ gels of **2a** were prepared according to the procedure in MeOH/H_20 (90/10 v/v). Various amounts (0, 0.5, 1, and 2 equiv.) of Bu_4NCl was added to the stable gel. Results were recorded 10 minutes after addition of Bu_4NCl, after system was allowed to equilibriate.

NMR Spectroscopy – ^1H and ^{13}C NMR spectra for all compounds were acquired in d_6-DMSO on a Varian MR400 Spectrometer operating at 400 MHz and 100 MHz, respectively. The chemical shift data are reported in units of δ (ppm) relative to tetramethylsilane and referenced with residual DMSO.

X-ray Crystallography – Colorless plates of **2a** were crystallized from a DMSO/H_2O solution at 23 ºC. A crystal of dimensions 0.23 x 0.12 x 0.03 mm was mounted on a standard Bruker SMART-APEX CCD-based X-ray diffractometer equipped with a low temperature device and fine focus Mo-target X-ray tube (l = 0.71073 Å) operated at 1500 W power (50 kV, 30 mA). The X-ray intensities were measured at 85(2) K; the detector was placed at a distance 5.055 cm from the crystal. A total of 5190 frames were collected with a scan width of 0.5º in Φ and 0.45º with an exposure time of 25 s/frame. The frames were integrated with the Bruker SAINT software package with a narrow frame algorithm. The integration of the data yielded a total of 17188 reflections to a maximum 2q value of 59.26º of which 1952 were independent and 1952 were greater than 2s(I). The final cell constants were based on the xyz centroids of 9871 reflections above 10s(I). Analysis of the data showed negligible decay during data collection; the data were processed with SADABS and corrected for absorption. The structure was solved and refined with the Bruker SHELXTL (version 2008/4) software

package,[1] using the space group P1bar with Z = 1 for the formula $C_{16}H_{10}N_4O_2Hg$. All non-hydrogen atoms were refined anisotropically with the hydrogen atoms placed in idealized positions. The complex occupies an inversion center in the crystal lattice. Full-matrix least-squares refinement based on F^2 converged at R1 = 0.0320 and wR2 = 0.0777 [based on I > 2sigma(I)], R1 = 0.0320 and wR2 = 0.0777 for all data. Additional details are presented in Figures S7-S8 and are also given as Supporting Information in a CIF file.

Colorless plates of **S1** were crystallized from a MeOH solution at 23 ºC. A crystal of dimensions 0.37 x 0.34 x 0.10 mm was mounted on a standard Bruker SMART-APEX CCD-based X-ray diffractometer equipped with a low temperature device and fine focus Mo-target X-ray tube (l = 0.71073 Å) operated at 1500 W power (50 kV, 30 mA). The X-ray intensities were measured at 85(2) K; the detector was placed at a distance 5.055 cm from the crystal. A total of 2085 frames were collected with a scan width of 1.5º in Φ and f with an exposure time of 5 s/frame. The frames were integrated with the Bruker SAINT software package with a narrow frame algorithm. The integration of the data yielded a total of 18315 reflections to a maximum 2q value of 60.04º of which 2315 were independent and 2308 were greater than 2s(I). The final cell constants were based on the xyz centroids of 9861 reflections above 10s(I). Analysis of the data showed negligible decay during data collection; the data were processed with SADABS and corrected for absorption. The structure was solved and refined with the Bruker SHELXTL (version 2008/4) software package,[1] using the space group P1bar with Z = 1 for the formula $C_{16}H_{12}N_4O_2HgCl_2$. All non-hydrogen atoms were refined anisotropically with the hydrogen atoms placed in idealized positions. The complex occupies an inversion center in the crystal lattice. Full-matrix least-squares refinement based on F^2 converged at R1 = 0.0596 and wR2 = 0.1670 [based on I > 2sigma(I)], R1 = 0.0600 and wR2 = 0.1677 for all data. Additional details are presented in Figures S9-S10 and are given as Supporting Information in a CIF file.

Powder X-ray Diffraction – Powder X-ray diffraction (PXRD) patterns were collected at ambient temperature using a Bruker D8 Advance diffractometer with a LynxEye detector

using graphite monochromated Cu-Kα radiation (1.5406 Å). The samples were loaded onto glass microscope slides. The software used for data analysis was JADE.

Scanning Electron Microscopy (SEM) – Gels were prepared according to the general procedure. Wet gels were placed in an SEM holder mounted onto SEM stubs with copper tape, and observed using the low vacuum mode of a Philips XL30FEG SEM and a 15-kV accelerating voltage. The images were digitally recorded and processed using Adobe Illustrator.

Rheology – Rheological measurements were taken on an AR2000ex rheometer (TA Instruments) with a 25 mm parallel plate. The gap was fixed at 300 μm. A gel sample was pre-formed in a 4 mL vial and transferred onto the Peltier plate. To prevent solvent evaporation, the loaded sample was covered with a solvent trap. All measurements were performed at 25 ºC. The frequency sweep study was performed under 0.2 Pa stress with a frequency range from 0.628 rad/s to 628 rad/s (i.e., 0.1 Hz – 100 Hz). The strain sweep study was performed with a strain ramp from 0.0174% to 10% at a frequency of 1 Hz. The oscillation stress sweep was performed at 1 Hz, with a stress ranging from 0.008 Pa to 100 Pa.

Inductively Coupled Plasma-Optical Emission Spectroscopy – Inductively coupled plasma-optical emission spectroscopy (ICP-OES) measurements were taken on a Perkin-Elmer Optima 2000 DV. The detection limit for mercury was approximately 10 ppb. Mercury was analyzed with a wavelength of 253.652 nm. Yttrium was used as an internal standard and detected with a wavelength of 371.029 nm. A calibration curve was generated by preparing 4 standard solutions (1 ppm Y; 0, 1, 5, 10 ppm Hg, Figure S19). Three measurements were taken for each sample and averaged.

III. Synthetic Procedures[2]

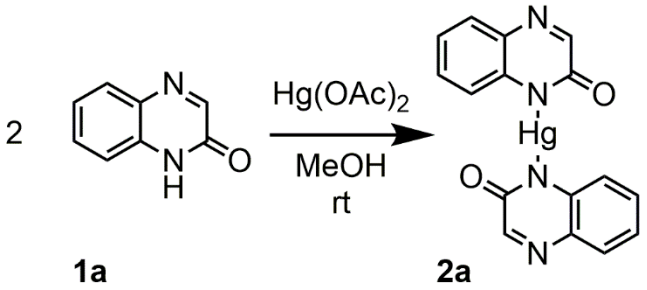

1a **2a**

2a: **1a** (46 mg, 0.31 mmol) was dissolved in MeOH (20 mL). Then $Hg(OAc)_2$ (50 mg, 0.16 mmol) was dissolved in MeOH (5 mL) and added to produce an off-white precipitate (**2a**). The precipitate was filtered and washed with H_2O (1 x 20 mL). **2a** was purified by recrystallization from MeOH to give 67 mg (86% yield) of a light brown solid. HRMS (ESI): Calcd for $C_{16}H_{10}N_4O_2Hg$, 492.0510; found, 492.0522. Elemental analysis: Calcd for $C_{16}H_{10}N_4O_2Hg$: C, 39.15%; H, 2.05%; N, 11.41%; found: C, 39.21%; H, 2.05%; N, 11.53%.

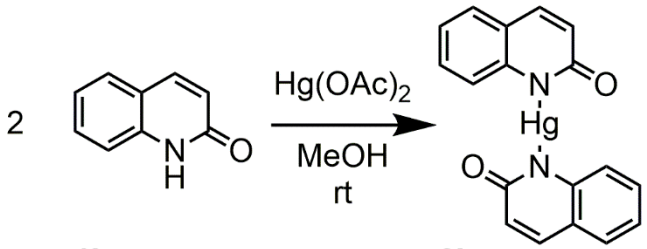

1b **2b**

2b: **1b** (46 mg, 0.31 mmol) was dissolved in MeOH (20 mL). Then $Hg(OAc)_2$ (50 mg, 0.16 mmol) was dissolved in MeOH (5 mL) and added to produce an off-white precipitate (**2b**). The precipitate was filtered and washed with H_2O (1 x 20 mL). **2b** was purified by recrystallization from MeOH to give 64 mg (82% yield) of a white solid. HRMS (ESI): Calcd. For $C_{18}H_{12}N_2O_2Hg$, 490.0605; found, 490.0617.

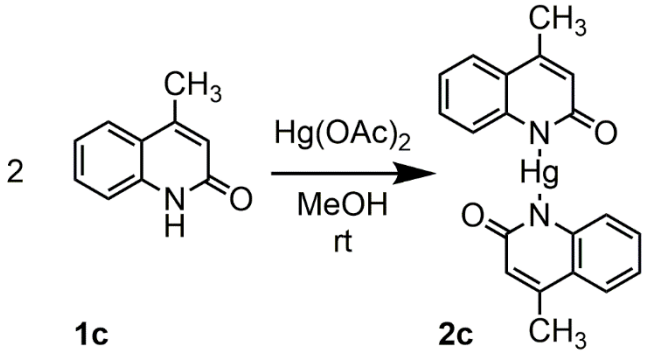

1c **2c**

2c: **1c** (50 mg, 0.31 mmol) was dissolved in MeOH (20 mL). Then $Hg(OAc)_2$ (50 mg, 0.16 mmol) was dissolved in MeOH (5 mL) and added to produce an off-white precipitate (**2c**). The precipitate was filtered and washed with H_2O (1 x 20 mL). **2c** was purified by recrystallization from MeOH to give 73 mg (88% yield) of a white solid. HRMS (ESI): Calcd. For $C_{20}H_{16}N_2O_2Hg$, 518.0918; found, 518.0923.

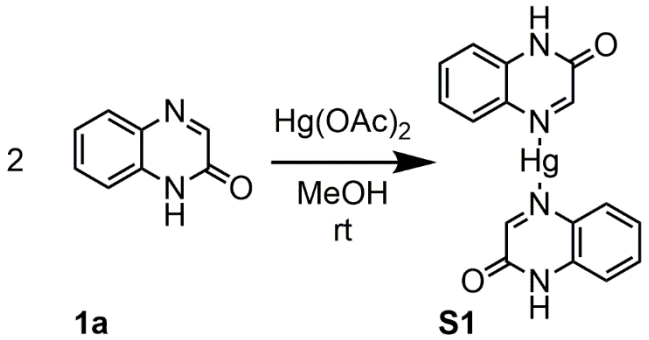

1a **S1**

S1: **1a** (46 mg, 0.31 mmol) was dissolved in MeOH (20 mL). Then $HgCl_2$ (50 mg, 0.18 mmol) was dissolved in MeOH (5 mL) and added to produce light brown crystals (**S1**). The precipitate was filtered and washed with H_2O (1 x 20 mL). **S1** was purified by recrystallization from MeOH to give 49 mg (48% yield) of a light brown solid.

IV. NMR Spectra

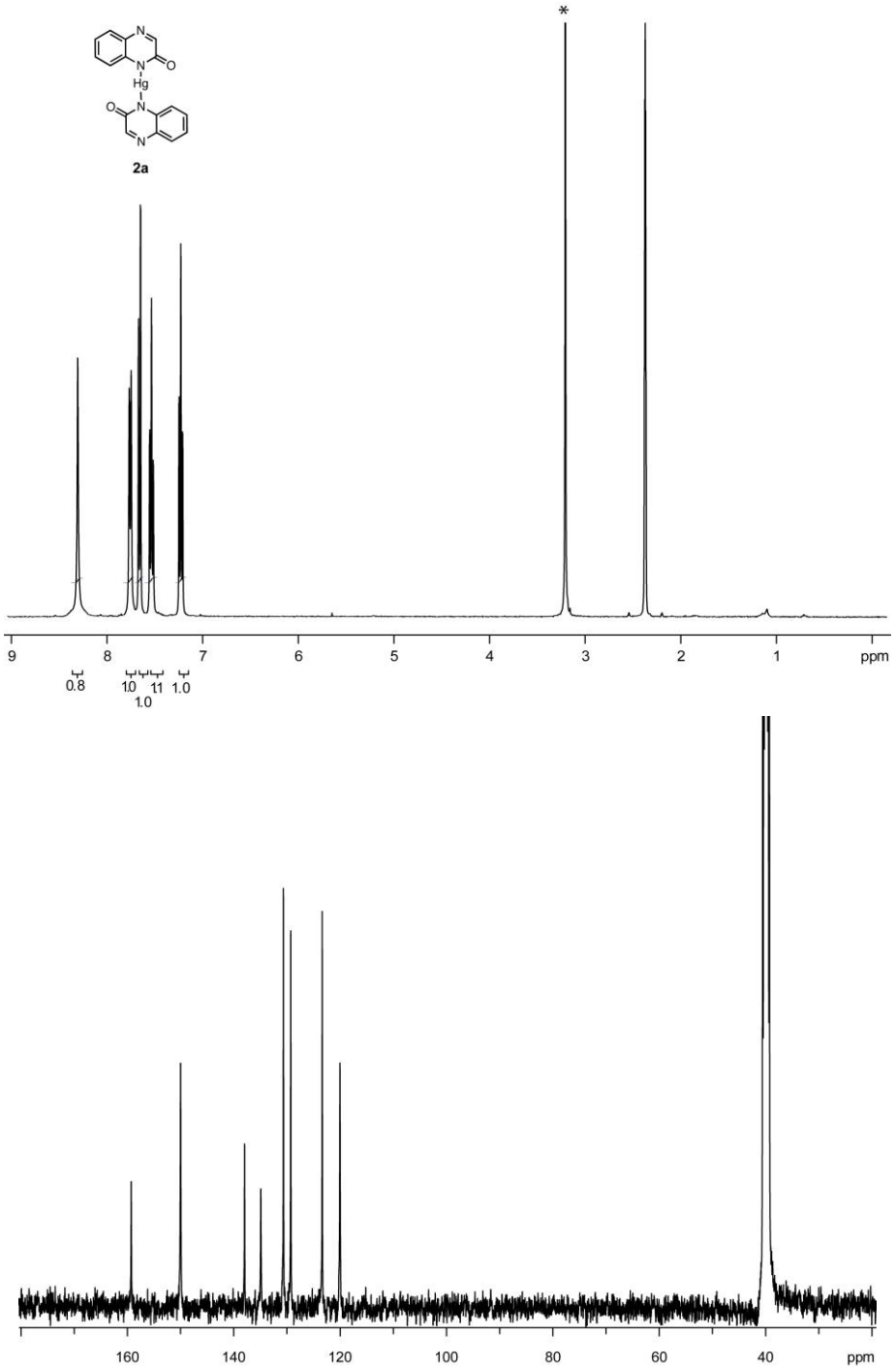

Figure S1-1. ^{1}H and ^{13}C NMR spectra of **2a**. ^{1}H NMR (400 MHz, d_6- DMSO) δ 8.40 (s, 1H), 7.80 (d, J = 7.8 Hz, 1H), 7.70 (d, J = 7.8 Hz, 1H), 7.58 (dt, J = 1.2, 7.0 Hz, 1H), 7.27 (dt, J = 1.2, 7.0 Hz, 1H). ^{13}C NMR (100 MHz, d_6-DMSO) δ 159.26, 149.98, 137.96, 134.89, 130.64, 129.27, 123.35, 120.02. *denotes residual H_2O in d_6-DMSO.

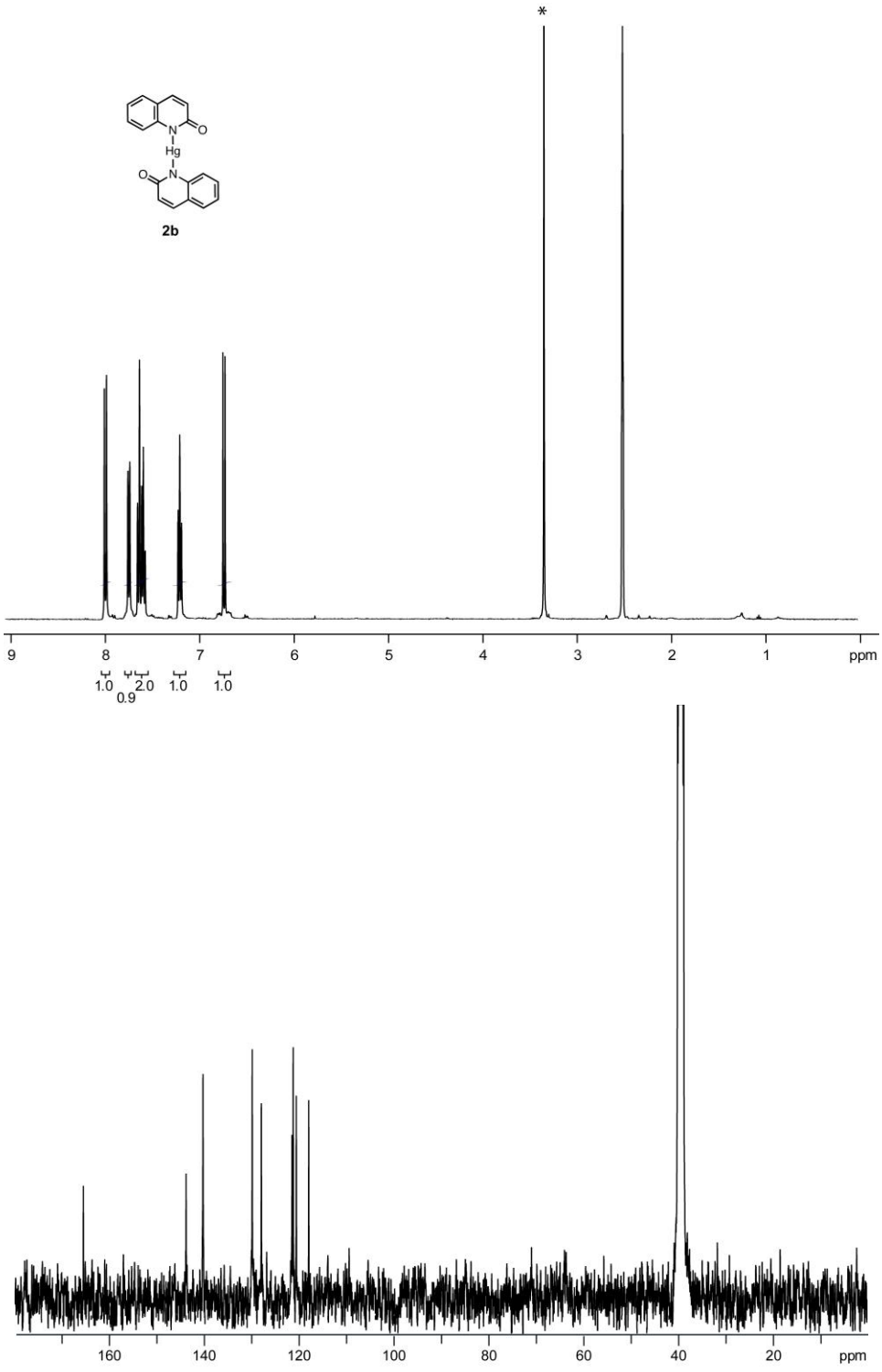

Figure S1-2. ^{1}H and ^{13}C NMR spectra of **2b**. ^{1}H NMR (400 MHz, d_6-DMSO) δ 7.92 (d, J = 9.2 Hz, 1H), 7.67 (d, J = 7.8 Hz, 1H), 7.54 (m, 2H), 7.13 (dt, J = 1.2, 6.6 Hz, 1H), 6.66 (d, J = 9.2 Hz, 1H). ^{13}C NMR (100 MHz, d_6-DMSO) δ 166.07, 144.36, 140.81, 130.40, 128.49, 122.00, 121.75, 121.10, 118.47. *denotes residual H_2O in d_6-DMSO.

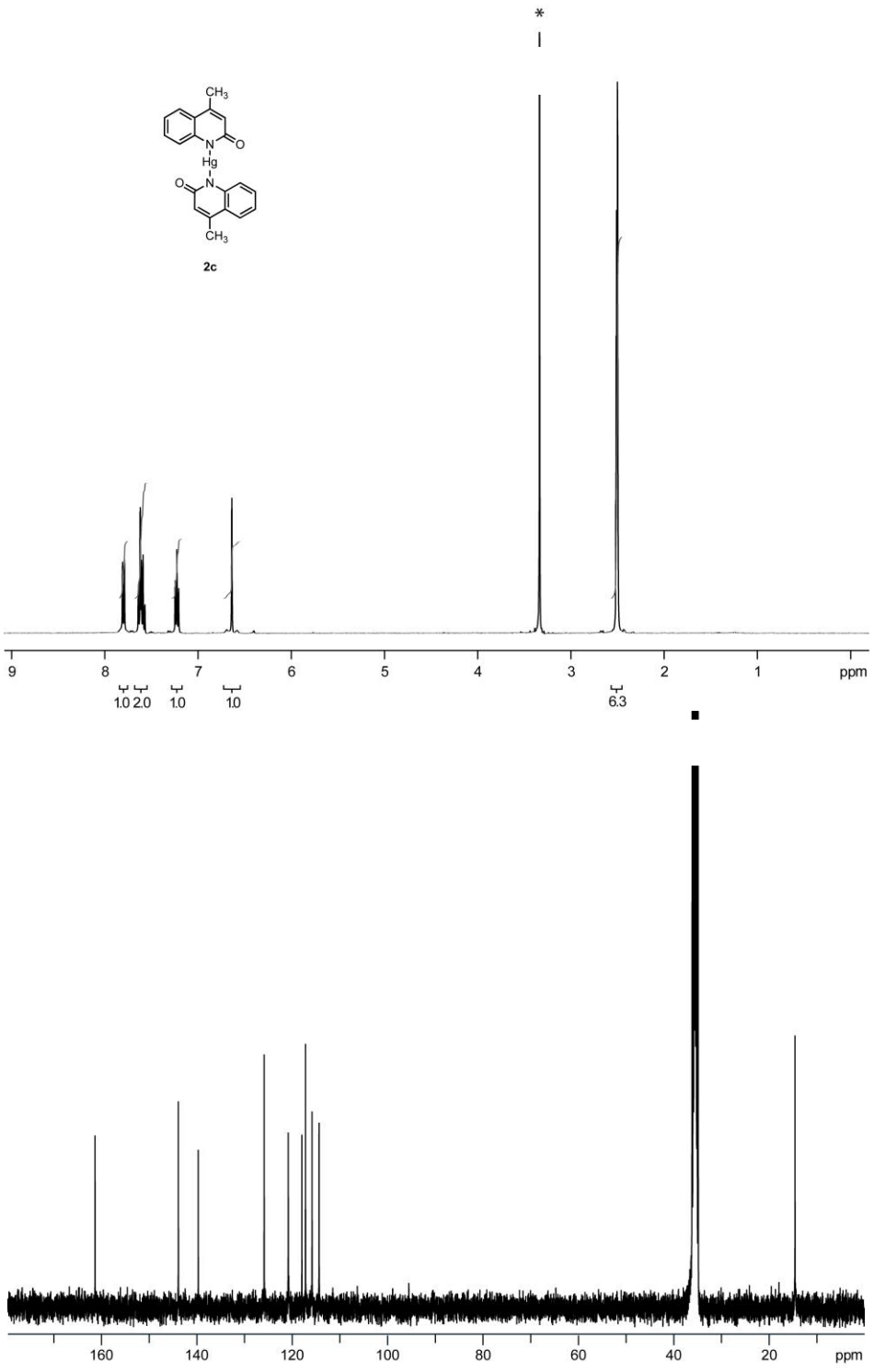

Figure S1-3. ^{1}H and ^{13}C NMR spectra of **2c**. ^{1}H NMR (400 MHz, d_6-DMSO) δ 7.79 (d, J = 8.0 Hz, 1H), 7.62 (m, 2H), 7.23 (dt, J = 1.5, 5.3 Hz, 1H), 6.64 (d, J = 1.0 Hz, 1H), 2.51 (3H, overlap with solvent peak). ^{13}C NMR (100 MHz, d_6-DMSO) δ 161.32, 143.86, 139.69, 125.88, 120.82, 117.97, 117.21, 115.84, 114.36, 14.56. *denotes residual H_2O in d_6-DMSO.

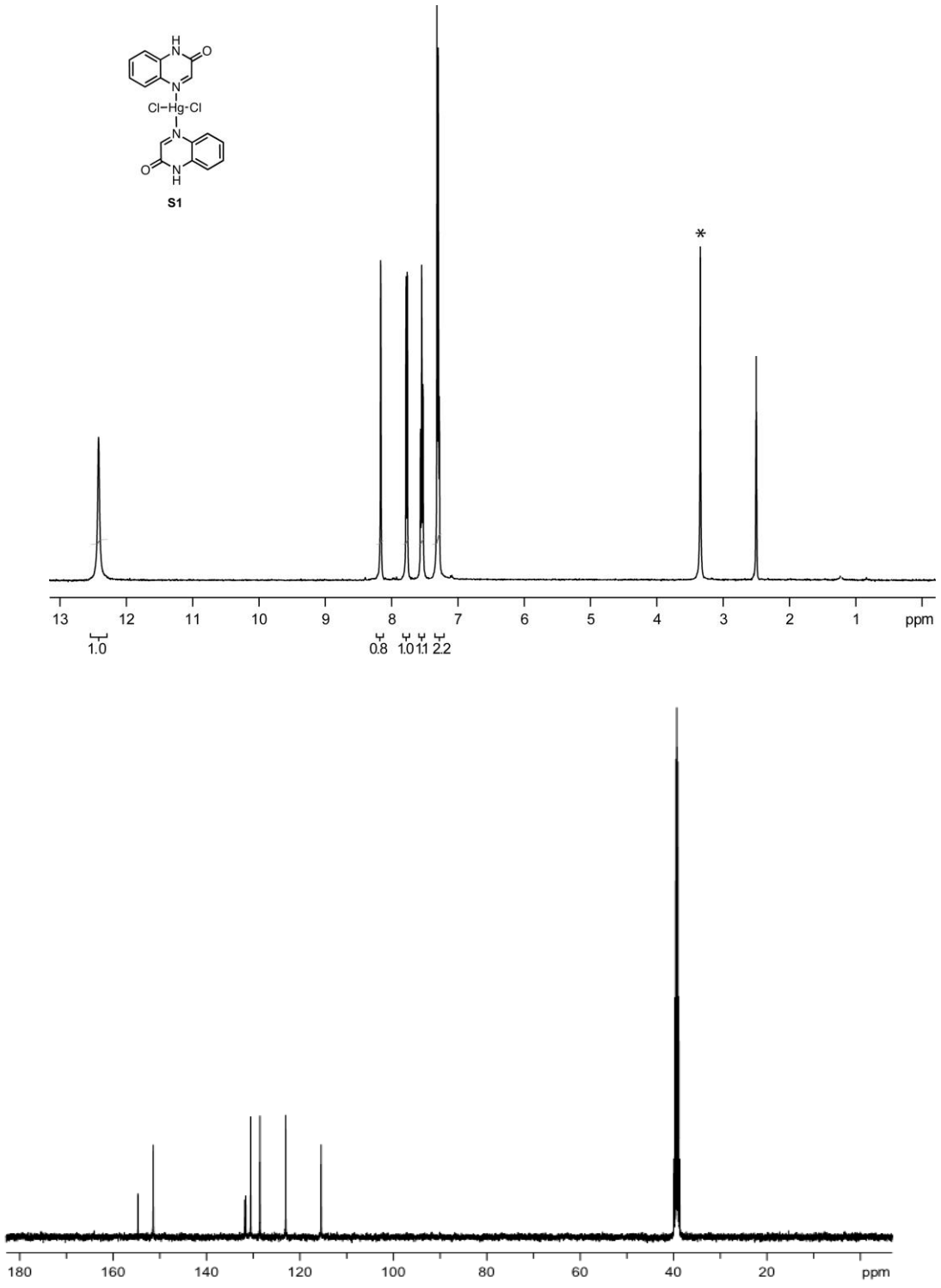

Figure S1-4. ^{1}H and ^{13}C NMR spectra of **S1**. ^{1}H NMR (400 MHz, d_6-DMSO) δ 12.38 (s, 1H), 8.16 (s, 1H), 7.77 (dd, J = 1.1, 7.4 Hz, 1H), 7.53 (dt, J = 1.1, 6.7 Hz, 1H), 7.30 (t, J = 7.4 Hz, 2H). ^{13}C NMR (100 MHz, d_6-DMSO) δ 154.67, 151.42, 131.79, 131.59, 130.54, 128.56, 123.04, 115.48. *denotes residual H_2O in d_6-DMSO.

V. Gelation Tests

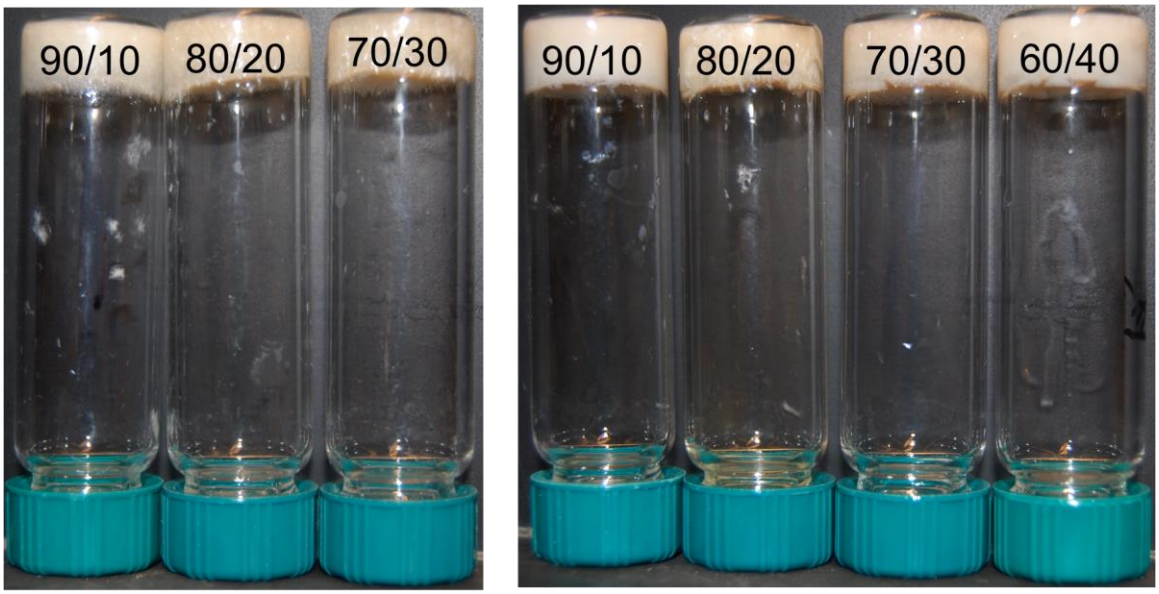

Figure S1-5. Gels of **2a** at their respective critical gel concentrations (cgc) in 1 mL of varying MeOH/H_2O ratios (see Tables S1-1 and S1-2).

Table S1-1. Cgcs of **2a** (complex) in 1 mL of varying MeOH/H_2O ratios at 25 °C.

MeOH/H_2O (v/v)	Trial 1 (mM)	Trial 2 (mM)	Trial 3 (mM)	average cgc (mM)	wt % (average)
90/10	24	26	26	25 ± 1	1.6
80/20	24	22	26	24 ± 2	1.5
70/30	26	26	26	26 ± 0	1.6

Table S1-2. Cgcs of **2a** (in situ) in 1 mL of varying MeOH/H_2O ratios at 25 °C. The molarities were calculated assuming quantitative formation of **2a**.

MeOH/H_2O (v/v)	Trial 1 (mM)	Trial 2 (mM)	Trial 3 (mM)	average cgc (mM)	wt % (average)
90/10	24	21	24	23 ± 2	1.2
80/20	24	24	24	24 ± 0	1.3
70/30	21	21	24	22 ± 2	1.2
60/40	21	21	21	21 ± 0	1.1

Table S1-3. Cgcs of **1a** in 1 mL of varying MeOH/H_2O ratios at 25 °C

MeOH/H_2O (v/v)	Trial 1 (mM)	Trial 2 (mM)	Trial 3 (mM)	average cgc (mM)	wt % (average)
90/10	191	185	198	191 ± 6	3.4
80/20	164	164	157	162 ± 4	2.5
70/30	150	157	157	155 ± 4	2.4

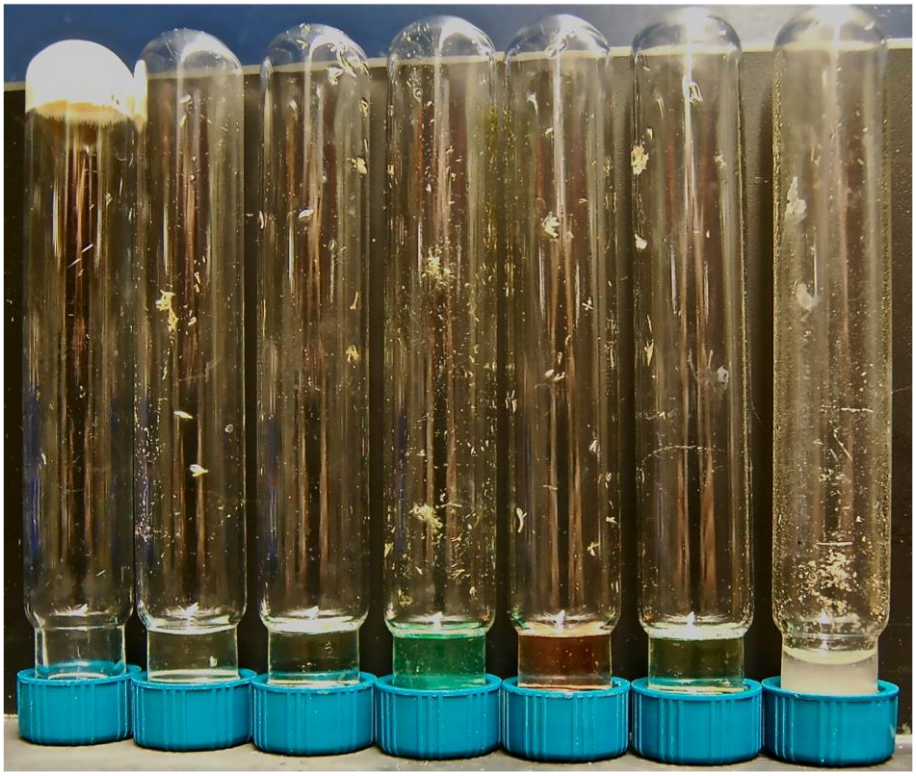

Figure S1-6. Selectivity tests showing the results of adding aq. solutions of an array of metal acetate salts (0.2 mL, 0.157 M) to a solution of **1a** (10 mg, 0.068 mmol) in MeOH (0.8 mL). Metal salts from left to right: $Hg(OAc)_2$, $Ba(OAc)_2$, $Cd(OAc)_2$, $Cu(OAc)_2$, $Co(OAc)_2$, $Ni(OAc)_2$, AgOAc. The only gel that formed was with $Hg(OAc)_2$.

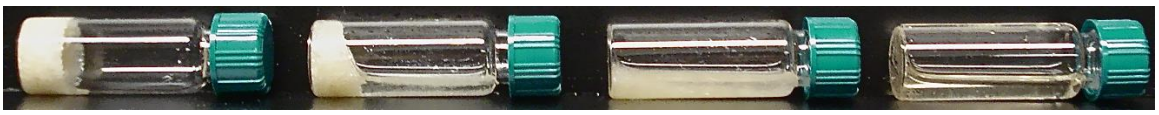

Figure S1-7. The effect of a chloride source (Bu_4NCl) on **2a** in situ gel above cgc (20 mg/mL). Pictures depict gels 10 minutes after the addition of 0, 0.5, 1, and 2 equiv. of Bu_4NCl.

VI. X-ray Crystal Structures

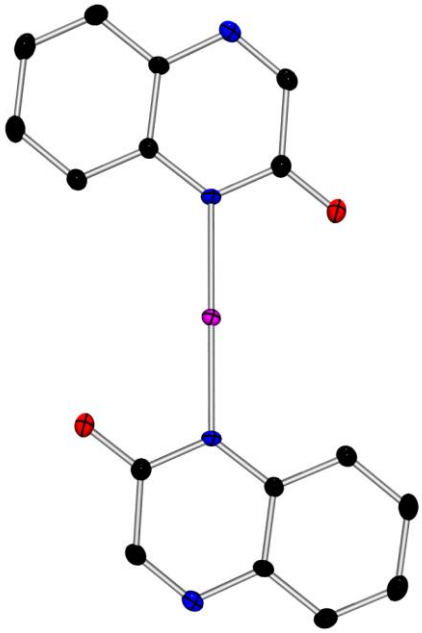

Figure S1-8. Crystal structure of **2a**. The torsion angle between the quinoxalinone ligands is 4.41°. The Hg-N bond length is 2.04 Å and the N-Hg-N bond angle is 180.00°. The hydrogen atoms were omitted for clarity.

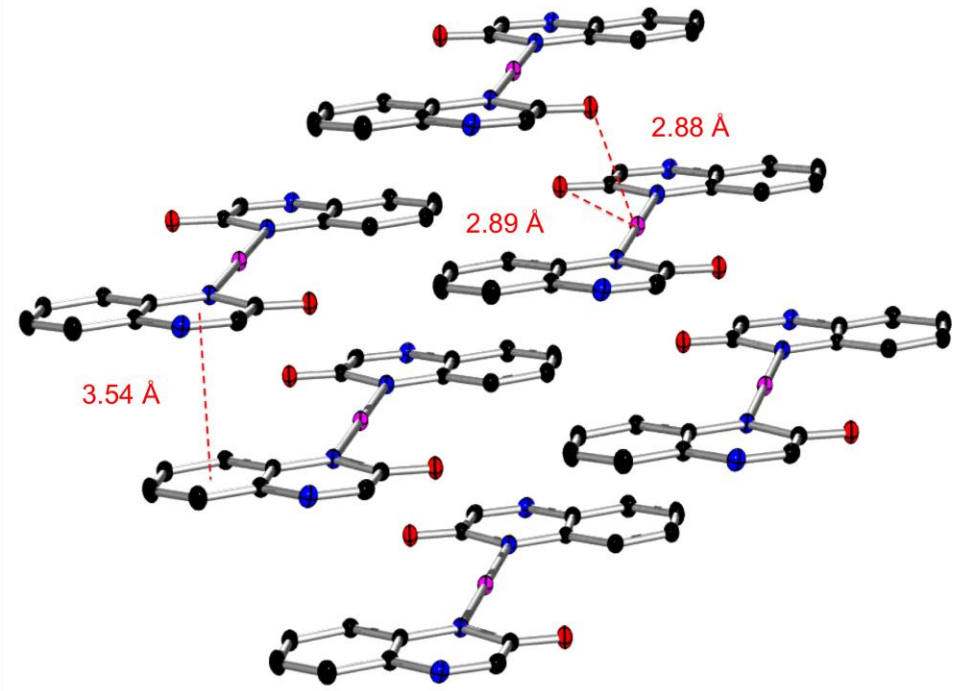

Figure S1-9. Solid-state packing of **2a**. The aryl-aryl π-stacking distance is 3.54 Å. The intramolecular Hg-O distance is 2.89 Å while the intermolecular Hg-O distance is 2.88 Å. The hydrogen atoms were omitted for clarity.

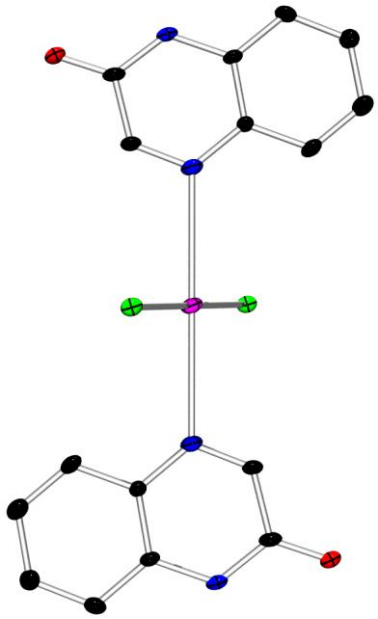

Figure S1-10. Crystal structure of **S1**. The torsion angle between the quinoxalinone ligands is 14.47°. The Hg-N bond length is 2.74 Å and the N-Hg-N bond angle is 180.00°. The hydrogen atoms were omitted for clarity.

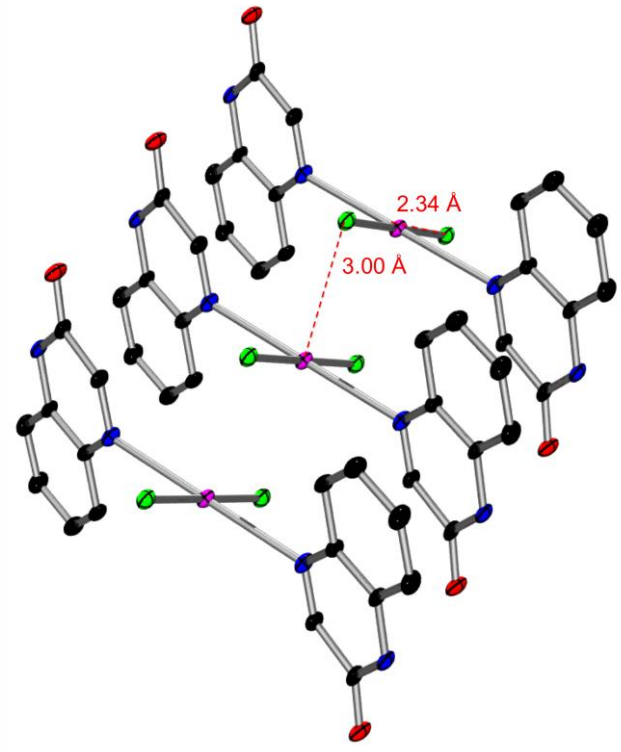

Figure S1-11. Solid-state packing of **S1**. The Hg-Cl bond length is 2.34 Å and the intermolecular distance between Hg-Cl atoms is 3.00 Å. The distance between offset aryl rings is 3.78 Å. The hydrogen atoms were omitted for clarity.

VII. SEM Images

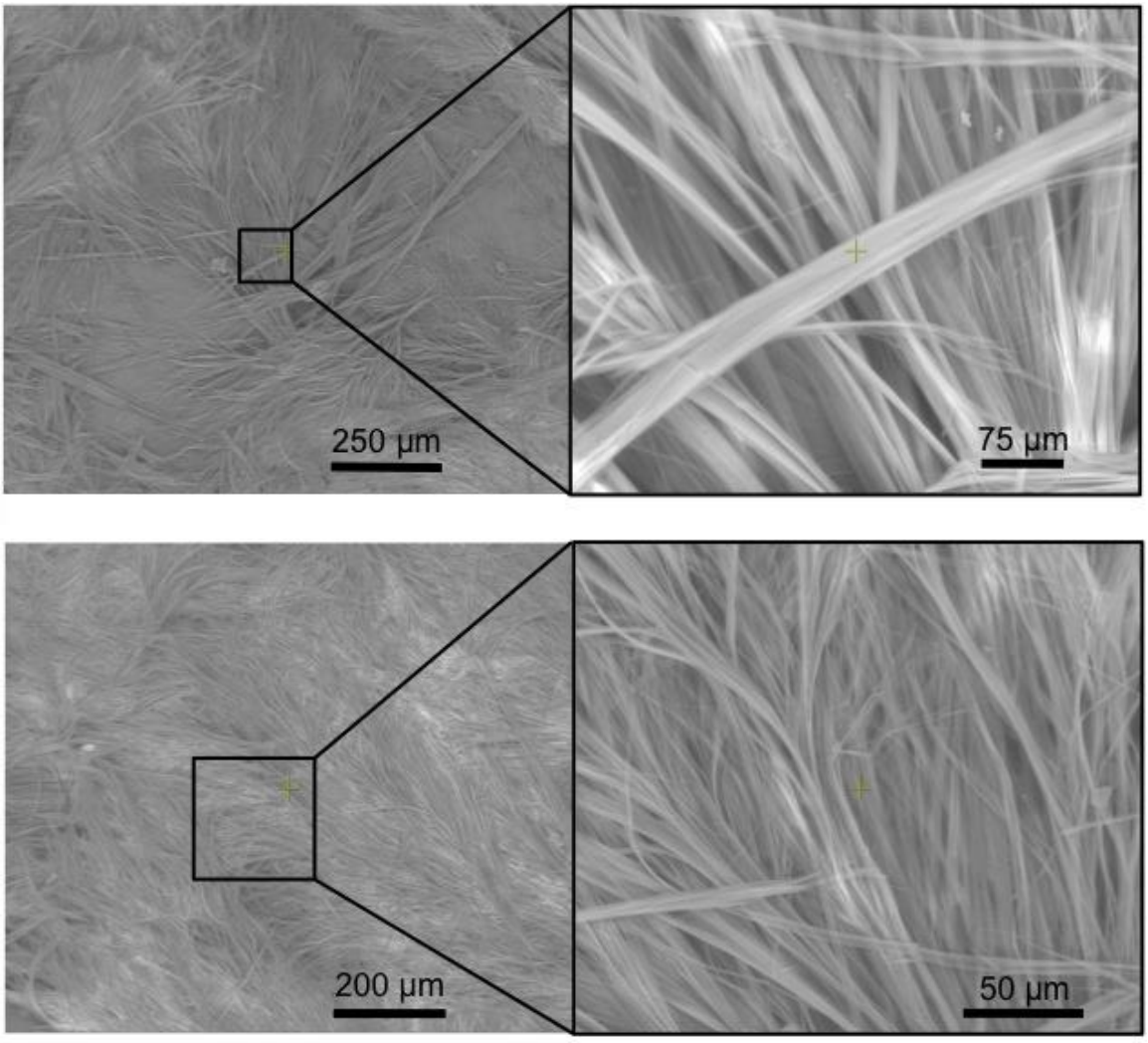

Figure S1-12. SEM images of an in situ gel of **2a** (24 mM) in 90/10 MeOH/H_2O. The images on the right are at a higher magnification.

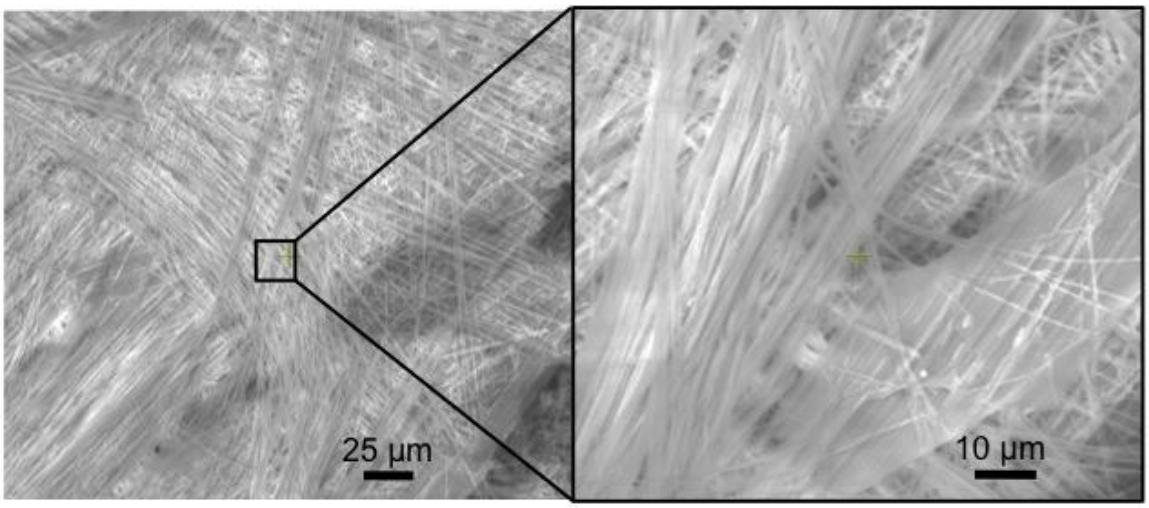

Figure S1-13. SEM image of a gel of **2a** (complex) (25 mM) in 90/10 MeOH/H_2O. The image on the right is at a higher magnification.

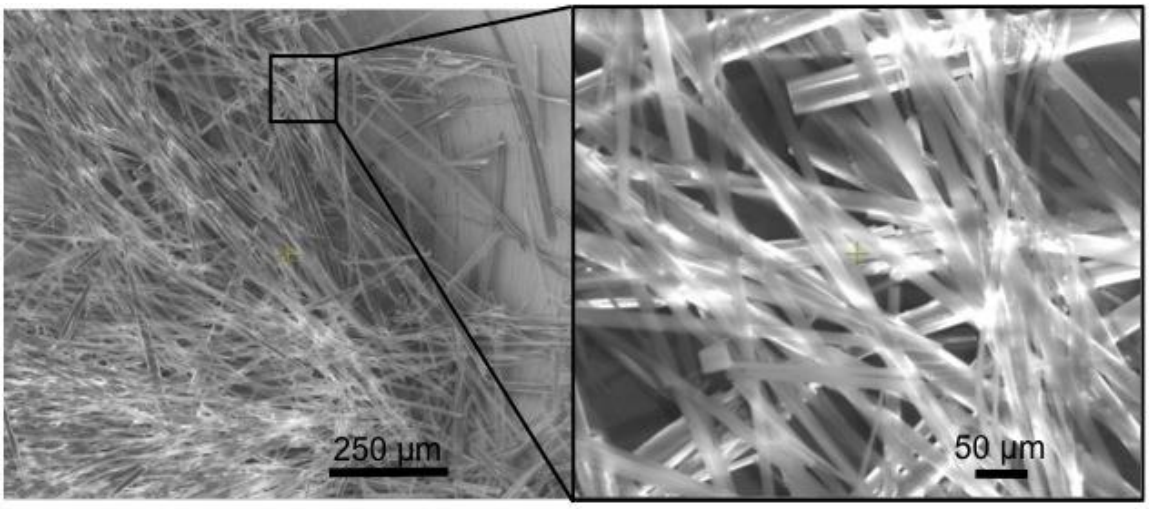

Figure S1-14. SEM image of **1a** (191 mM) in 70/30 MeOH/H_2O. The image on the right is at a higher magnification.

VIII. Powder X-ray Diffraction Data

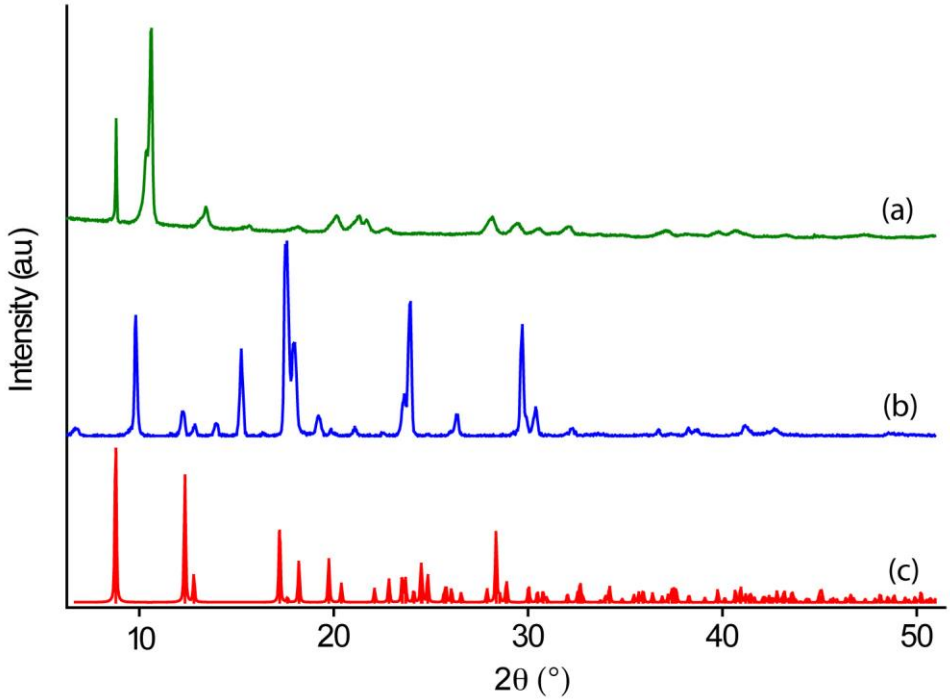

Figure S1-15. Powder X-ray diffraction patterns of (a) **2a** precipitated from MeOH, (b) a gel of **2a** (from isolated complex, 90/10 MeOH/H_2O), and (c) simulated from the crystal structure of **2a**.

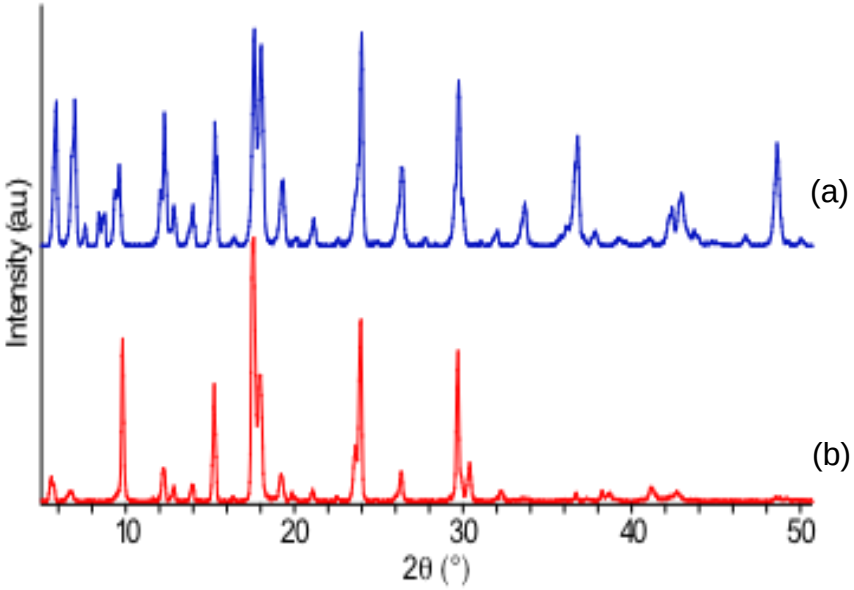

Figure S1-16. Powder X-ray diffraction patterns for gels of (a) **2a** (in situ) and (b) **2a** (isolated complex).

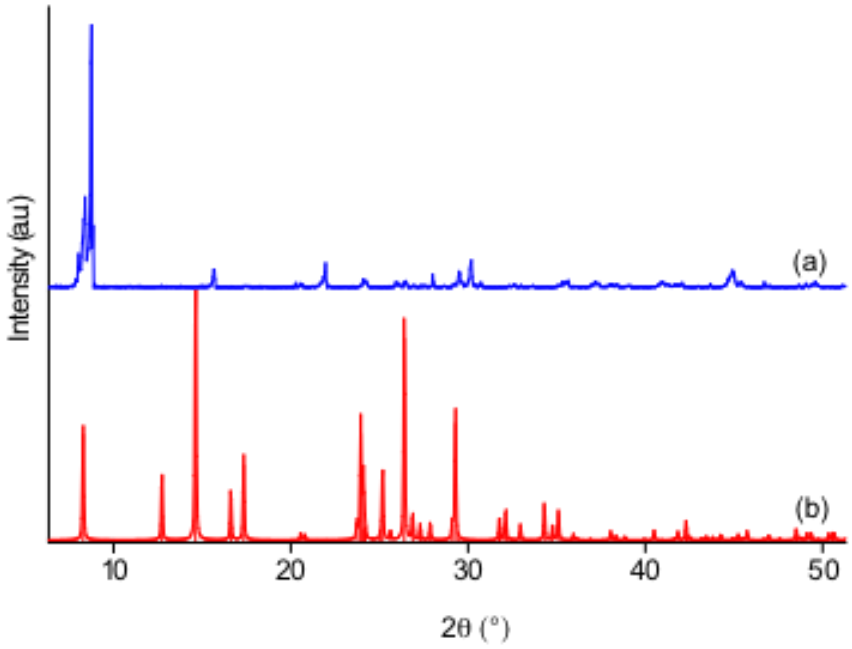

Figure S1-17. Powder X-ray diffraction patterns for (a) $Hg(OAc)_2$ and (b) **1a** simulated from the crystal structure.

IX. Rheological Data

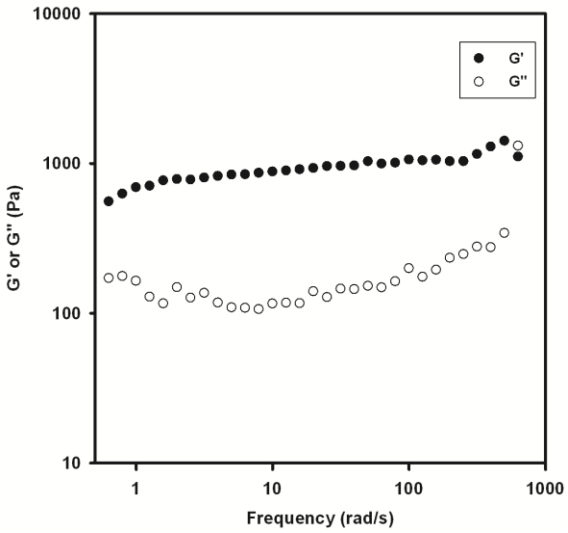

Figure S1-18. Frequency sweep data under a constant stress (0.2 Pa) for a gel of **2a** (20 mg/mL) in MeOH/H_2O (90/10 v/v). The samples are viscoelastic, with the storage modulus (G') 5 times larger than loss modulus (G'').

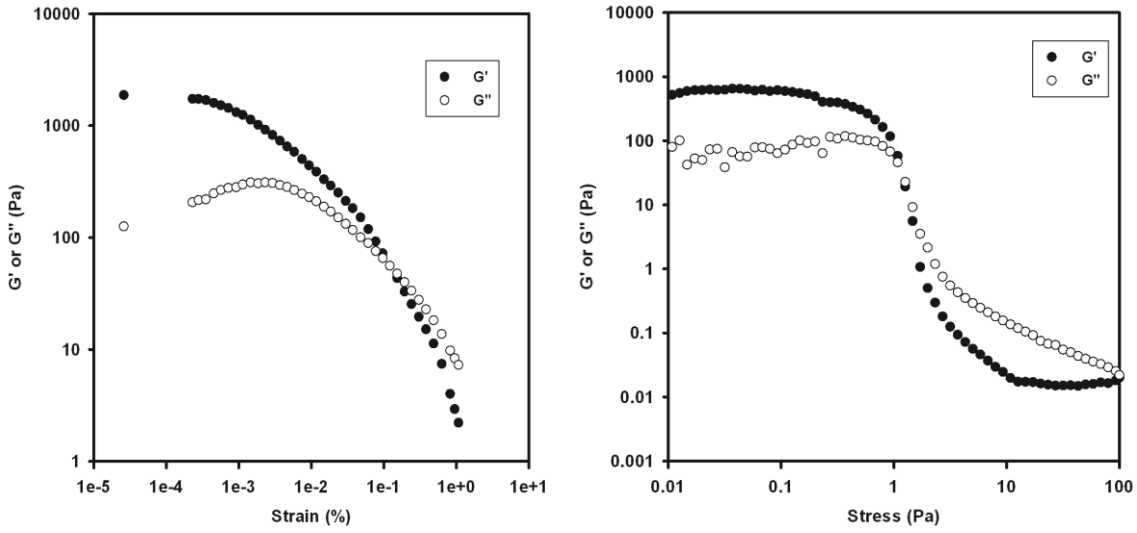

Figure S1-19. Left: Strain sweep data for a gel of **2a** (20 mg/mL, 90/10 MeOH/H_2O) acquired under constant frequency (1 Hz). The gel network completely breaks down above strain of 0.1%. **Right:** Oscillatory stress sweep measurements for a gel of **2a** (20 mg/mL, 90/10 MeOH/H_2O) under constant frequency (1 Hz). The gel network completely breaks down at a stress of 3.7 Pa.

X. ICP-OES Data

Representitive Procedure for ICP Samples. The samples were prepared by extraction of the syneresis (30 μL) from an in situ **2a** gel by micropipet and diluted with H_2O (to 1 mL). Residual MeOH was evaporated off using a rotary evaporator and the remaining solution was filtered using a syringe filter. The yttrium internal standard was added and samples were diluted further to 10 mL total volume with H_2O. Each sample was injected three times and the average response was used to determine [Hg] with the calibration curve.

Table S1-4. ICP-OES data of the mercury concentration remaining after gelation. The table displays (from left to right) the initial mass of **1a**, the initial mass of $Hg(OAc)_2$, the initial Hg^{2+} concentration ($[Hg]_0$), the concentration of Hg^{2+} detected after gelation and sample dilution ($[Hg]_d$), and the corresponding concentration of Hg^{2+} in the gel ($[Hg]_a$).

Sample	**1a** (mg)	$Hg(OAc)_2$ (mg)	$[Hg]_0$ (ppm)	$[Hg]_d$ (ppm)	$[Hg]_a$ (ppm)
1	7	7	4400	1.07 ± 0.02	358
2	7	8	5000	1.86 ± 0.01	621
3	7	6	3800	0.867 ± 0.006	289
4	7	6	3800	0.992 ± 0.005	331

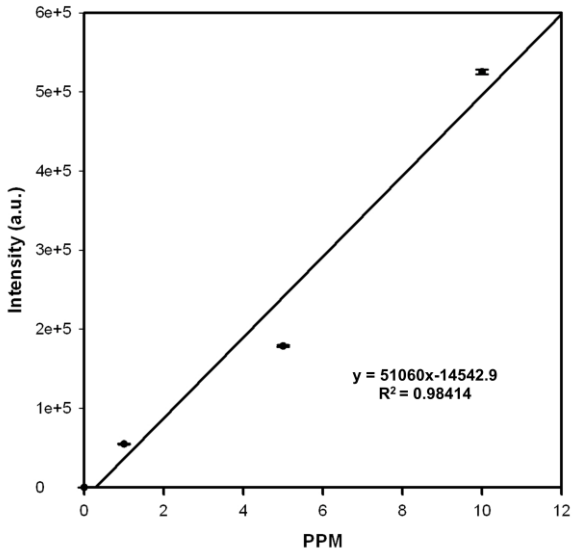

Figure S1-20. Calibration curve for ICP-OES detection of Hg^{2+}.

References

[1]Software for X-ray Crystallography: (a) Sheldrick, G.M. SHELXTL, v. 2008/4; Bruker Analytical X-ray, Madison, WI, 2008. (b) Sheldrick, G.M. SADABS, v. 2008/1. Program for Empirical Absorption Correction of Area Detector Data, University of Gottingen: Gottingen, Germany, 2008. (c) Saint Plus, v. 7.34, Bruker Analytical X-ray, Madison, WI, 2006.

[2]Goodgame, D. M. L.; Hill, S. P. W.; Williams, D. J. *Polyhedron* **1992**, *11*, 1507-1512.

Appendix 2.
Supporting Information for Chapter 3
Improving Hg-triggered Gelation via Structural Modifications

Contents

I. Materials 78
II. General Experimental Procedures 78
III. Synthetic Procedures 80
IV. ^{1}H and ^{13}C NMR Spectroscopic Data 87
V. ^{19}F NMR Spectroscopic Data 104
VI. X-ray Crystal Structures 107
VII. Powder X-Ray Diffraction Patterns 109
VIII. Differential Scanning Calorimetry 114
IX. Gel Screening 117
X. Solubility and Dissolution Parameters 123
XI. Rheological Data 130
XII. Scanning Electron Microscopy Images 133
XIII. Gel Experiments 135
XIV. Hg^{2+} Remediation 138
XV. Thermogravimetric Analysis 141

I. Materials

Column chromatography was performed using a Biotage Isolera One flash purification system. Thin layer chromatography was performed on Merck TLC plates pre-coated with silica gel 60 F254. All reagent grade materials and solvents were purchased from Sigma-Aldrich, Acros, or TCI and used without further purification. Compounds **S1**–**S7**[1,2] and **1a**–**5**[3,4] were prepared from modified literature procedures. Throughout this document, H_2O refers to deionized H_2O, unless otherwise noted.

II. General Experimental Procedures

^{1}H and ^{13}C NMR Spectroscopy – ^{1}H and ^{13}C NMR spectra for all compounds were acquired in DMSO-d_6 on a Varian vnmr 700 operating at 700 and 176 mHz, a Varian Inova 500 operating at 500 and 126 mHz, or a Varian MR400 spectrometer operating at 400 and 100 MHz. The chemical shift data are reported in units of δ (ppm) relative to

tetramethylsilane and referenced by residual protic DMSO. An asterisk was used to indicate residual H_2O in all spectra while double bars are used to indicate peaks that have been truncated for clarity. The abbreviations s, d, t, dd, td, and m were used to signify singlet, doublet, triplet, doublet of doublet, triplet of doublet and multiplet, respectively.

^{19}F NMR Spectroscopy – ^{19}F NMR spectra for all compounds were acquired in DMSO-d_6 on a Varian vnmr 500 operating at 470 mHz. The chemical shift data are reported in units of δ (ppm) relative to $CFCl_3$ and referenced by residual protic DMSO.

High Resolution Mass Spectrometry – HRMS data were obtained on a Micromass AutoSpec Ultima Magnetic Sector mass spectrometer via electron impact ionization on a desorption probe.

UV-Vis Spectroscopy – UV-vis spectra were taken on a Perkin-Elmer Lambda 850 UV-visible spectrometer. Calibration curves were measured at the λ_{max} for each compound on the same day measurements were taken.

X-Ray Crystallography –

Structure Determination.

Gold plates of 7-chloroquinoxalinone (**S6**) were grown from an acetone solution at 25 °C. A crystal of dimensions 0.17 x 0.17 x 0.09 mm was mounted on a Rigaku AFC10K Saturn 944+ CCD-based X-ray diffractometer[5] equipped with a low temperature device and Micromax-007HF Cu-target micro-focus rotating anode (l=1.54187 Å) operated at 1.2 kW power (40 kV, 30 mA). The X-ray intensities were measured at 85(1) K with the detector placed at a distance 42.00 mm from the crystal. A total of 3338 images were collected with an oscillation width of 1.0° in ω. The exposure time was 1 s for the low angle images, 3 s for high angle. The integration of the data yielded a total of 15464 reflections to a maximum 2θ value of 136.42° of which 1313 were independent and 1197 were greater than 2s(I). The final cell constants were based on the xyz centroids of 10009 reflections above 10s(I). Analysis of the data showed negligible decay during data collection; the data were processed with CrystalClear 2.0 and corrected for absorption. The structure was solved and refined with the Bruker SHELXTL (version 2008/4) software package,[6] using the space group P2(1)/c with Z=4 for the formula $C_8H_5N_2OCl$. Full matrix least-squares refinement based on F^2 converged at R1=0.0454 and ωR2=0.1019 [based on I>2σ(I)], R1=0.0480 and ωR2=0.1036 for all data. Additional details are provided as Supporting Information in a CIF file. Acknowledgement is made for funding from NSF grant CHE-0840456 for X-ray instrumentation. Images were produced from the CIF file using Materials Studio[7] software suite for Windows.

Colorless plates of **1a** were grown from a MeOH/H_2O solution of the compound at 25 ºC. A crystal of dimensions 0.08 x 0.08 x 0.06 mm was mounted on a Rigaku AFC10K Saturn 944+ CCD-based X-ray diffractometer[5] equipped with a low temperature device and Micromax-007HF Cu-target micro-focus rotating anode (l=1.54187 Å) operated at 0.2 kW power (20 kV, 10 mA). The X-ray intensities were measured at 85(1) K with the detector placed at a distance 42.00 mm from the crystal. A total of 2967 images were collected with an oscillation width of 1.0° in ω. The exposure time was 10 s for the low

angle images, 25 s for high angle. The integration of the data yielded a total of 19699 reflections to a maximum 2θ value of 136.48° of which 3488 were independent and 3461 were greater than 2s(I). The final cell constants were based on the xyz centroids 3812 reflections above 10s(I). Analysis of the data showed negligible decay during data collection; the data were processed with CrystalClear 2.0 and corrected for absorption. The structure was solved and refined with the Bruker SHELXTL (version 2008/4) software package,[6] using the space group P2(1) with Z=2 for the formula $C_{16}H_{20}N_4O_7Hg$. All non-hydrogen atoms were refined anisotropically with the hydrogen atoms placed in a mixture of idealized and refined positions. Full matrix least-squares refinement based on F^2 converged at R1=0.0156 and ωR2=0.0368 [based on I>2σ(I)], R1=0.0157 and ωR2=0.0369 for all data. Additional details are provided as Supporting Information in a CIF file. Acknowledgement is made for funding from NSF grant CHE-0840456 for X-ray instrumentation. Images were produced from the CIF file using Materials Studio[7] software suite for Windows.

Thermogravimetric Analysis – TGA was performed on a TA Instruments TGA Q50. Data were analyzed with TA Universal Analysis software Version 4.3A. Thermal behavior of the samples was studied under a nitrogen purge at 10 ºC/min heating rate. The temperature range was 25 - 500 °C.

III. Synthetic Procedures

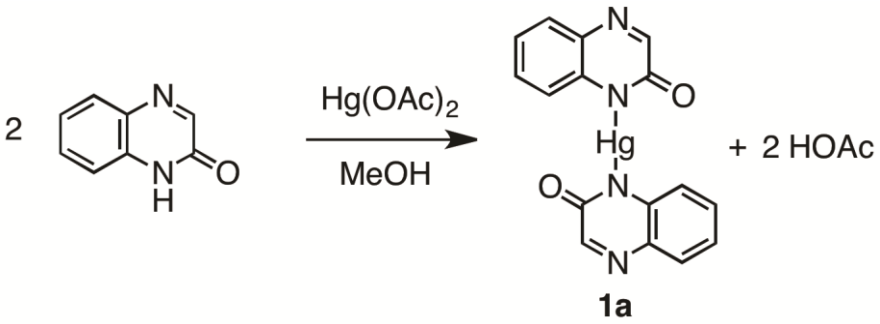

1a

1a[4,5]**:** 2-(1H)Quinoxalinone (2.558 g, 13.72 mmol) was dissolved in MeOH (60 mL) and added to a round-bottom flask. Then, $Hg(OAc)_2$ (3.356 g, 10.55 mmol) was added to the reaction flask to produce an off-white precipitate (**1a**). The mixture was filtered and the solid was washed with H_2O (1 x 20 mL). The product was purified via recrystallization from MeOH to give 2.221 g (4.542 mmol, 66% yield) of a light brown solid. HRMS (ESI): Calcd for $C_{16}H_{10}N_4O_2Hg$, 492.0510; found, 492.0522. Elemental analysis: [M+] Calcd for $C_{16}H_{10}N_4O_2Hg$: C, 39.15%; H, 2.05%; N, 11.41%; found: C, 39.21%; H, 2.05%; N, 11.53%.

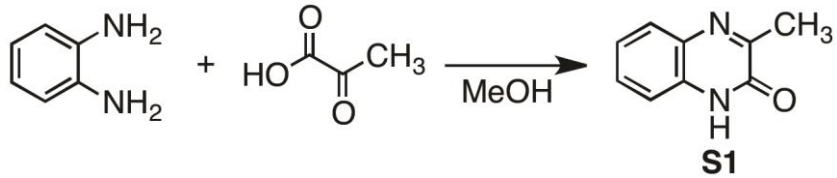

S1

S1[1]**:** To a round-bottom flask, 1,2-diaminobenzene (2.064 g, 19.08 mmol) was added and dissolved in H_2O (250 mL). Pyruvic acid (1.35 mL, 19.2 mmol) was added to the solution with stirring. The reaction was stirred until a white precipitate formed (~1 h). The mixture was filtered, washed with H_2O (2 x 10 mL), and dried in air to yield 2.040 g (12.74 mmol, 67% yield) of a yellow solid (**S1**).

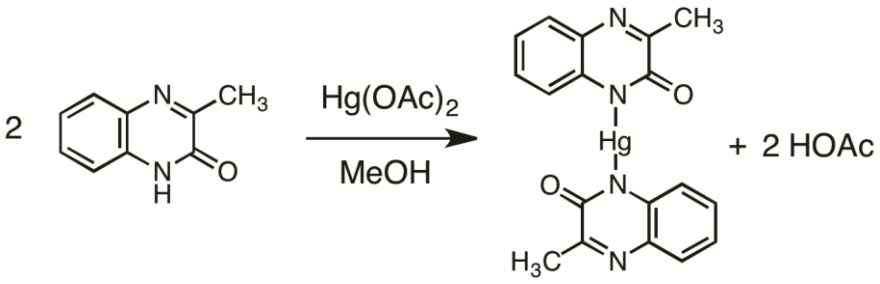

S1 **1b**

1b: To a round-bottom flask, **S1** (1.021 g, 6.375 mmol) was added and dissolved in MeOH (100 mL). Then, $Hg(OAc)_2$ (1.032 g, 3.244 mmol) was added to the solution and the flask was placed in the refrigerator until a yellow precipitate formed (~12 h at 11 °C). The mixture was filtered and the retentant was washed with H_2O (1 x 50 mL), yielding 1.443 g (2.812 mmol, 76% yield) of yellow crystals. HRMS (ESI): [M+] Calcd for $C_{18}H_{14}HgN_4O_2$, 520.0823; found, 520.0817.

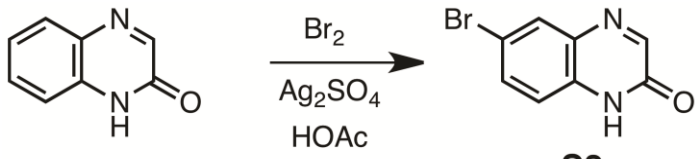

S2

S2[1]**:** 2-(1H)Quinoxalinone (1.029 g, 6.271 mmol) and Ag_2SO_4 (1.10 g, 3.53 mmol) were added to a round-bottom flask and dissolved in sulfuric acid (50 mL). Bromine (1.8 mL, 69.9 mmol.) was added dropwise to the flask with stirring. The solution was stirred for 24 h under nitrogen. The reaction was quenched with H_2O (100 mL) to form a yellow precipitate, which was filtered and washed with H_2O (2 x 20 mL). The crude product was dispersed in MeOH (100 mL), filtered, and the insoluble silver byproduct was retained in filter paper and was washed with MeOH (2 x 10 mL). The filtrate containing soluble **S2** was placed in the refrigerator to recrystallize (~12 h at 11 °C). The mixture was filtered and the solid was washed with H_2O (2 x 20 mL), then recrystallized in 2-methoxyethanol (100 mL) to yield 0.3150 g (1.559 mmol, 20% yield) of an orange solid.

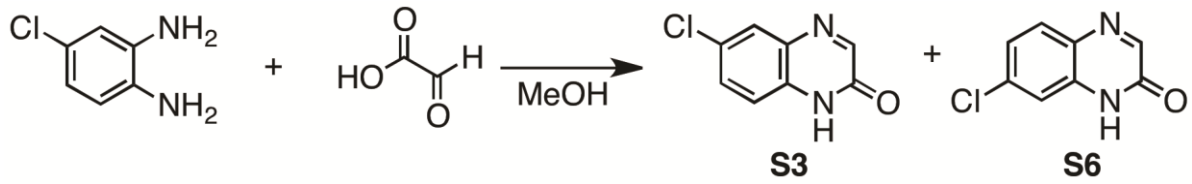

S3 **S6**

S3[1,2]**:** To a round-bottom flask was added 4-chloro-1,2-diaminophenylene (0.213 g, 1.50 mmol) and dissolved in MeOH (20 mL). Glyoxylic acid (0.148 g, 2.00 mmol) was added to the solution and the flask was sonicated for ~45 min until a purple precipitate formed. The mixture was filtered and washed with H_2O (2 x 10 mL). The solid was recrystallized in 2-methoxyethanol to produce 0.129 g of **S3** (0.714 mmol, 48% yield). Further precipitation in the filter flask was observed and the mixture was filtered and the solid from the second filtration (crude **S6**) was purified via column chromatography using 60/40 EtOAc/hexanes as the eluent to give 0.137 g of a pink powder (0.759 mmol, 51% yield). Additionally, isomer regioisomers were identified via single crystal X-ray crystallography (Figure S21). HRMS (ESI) for **S6**: [M+] Calcd for $C_8H_4ClN_2O$, 180.0090; found 180.0088.

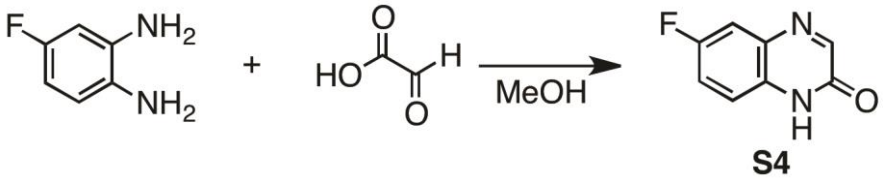

S4

S4[1]**:** To a round-bottom flask was added 4-fluoro-1,2-diaminophenylene (0.260 g, 2.06 mmol) and dissolved in MeOH (10 mL). Glyoxylic acid (0.160 g, 2.16 mmol) was added and the solution was stirred for 4 h to form a dark precipitate. The solvent was removed via rotary evaporation. Crude **S4** was purified via column chromatography using 60/40 EtOAc/hexanes as the eluent, yielding 0.0592 g (0.361 mmol, 18% yield).

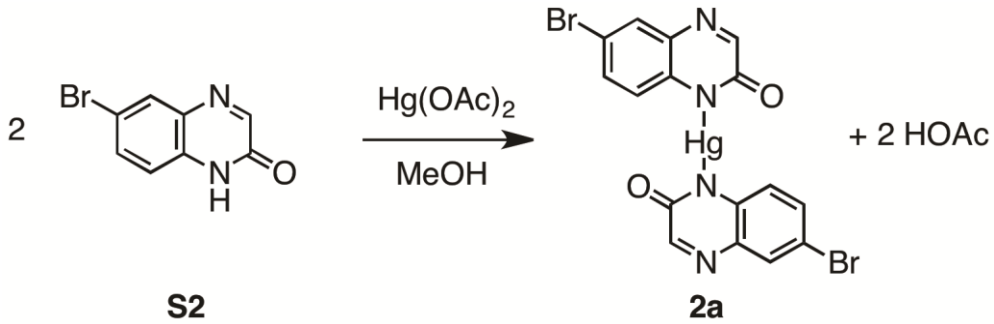

S2 **2a**

2a: To a round-bottom flask, **S2** (0.256 g, 0.394 mmol) was added and dissolved in MeOH (100 mL). Then $Hg(OAc)_2$ (0.181 g, 0.568 mmol) was added and the flask was placed in the refrigerator until a yellow precipitate formed (~12 h at 11 °C). The mixture was filtered and the solid (**2a**) was washed with H_2O (1 x 20 mL) to yield 0.360 g (0.567 mmol, 98% yield) of a light brown powder. HRMS (ESI): [M+] Calcd for $C_{16}H_8Br_2HgN_4O_2$, 647.8720; found, 647.8743.

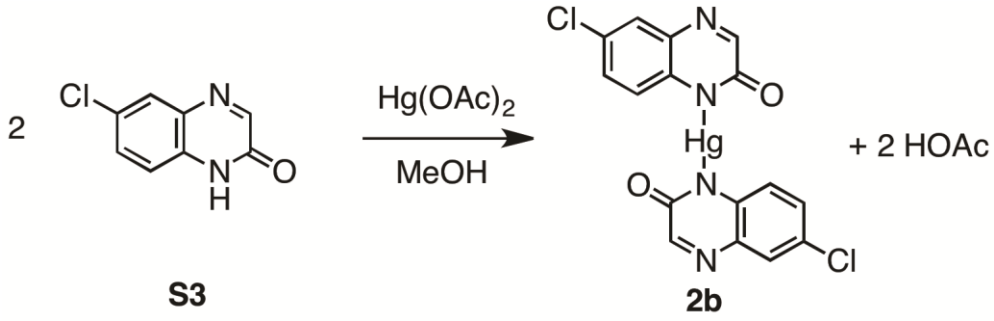

S3 **2b**

2b: To a round-bottom flask, **S3** (0.091 g, 0.50 mmol) was added and dissolved in MeOH (20 mL). Then $Hg(OAc)_2$ (0.081 g, 0.25 mmol) was added and the flask was placed in the refrigerator until a green precipitate formed (~12 h at 11 °C). The mixture was filtered and the solid (**2b**) was washed with H_2O (2 x 20 mL) to yield 0.095 g (0.25 mmol, 80% yield) of a green powder. HRMS (ESI): [M+] Calcd for $C_{16}H_8Cl_2HgN_4O_2$, 559.9731; found, 559.9705.

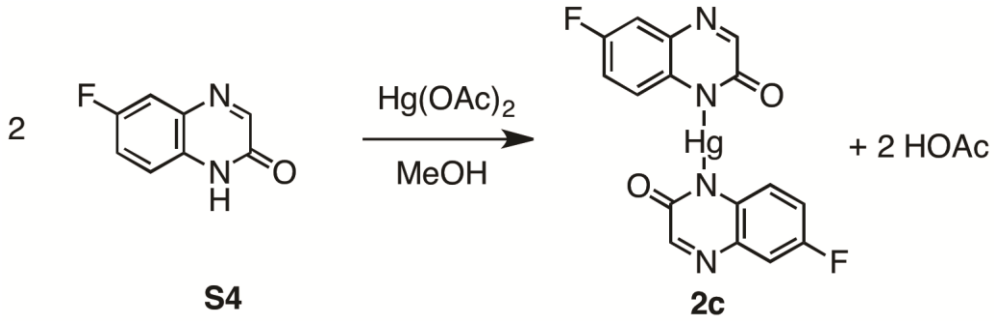

S4 **2c**

2c: To a round-bottom flask, **S4** (0.091 g, 0.55 mmol) was added and dissolved in MeOH (~50 mL). Then, $Hg(OAc)_2$ (0.0931 g, 0.29 mmol) was added and the flask was placed in the refrigerator until a tan precipitate formed (~12 h at 11 °C). The mixture was filtered and the solid (**2c**) was washed with H_2O (2 x 20 mL) to yield 0.080 g (0.16 mmol, 54% yield) of a light brown powder. HRMS (ESI): [M+] Calcd for $C_{16}H_8F_2HgN_4O_2$, 528.0322; found, 528.0339.

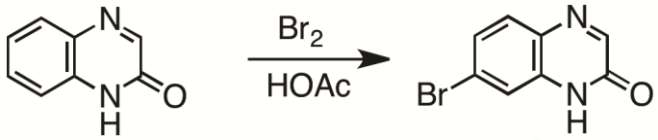

S5

S5[1]**:** 2-(1H)Quinoxalinone (1.196 g, 8.182 mmol) was dissolved in HOAc (110 mL) in a round-bottom flask. Bromine (0.15 mL) was added dropwise to the flask with stirring. The flask was stirred for 6 h under nitrogen. The reaction was quenched with H_2O (100 mL), resulting in a white precipitate. The mixture was filtered and washed with H_2O (1 x 20 mL). Finally, **S5** was recrystallized in MeOH (30 mL) to give 0.502 g (2.24 mmol, 27% yield) of tan powder.

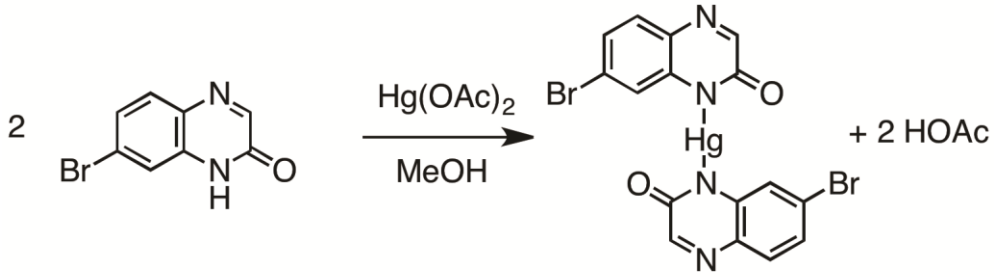

S5 **3a**

3a: To a round-bottom flask, **S5** (0.211 g, 0.938 mmol) was added and dissolved in MeOH (30 mL). Then, $Hg(OAc)_2$ (0.307 g, 0.964 mmol) was added and the flask was placed in the refrigerator until a white precipitate formed (~12 h at 11 °C). The mixture was filtered and the solid was washed with H_2O (~50 mL) to yield 0.104 g (0.161 mmol, 95% yield) of white powder. HRMS (ESI): [M+] Calcd for $C_{16}H_8Br_2HgN_4O_2$, 647.8720; found, 647.8708.

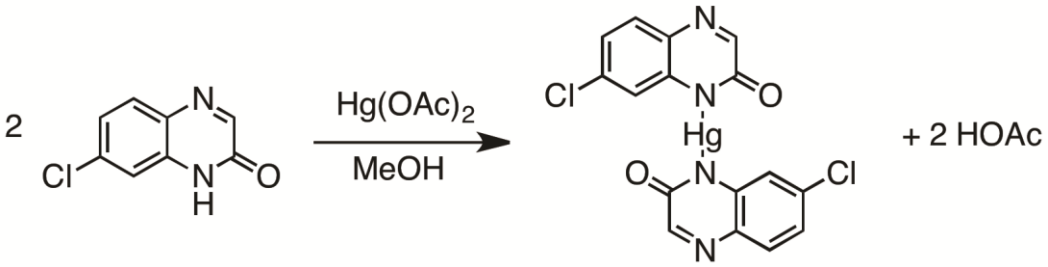

S6 **3b**

3b: To a round-bottom flask, **S6** (0.018 g, 0.099 mmol) was added and dissolved in MeOH (~1 mL). Then, $Hg(OAc)_2$ (0.017 g, 0.054 mmol) was added and the flask was placed in the refrigerator until a precipitate formed (~12 h at 11 °C). Then, the mixture was filtered and the solid was washed with H_2O (~10 mL) to yield 0.016 g (0.028 mmol, 57% yield) of a pink powder. HRMS (ESI): [M+] Calcd for $C_{16}H_8Cl_2HgN_4O_2$, 559.9731; found, 559.9715.

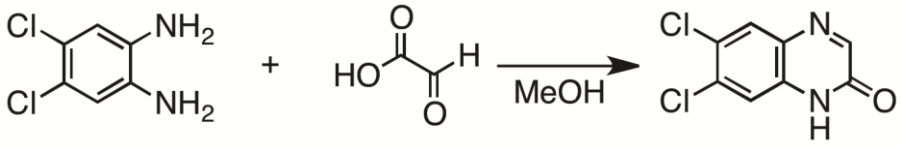

S7

S7: To a round-bottom flask, 4,5-dichloro-1,2-diaminophenylene (0.151 g, 0.852 mmol) was added and dissolved in MeOH (~40 mL). Glyoxylic acid (0.112 mg, 1.51 mmol) was added with stirring. The solution was stirred for 4 h and a dark red precipitate formed (**S7**). The mixture was filtered and the solid was washed with H_2O (2 x 20 mL), which yielded 0.126 g (0.588 mmol, 69% yield) of a dark red solid. HRMS (ESI): [M+] Calcd for $C_8H_4Cl_2N_2O$, 213.9701; found, 213.9702.

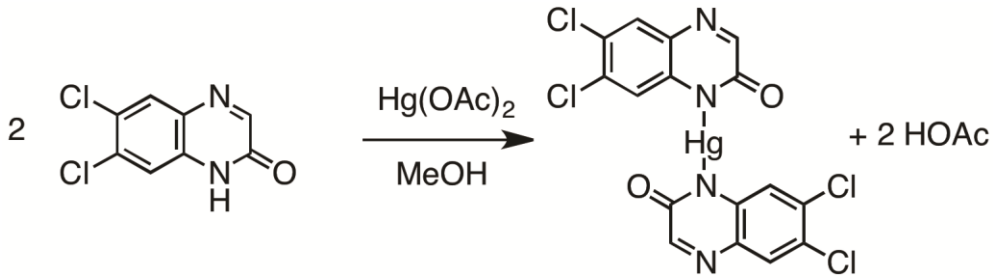

S7 **4**

4: To a round-bottom flask, **S7** was added (0.126 g, 0.588 mmol) and dissolved in MeOH (100 mL). Then, $Hg(OAc)_2$ (0.123 g, 0.385 mmol) was added and the flask was placed in the refrigerator until a purple precipitate formed (~24 h at 11 °C). Then, the mixture was filtered and the purple solid (**4**) was washed with H_2O (~50 mL). The reaction yielded 0.138 mg (0.220 mmol, 75% yield) of purple powder. HRMS (ESI): [M+] Calcd for $C_{16}H_6Cl_4HgN_4O_2$, 627.8951; found, 627.8947.

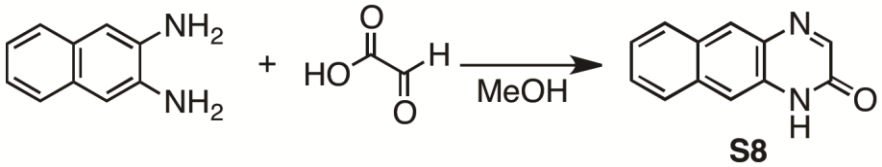

S8

S8: To a round-bottom flask, 1,2-napthalenediamine (0.212 g, 1.34 mmol) was added and dissolved in MeOH (~50 mL). Glyoxylic acid (0.109 g, 1.47 mmol) was added with stirring. The solution was stirred for 4 h and a dark red precipitate formed (**S8**). The mixture was filtered and recrystallized in 2-methoxyethanol, which yielded 0.111 g (0.566 mmol, 42% yield) of a brown solid. HRMS (ESI): [M+] Calcd for $C_{12}H_8N_2O$, 196.0637; found, 196.0639

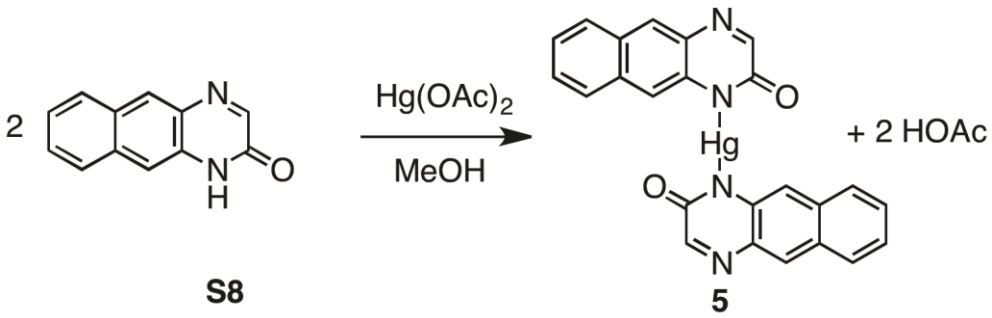

S8 **5**

5: To a round-bottom flask, **S8** (0.078 g, 0.40 mmol) was added and dissolved in MeOH (100 mL). Then, $Hg(OAc)_2$ (0.064 g, 0.20 mmol) was added and the flask was placed in the refrigerator until a yellow precipitate formed (~24 h at 11 °C). Then, the mixture was filtered and the solid was washed with H_2O (~50 mL). This reaction yielded 0.097 g (0.16 mmol, 82% yield) of yellow powder. HRMS (ESI): [M+] Calcd for $C_{24}H_{14}HgN_4O_2$, 592.0823; found, 592.0819

IV. ^{1}H and ^{13}C NMR Spectroscopic Data

i. NMR Spectra

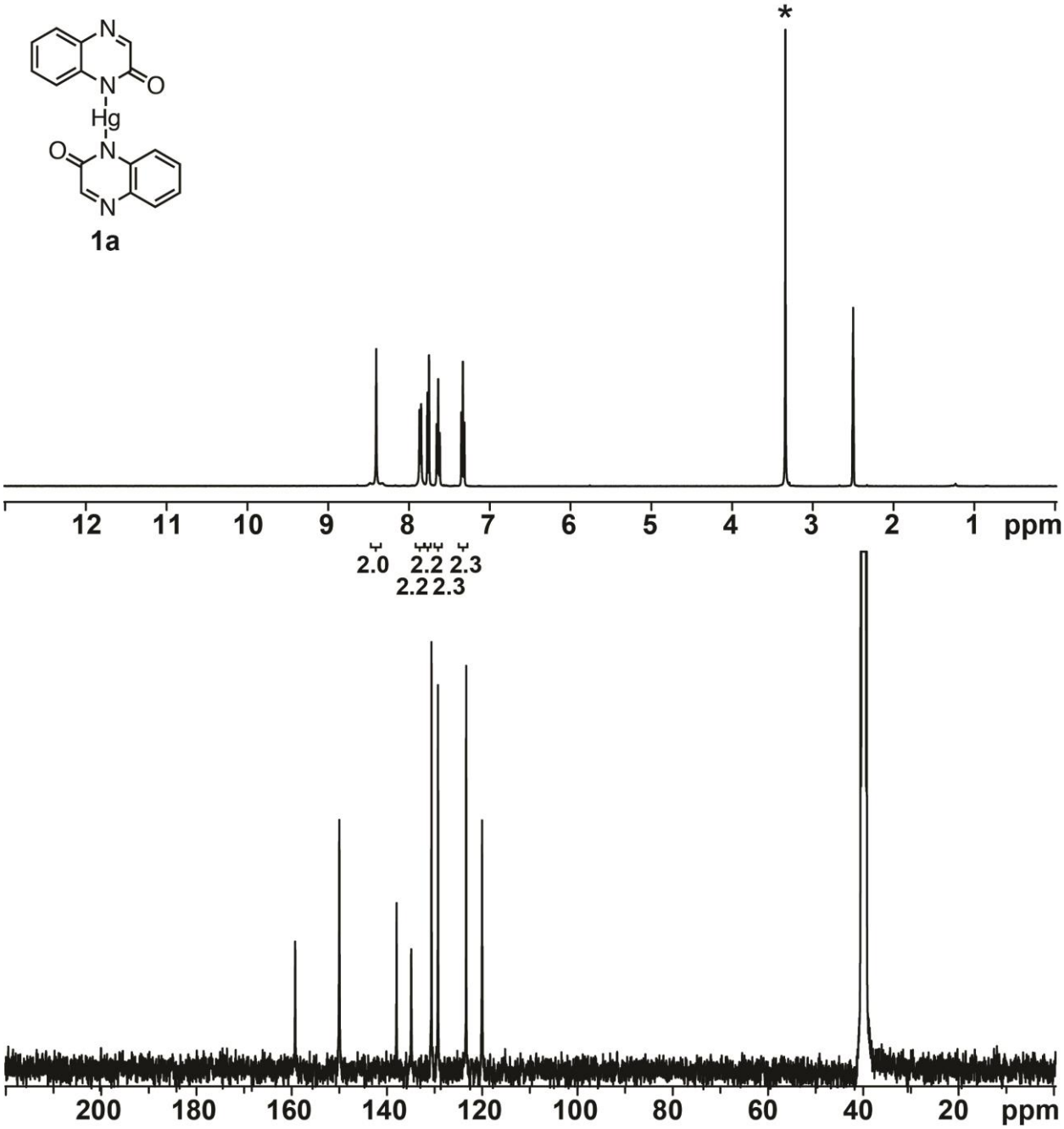

Figure S2-1. ^{1}H and ^{13}C NMR spectra of **1a**. ^{1}H NMR (400 MHz, DMSO-d_6) δ 8.40 (s, 2H), 7.87 (d, J = 8 Hz, 2H), 7.77 (d, J = 8 Hz, 2H), 7.65 (dd, J = 8, 1 Hz, 2H), 7.35 (ddd, J = 9, 6, 1 Hz, 2H). ^{13}C NMR (100 MHz, DMSO-d_6) δ 159.26, 149.98, 137.96, 134.89, 130.64, 129.27, 123.35, 120.02.

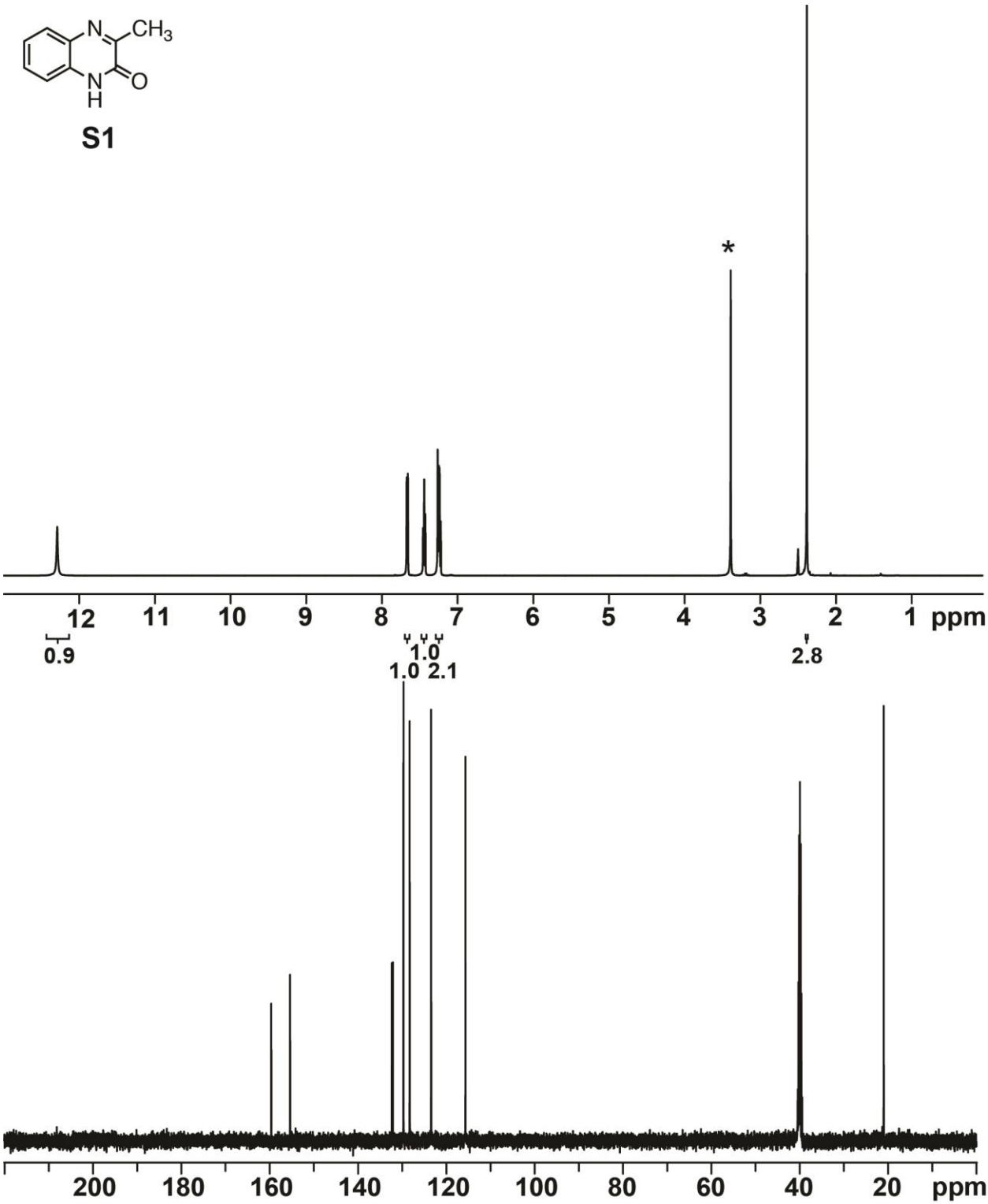

Figure S2-2. ^{1}H and ^{13}C NMR spectra of **S1**. ^{1}H NMR (500 MHz, DMSO-d_6) δ 12.29 (s, 1H), 7.67 (d, J = 8 Hz, 1H), 7.45 (dd, J = 9, 8 Hz, 1H), 7.26 (m, 2H), 2.38 (s, 3H). ^{13}C NMR (126 MHz, DMSO-d_6) 159.62, 155.36, 132.35, 132.09, 129.70, 128.29, 123.43, 115.65, 20.97.

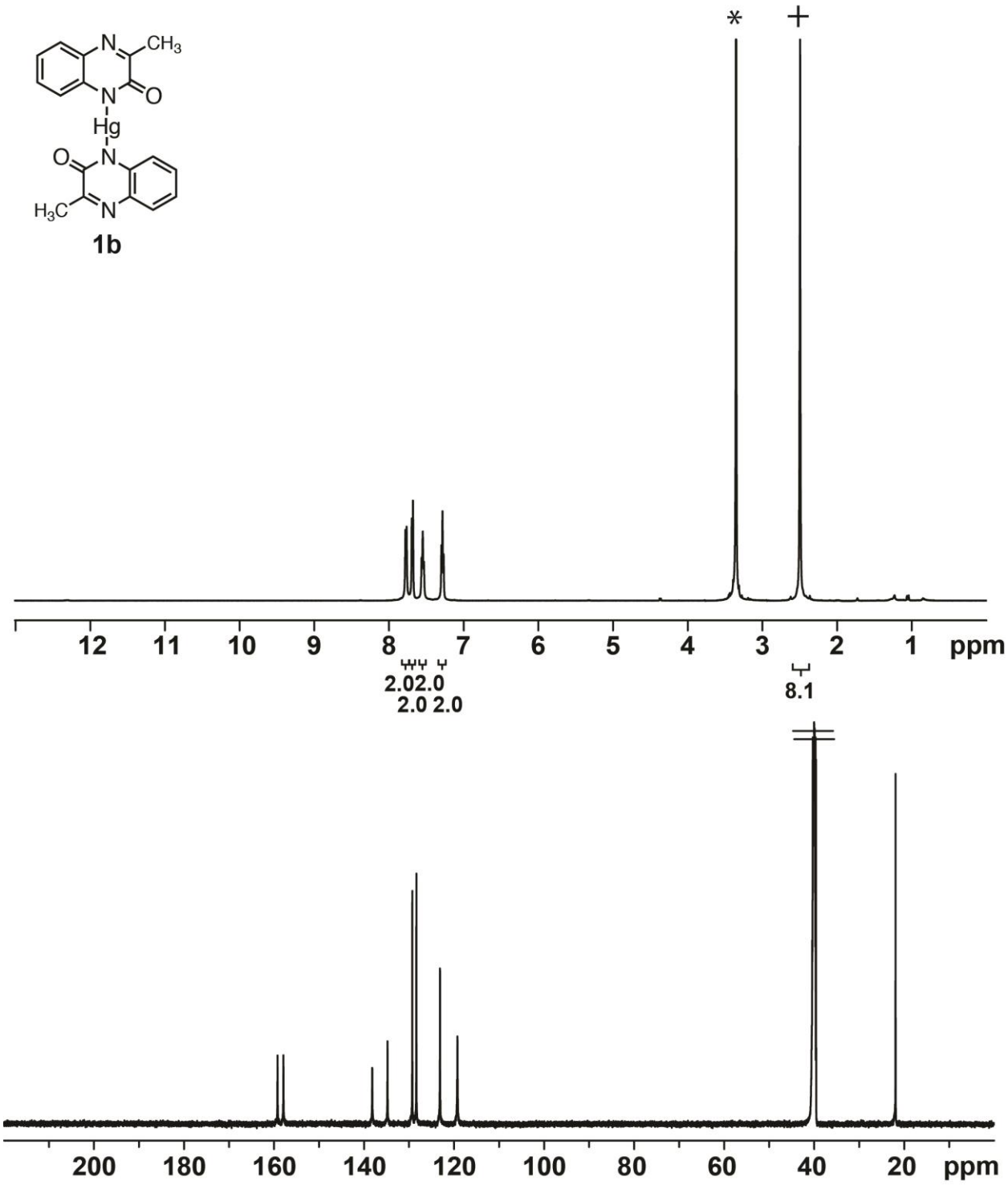

Figure S2-3. ^{1}H and ^{13}C NMR spectra of **1b**. ^{1}H NMR (500 MHz, DMSO-d_6) δ 7.79 (d, J = 8 Hz, 2H), 7.69 (d, J = 8 Hz, 2H), 7.56 (dd, J = 9, 7 Hz, 2H), 7.30 (dd, J = 9, 7 Hz, 2H), 2.50 (s, 6H). ^{13}C NMR (126 MHz, DMSO-d_6) δ 159.20, 157.90, 138.16, 134.77, 129.27, 128.37, 123.11, 119.23, 21.91. $^{+}$Note: integration is high due to peak overlap with residual protic DMSO.

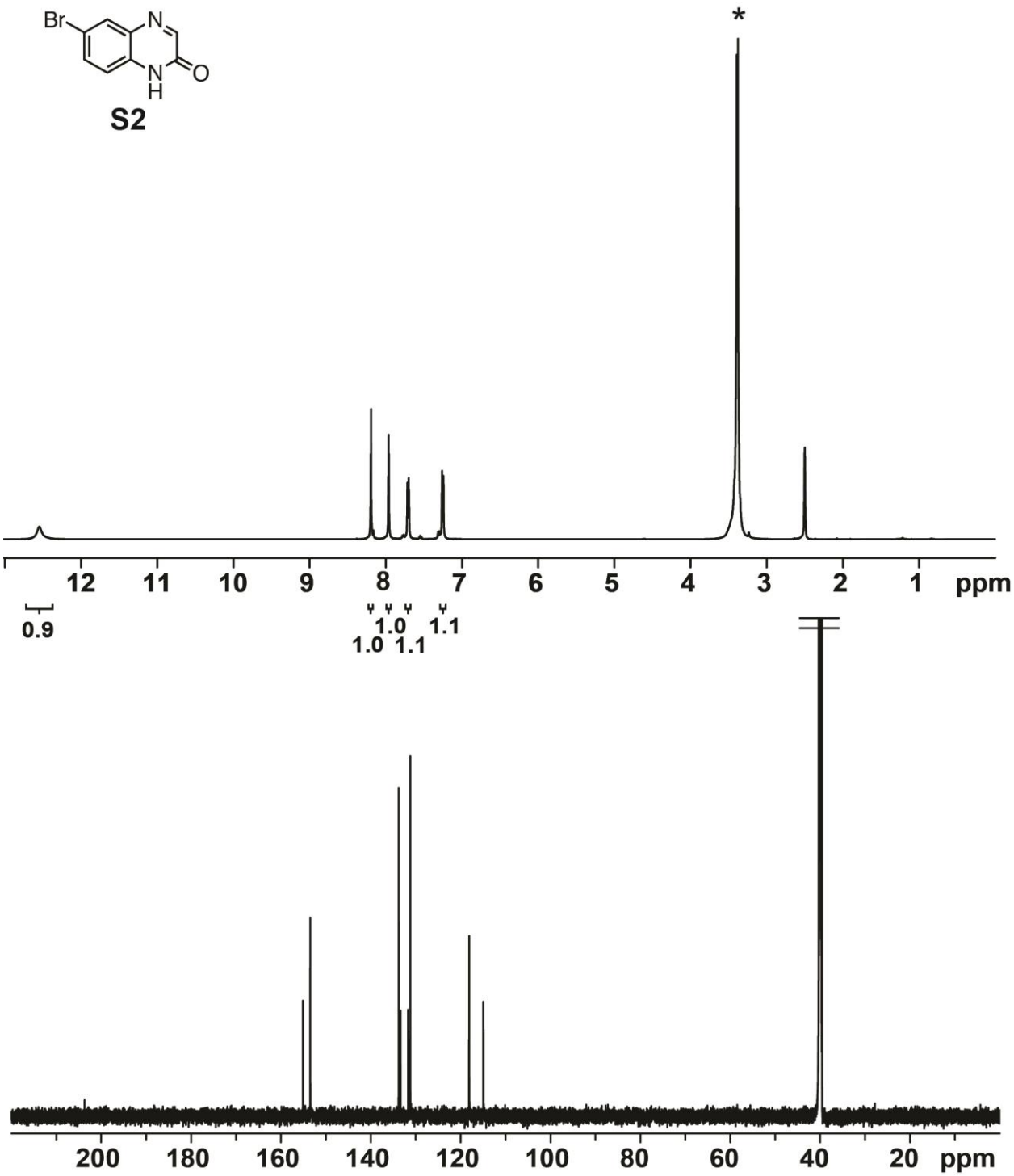

Figure S2-4. ^{1}H and ^{13}C NMR spectra of **S2**. ^{1}H NMR (500 MHz, DMSO-d_6) δ 12.55 (s, 1H) 8.20 (s, 1H), 7.98 (d, J = 2 Hz, 1H), 7.72 (d, J = 9 Hz, 1H) 7.26 (d, J = 9 Hz, 1H). ^{13}C NMR (176 MHz, DMSO-d_6) δ 155.08, 153.47, 133.76, 133.35, 131.66, 131.20, 118.09, 114.93.

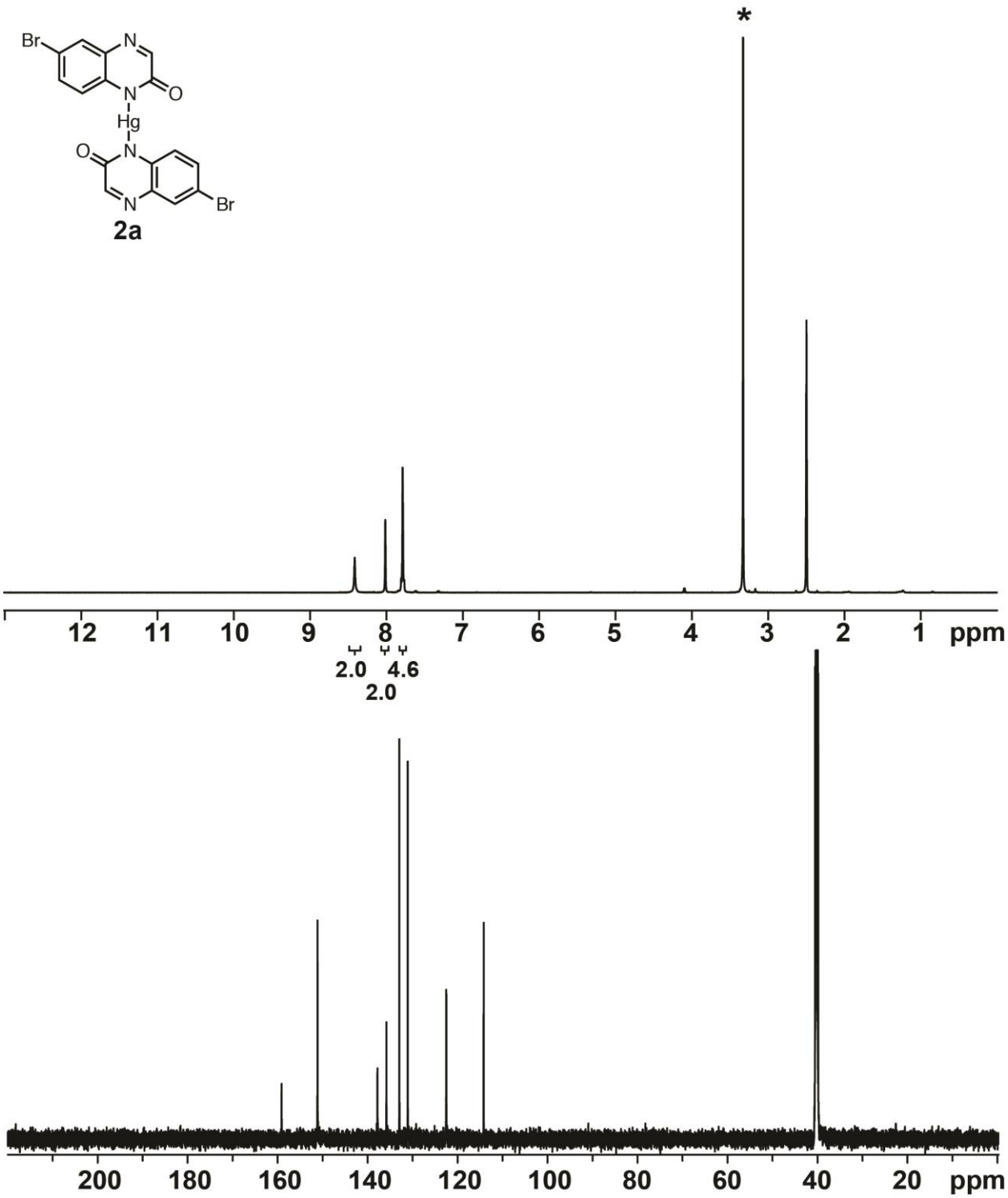

Figure S2-5. ^{1}H and ^{13}C NMR spectra of **2a**. ^{1}H NMR (500 MHz, DMSO-d_6) δ 8.39 (s, 2H), 8.00 (s, 2H), 7.76 (s, 4H). ^{13}C NMR (176 MHz, DMSO-d_6) δ 159.10, 151.11, 137.79, 135.19, 132.93, 131.06, 122.50, 114.19.

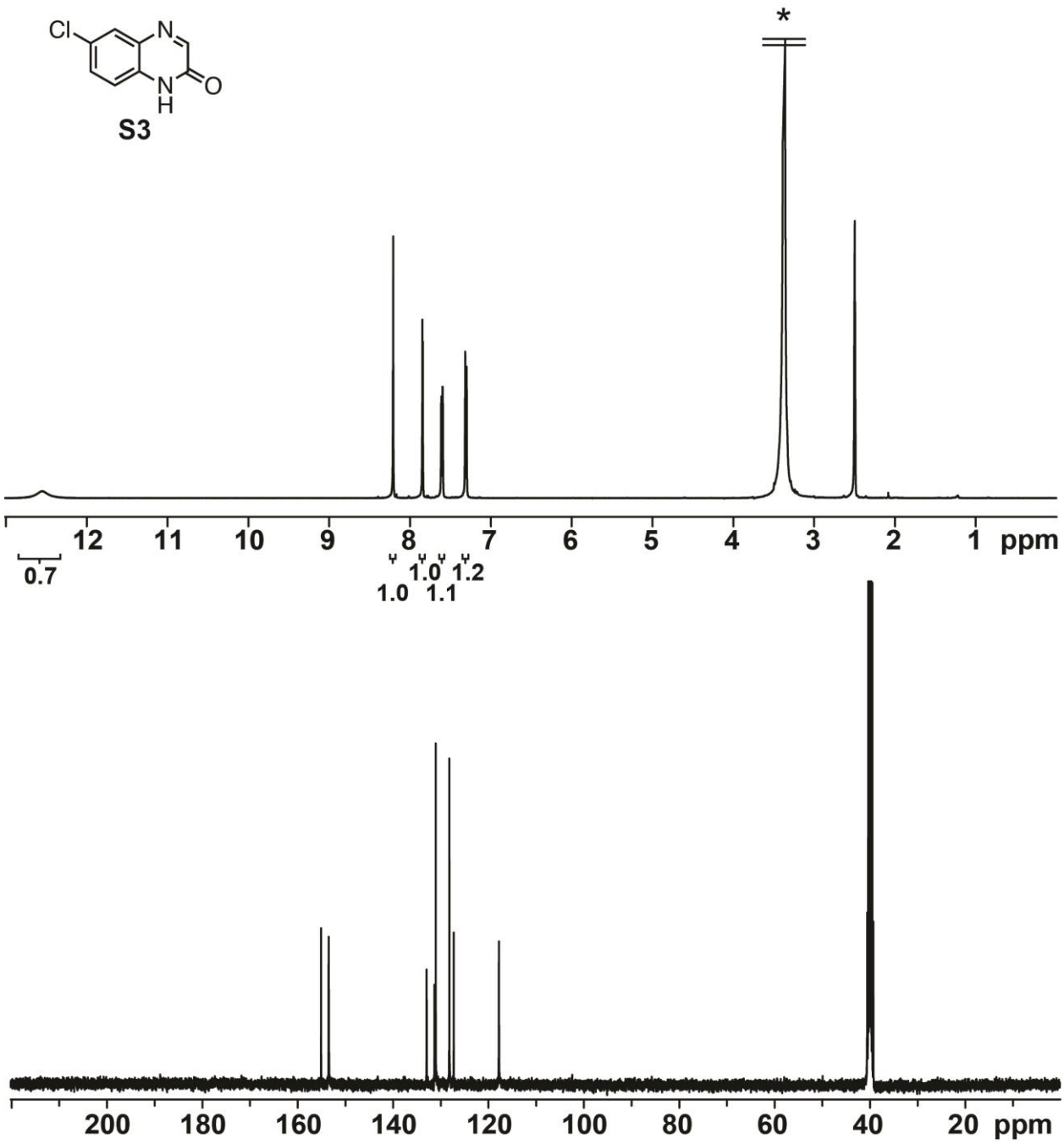

Figure S2-6. ^{1}H and ^{13}C NMR spectra of **S3**. ^{1}H NMR (500 MHz, DMSO-d_6) δ 12.55 (s, 1H) 8.21 (s, 1H), 7.85 (d, J = 2 Hz, 1H), 7.62 (dd, J = 9, 2 Hz, 1H), 7.32 (d, J = 9 Hz, 1H). ^{13}C NMR (126 MHz, DMSO-d_6) δ 155.09, 153.49, 132.95, 131.30, 131.05, 128.20, 127.27, 117.79.

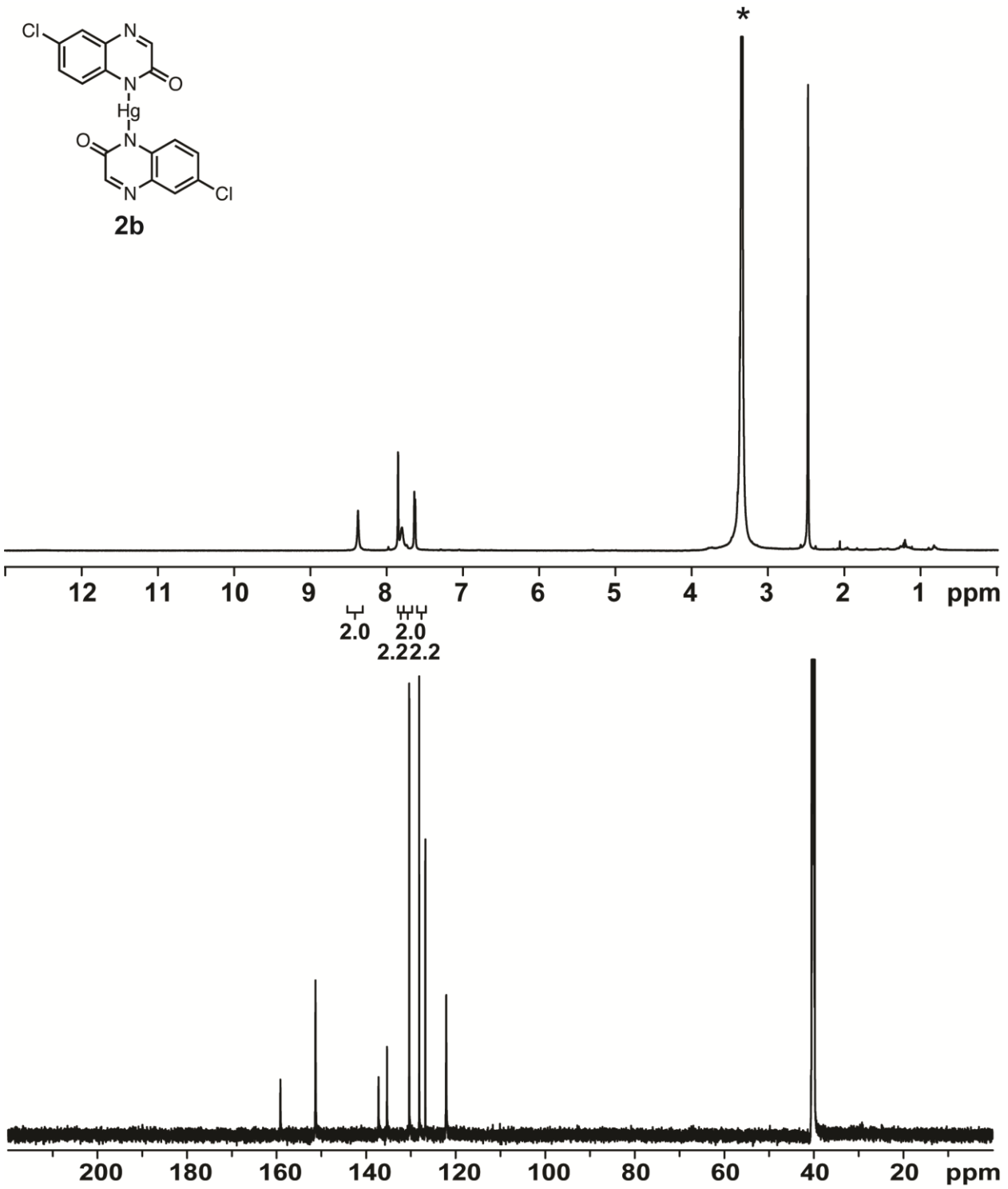

Figure S2-7. ^{1}H and ^{13}C NMR spectra of **2b**. ^{1}H NMR (500 MHz, DMSO-d_6) δ 8.37 (s, 2H), 7.85 (d, J = 2 Hz, 2H), 7.80 (s, 2H), 7.64 (d, J = 8 Hz, 2H). ^{13}C NMR (176 MHz, DMSO-d_6) δ 159.14, 151.29, 137.21, 135.33, 130.36, 128.13, 126.76, 122.09.

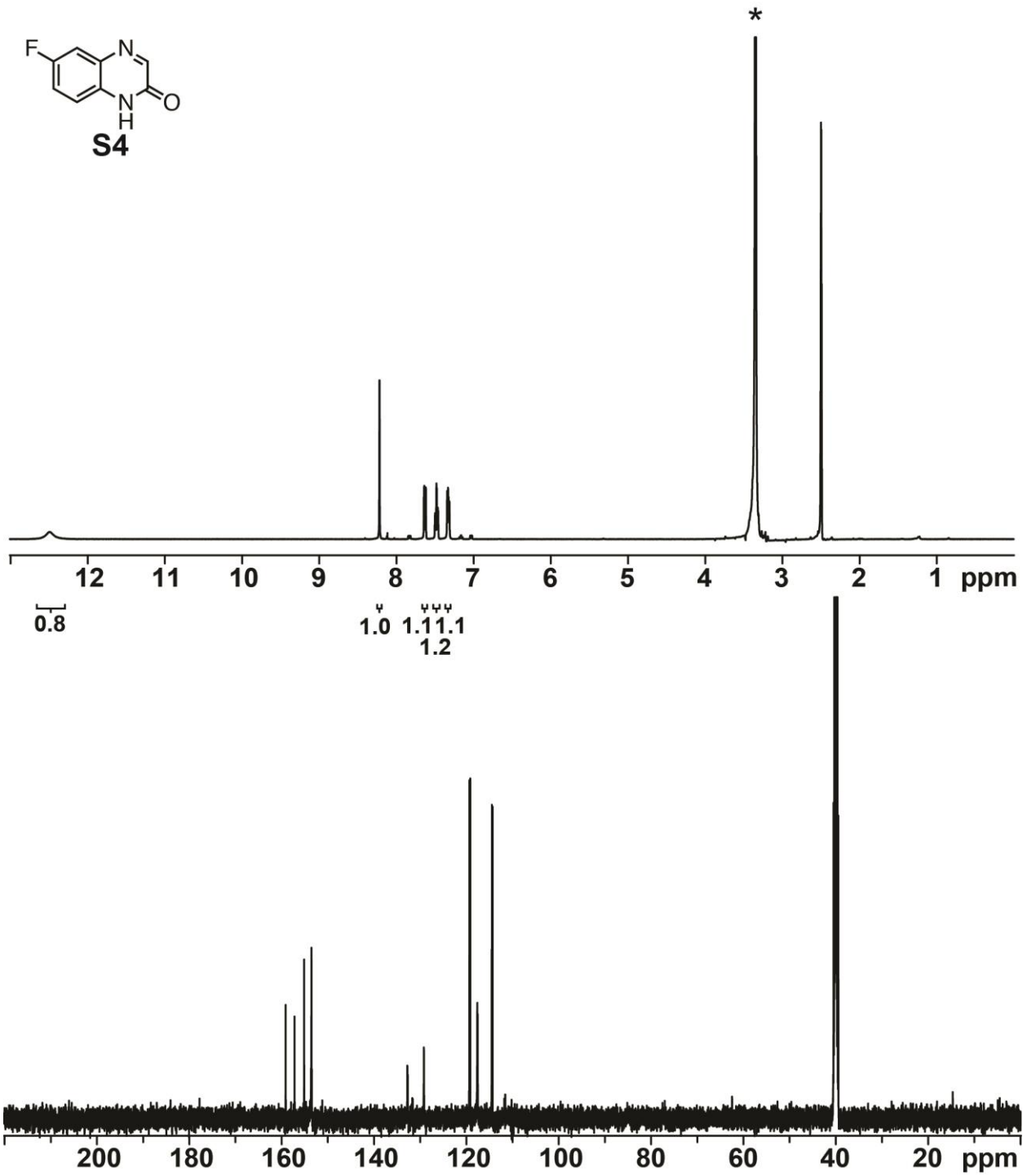

Figure S2-8. ^{1}H and ^{13}C NMR spectra of **S4**. ^{1}H NMR (500 MHz, DMSO-d_6) δ 12.50 (s, 1H), 8.22 (s, 1H), 7.65 (dd, J = 9, 3 Hz, 1H), 7.50 (ddd, J = 10, 9, 3 Hz, 1H), 7.34 (dd, J = 9, 5 Hz, 1H). ^{13}C NMR (176 MHz, DMSO-d_6) δ 158.73 (d, $J_{C\text{-}F}$ = 242 Hz), 154.98, 151.00, 132.36 (d, $J_{C\text{-}F}$ = 11.6 Hz), 127.63, 118.00 (d, $J_{C\text{-}F}$ = 25.2 Hz), 116.27 (d, $J_{C\text{-}F}$ = 8.3 Hz), 112.97 (d, $J_{C\text{-}F}$ = 23.2 Hz).

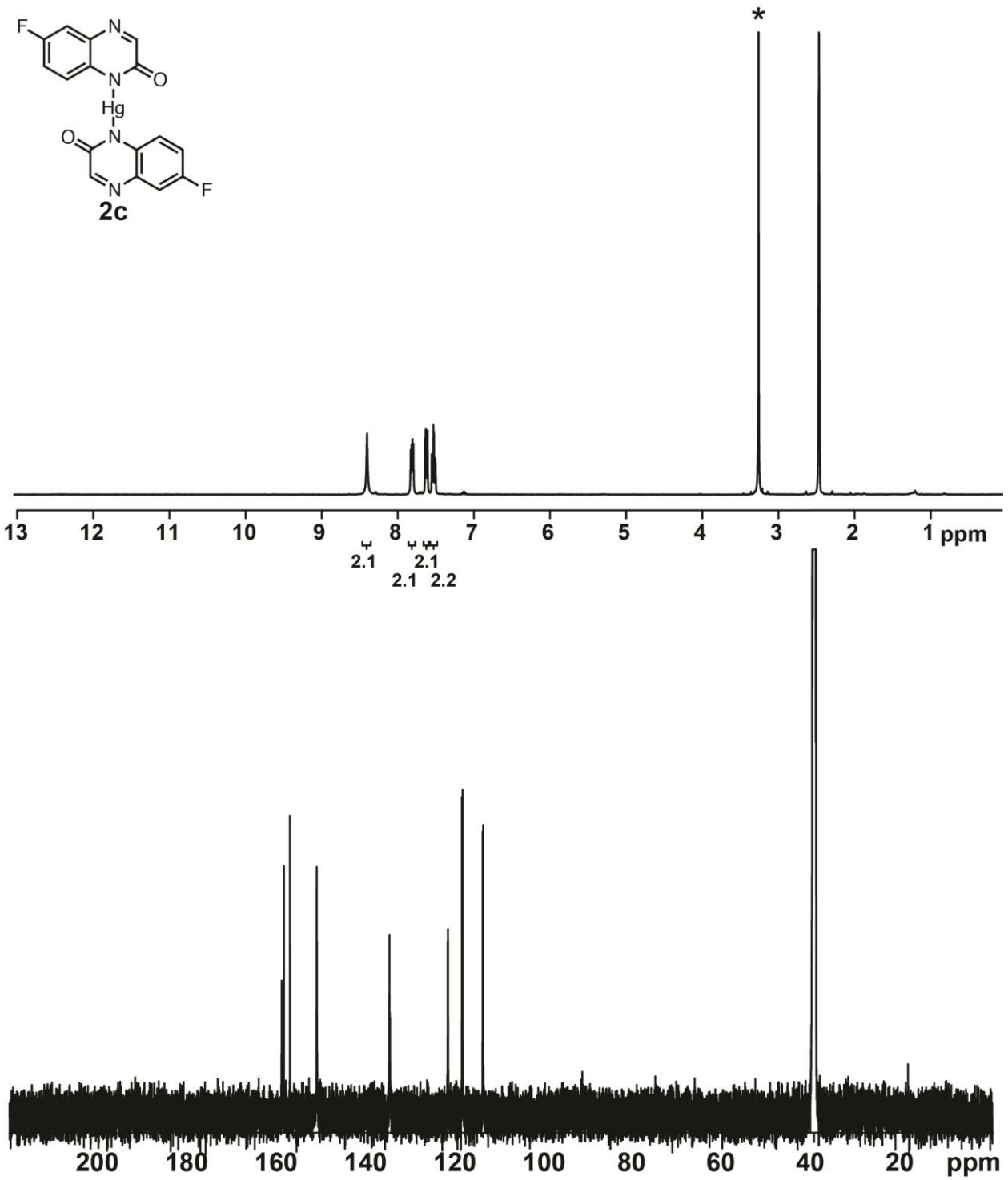

Figure S2-9. ^{1}H and ^{13}C NMR spectra of **2c**. ^{1}H NMR (400 MHz, DMSO-d_6) δ 8.43 (s, 2H), 7.86 (dd, J = 9, 5 Hz, 2H), 7.67 (dd, J = 9, 2 Hz, 2H), 7.59 (ddd, J = 10, 7, 2 Hz, 2H). ^{13}C NMR (100 MHz, DMSO-d_6) δ 159.04, 158.58, 157.22, 151.22, 134.96 (d, $J_{C\text{-}F}$ = 24 Hz), 121.89, 118.62 (d, $J_{C\text{-}F}$ = 25), 113.99 (d, $J_{C\text{-}F}$ = 22).

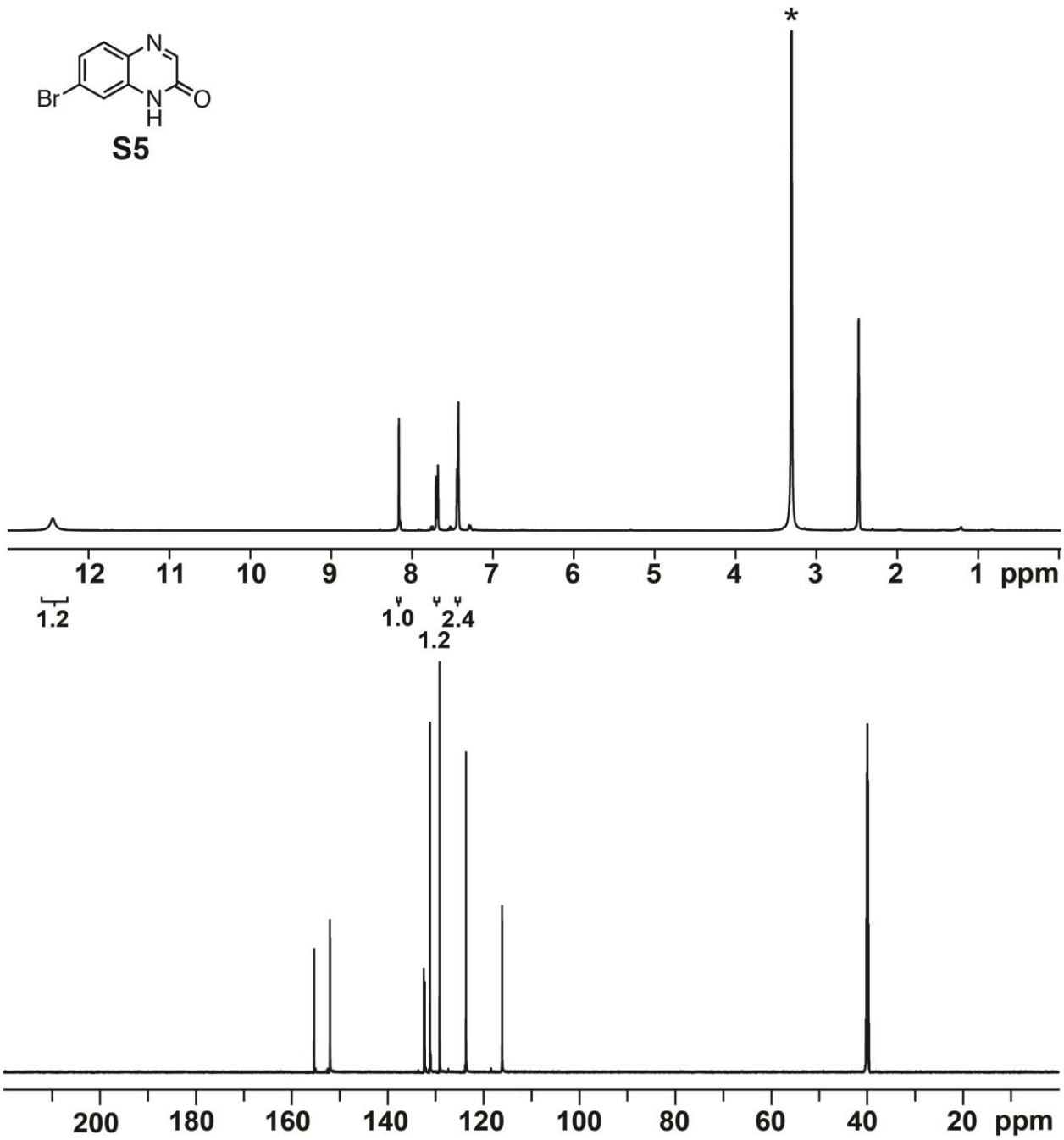

Figure S2-10. ^{1}H and ^{13}C NMR spectra of **S5**. ^{1}H NMR (500 MHz, DMSO-d_6) δ 12.49 (s, 1H) 8.19 (s, 1H), 7.72 (d, J = 9 Hz, 1H), 7.47 (d, J = 7 Hz, 1H), 7.45 (s, 1H). ^{13}C NMR (176 MHz, DMSO-d_6) δ 155.33, 152.02, 132.45, 132.24, 131.15, 129.19, 123.66, 116.13.

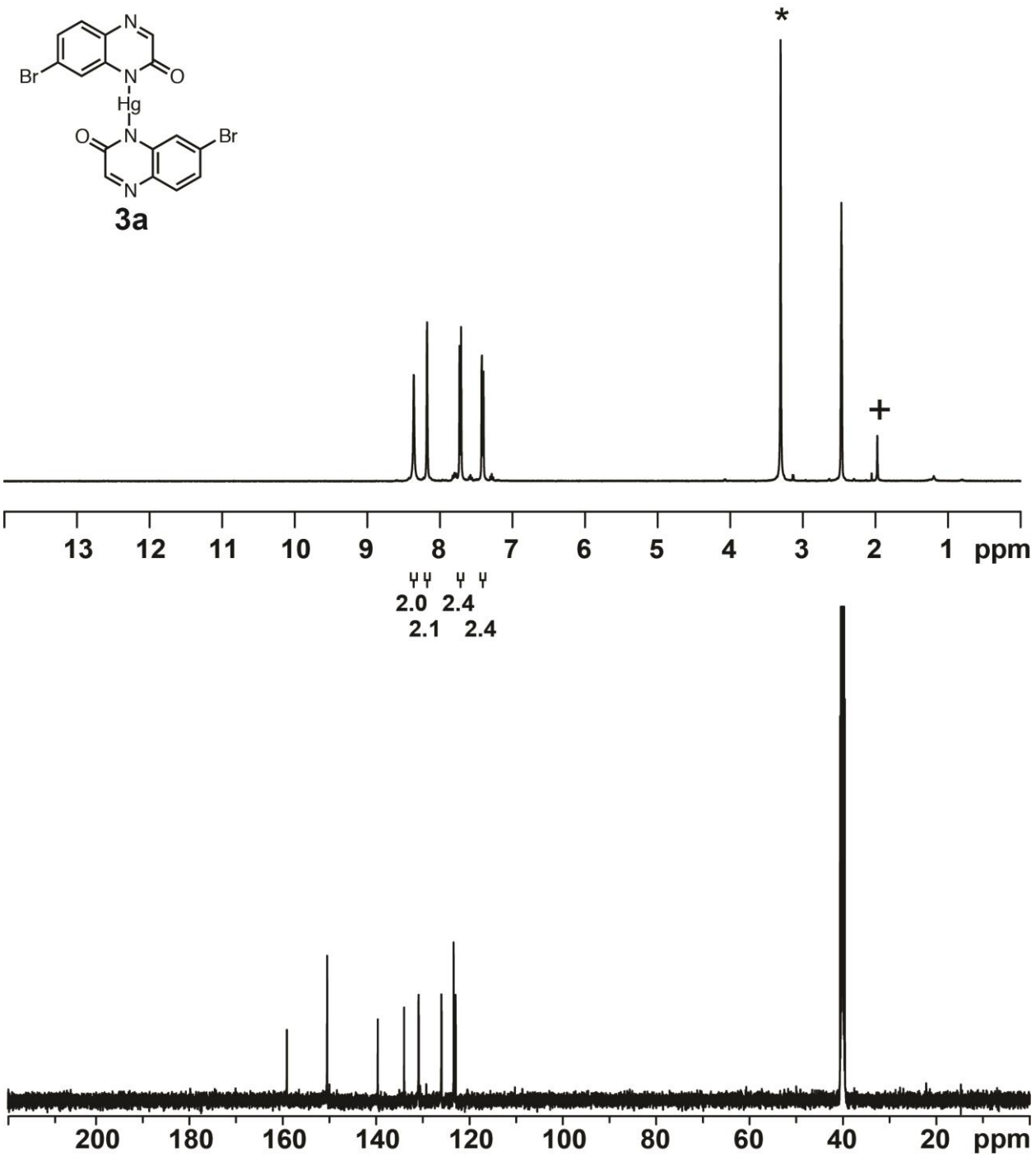

Figure S2-11. ^{1}H and ^{13}C NMR spectra of **3a**. ^{1}H NMR (400 MHz, DMSO-d_6) δ 8.35 (s, 2H), 8.17 (s, 2H), 7.73 (d, J = 10 Hz, 2H), 7.42 (d, J = 10 Hz, 2H). ^{13}C NMR (176 MHz, DMSO-d_6) δ 159.10, 150.47, 139.64, 133.98, 130.90, 126.00, 123.39, 122.98. Note: + indicates residual HOAc.

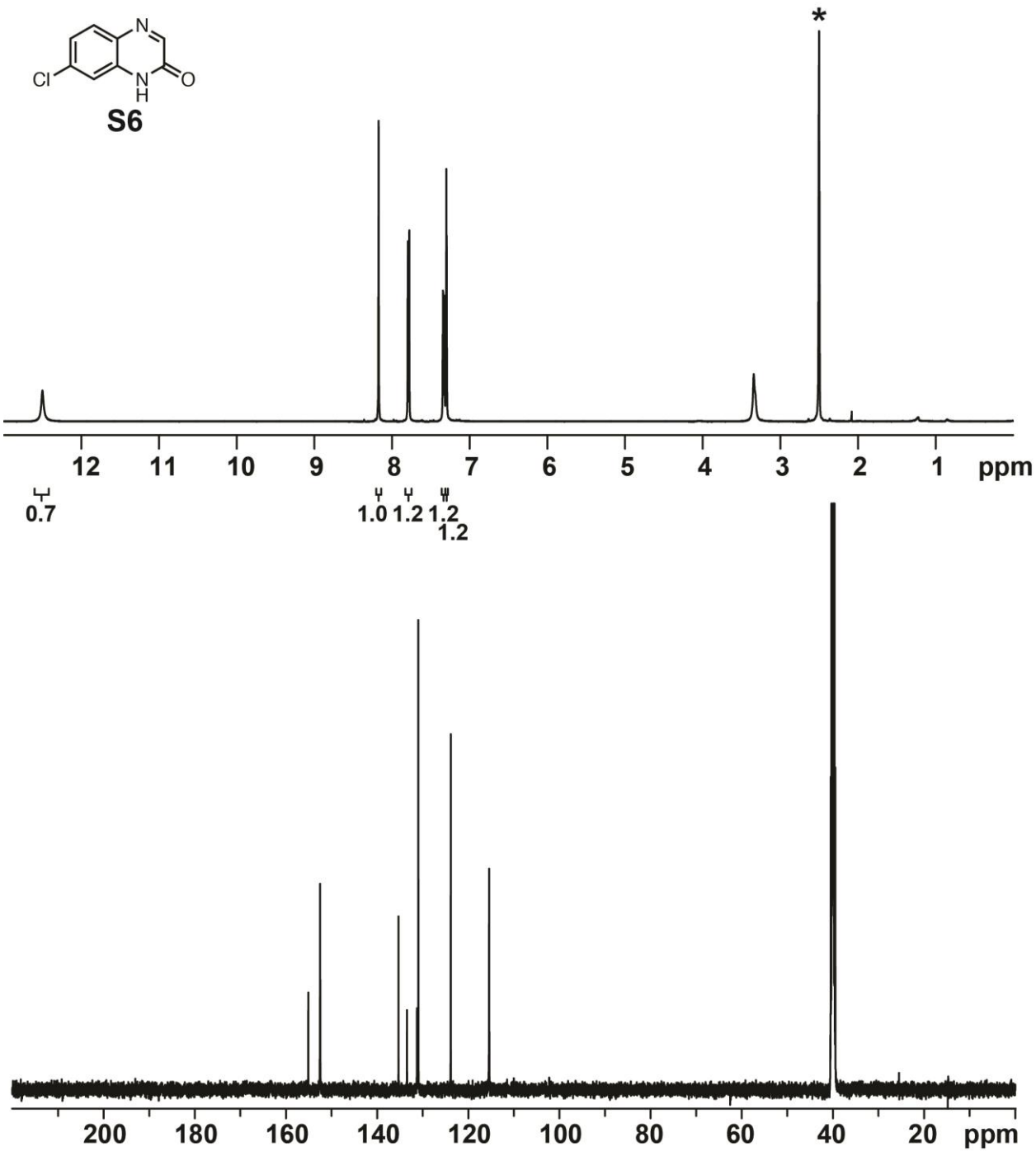

Figure S2-12. ^{1}H and ^{13}C NMR spectra of **S6**. ^{1}H NMR (500 MHz, DMSO-d_6) δ 12.50 (s, 1H), 8.17 (s, 1H), 7.78 (d, J = 8 Hz, 1H), 7.46 (dd, J = 9, 2 Hz, 1H), 7.44 (s, 1H). ^{13}C NMR (176 MHz, DMSO-d_6) δ 155.09, 152.49, 135.29, 133.44, 131.23, 130.95, 123.82, 115.41.

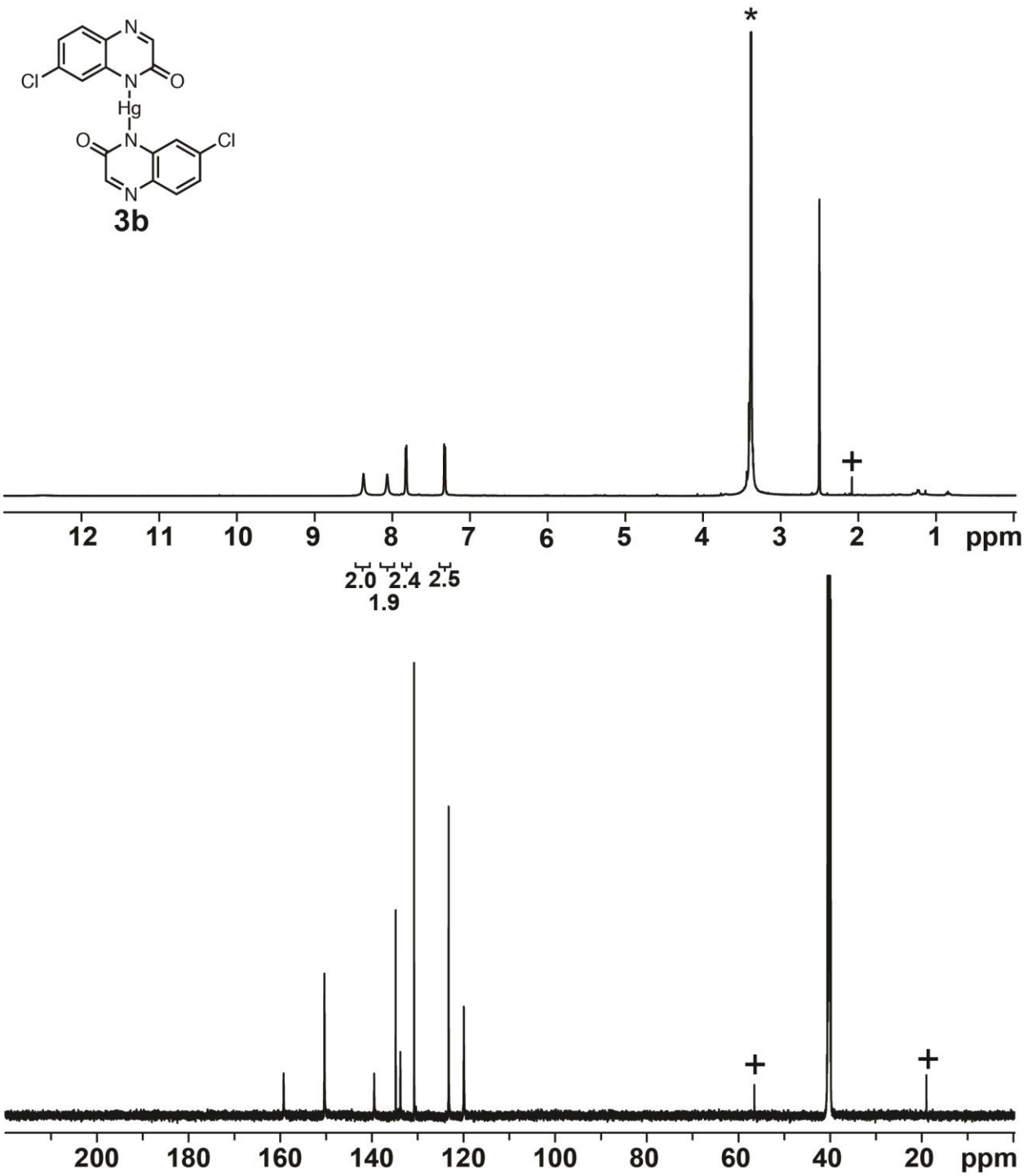

Figure S2-13. ^{1}H and ^{13}C NMR spectra of **3b**. ^{1}H NMR (500 MHz, DMSO-d_6) δ 8.37 (s, 2H), 8.07 (s, 2H), 7.83 (d, J = 8 Hz, 2H), 7.33 (d, J = 8 Hz, 2H). ^{13}C NMR (176 MHz, DMSO-d_6) δ 159.23, 150.34, 139.49, 134.79, 133.77, 130.78, 123.23, 119.91. Note: + represents residual HOAc in the ^{1}H spectrum and residual EtOH in the ^{13}C spectrum.

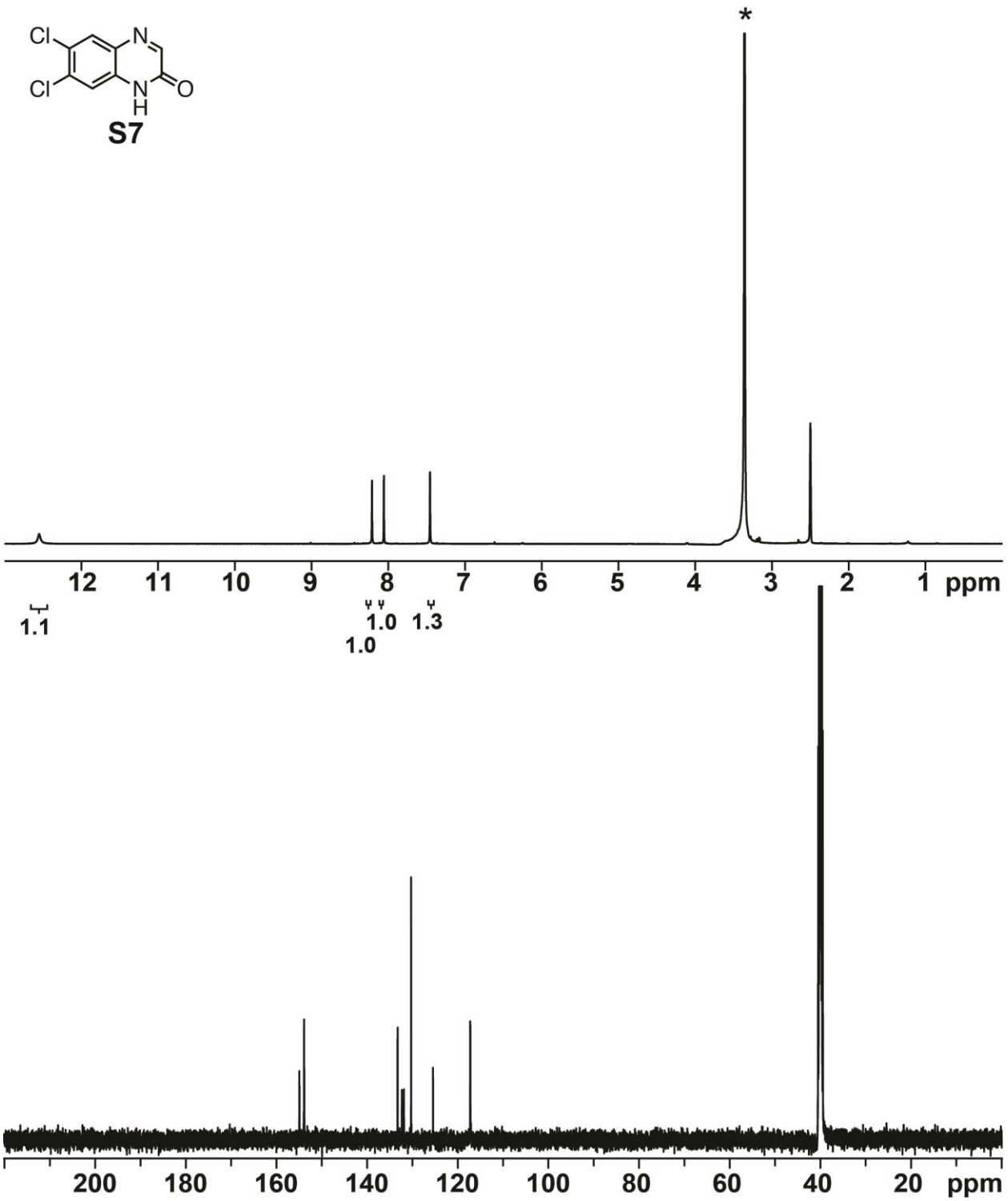

Figure S2-14. ^{1}H and ^{13}C NMR spectra of **S7**. ^{1}H NMR (500 MHz, DMSO-d_6) δ 12.58 (s, 1H), 8.22 (s, 1H), 8.06 (s, 1H), 7.46 (s, 1H). ^{13}C NMR (126 MHz, DMSO-d_6) δ 154.49, 153.89, 133.26, 132.30, 131.87, 130.27, 125.45, 117.22.

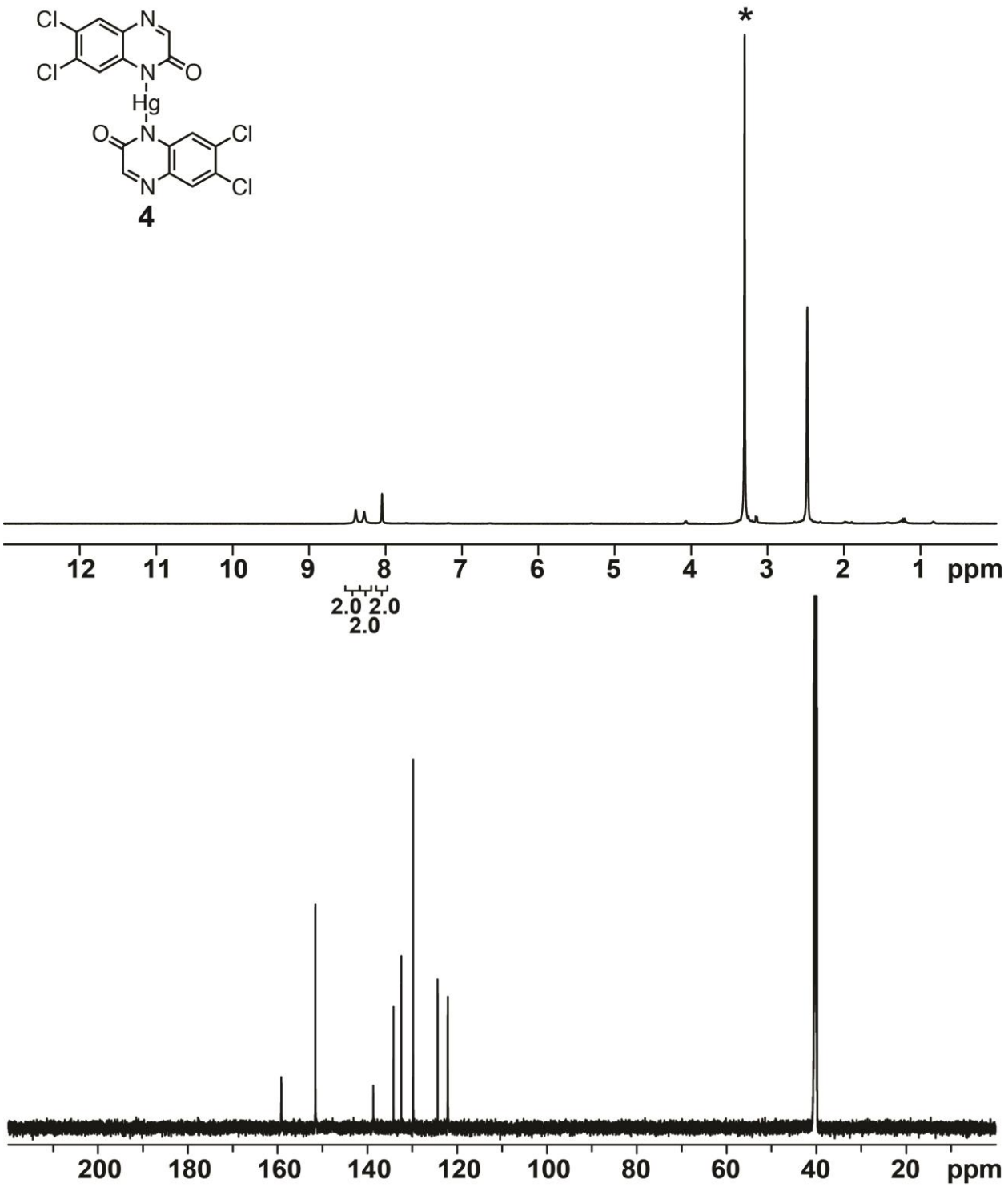

Figure S2-15. ^{1}H and ^{13}C NMR spectra of **4**. ^{1}H NMR (500 MHz, DMSO-d_6) δ 8.37 (s, 2H), 8.22 (s, 2H), 8.01 (s, 2H). ^{13}C NMR (176 MHz, DMSO-d_6) δ 159.16, 151.57, 138.66, 134.19, 132.44, 129.81, 124.34, 122.09.

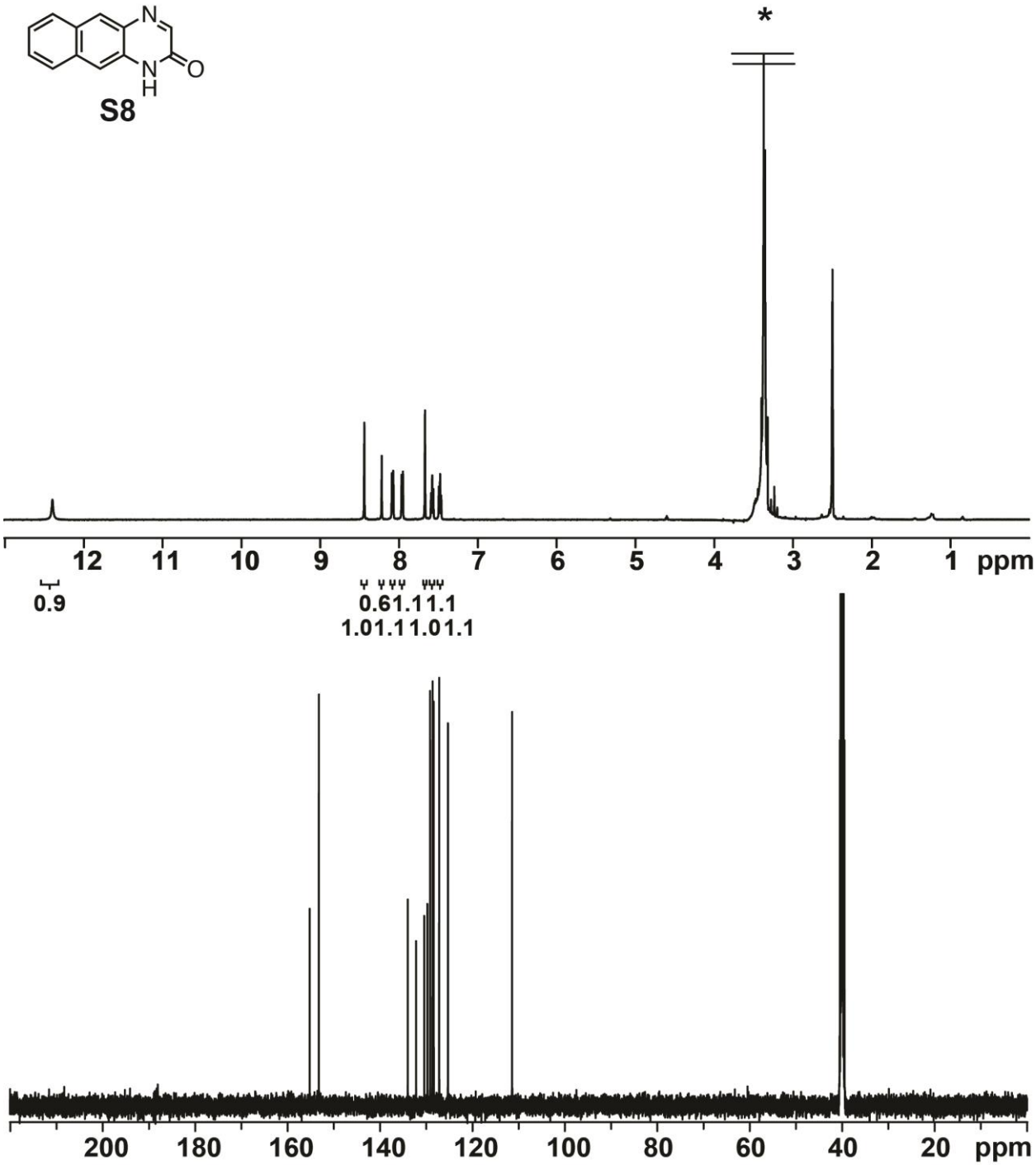

Figure S2-16. ^{1}H and ^{13}C NMR spectra of **S8**. ^{1}H NMR (500 MHz, DMSO-d_6) δ 12.40 (s, 1H), 8.44 (s, 1H), 8.22 (d, J = 2 Hz, 1H), 8.09 (d, J = 8 Hz, 1H), 7.96 (d, J = 8 Hz, 1H), 7.67 (s, 1H), 7.60 (dd, J = 9, 7 Hz, 1H), 7.50 (dd, J = 9, 7 Hz, 1H). ^{13}C NMR (126 MHz, DMSO-d_6) δ 155.21, 153.22, 133.99, 132.18, 130.41, 129.74, 129.15, 128.61, 128.37, 127.19, 125.29, 111.42.

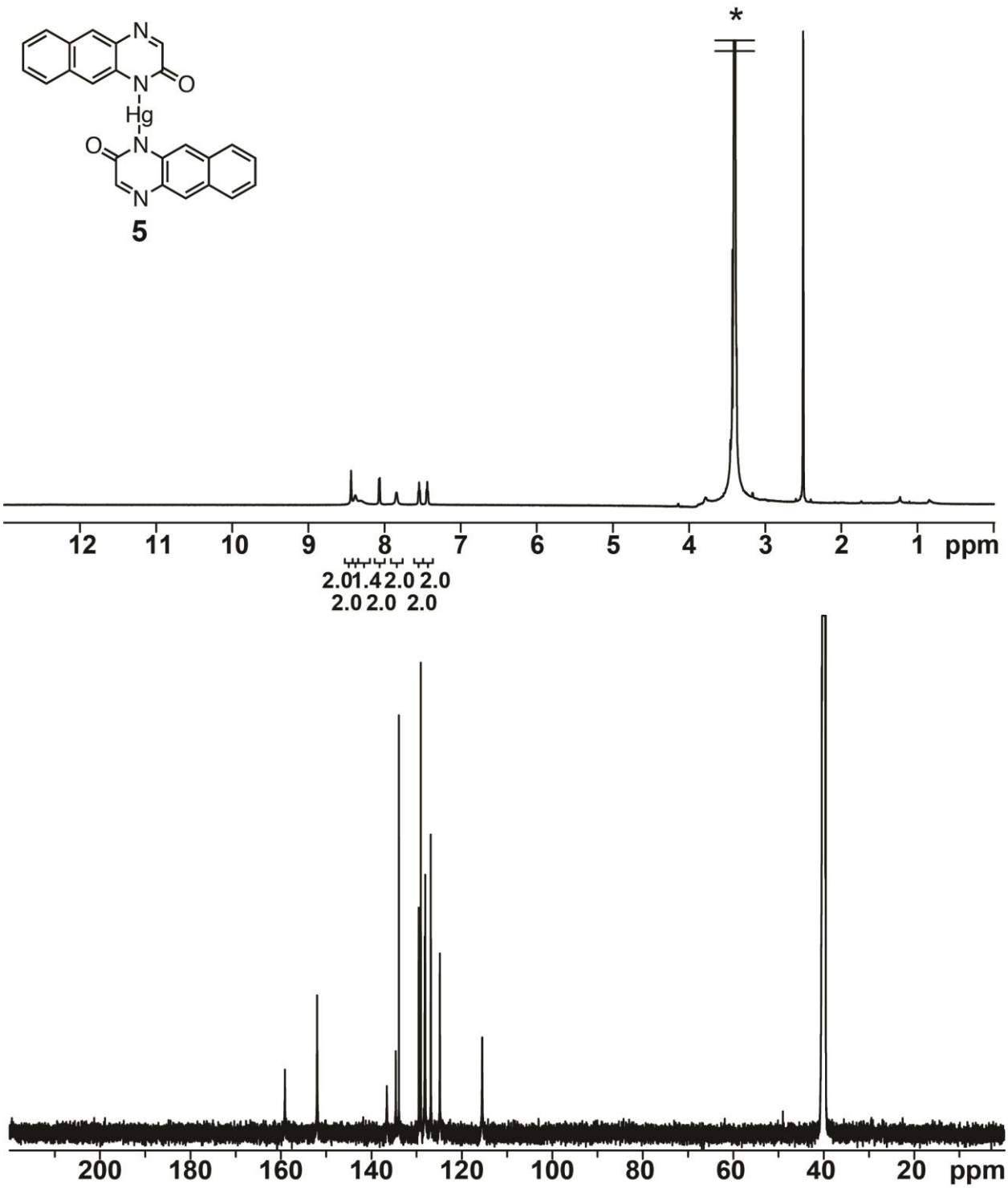

Figure S2-17. ^{1}H and ^{13}C NMR spectra of **5**. ^{1}H NMR (700 MHz, DMSO-d_6) δ 8.41 (s, 2H), 8.35 (s, 2H) 8.29 (s, 2H), 8.05 (d, J = 8 Hz, 2H), 7.81 (s, 2H), 7.53 (dd, J = 9, 7 Hz, 2H), 7.42 (dd, J = 9, 7 Hz, 2H). ^{13}C NMR (176 MHz, DMSO-d_6) δ 159.10, 151.98, 136.57, 134.58, 133.91, 129.52, 129.06, 128.20, 128.09, 126.86, 124.85, 115.50.

V. ^{19}F NMR Spectroscopic Data

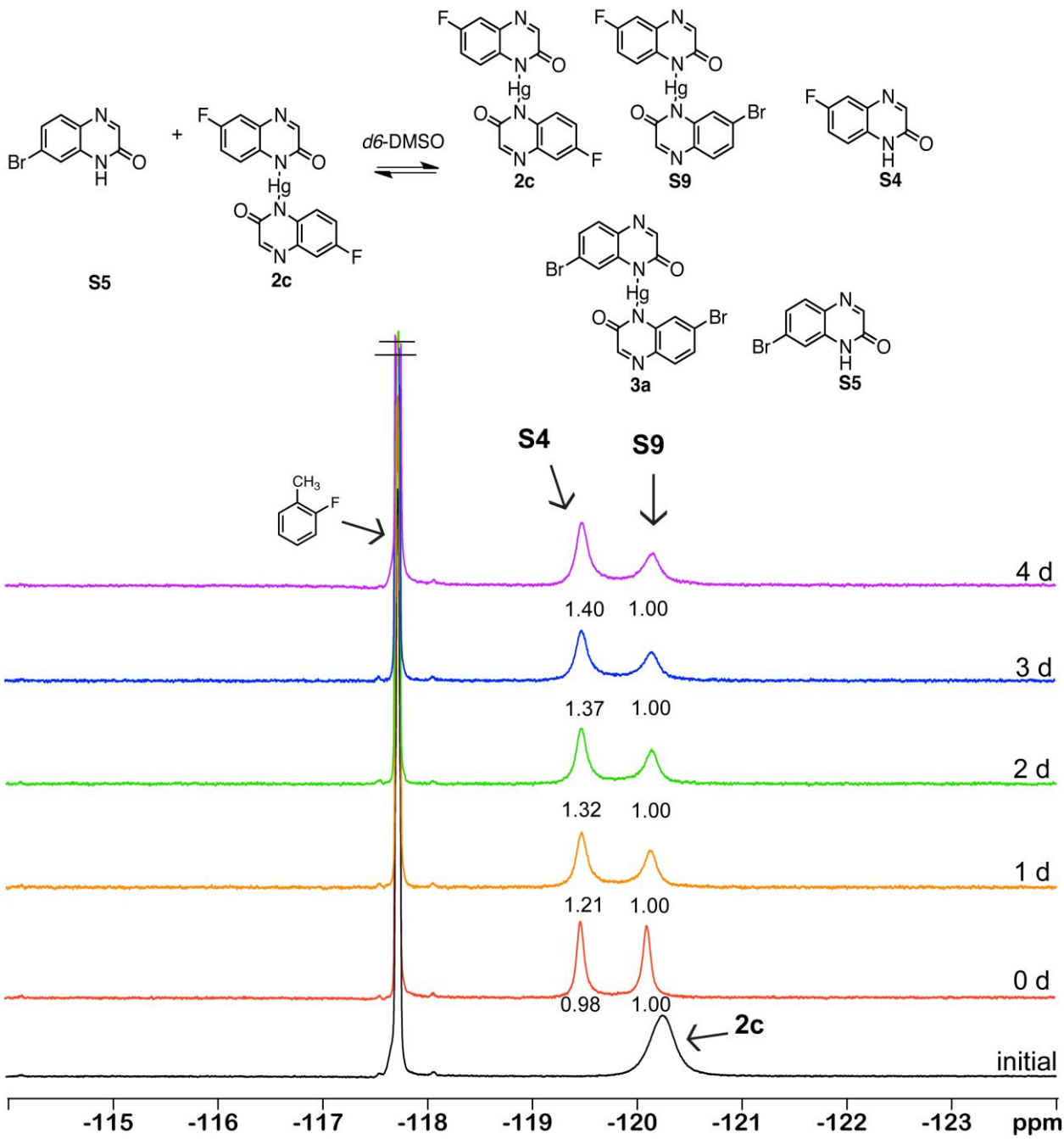

Figure S2-18. To a solution of **2c** (0.5 mL, 0.02 M, 1 equiv) in DMSO-d_6 in a J. Young NMR tube, *o*-fluorotoluene (4.2 µL, 1.5 equiv) and **S5** (0.5 mL, 0.04 M, 2 equiv) were added. The J. Young tube was sealed and heated at 100 ºC for 4 d. To determine quinoxalinone exchange, ^{19}F NMR spectra were taken before and after the addition of **S5** and every 24 h.

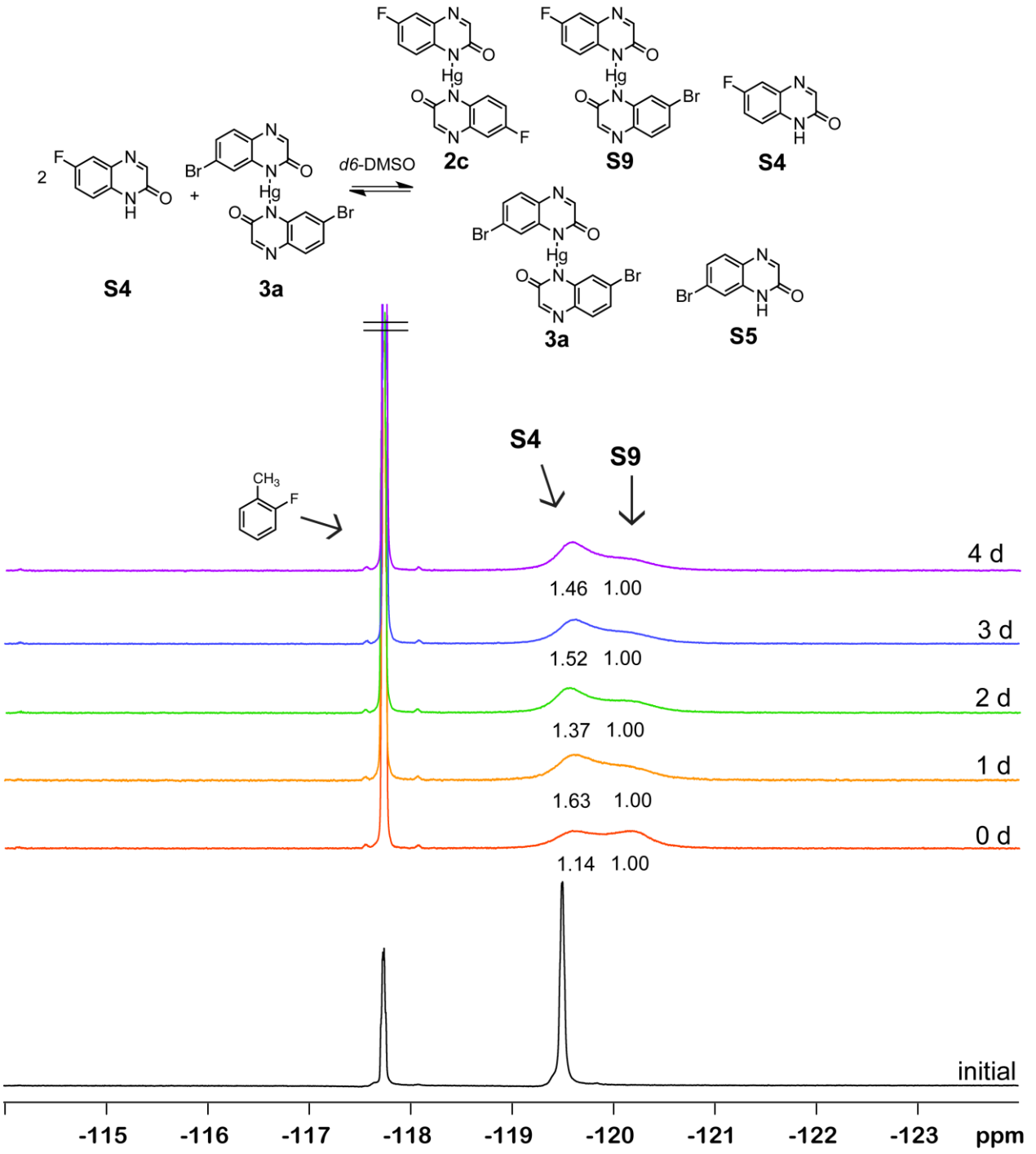

Figure S2-19. To a solution of **S4** (0.5 mL, 0.04 M, 2 equiv) in DMSO-d_6 in a J. Young NMR tube, *o*-fluorotoluene (4.2 µL, 1.5 equiv) and **3a** (0.5 mL, 0.019 M, 1 equiv) were added. The J. Young tube was sealed and heated at 100 ºC for 4 days. To determine quinoxalinone exchange, ^{19}F NMR spectra were taken before and after the addition of **3a** and after heating every 24 h. Manual integration to separate peaks was performed using MestReNova software for Windows.

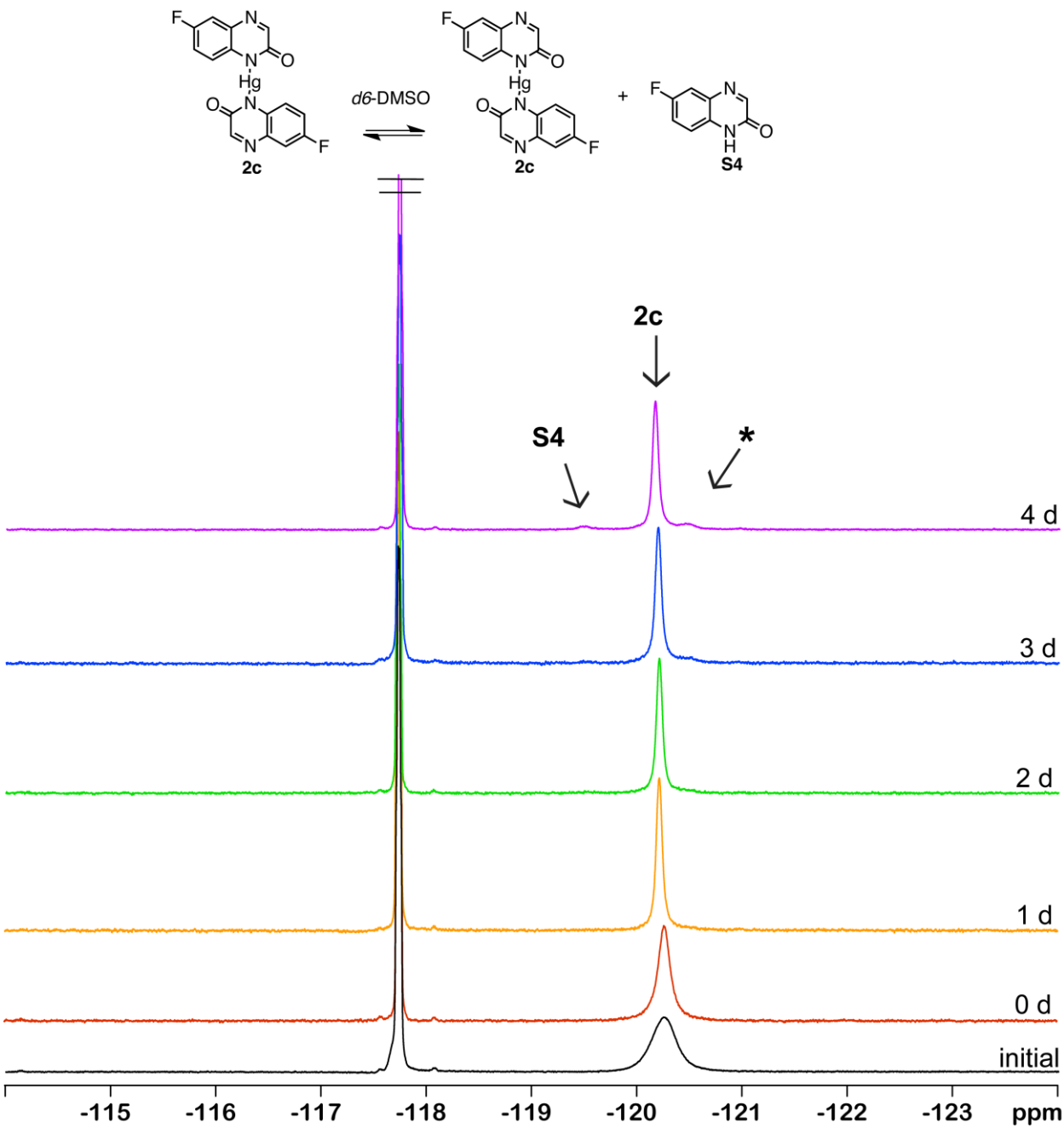

Figure S2-20. In a J. Young Tube, a solution of **2c** (1.0 mL, 0.02 mM, 1 equiv) in DMSO-d_6, *o*-fluorotoluene (4.2 µL, 1.5 equiv) were added. The J. Young tube was sealed and heated at 100 ºC for 4 days. To determine complex stability, ^{19}F NMR spectra were taken at the same time points as the ^{19}F NMR experiments in Figures S18-19. Note: * denotes unknown decomposition product.

VI. X-ray Crystal Structures

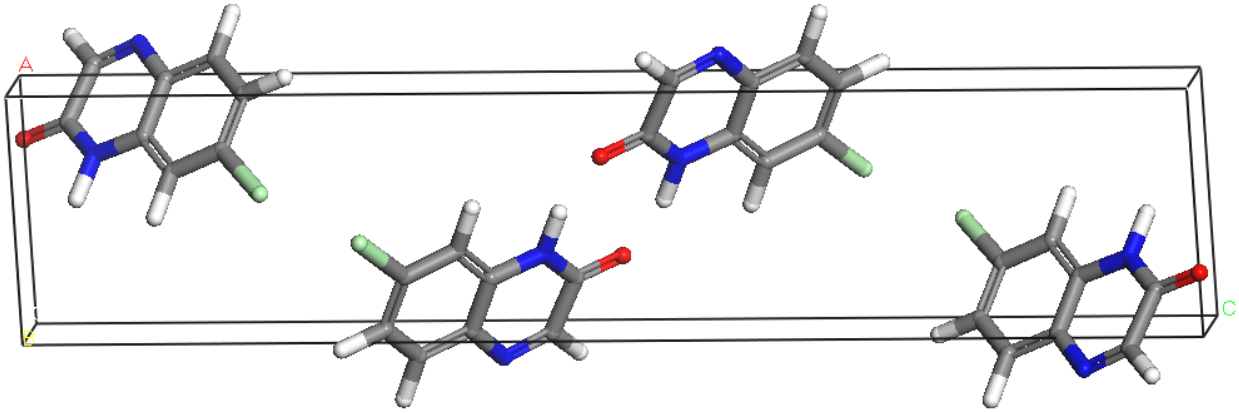

Figure S2-21. Representation of the crystal structure of **S6** determined by single crystal X-ray diffraction (SCXRD)**.** Crystals were grown by slow evaporation of MeOH. The crystal structure was used to confirm the identity of regioisomers from the synthesis of **S2**, **S3**, **S4**, **S5**, and **S6**.

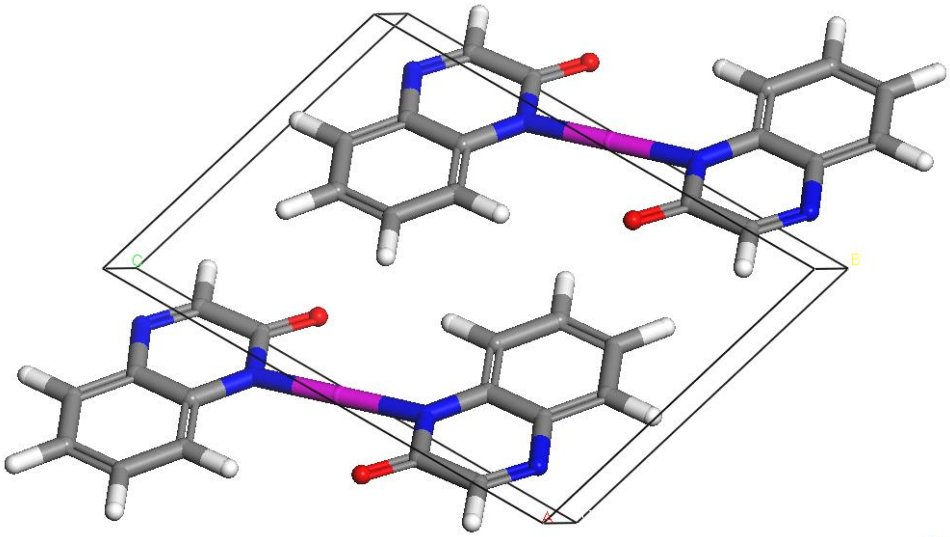

Figure S2-22. Representation of a crystal structure of **1a** grown from slow diffusion of H_2O into DMSO. The simulated powder X-ray diffraction (PXRD) pattern can be found in Figure S24, F.[3]

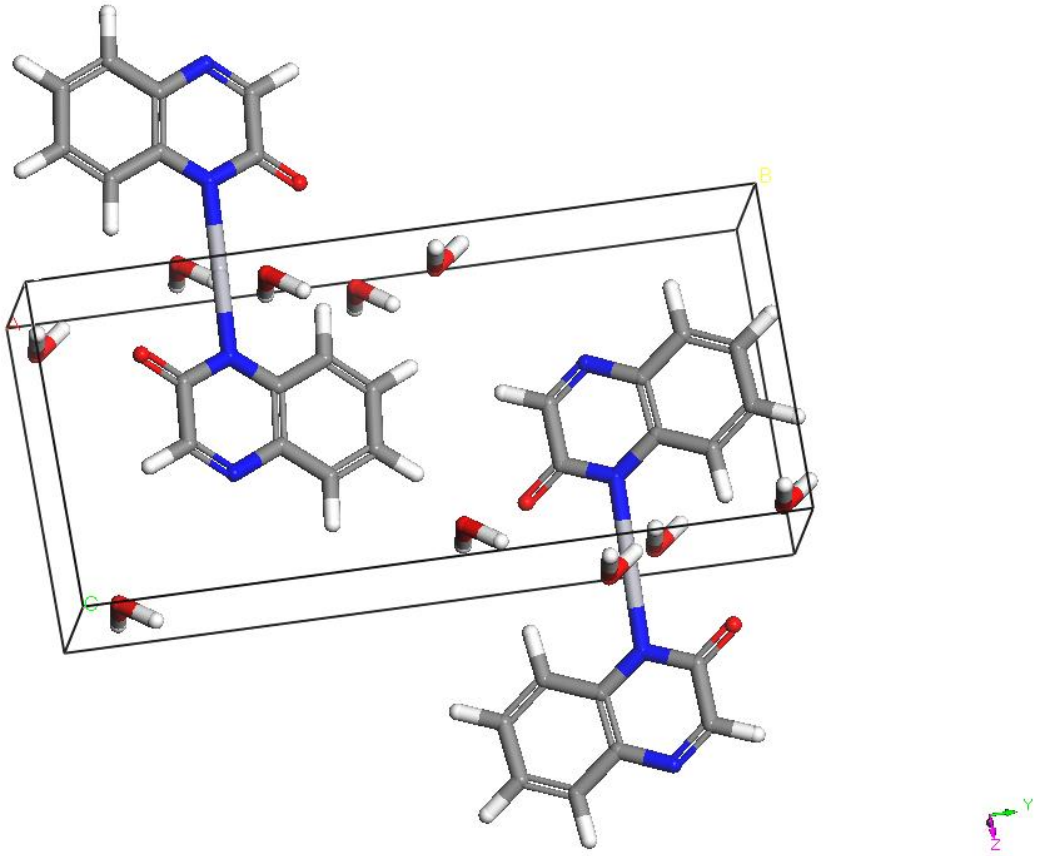

Figure S2-23. Representation of a crystal structure of **1a** grown by slow diffusion of MeOH into H_2O**.** The simulated PXRD pattern can be found in Figure S24, G.

VII. Powder X-Ray Diffraction Patterns

General Procedure – PXRD patterns were collected at ambient temperature using a Bruker D8 Avance diffractometer with a LynxEye detector using graphite monochromated Cu-Kα radiation (1.5406 Å). The samples were loaded onto glass microscope slides. The software used for data analysis was JADE.

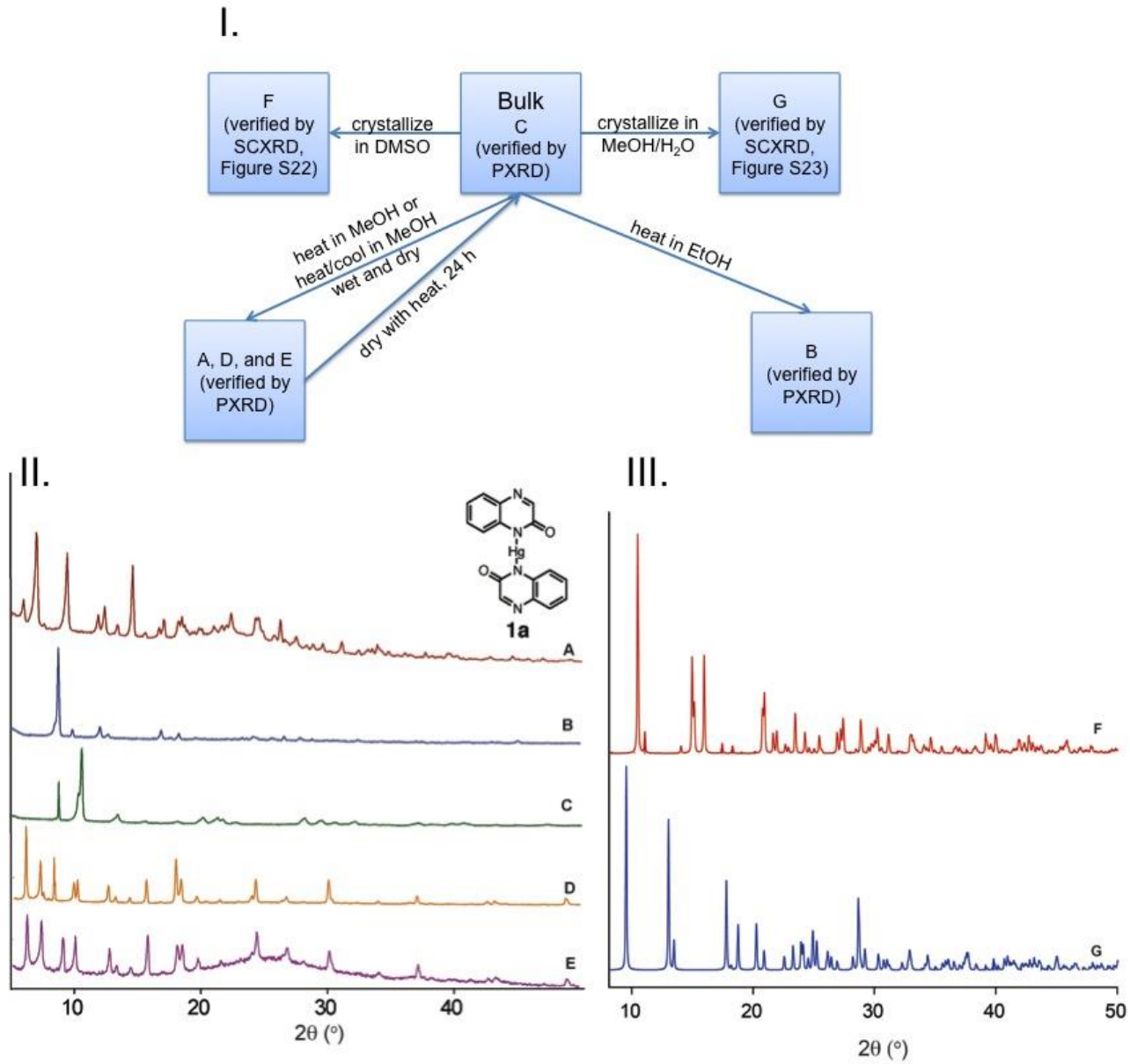

Figure S2-24. (I) Diagram showing how various forms of **1a** were obtained. (II) PXRD patterns for **1a** (A) heated in MeOH, (B) heated in EtOH, (C) bulk from synthesis, (D) dry gel, and (E) wet gel in MeOH. (III) Simulated PXRD patterns for crystal structures F and G, shown in Figures S22-23.

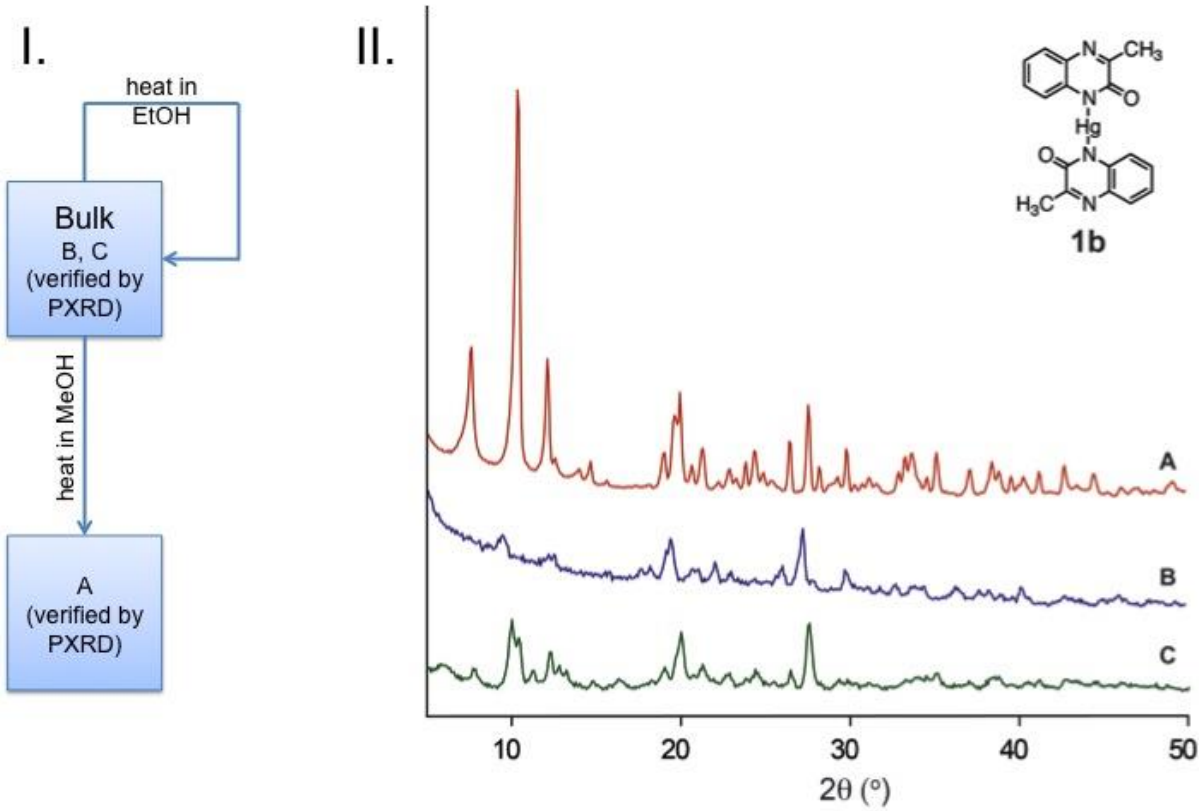

Figure S2-25. (I) Diagram showing how various solid forms of **1b** were obtained. (II) PXRD patterns for **1b** (A) heated in MeOH, (B) heated in EtOH, and (C) bulk from synthesis.

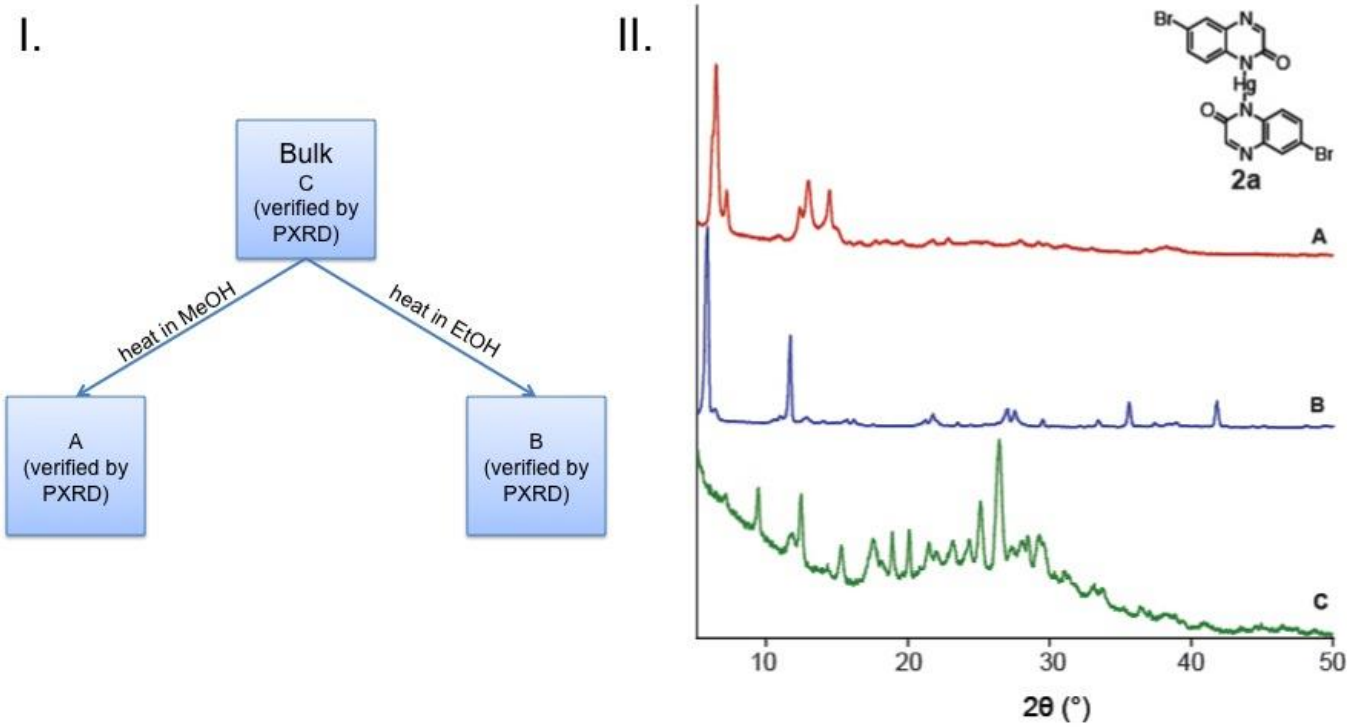

Figure S2-26. (I) Diagram showing how various solid forms of **2a** were obtained. (II) PXRD patterns for **2a** (A) heated in MeOH, (B) heated in EtOH, and (C) bulk from synthesis.

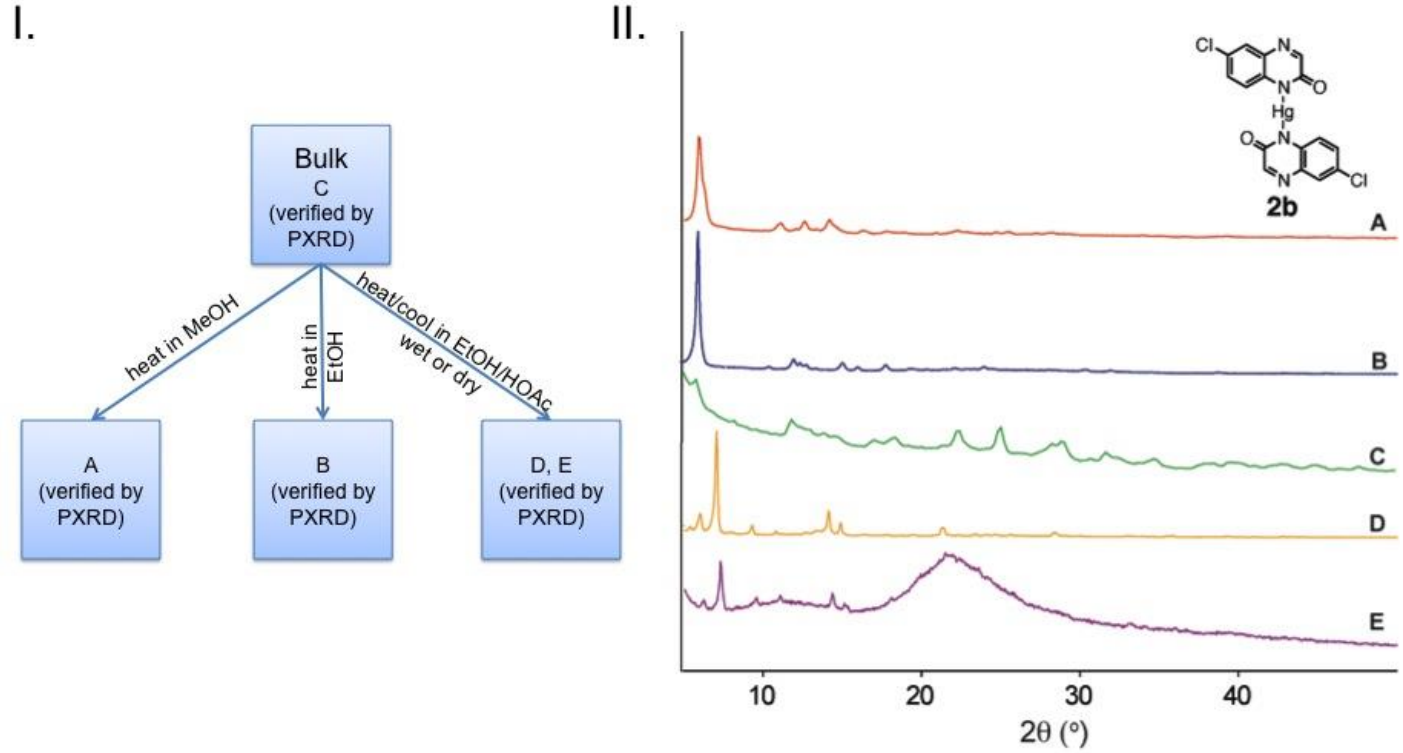

Figure S2-27. (I) Diagram showing how various solid forms of **2b** were obtained. (II) PXRD patterns for **2b** (A) heated in MeOH, (B) heated in EtOH, (C) bulk from synthesis, (D) dry gel formed at cgc in EtOH/HOAc, and (E) wet gel in EtOH/HOAc.

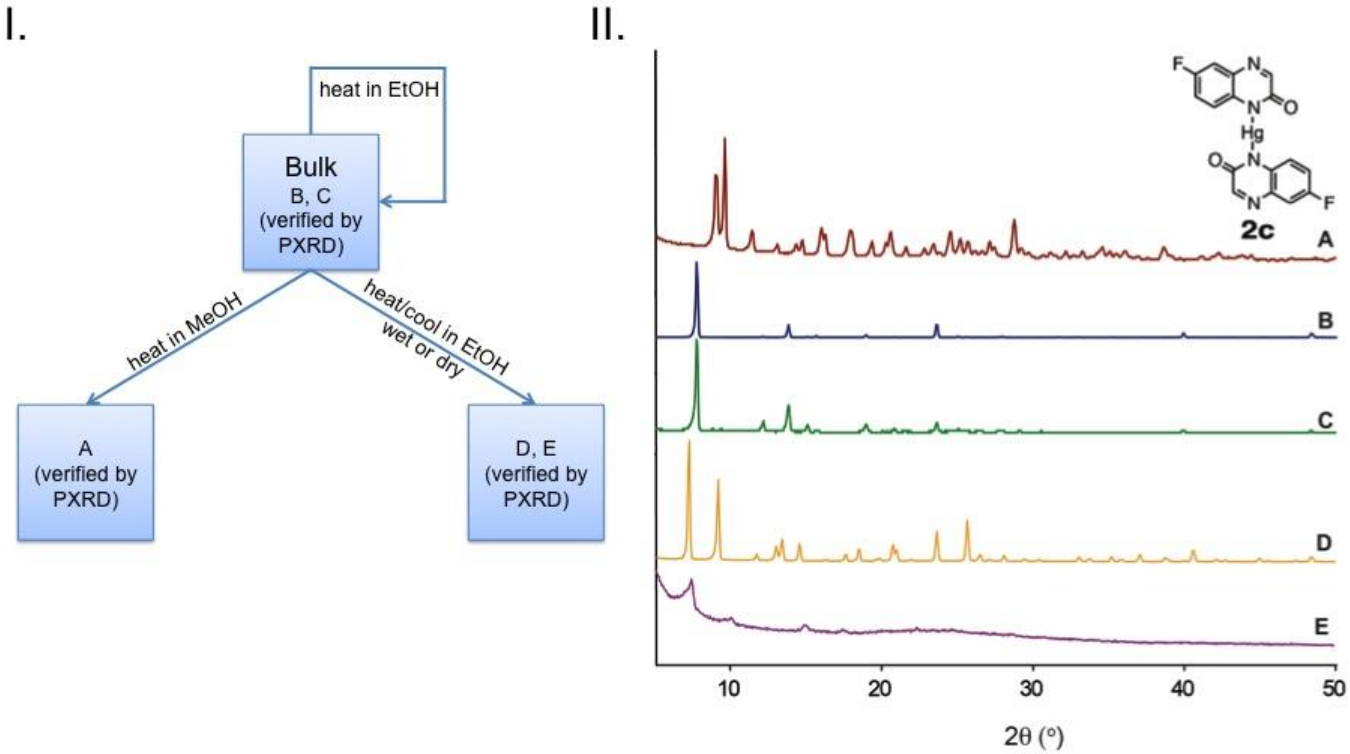

Figure S2-28. (I) Diagram showing how various solid forms of **2c** were obtained. (II) PXRD patterns for **2c** (A) heated in MeOH, (B) heated in EtOH, (C) bulk from synthesis, (D) dried gel formed at cgc in anhydrous EtOH, and (E) wet gel in anhydrous EtOH.

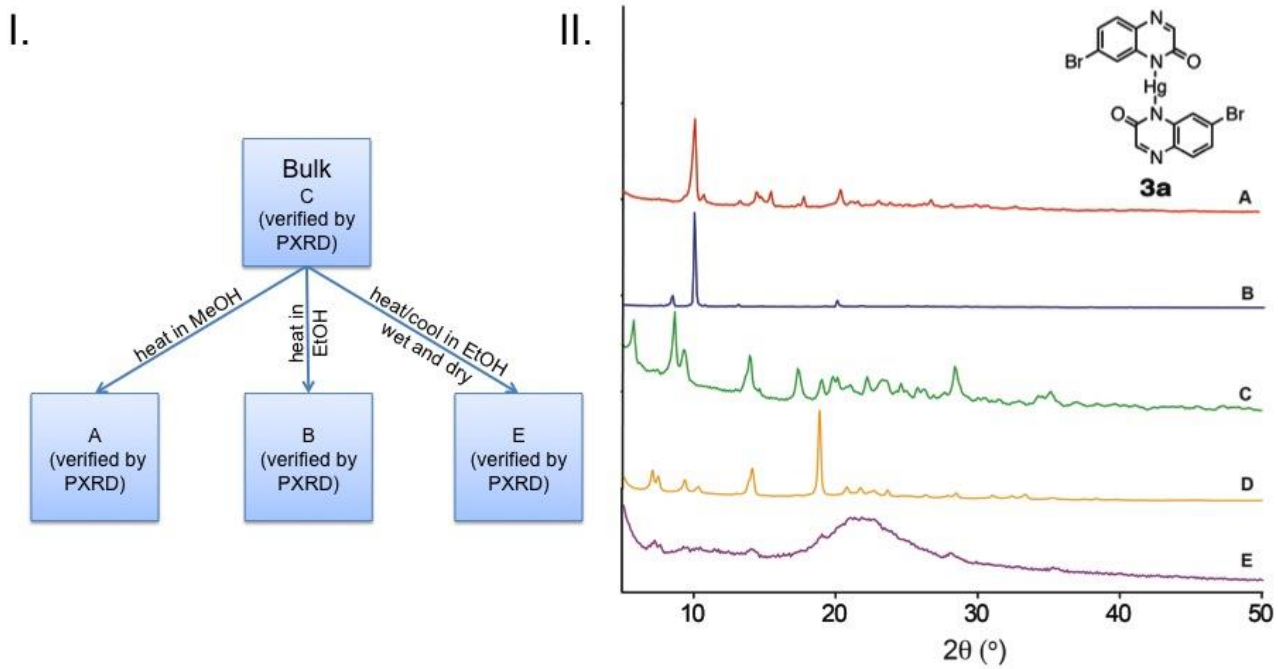

Figure S2-29. (I) Diagram showing how various solid forms of **3a** were obtained. (II) PXRD patterns for **3a** (A) heated in MeOH, (B) heated in EtOH, (C) bulk from synthesis, (D) dried gel formed at cgc in EtOH, and (E) wet gel formed at cgc in EtOH.

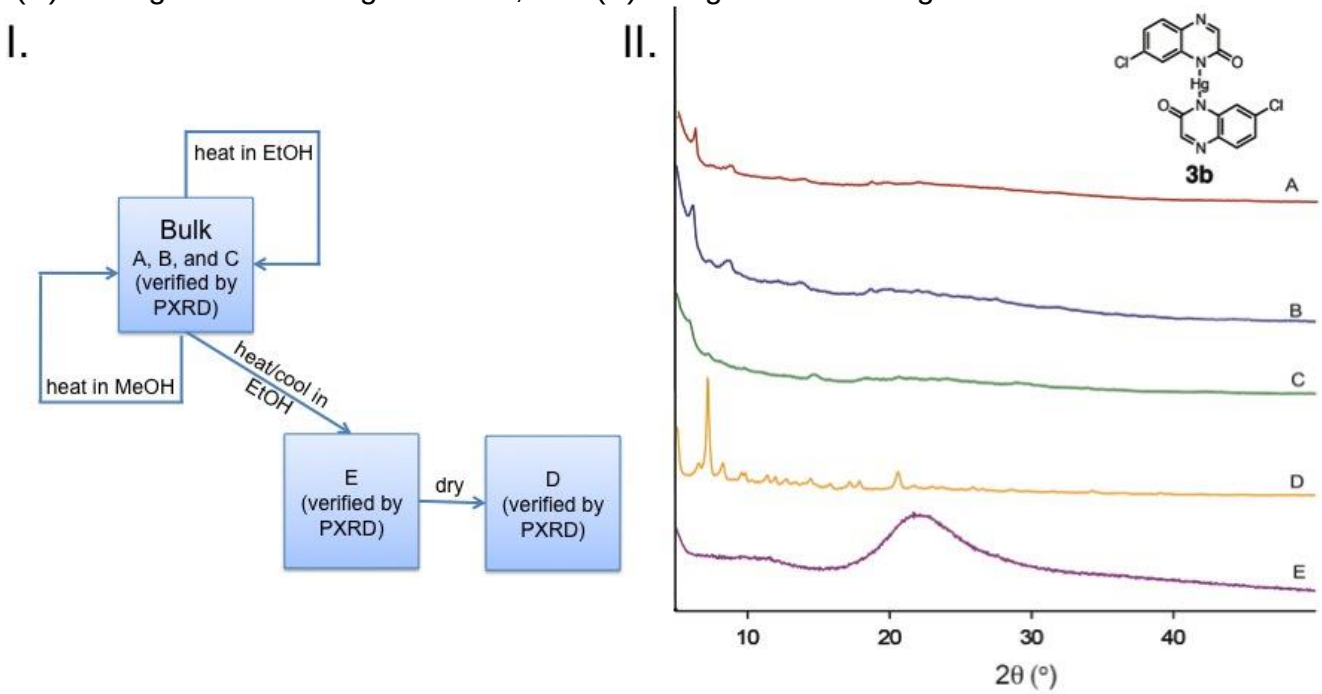

Figure S2-30. (I) Diagram showing how various forms of **3b** were obtained. (II) PXRD patterns for **3b** (A) heated in MeOH, (B) heated in EtOH, (C) bulk from synthesis, (D) dried gel formed at cgc in EtOH, and (E) wet gel formed at cgc in EtOH.

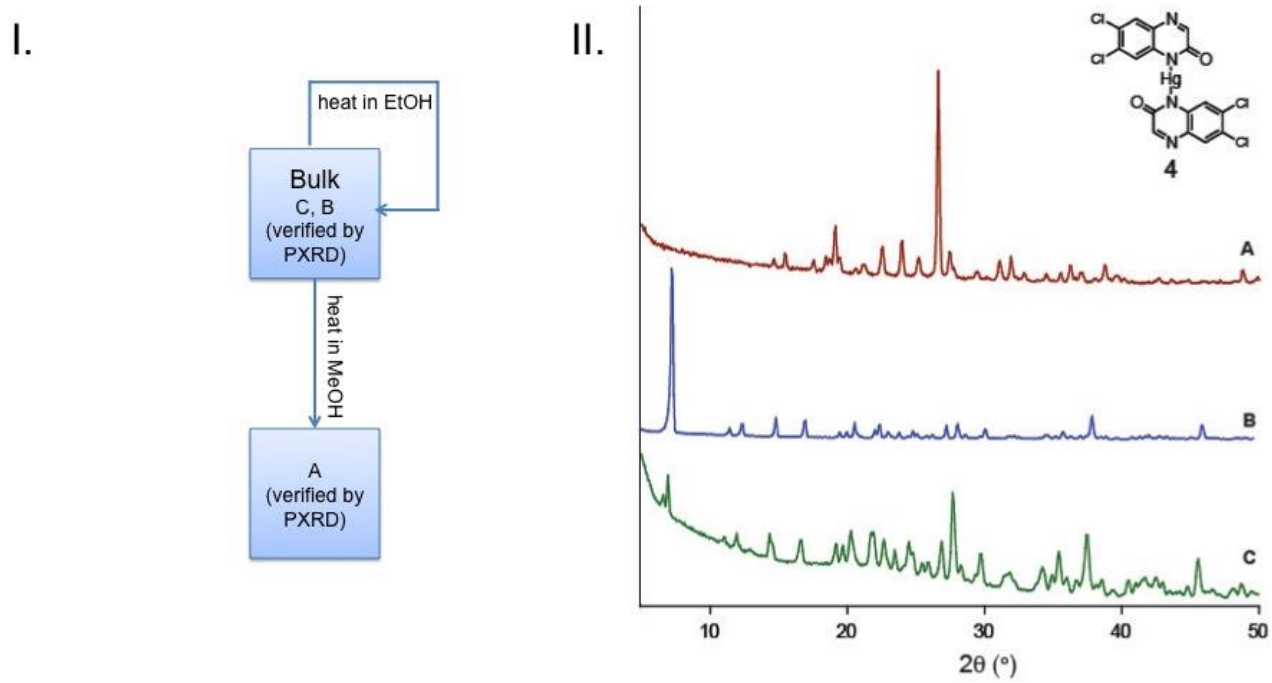

Figure S2-31. (I) Diagram showing how various solid forms of **4** were obtained. (II) PXRD patterns for **4** (A) heated in MeOH, (B) heated in EtOH, and (C) bulk from synthesis.

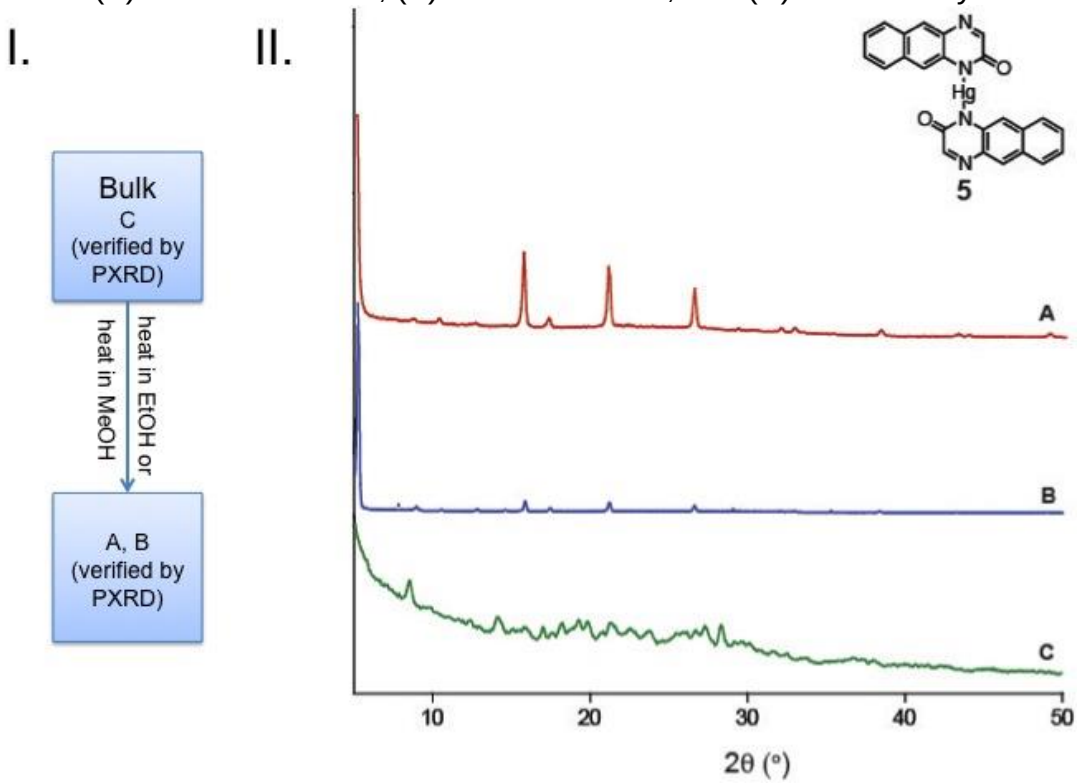

Figure S2-32. (I) Diagram showing how various solid forms of **5** were obtained. (II) PXRD patterns for **5** (A) heated in MeOH, (B) heated in EtOH, and (C) bulk from synthesis.

VIII. Differential Scanning Calorimetry

General Procedure: DSC was performed on a TA Instruments DSC Q2000. Samples were sealed in aluminum pans (Tzero Hermetic) and sealed using a TA Instruments crimper. A heat/cool/heat/cool cycle was used for all samples. Heating rates for all samples are 10 ºC/min, and cooling rates are 5 ºC/min.

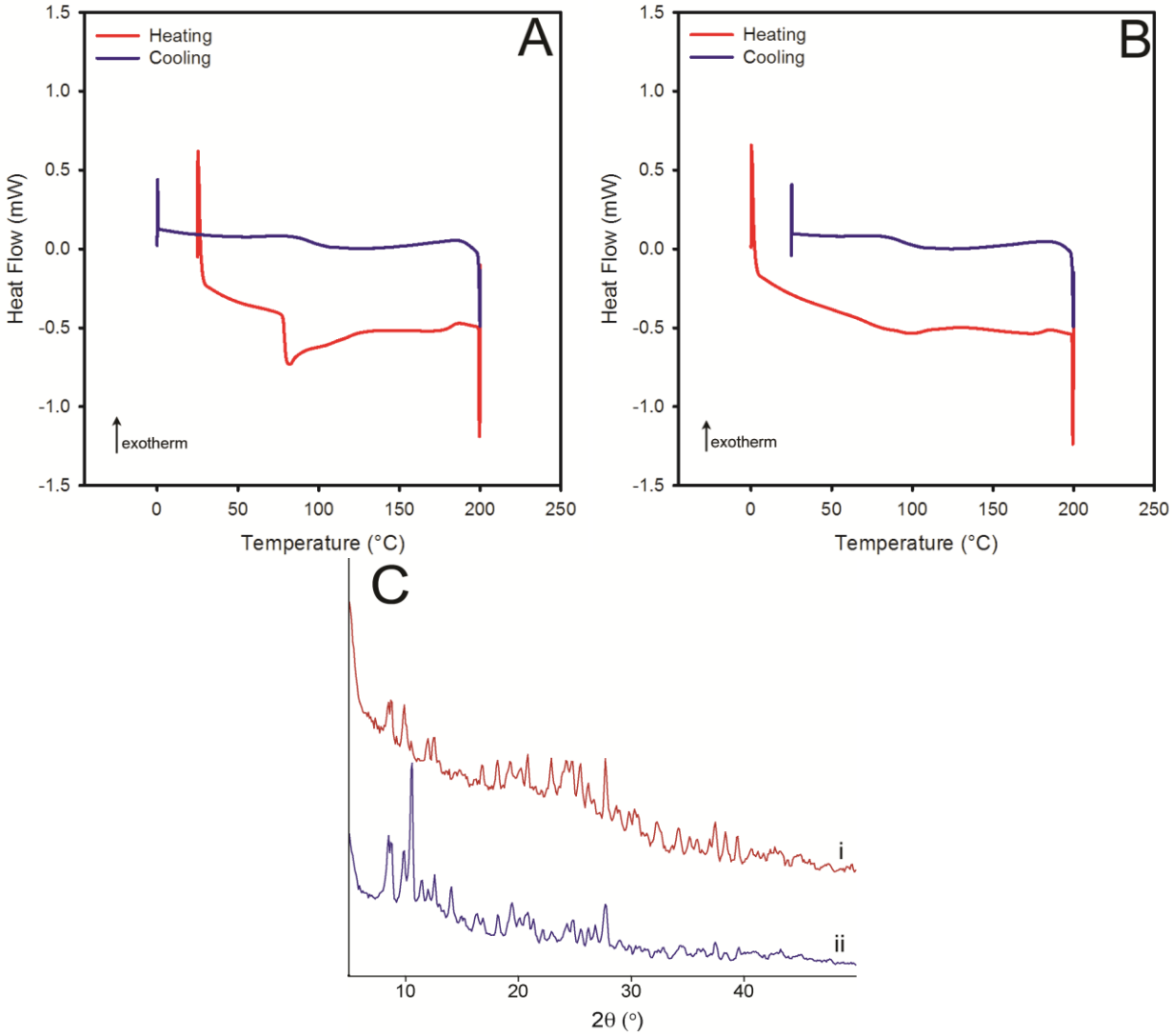

Figure S2-33. Heat/cool/heat/cool DSC scans of the bulk form of **1a** from synthesis. A) Cycle 1: Sample was heated from ~40 to 200 ºC, held at 200 ºC for 5 min, then cooled to 0 ºC, and equilibrated at 0 ºC for 5 min. B) Cycle 2: Sample was heated from 0 to 200 ºC, held at 200 ºC for 5 min, then cooled to 25 ºC. C) PXRD patterns of a bulk sample of **1a** before (i) and after (ii) DSC scans.

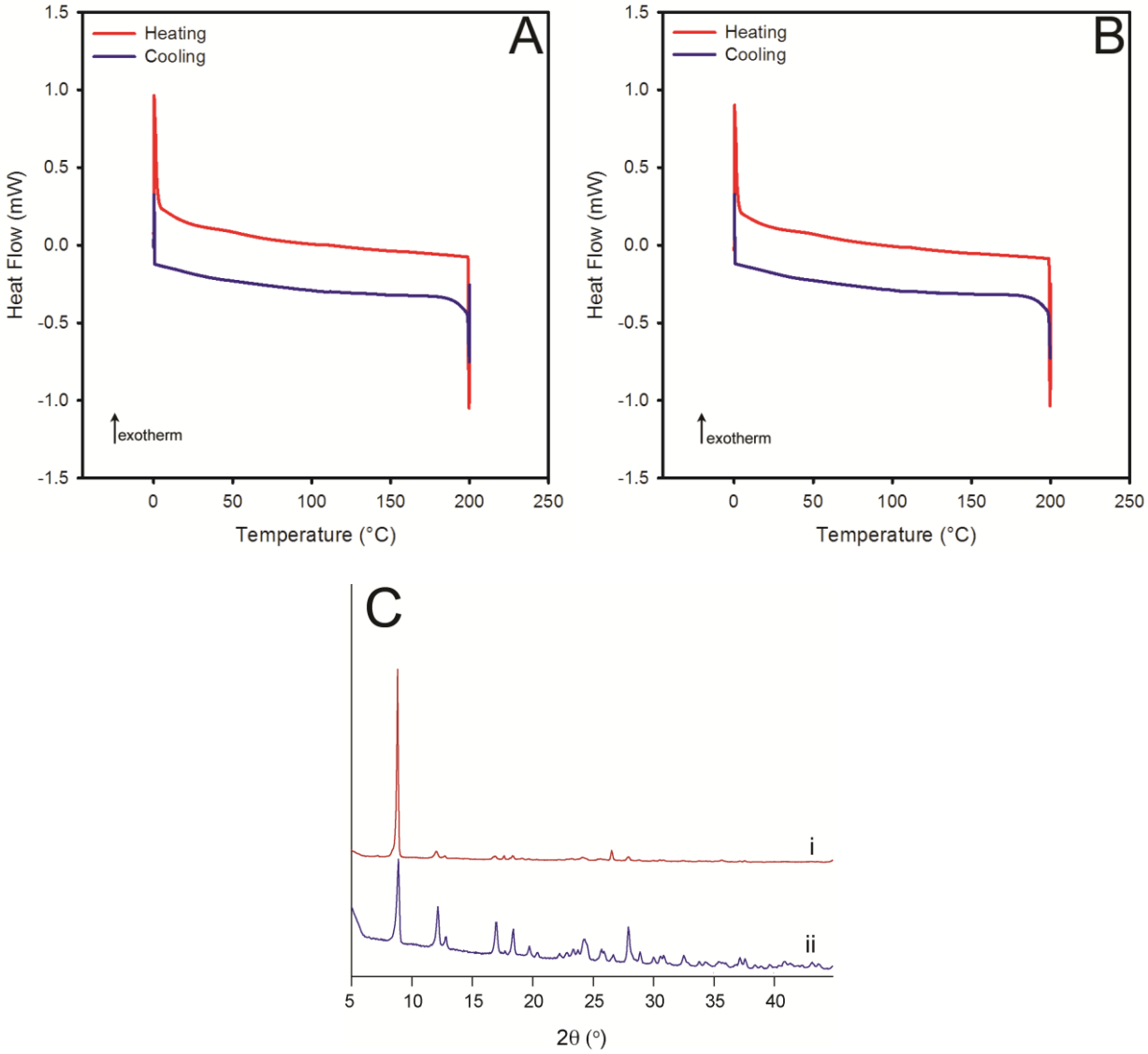

Figure S2-34. Heat/cool/heat/cool DSC scans of **1a** that has been heated in EtOH for 48 h. A) Cycle 1: Sample was heated from ~40 to 200 ºC, held at 200 ºC for 5 min, then cooled to 0 ºC, and equilibrated at 0 ºC for 5 min. B) Cycle 2: Sample was heated from 0 to 200 ºC, held at 200 ºC for 5 min, then cooled to 25 ºC. C) PXRD patterns for **1a** heated in EtOH before (i) and after (ii) DSC scans.

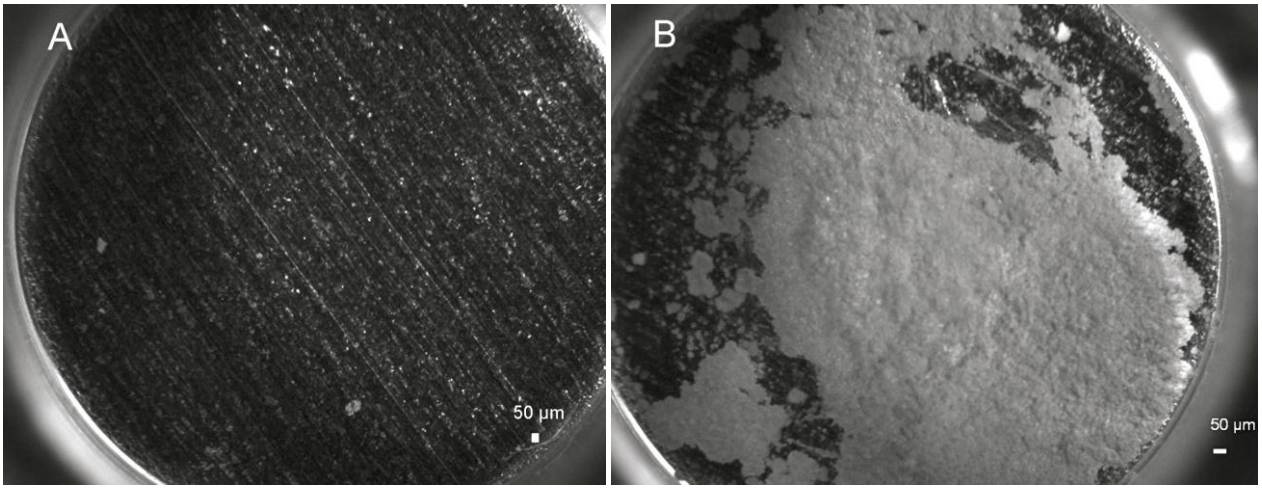

Figure S2-35. (A) Microscope images of a DSC pan before sample loading. (B) Microscope Image of the same pan after a suspension of **1a** in MeOH was added, left in air for MeOH to evaporate, then all material was removed and pan was washed with acetone.

IX. Gel Screening

i. cgc

Gel Screening and Critical Gel Concentration (cgc) Procedure **–** The cgc was determined by adding a known amount of compounds **1**–**5** (~1–10 mg) into an 8 mL vial containing 1 mL of solvent. The vial was capped, heated to dissolve the solid, and allowed to cool with approximately 20 s of sonication in a water bath (near ambient temperature). If the resulting gel was stable to inversion, then 0.1 mL of solvent was added and the procedure was repeated until the gel was no longer stable to inversion. If no gel formed initially, then additional Hg(quinoxalinone)$_2$ was added and the procedure was repeated until the solubility limit was reached.

In Situ Gelation Procedure **–** A known amount of quinoxalinone (~1-8 mg) was added to an 8 mL vial containing 0.8 mL of solvent. Then, Hg(OAc)$_2$ (~1-8 mg) was dissolved in 0.2 mL of solvent and added to the first vial. The vial was sealed and heated to dissolve, then allowed to cool with approximately 20 s of sonication in a water bath (near ambient temperature).

Table S2-1. Summary of cgcs for all gels. The solvent marked EtOH/HOAc refers to 1 mL of EtOH with 10 µL of HOAc added to increase gelator solubility.

	cgc (mM)			
Compound	**MeOH**	**EtOH**	**EtOH/HOAc**	**CF_3CH_2OH**
1a	30 ± 1	precip.	precip.	14 ± 0*
2b	precip.	precip.	3.5 ± 0.4*	precip.
2c	precip.	15 ± 0	precip.	precip.
3a	precip.	10.2 ± 0.3	5.0 ± 0.0	precip.
3b	3.5 ±0.1	3.9 ± 0.2	7.1 ± 0.3	precip.

*Note: indicated cgcs were formed by gelation with the complex.

ii. Gel Screening with Hansen Solubility Parameters

Procedure: Hansen solubility parameters were determined using HSPiP software.[7] **1a** was experimentally determined to be either soluble or insoluble in eight solvents. These solvents (soluble: EtOH, MeOH, acetone, DMSO, DMF; insoluble: hexanes, CH_2Cl_2, CCl_4) were used to generate a "sphere" of similar solvents based on Hansen Solubility Parameters. The software generated a list of 1,232 solvents, but only solvents that were a Relative Energy Difference (RED, distance from center of sphere/radius) of less than or approximately 1.0 were considered, resulting in a list of ~300 solvents. The results were narrowed down further to nine solvents based several factors, such as stability to heat, boiling point, availability, and variety. Hansen Solubility Parameters are reported in Table S2 for all solvents included in gel screening with **1a**.

A gel of **1a** formed in only one case (2,2,2-trifluoroethanol). The remaining gelators were subsequently screened for gelation in this solvent, but no others resulted in a gel. The cgc of **1a** in 2,2,2-trifluoroethanol is reported in Table S1.

Table S2-2. Summary of all solvents used in screening for gels of **1a** identified using HSPiP software. The solvents used to generate the sphere are indicated below with either (+) for those marked as soluble and (-) for those marked as insoluble. The solution parameters are listed, as well as the RED.

Solvent	δD	δP	δH	RED
2-Pentanol	15.6	6.4	13.3	0.39
2-Methoxyethanol	16.0	8.2	15.0	0.48
3-Methoxypropanol	15.6	6.3	11.6	0.48
2,2,2-Trifluoroethanol	15.4	8.3	16.4	0.49
Dimethyl formamide (+)	17.4	13.7	11.3	0.62
2-Propanol	15.8	6.1	16.4	0.62
1-Octanol	16.0	5.0	11.2	0.69
1-Propanol	16.0	6.8	17.4	0.72
Ethanol (+)	15.8	8.8	19.4	0.78
Acetone (+)	15.5	10.4	7.0	0.99
MeOH (+)	14.7	12.3	22.3	0.99
Dimethyl sulfoxide (+)	18.4	16.4	10.2	1.0
Ethyl acetate	15.8	5.3	7.2	1.05
Ethylene glycol dimethyl ether	15.4	6.3	6.0	1.13
Chloroform (-)	17.8	3.1	5.7	1.73
Hexane (-)	14.9	0.0	0.0	2.43
H_2O (-)	15.5	16.0	42.3	3.49

X. Solubility and Dissolution Parameters

Procedure for Measuring Equilibrium Solubilities – Compounds **1**–**5** (10 mg x 3 vials per compound) and ~7.5 mL of solvent (EtOH or MeOH) were each added to an 8 mL vial and heated at 45 °C for 7 d. PXRD analysis was used to identify the solid form that was present before and after heating. (Samples were prepared for PXRD by pipetting the mixture onto a microscope slide and allowing the solvent to evaporate prior to analysis.) The solvent was then evaporated from the vials by heating at 45 °C for 5 h with the caps removed. PXRD analysis was again performed to verify that the solid form remained unchanged after evaporation. New solvent (~6-7 mL of EtOH or MeOH) was added to the vials and the mixtures were equilibrated for 48 h at 25, 30, 40, and 50 °C. Aliquots (200 μL) were taken at each temperature and diluted with a known amount of solvent (~3-4 mL). The solution concentration was determined using UV-vis spectroscopy and a calibration curve (Figure S2-54 in SI). To minimize sampling error, the solubility was determined by averaging the results of three aliquots from each vial (9 aliquots total) at each temperature. van′t Hoff plots (ln(*x*) versus 1/T, where *x* is the mole fraction solubility) were employed to determine the dissolution enthalpies (ΔH_{diss}) and entropies (ΔS_{diss}) using eq 1. The error bars reported at each point on the van′t Hoff plots were calculated as the relative error ($\Delta x/x$).

$$\ln(x) = -\frac{\Delta H_{diss}}{RT} + \frac{\Delta S_{diss}}{R} \qquad (1)$$

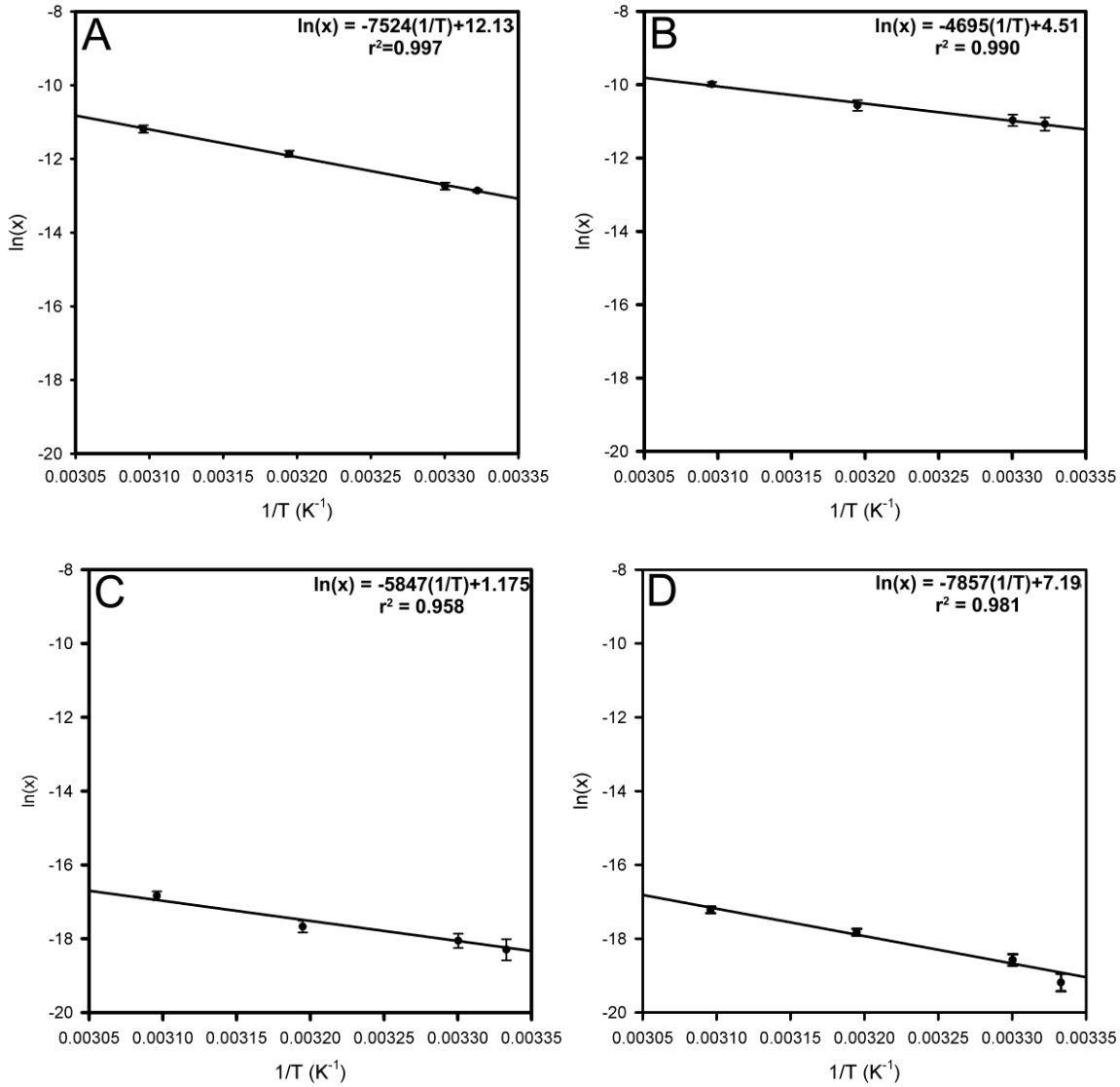

Figure S2-36. van't Hoff plots of (A) **1a**, (B) **1b**, (C) **2a**, and (D) **2b** in MeOH.

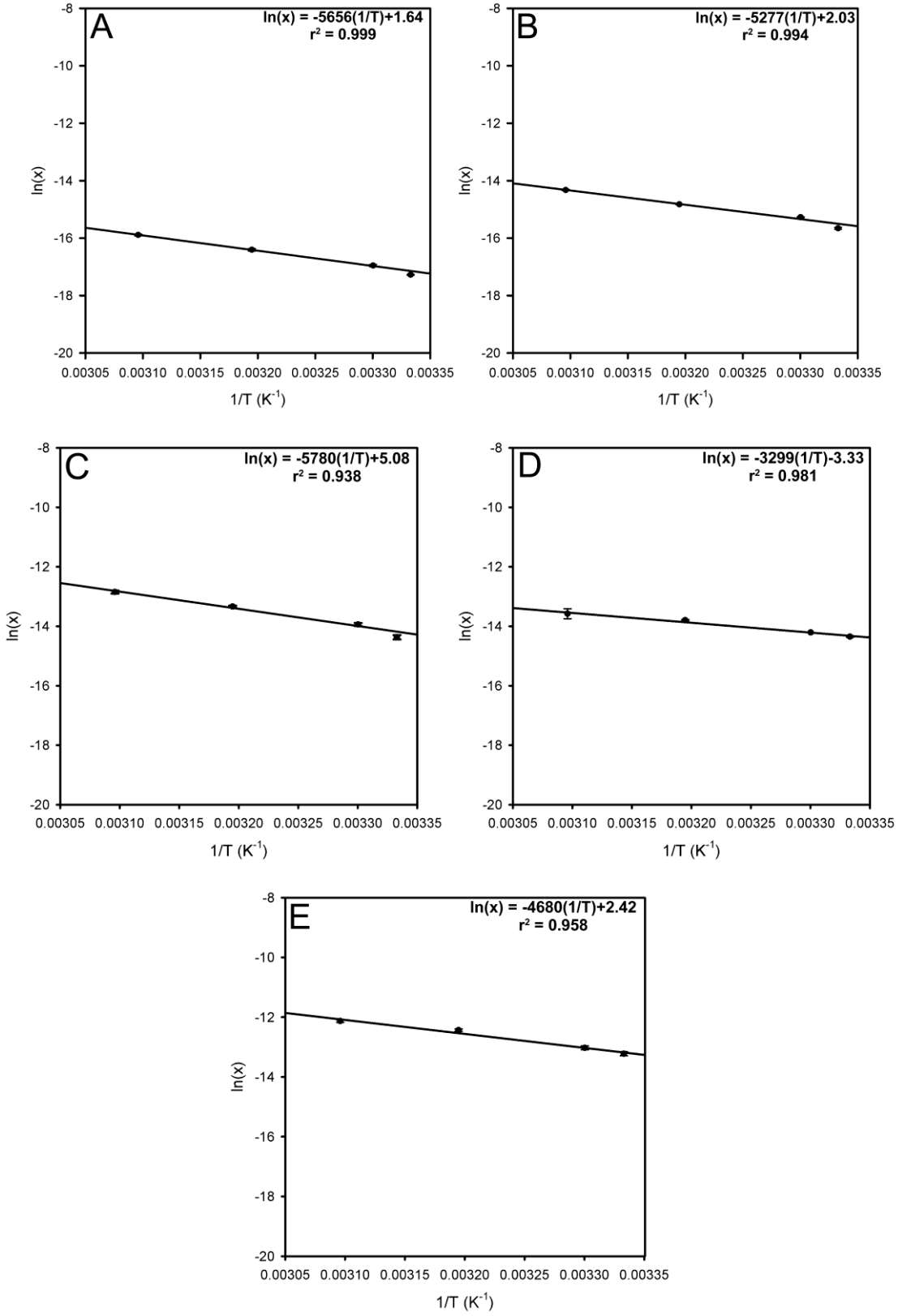

Figure S2-37. van't Hoff plots for (A) **2c**, (B) **3a**, (C) **3b**, (D) **4**, and (E) **5** in MeOH.

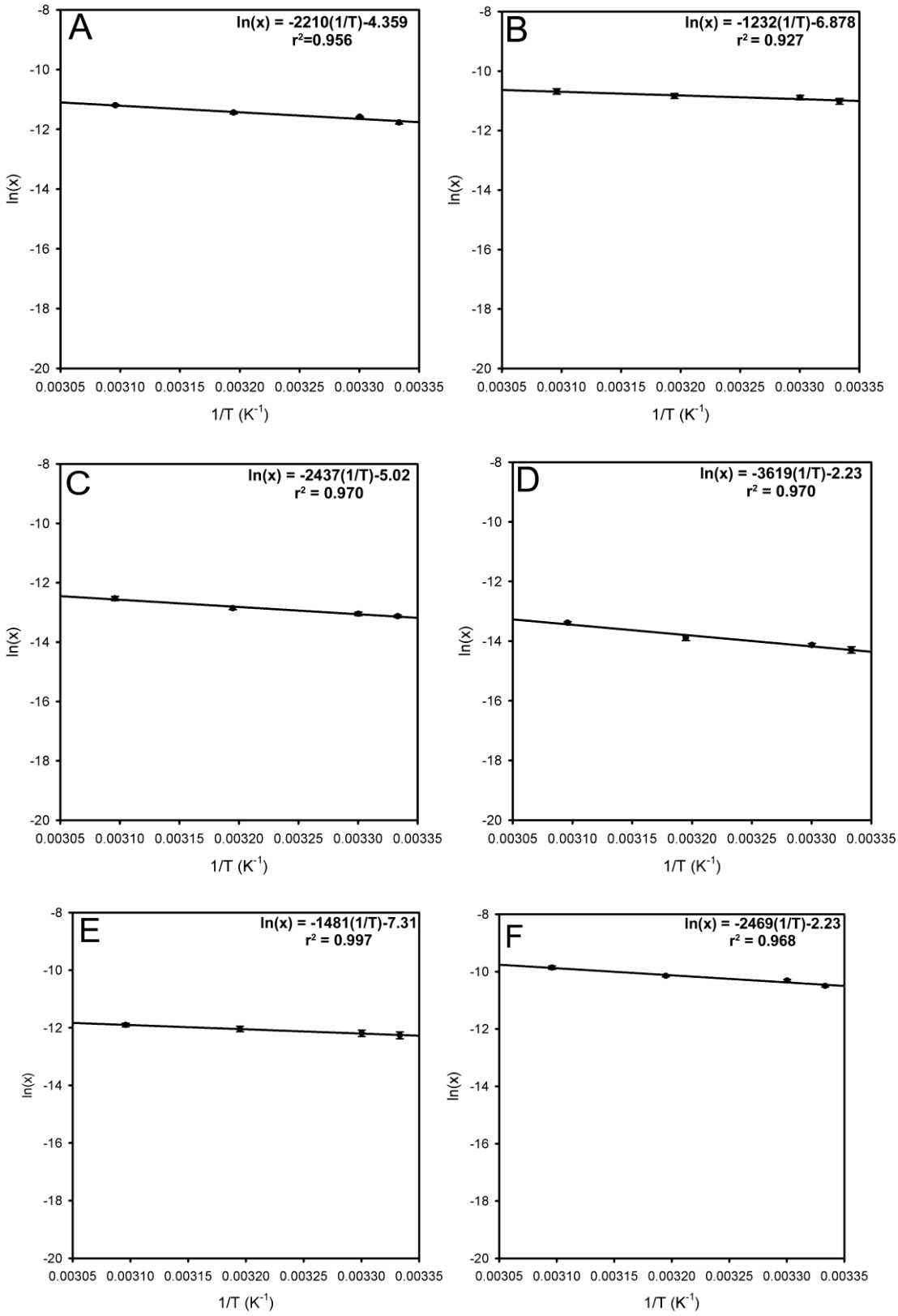

Figure S2-38. van't Hoff plots for (A) **1a**, (B) **1b**, (C) **2a**, (D) **2b**, (E) **2c**, and (F) **3a** in EtOH.

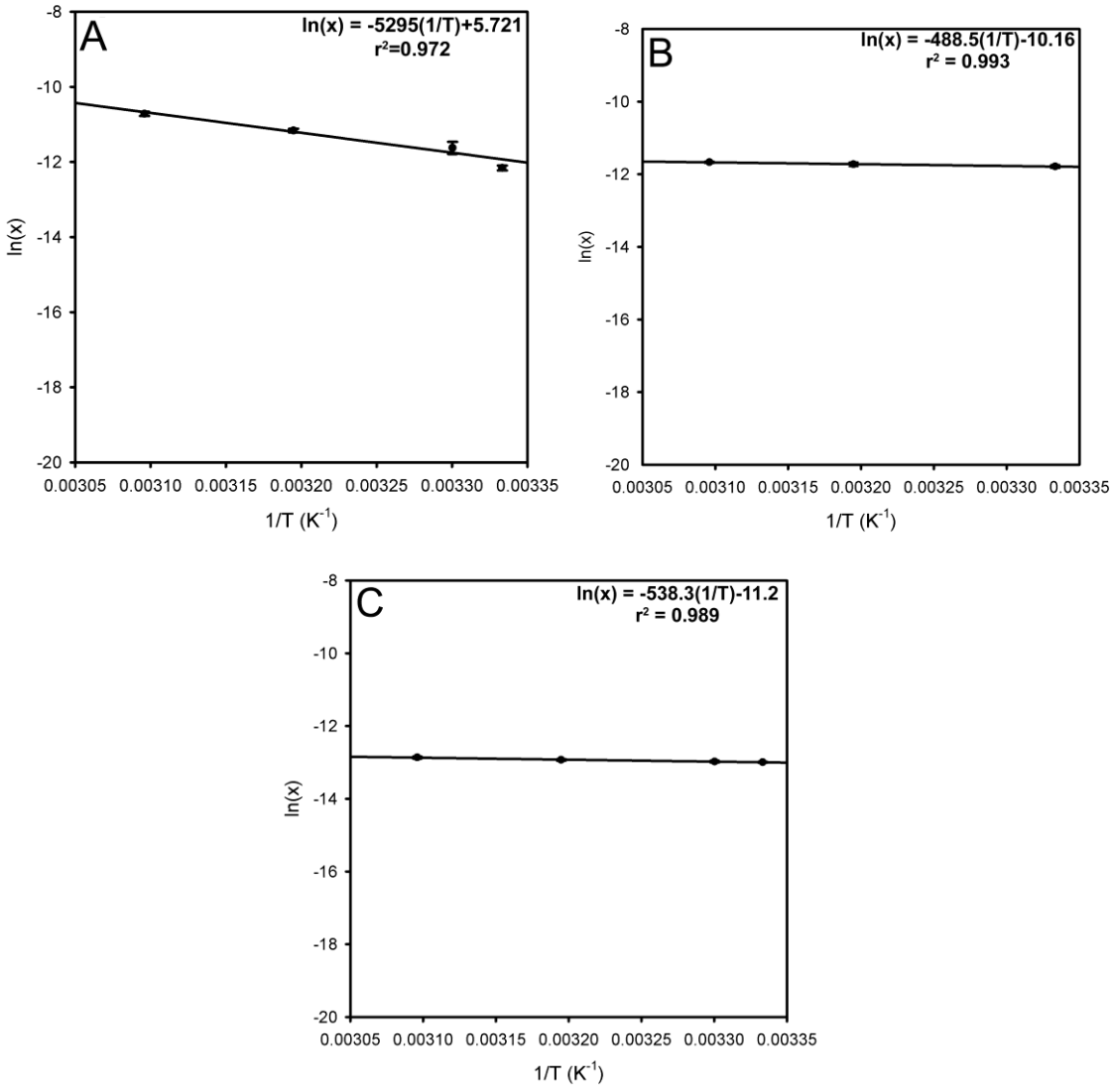

Figure S2-39. van't Hoff plots for (A) **3b**, (B) **4**, and (C) **5** in EtOH.

Table S2-3. Summary of dissolution enthalpies and entropies for complexes **1**–**5**

	Dissolution Parameters in MeOH		Dissolution Parameters in EtOH	
Compounds	**ΔH (kcal/mol)**	**ΔS (kcal/mol*K)**	**ΔH (kcal/mol)**	**ΔS (kcal/mol*K)**
1a	15.1±0.5	$2.4\pm0.2\times10^{-2}$	4.4±0.6	$-9\pm2\times10^{-3}$
1b	9.4±0.7	$9\pm2\times10^{-3}$	2.5±0.5	$-1.3\pm0.2\times10^{-2}$
2a	12±1	$2\pm5\times10^{-3}$	4.9±0.5	$-1.0\pm0.2\times10^{-2}$
2b	16±2	$1.4\pm0.7\times10^{-2}$	7.2±0.9	$-4\pm3\times10^{-3}$
2c	11±2	$3\pm2\times10^{-3}$	3.0±0.1	$-1.46\pm0.04\times10^{-2}$
3a	10±1	$4\pm4\times10^{-3}$	4.9±0.6	$-4\pm2\times10^{-3}$
3b	11.6±0.7	$1.0\pm0.2\times10^{-2}$	10±1	$1.1\pm0.4\times10^{-2}$
4	6.6±0.6	$-7\pm2\times10^{-3}$	0.98±0.08	$-2.03\pm0.03\times10^{-2}$
5	9.3±0.9	$4\pm3\times10^{-3}$	1.08±0.08	$-2.24\pm0.03\times10^{-2}$

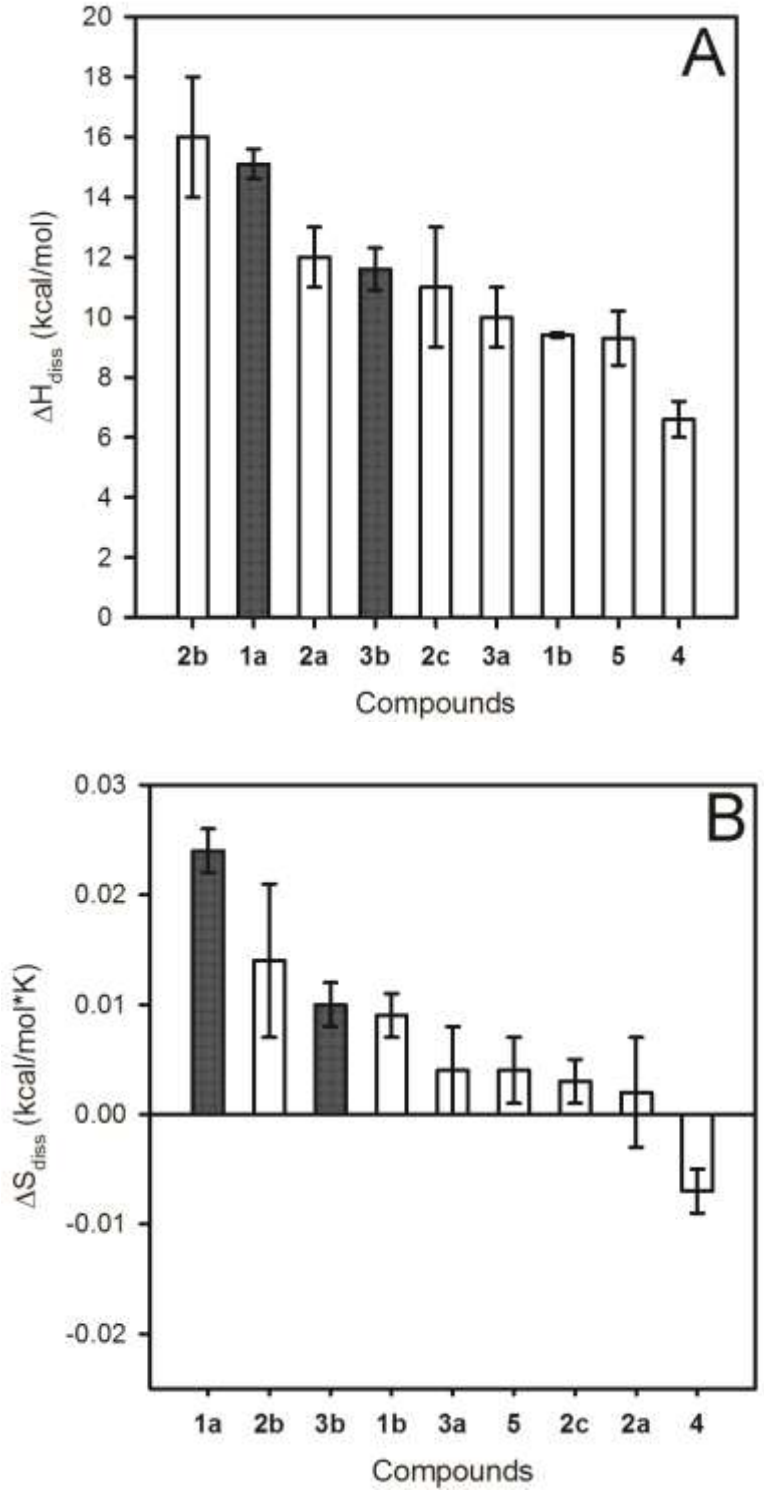

Figure S40. Plots of all compounds showing (A) ΔH_{diss} and (B) ΔS_{diss} in MeOH. Grey bars represent gelators in this solvent system, while nongelators are shown in white.

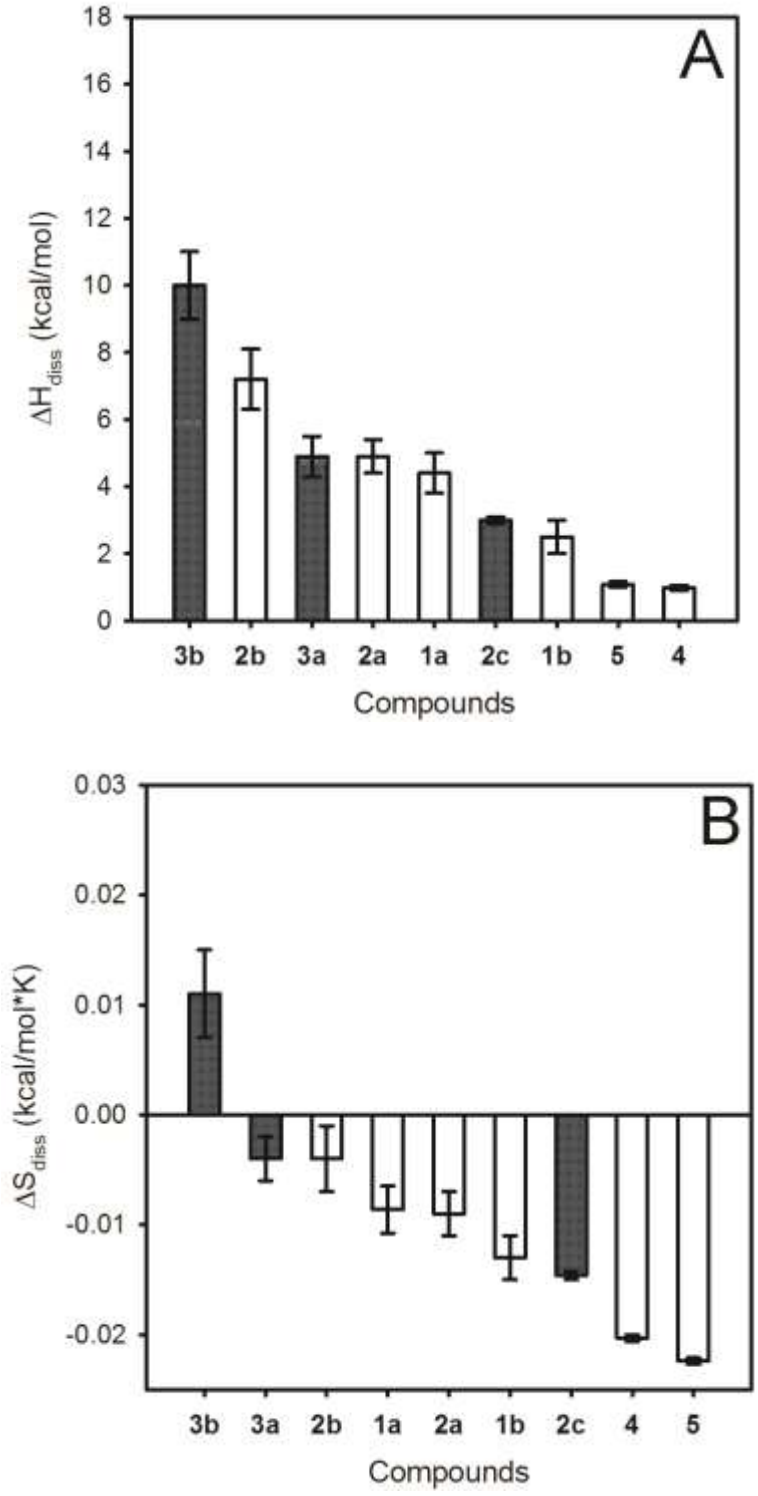

Figure S2-41. Plots of all compounds showing (A) ΔH_{diss} and (B) ΔS_{diss} in EtOH. Grey bars represent gelators in this solvent system, while nongelators are shown in white.

XI. Rheological Data

General Procedure – Rheological measurements were taken on an AR2000ex rheometer (TA Instruments) with a 25 mm serrated parallel plate. A gel (1.5x cgc) was loaded onto the plate. The gap was then fixed at 400 μm. A solvent trap was used to limit solvent evaporation. After 30 min, the sample was pre-sheared under a stress of 0.1 Pa for 30 s before conducting the frequency sweep and oscillating stress sweep experiments. All measurements were repeated an average of 5 times to verify reproducibility. The frequency sweep experiment was performed under 0.1 Pa stress with a frequency range from 0.628 to 628 rad/s (i.e., 0.1 Hz–100 Hz). The oscillating stress sweep experiment was performed at 1 Hz, with a stress range from 0.03 to 150 Pa.

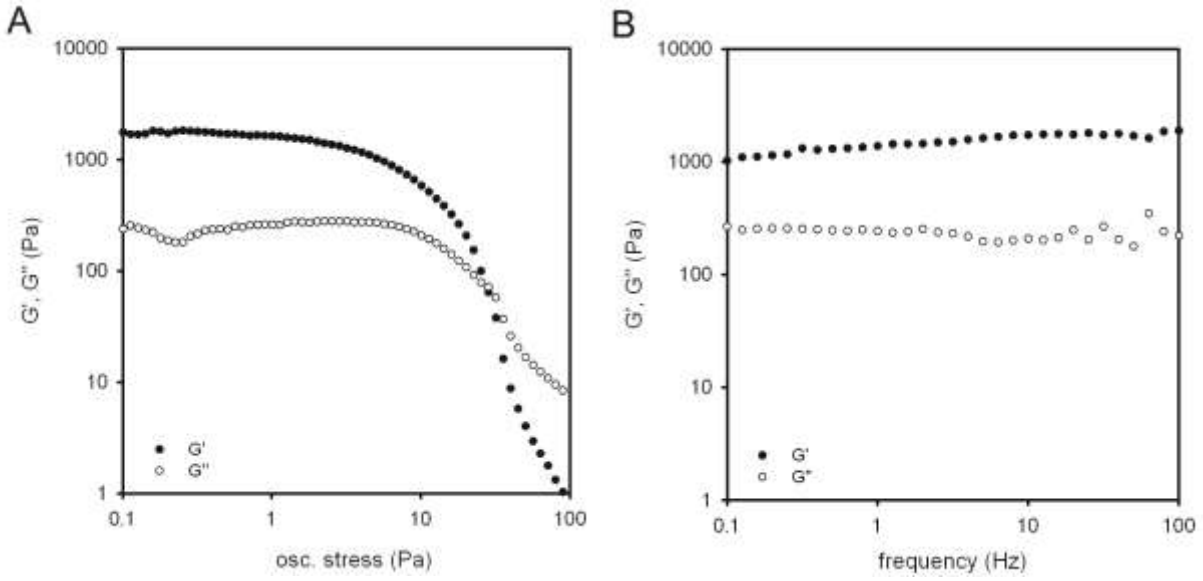

Figure S2-42. (A) Oscillating stress sweep and (B) frequency sweep of a gel of **2b** formed from the isolated complex (5.3 mM in EtOH/HOAc).

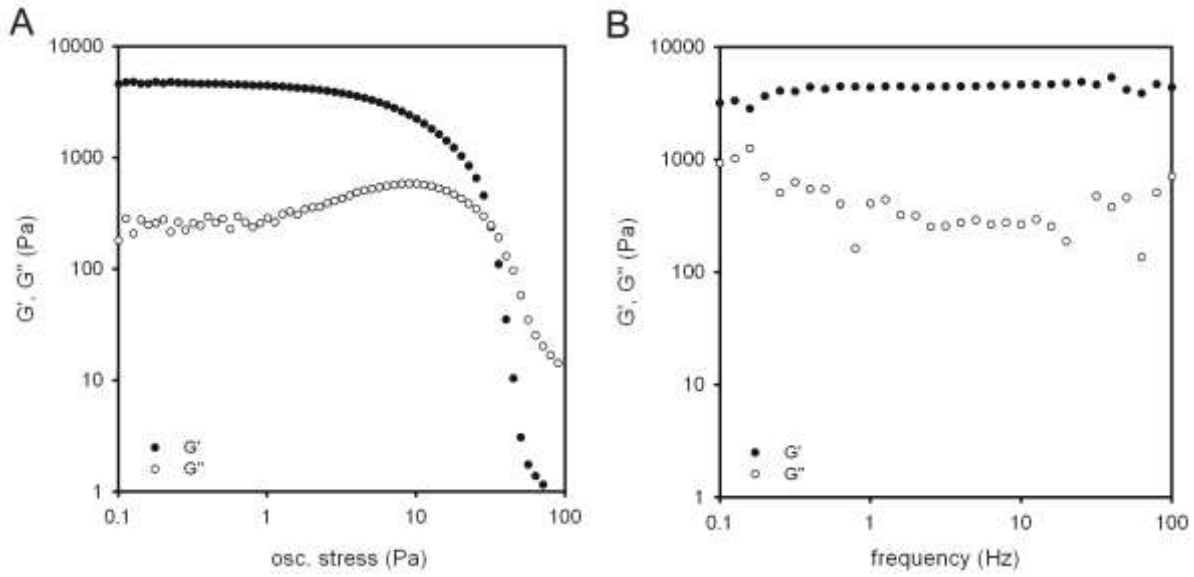

Figure S2-43. (A) Oscillating stress sweep and (B) frequency sweep of a gel of **2c** formed in situ (22.5 mM in EtOH).

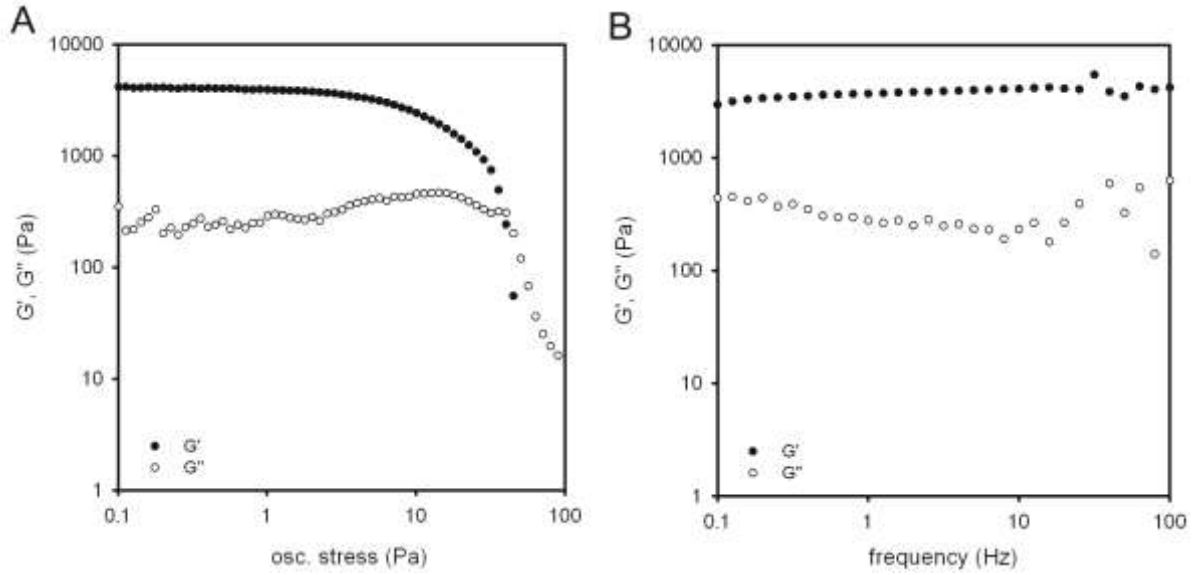

Figure S2-44. (A) Oscillating stress sweep and (B) frequency sweep of a gel of **3a** formed in situ (15 mM in EtOH).

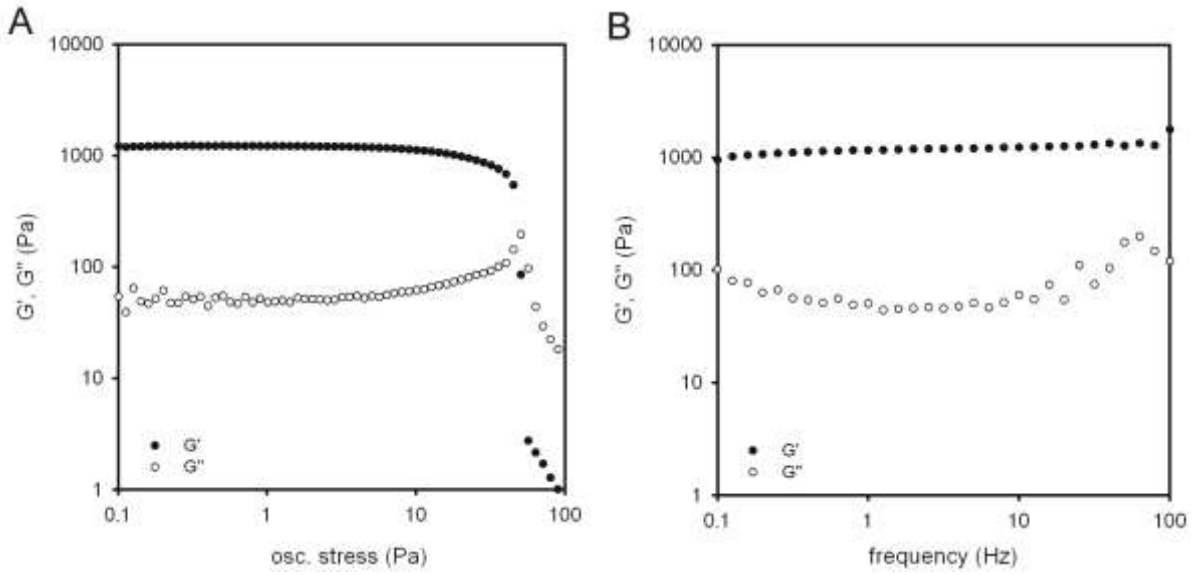

Figure S2-45. A) Oscillating stress sweep and B) frequency sweep of a gel of **3b** formed in situ (5.9 mM in EtOH).

XII. Scanning Electron Microscopy Images

General Procedure – Gels were formed via standard in situ procedure unless otherwise noticed, after which gels were heated again to dissolve, cooled with ~20 s of sonication to trigger gelation, then left untouched for 24 h to ensure full fiber formation. Wet gel samples of **1a**, **2b**, **2c**, **3a** and **3b** were mounted with copper tape onto a stainless steel SEM holder and allowed to air dry. Samples were sputter-coated with Au for 30 s to reduce charge build-up during imaging. All gels were imaged using the high vacuum mode on a Hitachi S3200N SEM using a 15-kV accelerating voltage. The images were digitally recorded and processed using Adobe Photoshop.

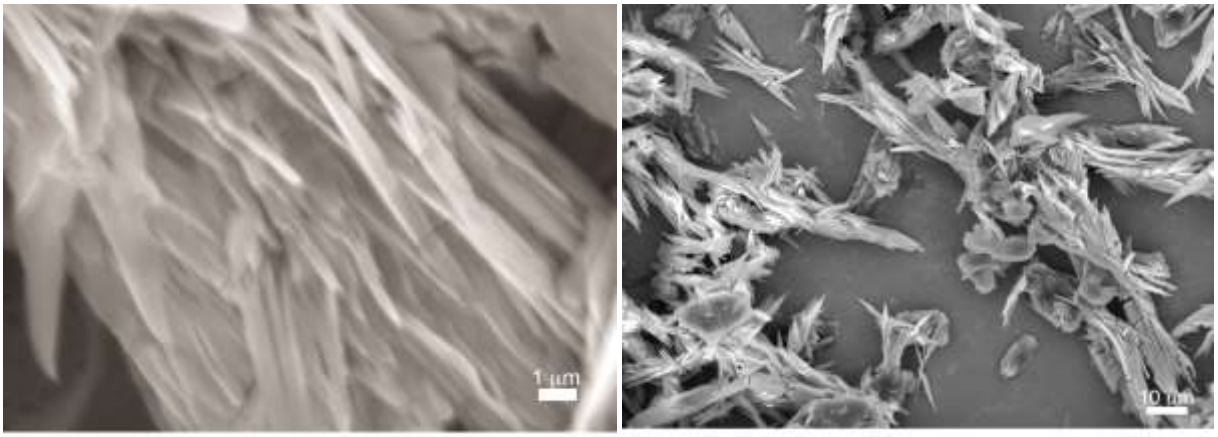

Figure S2-46. SEM images of a gel at cgc of **1a** formed in situ in 1 mL of MeOH/H_2O (80/20 v/v).

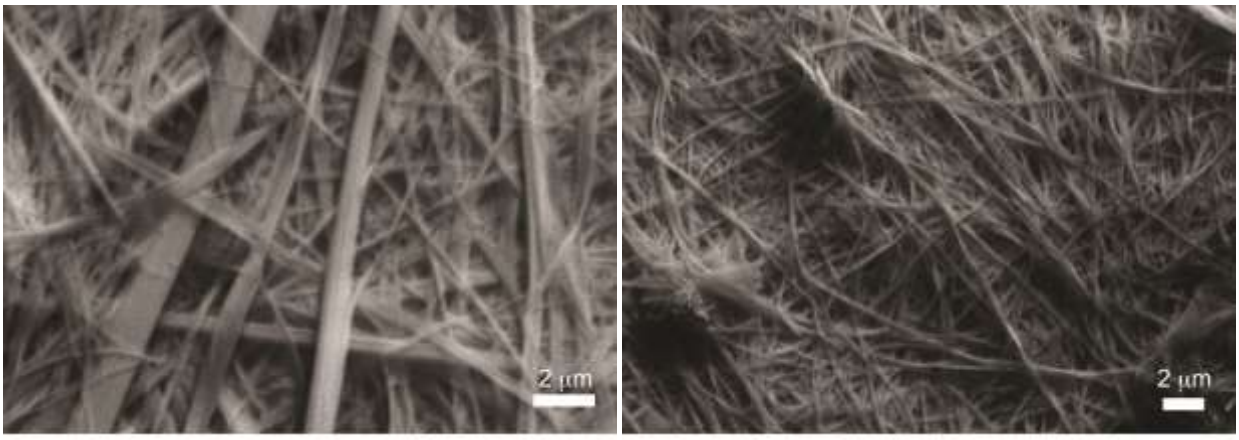

Figure S2-47. SEM images of a gel at cgc of **2b** formed from the isolated gelator in 1 mL of EtOH/HOAc.

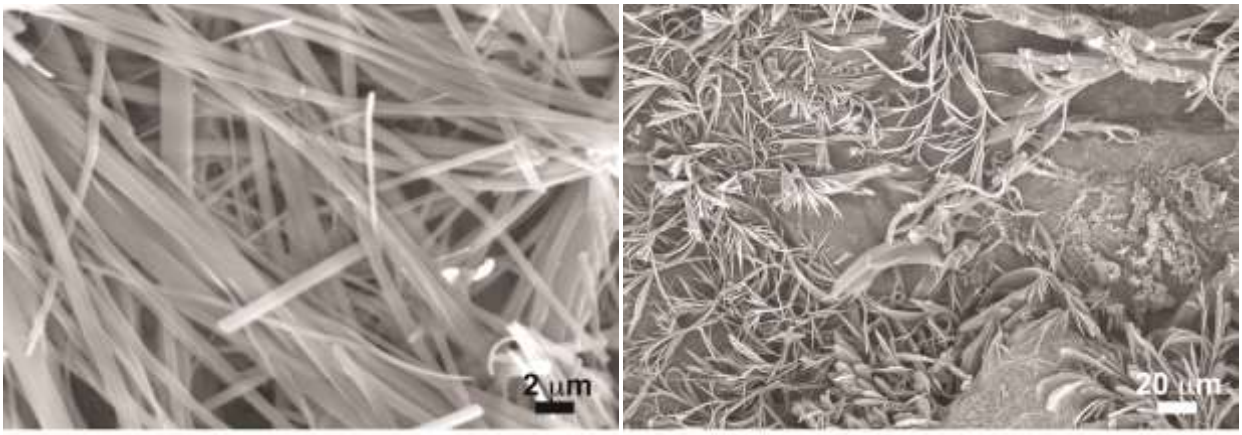

Figure S2-48. SEM images of a gel of **2c** at cgc formed in situ in 1 mL of EtOH.

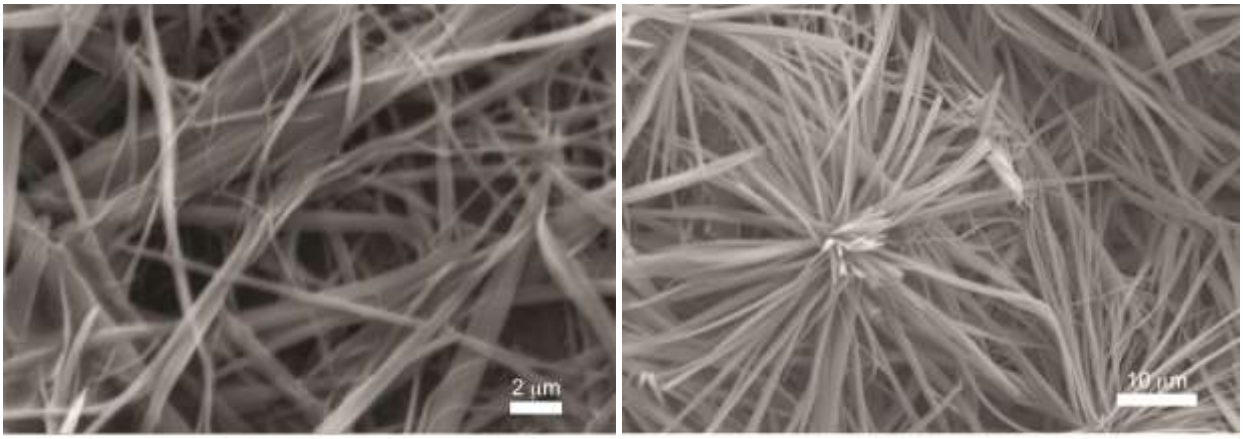

Figure S2-49. SEM images of a gel of **3a** at cgc formed in situ in 1 mL EtOH/HOAc.

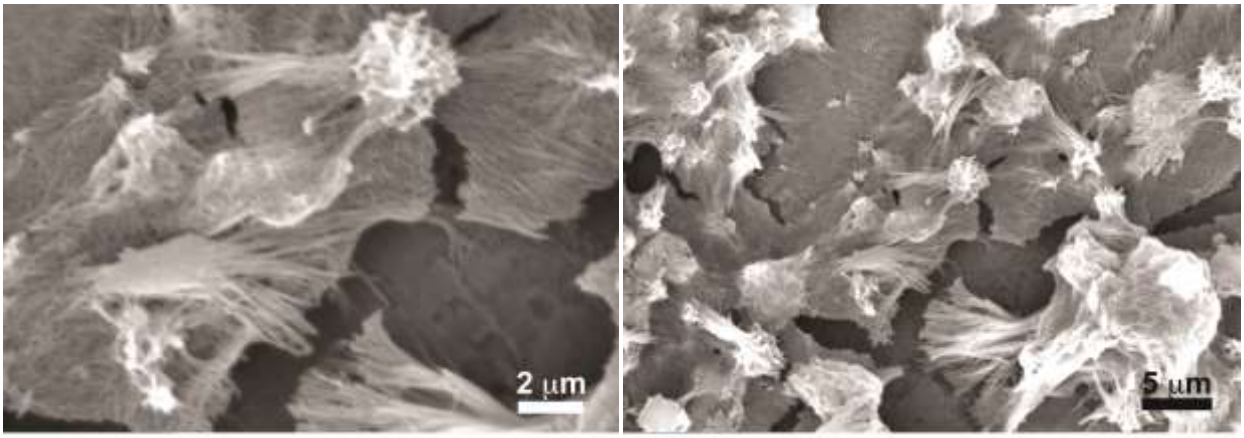

Figure S2-50. SEM images of a gel of **3b** at cgc formed in situ in 1 mL EtOH.

XIII. Gel Experiments

i. Cation Selectivity

Procedure: Samples were prepared by the in situ gelation procedure. A 1:2 metal to ligand ratio was calculated at the cgc of each gelator. The metal acetate salt is dissolved in 0.2 mL of H_2O (except for **2c** which used 0.2 mL of EtOH), and the quinoxalinone was dissolved in 0.8 mL of organic solvent (MeOH for **1a**, EtOH/HOAc for **2b**, and EtOH for **2c**, **3a**, and **3b**.)

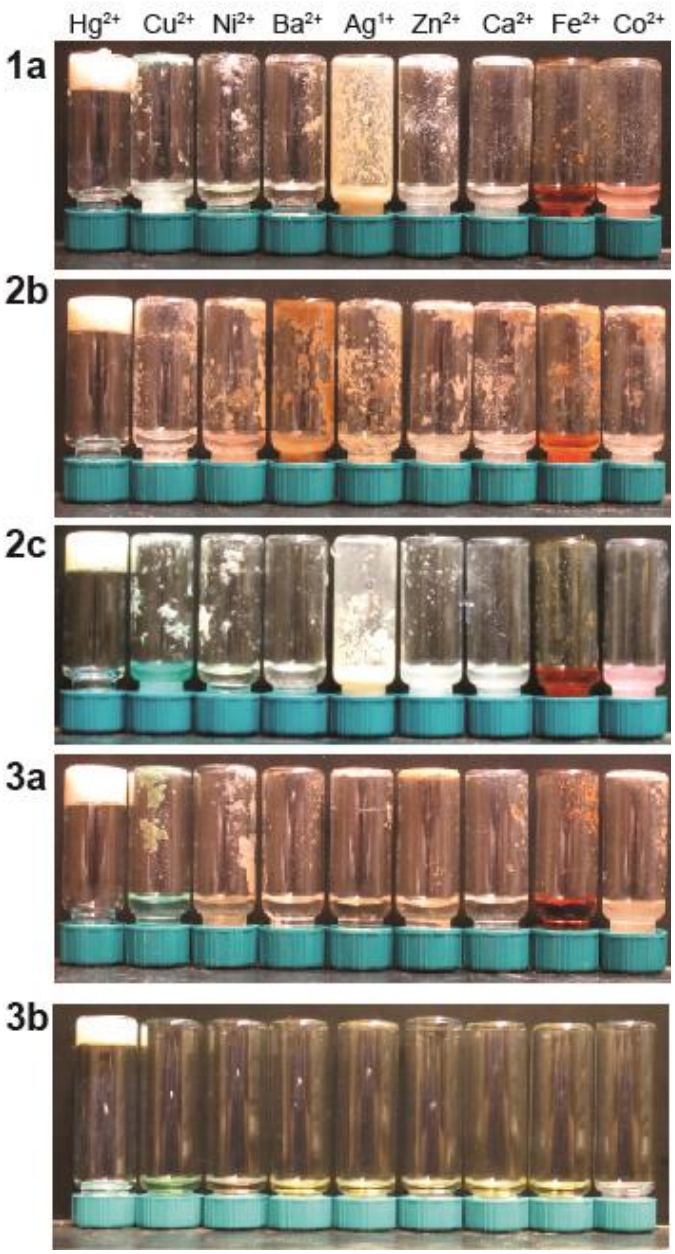

Figure S2-51. Selectivity tests showing the results of adding solutions of an array of metal acetate salts.

ii. Chloride Tolerance Experiment

Procedure: Gels were formed via the in situ gelation method at the cgc of each gelator. Gels of **2c**, **3a**, and **3b** were formed in EtOH, while **1a** was formed in MeOH and **2b** was formed in EtOH/HOAc. The chloride source, NBu_4Cl was dissolved in 10 µL of H_2O and added to the gel. To the control gel, 10 µL of H_2O were added. Pictures were taken at least 10 min after addition of NBu_4Cl.

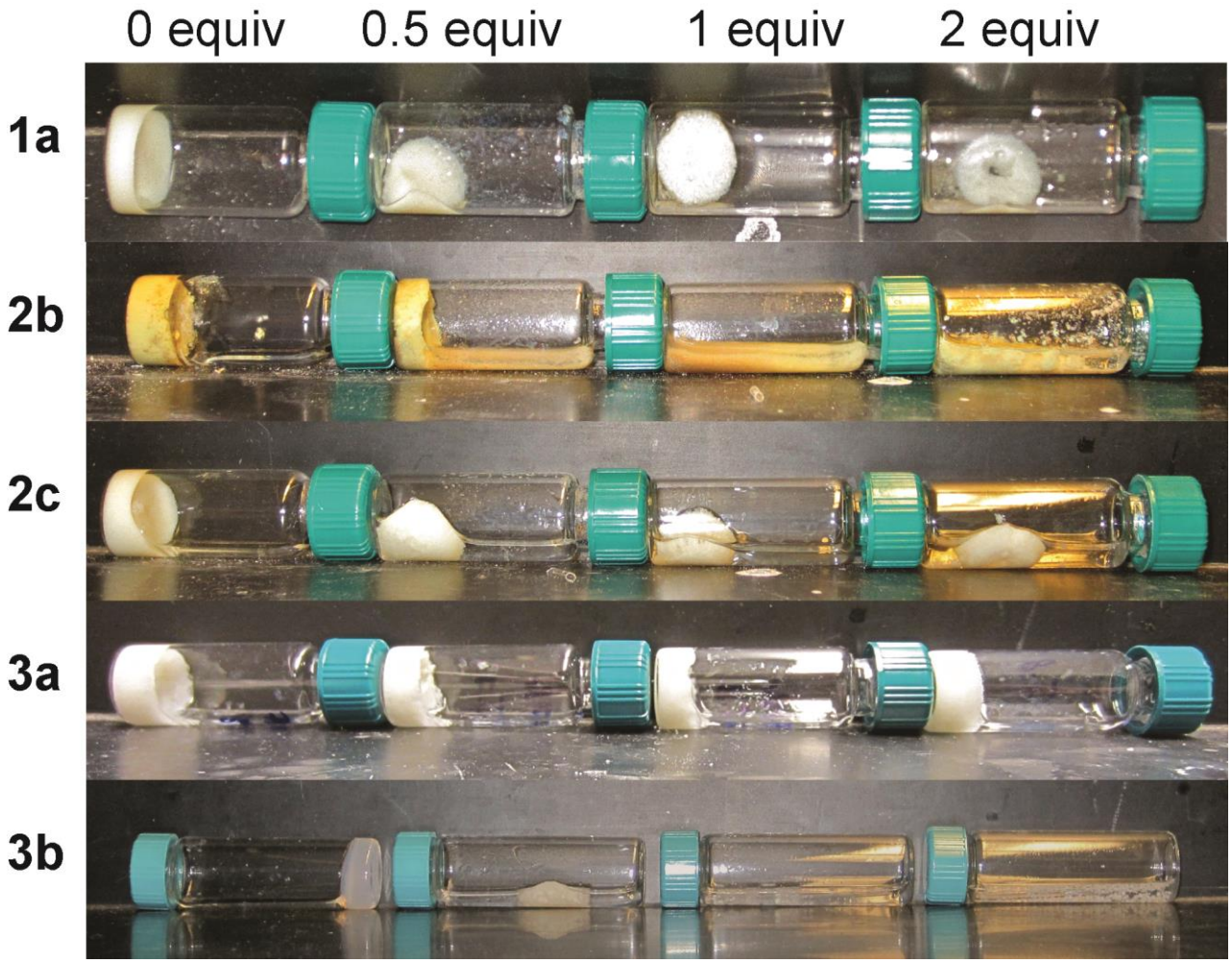

Figure S2-52. Tolerance tests showing the results of the addition of 0, 0.5, 1, and 2 equiv of NH_4Cl as a chloride source.

iv. Gelation in Environmental Conditions

General Procedure: H_2O from three different sources were spiked with enough $HgOAc_2$ to trigger in situ gelation. Gels were formed via the standard in situ procedure, but instead of DI H_2O, $HgOAc_2$ was dissolved in H_2O taken from commonly encountered sources, specifically bottled, tap, and river H_2O. Additionally, controls were run side by side in which no $Hg(OAc)_2$ was added. The solvent conditions were 80/20 (v/v) solvent/ H_2O where solvent was MeOH for **1a**, and EtOH/HOAc for **3a**.

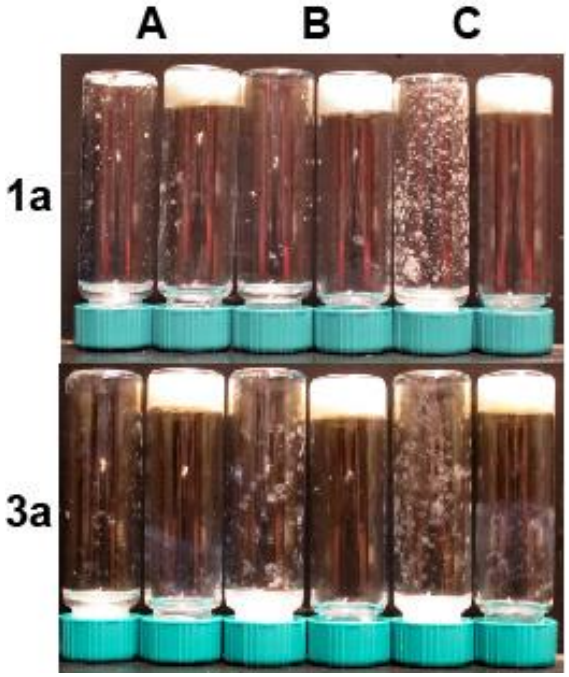

Figure S2-53. Gels and control experiments formed in 80/20 (v/v) of solvent and H_2O where the water was sourced from A) bottled spring H_2O,[8] B) tap H_2O, and C) H_2O from the Huron River in Ann Arbor, MI.

Table S2-4. Data for the in situ gel formation for **3a** with three different water sources. Controls were performed in identical conditions without additional $Hg(OAc)_2$ but are not included in the data below.

Water Source	$Hg(OAc)_2$ (mmol)	S5 (mmol)	3a (mmol)	3a (mM)
Tap	0.006 ± 0.000	0.011 ± 0.001	0.005 ± 0.000	5.5 ± 0.5
River	0.006 ± 0.000	0.011 ± 0.001	0.005 ± 0.001	5.4 ± 0.5
Bottle	0.007 ± 0.000	0.012 ± 0.001	0.006 ± 0.000	5.9 ± 0.3

Table S2-5. Data for the in situ gel formation for **1a** with three different water sources. Controls were performed in identical conditions without additional $Hg(OAc)_2$ but are not included in the data below.

Water Source	$Hg(OAc)_2$ (mmol)	2(1H)-quinoxalinone (mmol)	1a (mmol)	1a (mM)
Tap	0.036 ± 0.002	0.063 ± 0.003	0.032 ± 0.001	32 ± 1
River	0.034 ± 0.003	0.067 ± 0.004	0.034 ± 0.002	34 ± 2
Bottle	0.037 ± 0.000	0.062 ± 0.003	0.031 ± 0.002	31 ± 1

XIV. Hg^{2+} Remediation

i. Inductively-Coupled Plasma Optical Emission Spectroscopy

General Procedure – Inductively coupled plasma-optical emission spectroscopy (ICP-OES) measurements were taken on a Perkin-Elmer Optima 2000 DV. The detection limit for Hg^{2+} was approximately 10 ppb and was analyzed with a wavelength of 194.167 nm. Yttrium was used as an internal standard and detected with a wavelength of 371.029 nm.

Calibration Curve Procedure – A calibration curve was constructed using a blank and three mercury standards, 0.1 ppm, 0.5 ppm, and 1.0 ppm. All standards contained 1 ppm commercial yttrium internal standard and 1% v/v nitric acid/H_2O. The concentration of Hg^{2+} was analyzed using a wavelength of 194.167 nm.

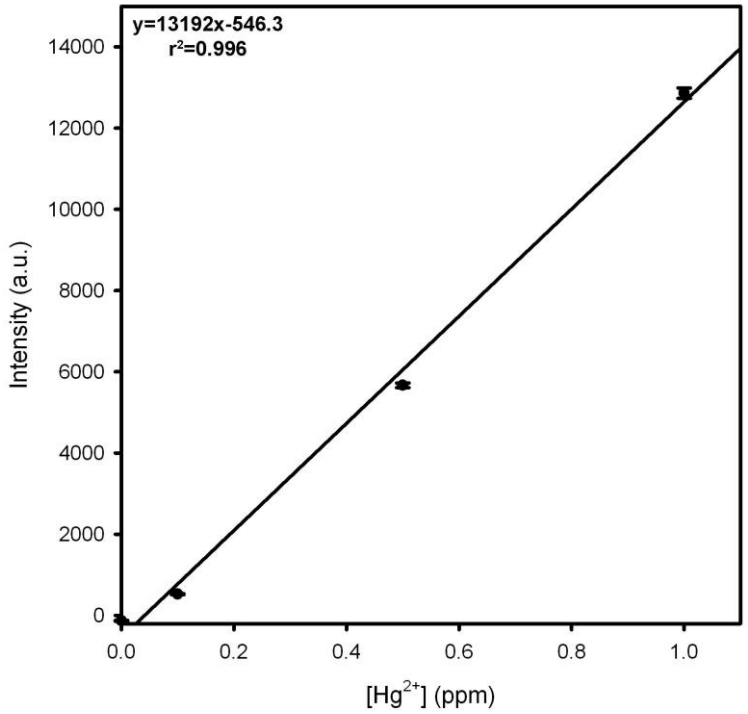

Figure S2-54. Calibration curve for Hg^{2+} concentration for ICP-OES analysis.

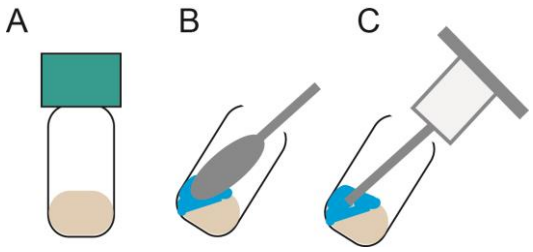

Figure S2-55. Cartoon of the procedure for the removal of solvent from gels of **1a**, **2c**, **3a**, and **3b**. (A) A gel was formed via the in situ method. (B) A spatula was used to gently compress the fibers to release entrapped solvent. (C) Released solvent was removed using a syringe.

Representative Procedure for Hg^{2+} Remediation – A gel of **1a** was prepared by mixing quinoxalin-2(1H)-one (9.4 mg, 0.064 mmol) and $Hg(OAc)_2$ (9.6 mg, 0.030 mmol) in $MeOH/H_2O$ (1 mL, 70/30 v/v). A spatula was used to gently compress the gel and release the entrapped solvent. An aliquot (~20 µL) was taken and the solvent was removed in vacuo. Then, 2.8 mL HNO_3/H_2O (5/95 v/v) and a yttrium standard (0.140 µL of a 100 ppm stock solution) were added to the vial. The solutions were diluted to 14 mL with deionized H_2O. Inductively coupled plasma-optical emission spectroscopy (ICP-OES) measurements were taken on a Perkin-Elmer Optima 2000 DV. The detection limit for Hg^{2+} was approximately 10 ppb and was analyzed with a wavelength of 194.167 nm. Yttrium was used as an internal standard and detected with a wavelength of 371.029 nm. To minimize sampling error, the experiment was repeated three times for each gel and each sample was analyzed by ICP-OES in triplicate.

Table S2-6. Summary of data for ICP-OES analysis. The notation, $[Hg^{2+}]_d$, is the detected concentration of Hg^{2+} by the instrument, and $[Hg^{2+}]_a$ is the concentration of Hg^{2+} calculated for the entire sample.

	Quinox. mass (mg)	$Hg(OAc)_2$ mass (mg)	Initial $[Hg^{2+}]$ (ppm)	$[Hg^{2+}]_d$ (ppm)	Extracted volume (mL)	$[Hg^{2+}]_a$ (ppm)	Hg^{2+} Remediated (%)
1a	9.4	9.7	6100	3.03±0.08	0.19	23	96.2%
	9.4	9.7	6100	0.38±0.01	0.14	40	99.3%
	9.3	9.7	6100	1.29±0.08	0.19	97	98.4%
					Average	**53**	**98.0%**
3a	5.1	3.4	2200	0.34±0.01	0.37	13	99.4%
	5.1	3.4	2200	0.45±0.00	0.27	24	98.9%
	5.1	3.4	2200	0.14±0.00	0.24	8.3	99.6%
					Average	**15**	**99.3%**
2c	3.9	3.6	2300	0.13±0.00	0.25	7.4	99.7%
	3.9	3.6	2300	0.25±0.01	0.20	18	99.2%
	3.9	3.6	2300	0.21±0.01	0.19	16	99.3%
					Average	**14**	**99.4%**
3b	2.8	2.3	1400	0.17±0.00	0.31	7.5	99.5%
	2.7	2.3	1400	0.28±0.01	0.23	17	98.8%
	2.9	2.3	1400	0.40±0.02	0.32	17	98.8%
					Average	**14**	**99.0%**

XV. Thermogravimetric Analysis.

Sample Preperation Procedure – Heated forms identified by PXRD (Figures S2-24–32 on pages S2-32–36) for compounds 1a, 2b, 2c, and 3a were prepared by heating the bulk forms in methanol and ethanol. The majority of solvent was removed by evaporation at 45 degrees, but a small amount (~0.1 mL) was left to prevent desolvation. Samples (1-20 mg) were loaded on to a platinum TGA pan and held under a nitrogen purge until dry, which was indicated by stabilization of the sample weight.

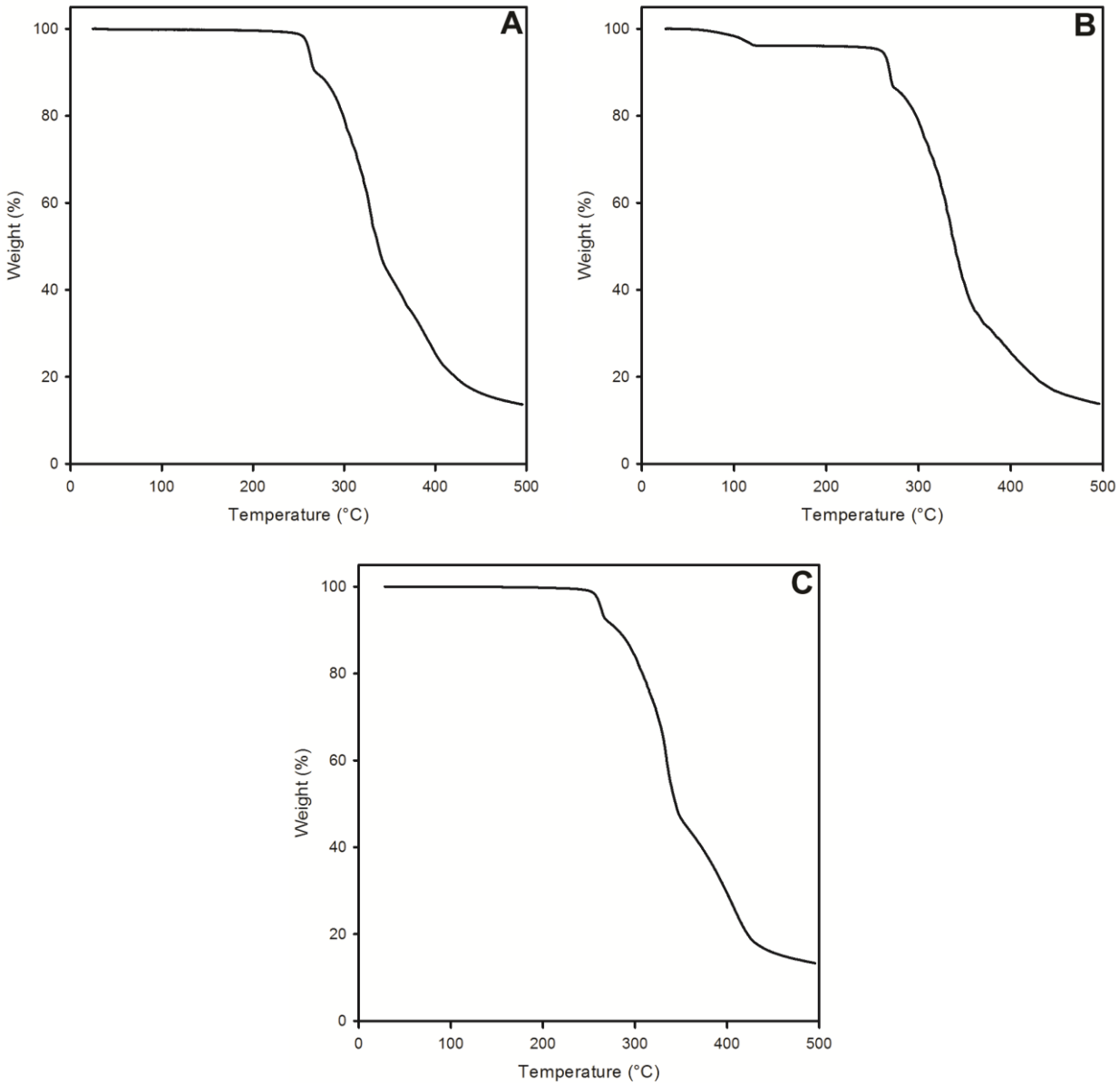

Figure S2-56. Thermogravimetric analysis (TGA) of (A) the bulk form of **1a**, (B) the heated form of **1a** in MeOH, and (C) the heated form of **1a** in EtOH.

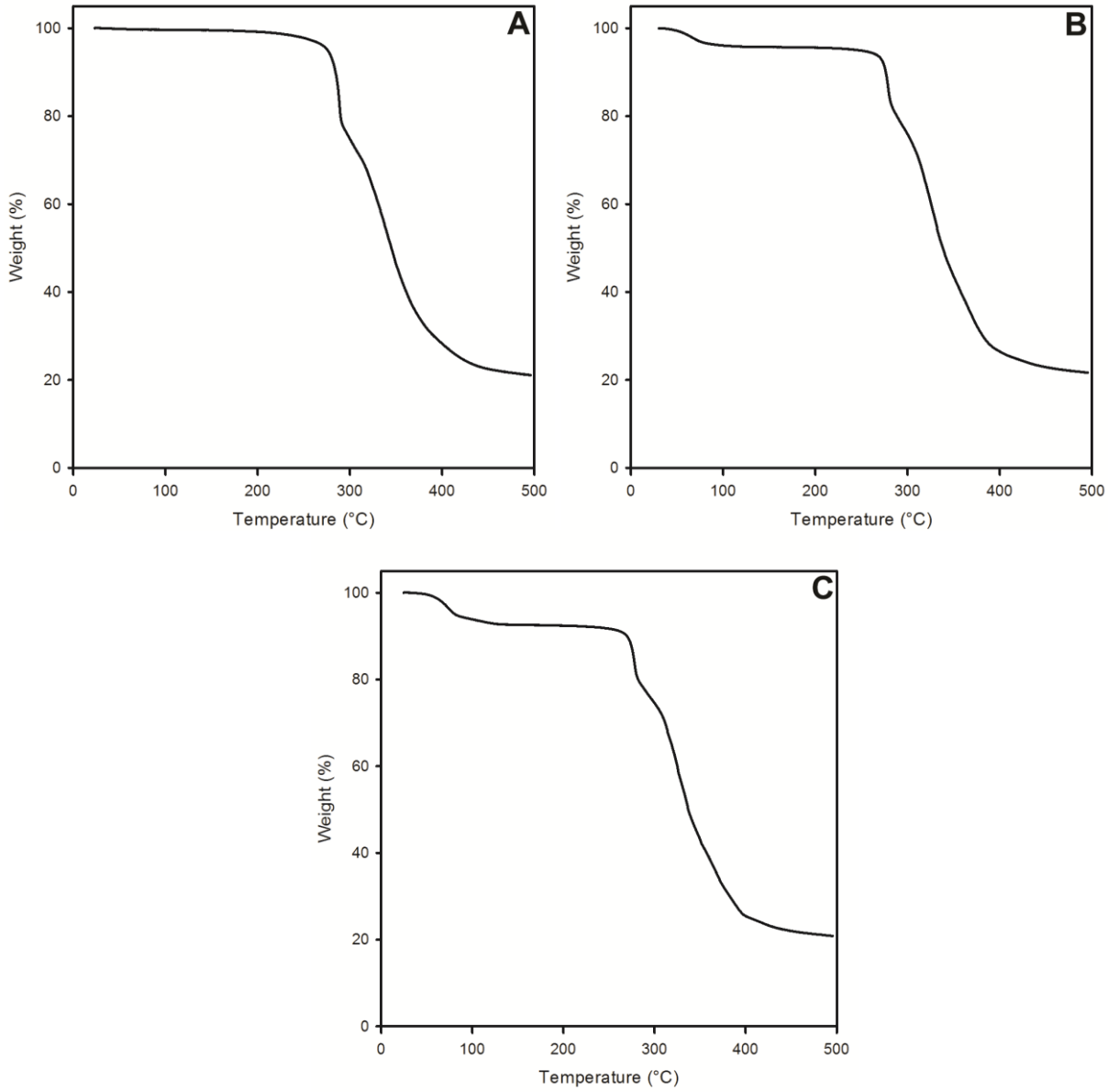

Figure S2-57. TGA data for (A) the bulk form of **2b**, (B) the heated form of **2b** in MeOH, and (C) the heated form of **2b** in EtOH.

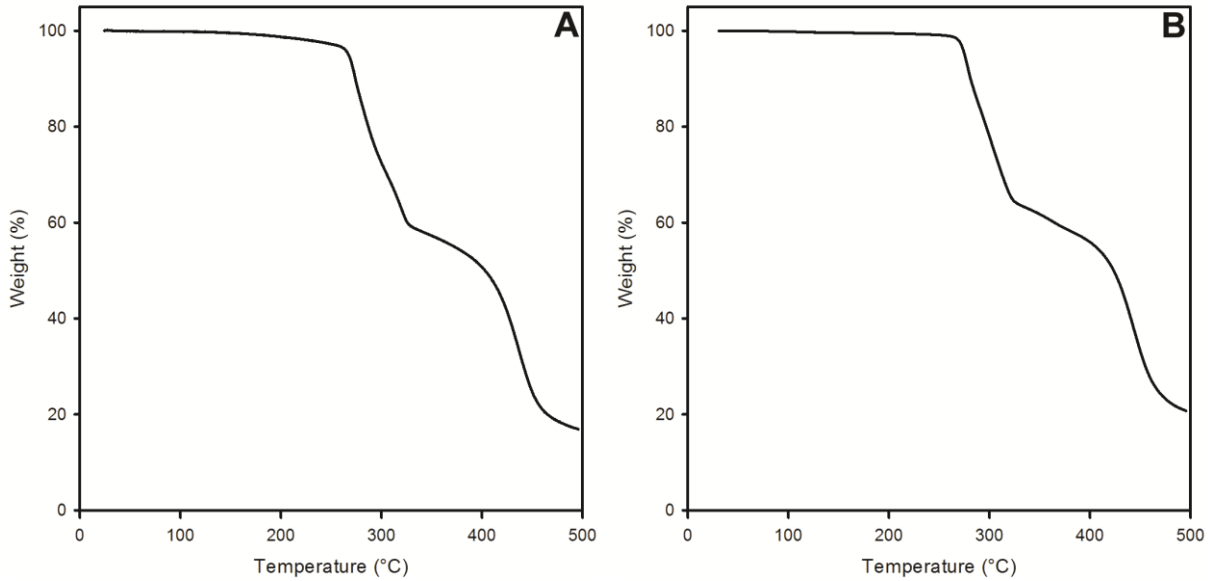

Figure S2-58. TGA data for (A) the bulk form of **2c** and (B) the heated form of **2c** in MeOH.

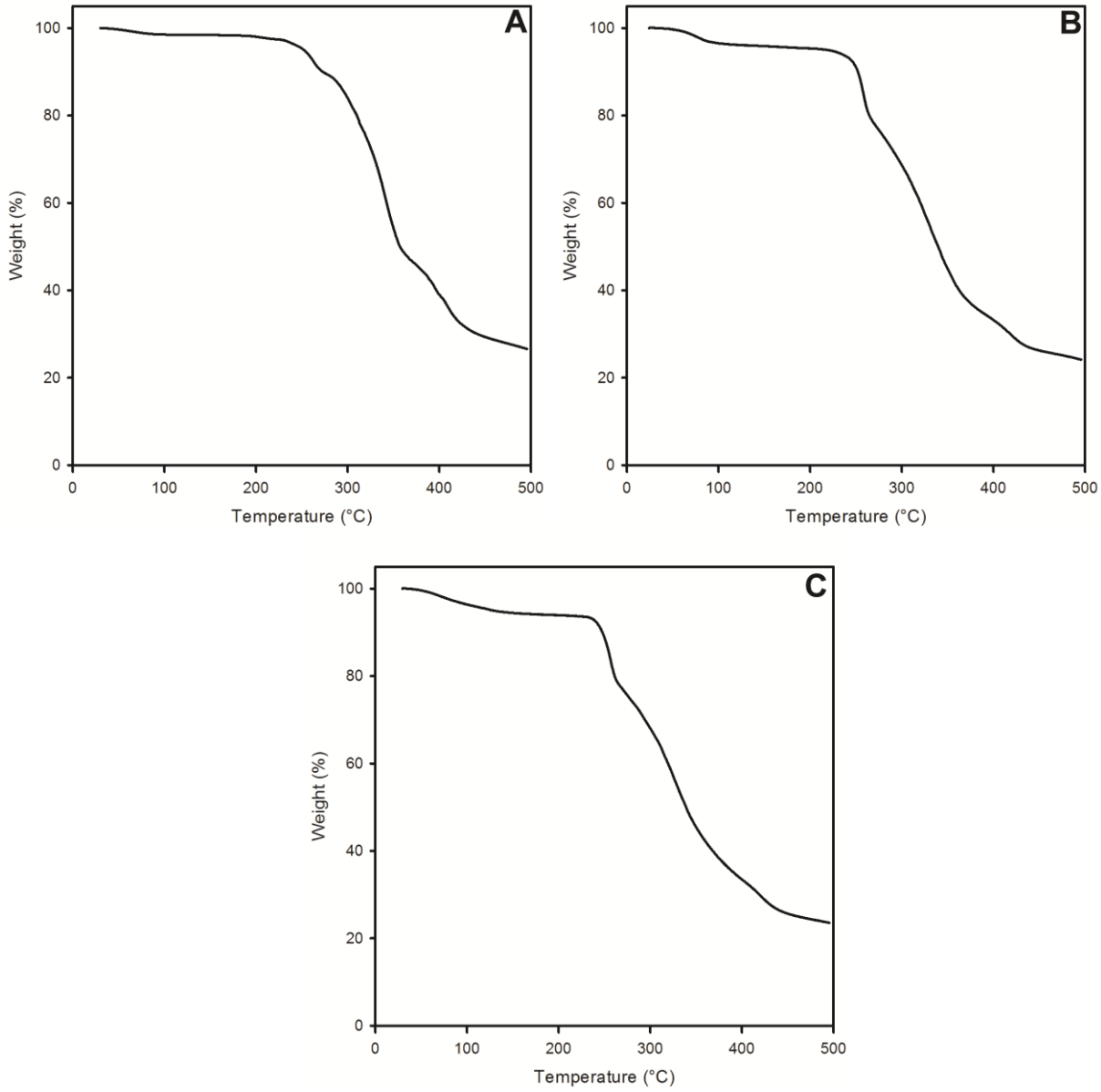

Figure S2-59. TGA data for (A) the bulk form of **3a**, (B) the heated form of **3a** in MeOH, and (C) the heated form of **3a** in EtOH.

References

[1]Lumma, W. C. Jr.; Hartman, R. D.; Saari, W. S.; Engelhardt, E. L.; Lotti, V. J; Stone, C. A. *J. Med. Chem*. **1981**, *24*, 93–101.

[2]Saari, W. S.; Lumma, W. C. Jr. *J. Labelled Compd. Radiopharm.* **1978***, 14*, 349−353.

[3]King, K.N.; McNeil, A. J. *Chem. Commun.* **2010**, *46*, 3511–3513.

[4]Goodgame, D. M. L.; Hill, S. P. W.; Williams, D. J. *Polyhedron,* **1992**, *11*, 1507−1512.

[5]CrystalClear Expert 2.0 r12, Rigaku Americas and Rigaku Corporation (2011), Rigaku Americas, 9009, TX, USA 77381-5209, Rigaku Tokyo, 196-8666, Japan.

[6]Sheldrick, G.M. SHELXTL, v. 2008/4; Bruker Analytical X-ray, Madison, WI, 2008.

[7]Abbott, S.; Yamamoto, H.; Hanson, C. M. Hanson Solubility Parameters in Practice – HSPiP. For reference, see www.hanson-solubility.com.

[8]Arbor Spring Water, Ann Arbor, MI http://www.arborspringswater.com/.

Appendix 3.

Supporting Information for

Chapter 4. A strategy to analyze intermolecular interactions and predict new gelators using morphology prediction.

Kelsey K. Carter, Sarah J. Cox, and Anne J. McNeil

Department of Chemistry and Macromolecular Science and Engineering Program
University of Michigan, 930 North University Avenue, Ann Arbor, Michigan 48109-1055

Contents

I. Materials 145
II. General Procedures 145
III. Synthetic Procedures 146
IV. ^{1}H and ^{13}C NMR Spectroscopic Data 148
V. Materials Studio Calculations 154
A. Procedure for Cambridge Structural Database Search 154
B. Procedure for Morphology Prediction 158
C. Geometry Optimization Data 167
D. Morphology Prediction Data 174
E. Top 5% Aspect Ratio Data 181
F. Input Methods Data 185
VI. Rheological Data 188
VII. Scanning Electron Microscopy Images 190

I. Materials

Column chromatography was performed using a Biotage Isolera One flash purification system. Thin layer chromatography was performed on Merck TLC plates pre-coated with silica gel 60 F254. All reagent grade materials and solvents were purchased from Sigma Aldrich, Acros Organics, or TCI. Amines were subjected to vacuum distillation to purify and all other compounds were used without further purification unless otherwise noted. Compounds **1a–d** and **2a–b** were prepared from modified literature procedures.[1–3]Throughout this document, H_2O refers to deionized H_2O, unless otherwise noted.

II. General Procedures

^1H and ^{13}C NMR Spectroscopy – ^1H and ^{13}C NMR spectra for all compounds were acquired in DMSO-d_6 on a Varian vnmr 700 operating at 700 and 176 MHz, a Varian Inova 500 operating at 500 and 126 MHz or a Varian MR500 spectrometer operating at 400 and 100 MHz. The chemical shift data are reported in units of δ (ppm) relative to tetramethylsilane and referenced by residual protic DMSO. An asterisk was used to indicate residual H_2O in all spectra while double bars are used to indicate peaks that have been truncated. The abbreviations s, d, t, dd, td, and m were used to signify singlet, doublet, triplet, doublet of doublet, triplet of doublet and multiplet respectively.

High Resolution Mass Spectrometry – HRMS data were obtained on a Micromass AutoSpec Ultima Magnetic Sector mass spectrometer via electron impact ionization on a desorption probe.

Cambridge Structural Database (CSD) – All crystal structures were obtained through a search of the CSD and previously reported in the literature. Each crystal structure can be found through the six-letter tag (e.g., NAYNUW). CIF files representing crystal structures were used without alteration unless otherwise noted. Structures used can be found in Table S3-1.

Materials Studio Calculations – All calculations were performed with Materials Studio 6.0 by Accelrys Software Inc.[4]

III. Synthetic Procedures

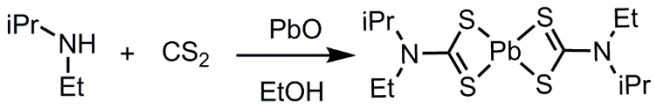

1a

1a. *N*-isopropyl-*N*-ethyl-amine (0.16 mL, 2.5 mmol) and carbon disulfide (0.23 mL, 2.5 mmol) were added to a round-bottom flask and dissolved in EtOH (50 mL). Lead oxide (0.27 g, 1.2 mmol) was added. The flask was sealed and stirred under N_2 for 12 h, forming a white precipitate after a few hours. Then, CH_2Cl_2 (100 mL) was added to dissolve the precipitate and the solution was filtered to remove unreacted PbO. The filtrate was collected and the solvent was removed under vacuum, yielding a white solid (0.17 g, 39%). HRMS (EI): Calcd for $C_{12}H_{24}N_2S_4Pb$, 532.0589. Found, 532.0602.

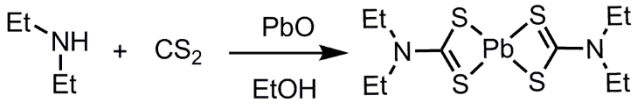

1b

1b. *N*,*N*-Diethylamine (0.13 mL, 2.5 mmol) and carbon disulfide (0.23 mL, 2.5 mmol) were added to a round-bottom flask and dissolved in EtOH (30 mL). Lead oxide (0.27 g, 1.2 mmol) was added. The flask was sealed and stirred under N_2 for 12 h, forming a precipitate after a few hours. Then, CH_2Cl_2 (50 mL) was added to dissolve the precipitate and the solution was filtered to remove unreacted PbO. The filtrate was collected and the solvent was removed under vacuum, yielding a white solid (0.43 g, 45%). HRMS (EI): Calcd for $C_{10}H_{20}N_2S_4Pb$ 504.0276. Found, 504.0284.

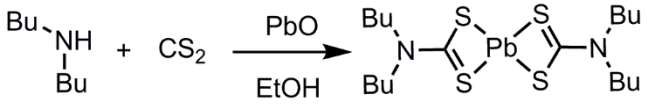

1c

1c. *N*,*N*-Dibutylamine (0.24 mL, 2.4 mmol) and carbon disulfide (0.23 mL, 2.5 mmol) were added to a round-bottom flask and dissolved in EtOH (50 mL). Lead oxide (0.27 g, 1.2 mmol) was added. The flask was sealed and stirred under N_2 for 12 h, forming a white precipitate after a few hours. Then, CH_2Cl_2 (100 mL) was added to dissolve the precipitate and the solution was filtered to remove unreacted PbO. The filtrate was collected and the solvent was removed under vacuum, yielding a white solid (0.41 g, 54%). HRMS (EI): Calcd for $C_{18}H_{36}N_2S_4Pb$ 161.1528. Found, 161.1528.

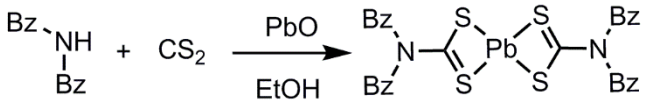

1d

1d. *N*,*N*-Dibenzylamine (0.5 mL, 2.5 mmol) and carbon disulfide (0.23 mL, 2.5 mmol) were added to a round-bottom flask and dissolved in EtOH (20 mL). Lead oxide (0.27 g, 1.2 mmol) was added. The flask was sealed and stirred under N_2 for 12 h, forming a white precipitate after a few hours. Then, CH_2Cl_2 (100 mL) was added to dissolve the precipitate and the solution was filtered to remove unreacted PbO. The filtrate was collected and the solvent was removed under vacuum, yielding a white solid (0.58 g, 63%). HRMS (EI): Calcd for $C_{30}H_{28}N_2S_4Pb$, 752.0902. Found, 752.0910.

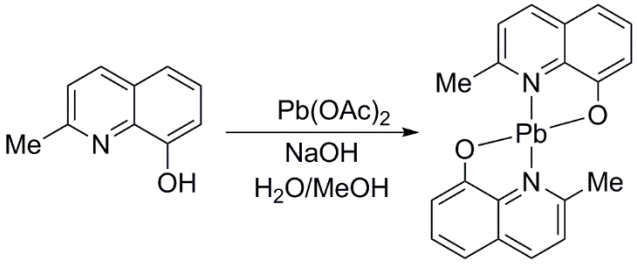

2a

2a. A round-bottom flask equipped with a stir bar was charged with H_2O (20 mL), MeOH (20 mL), and NaOH (0.21 g, 5.2 mmol). 8-Hydroxyquinaldine (0.093 g, 0.59 mmol) was added and stirred to dissolve. Lead acetate (0.12 g, 0.31 mmol) was added and stirred for 20 min. A yellow precipitate formed and the solution was filtered, and then washed with H_2O (~20 mL), yielding 0.13 g of a yellow solid (80% yield). MS (EI): Calcd for $C_{20}H_{18}N_2O_2Pb$, 524.1. Found, 524.0.

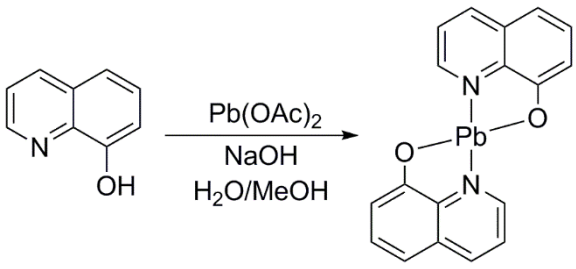

2b

2b. A round-bottom flask equipped with a stir bar was charged with H_2O (20 mL), MeOH (20 mL), and NaOH (0.13 g, 3.3 mmol). 8-hydroxyquinoline (0.20 g, 1.3 mmol) was added and stirred to dissolve. Lead acetate (0.27 g, 0.71 mmol) was added and stirred for 20 min. A yellow precipitate formed and the solution was filtered, and then washed with H_2O (~20 mL), yielding 0.32 g of a yellow solid (94% yield). HRMS (EI): Calcd for $C_{18}H_{12}N_2O_2Pb$, 496.9665. Found, 496.0663.

IV. ^{1}H and ^{13}C NMR Spectroscopic Data

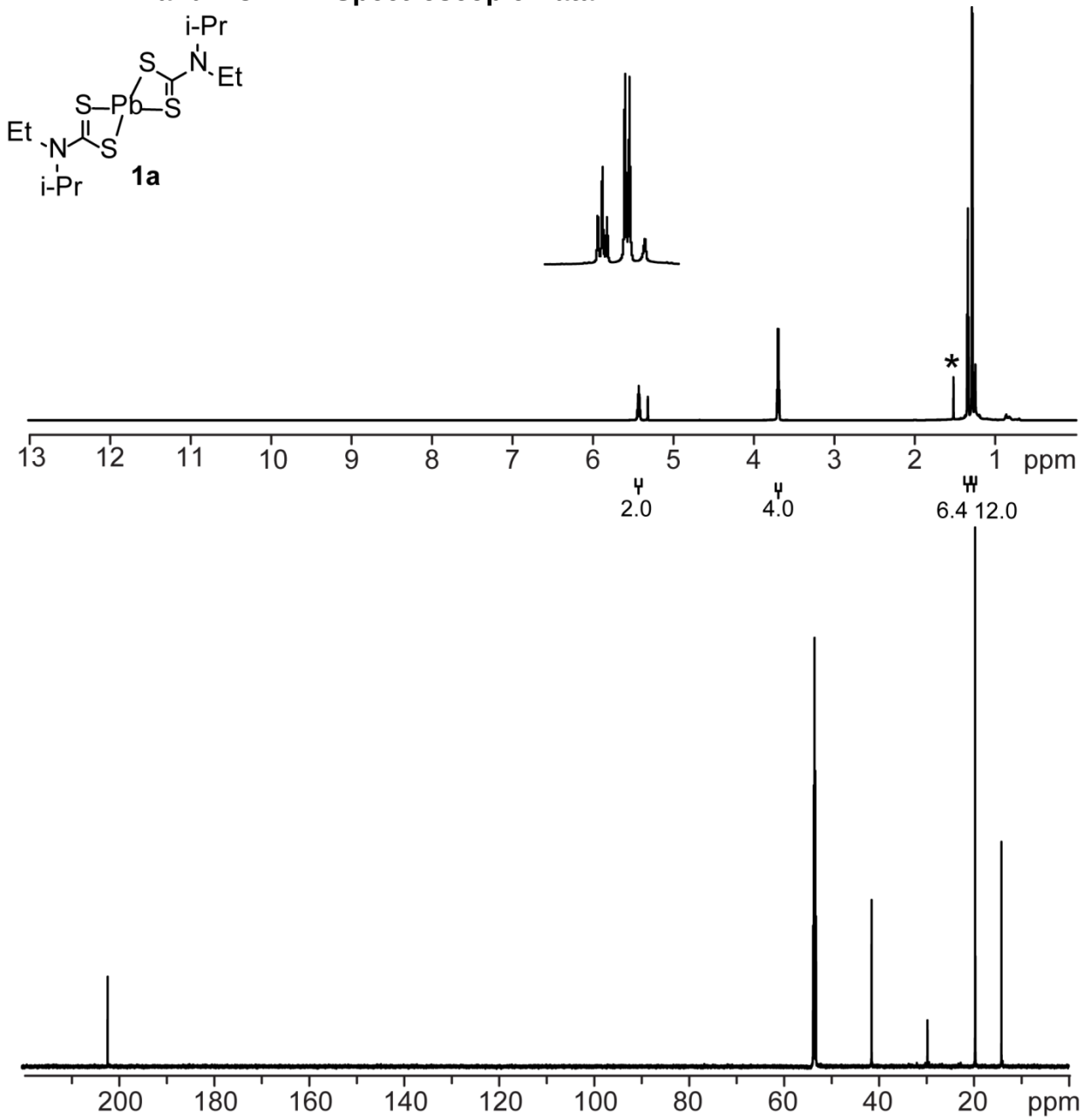

Figure S3-1. ^{1}H and ^{13}C NMR spectra of **1a**. ^{1}H NMR (700 MHz, CD_2Cl_2) δ 5.43 (sept, J = 7 Hz, 2H), 3.71 (q, J = 7 Hz, 4H), 1.36 (t, J = 7 Hz, 6H), 1.30 (d, J = 7 Hz, 12H). ^{13}C NMR (176 MHz, CD_2Cl_2) δ 202.46, 41.81, 30.04, 20.03, 14.50. * denotes residual H_2O.

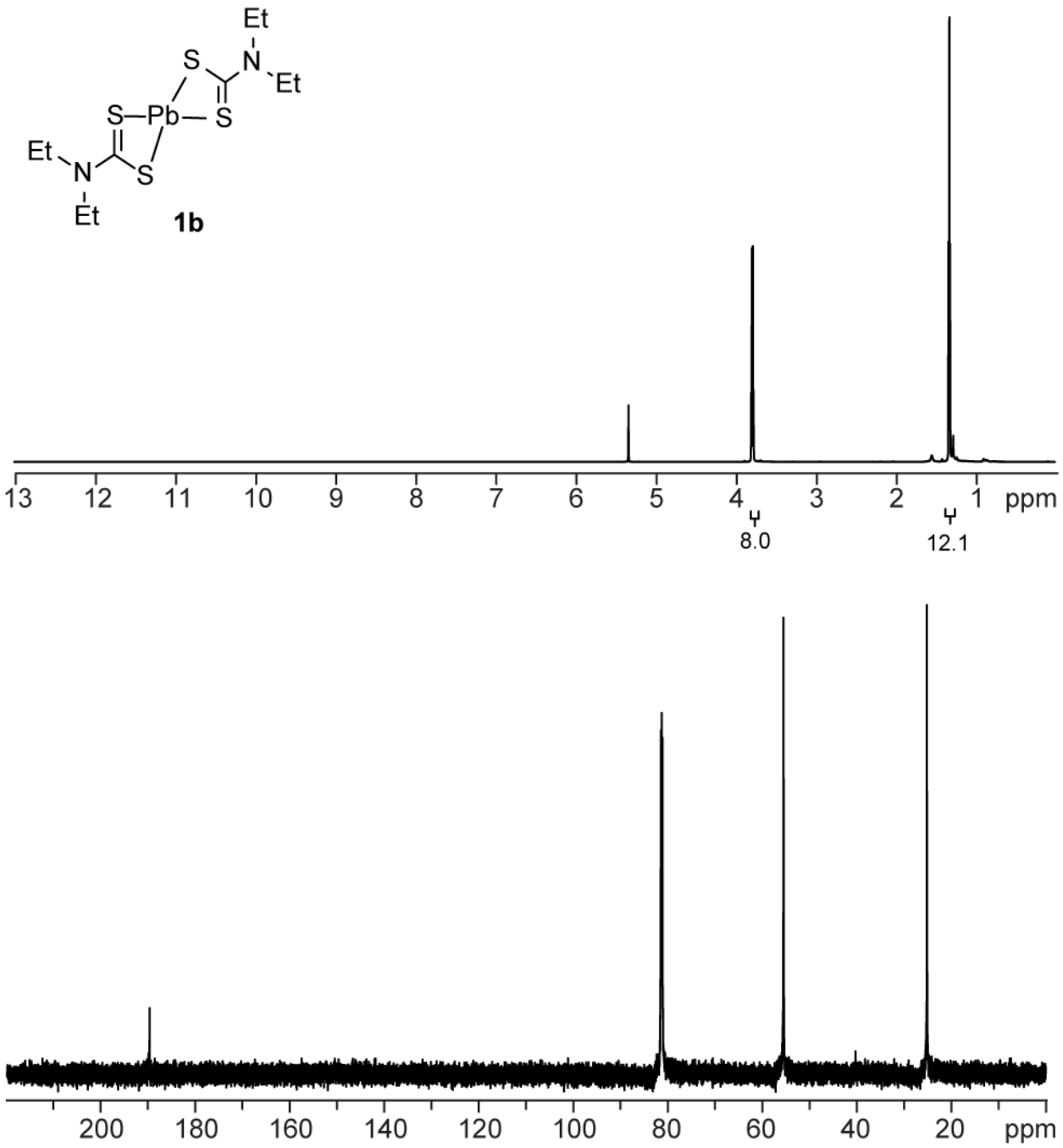

Figure S3-2. ^{1}H and ^{13}C NMR spectra of **1b**. ^{1}H NMR (700 MHz, CD_2Cl_2) δ 3.77 (q, J = 7 Hz, 8H), 1.31 (t, J = 7 Hz, 12H). ^{13}C NMR (176 MHz, $CDCl_3$) δ 202.04, 47.26, 12.24.

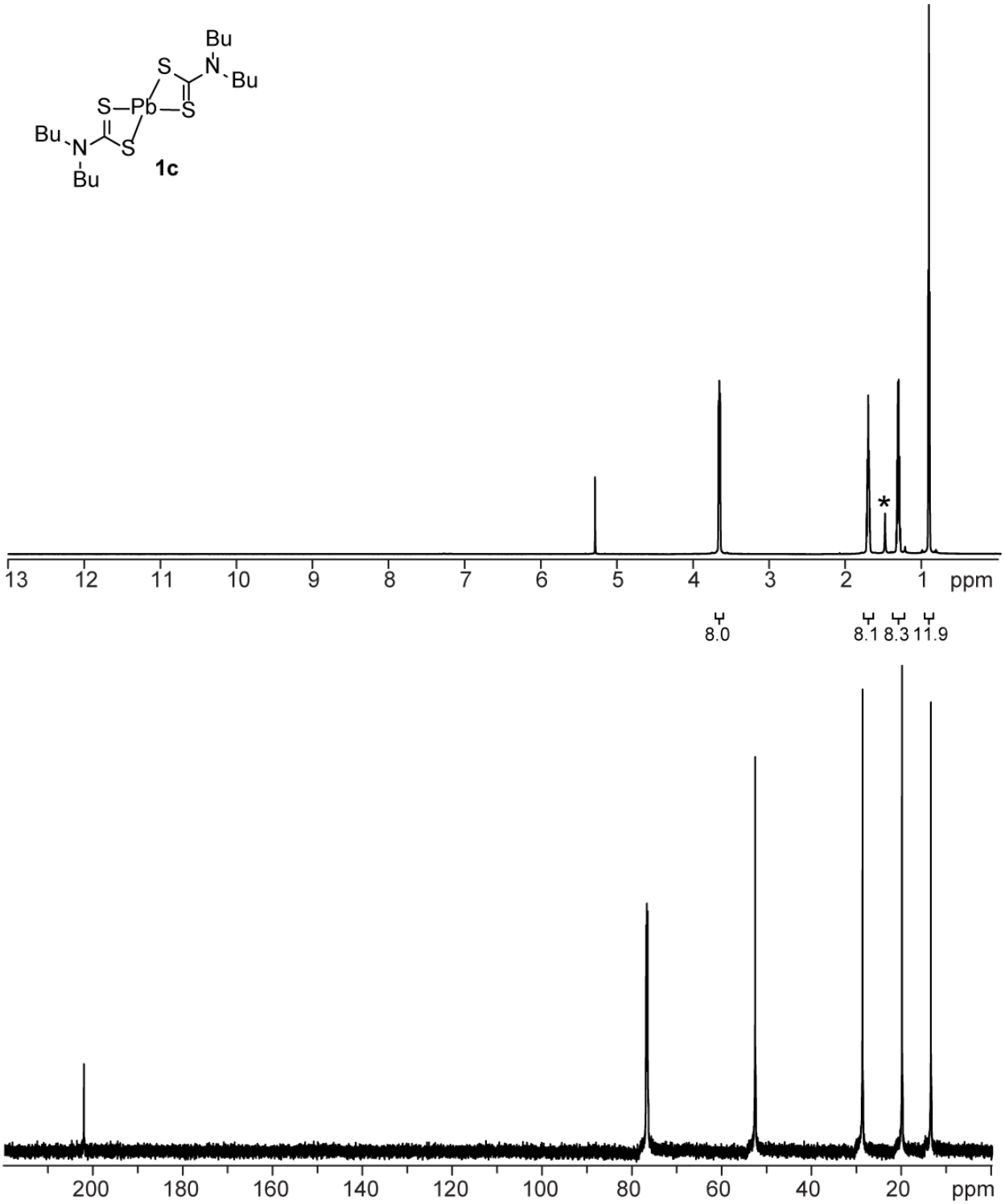

Figure S3-3. ^{1}H and ^{13}C NMR spectra of **1c**. ^{1}H NMR (700 MHz, CD_2Cl_2) δ 3.69 (t, J = 8 Hz, 8H), 1.75 (t of t, J = 8 Hz, 8 Hz, 8H), 1.33 (t of q, J = 8 Hz, 8 Hz, 8H), 0.92 (t, J = 8 Hz, 12H). ^{13}C NMR (176 MHz, $CDCl_3$) δ 202.35, 52.90, 29.01, 20.21, 13.78.

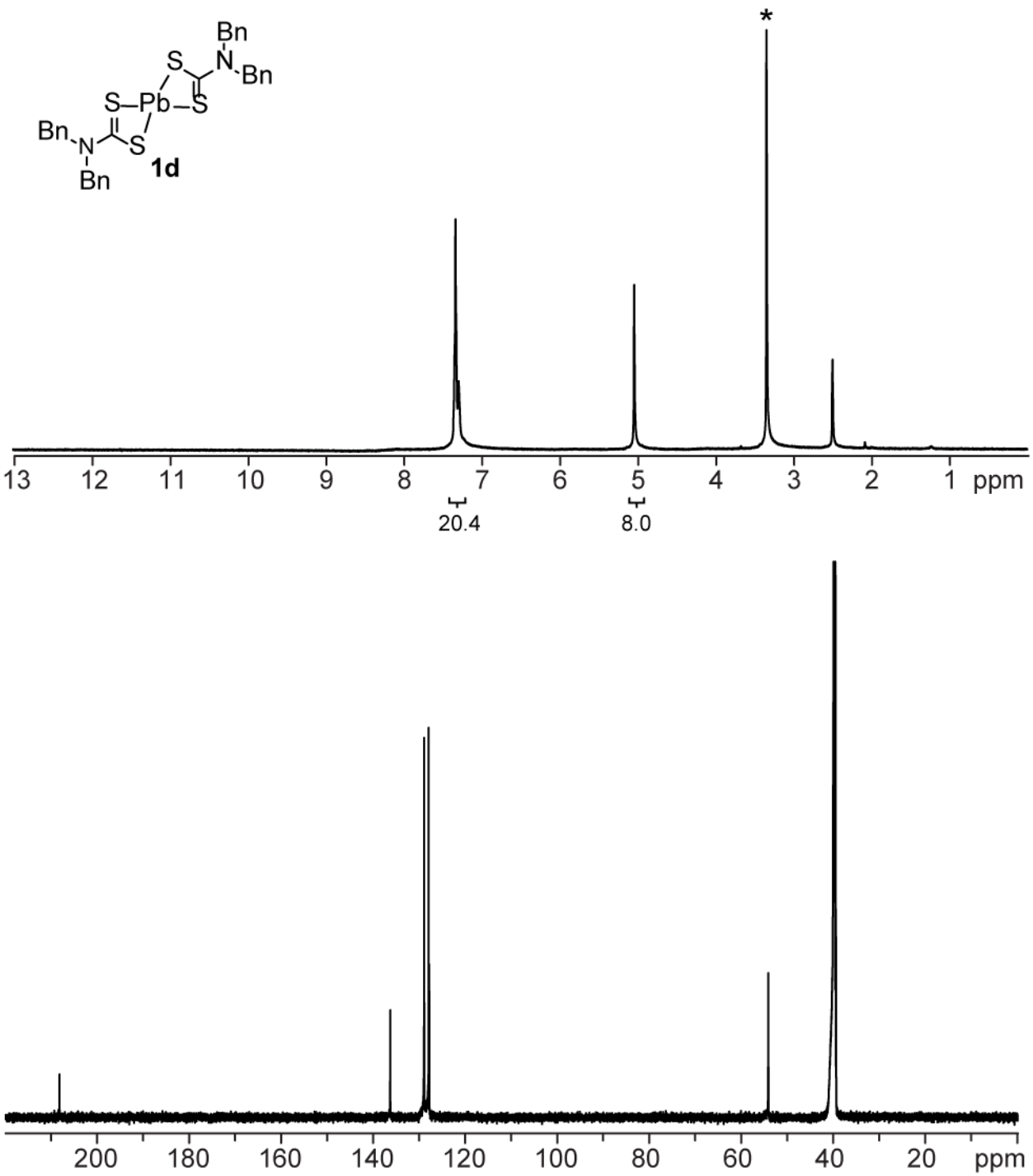

Figure S3-4. ^{1}H and ^{13}C NMR spectra of **1d**. ^{1}H NMR (700 MHz, d_6-DMSO) δ 7.33 (m, 20H), 5.04 (s, 8H). ^{13}C NMR (176 MHz, d_6-DMSO) δ 208.08, 136.32, 128.97, 127.99, 127.89, 54.30.*denotes residual H_2O.

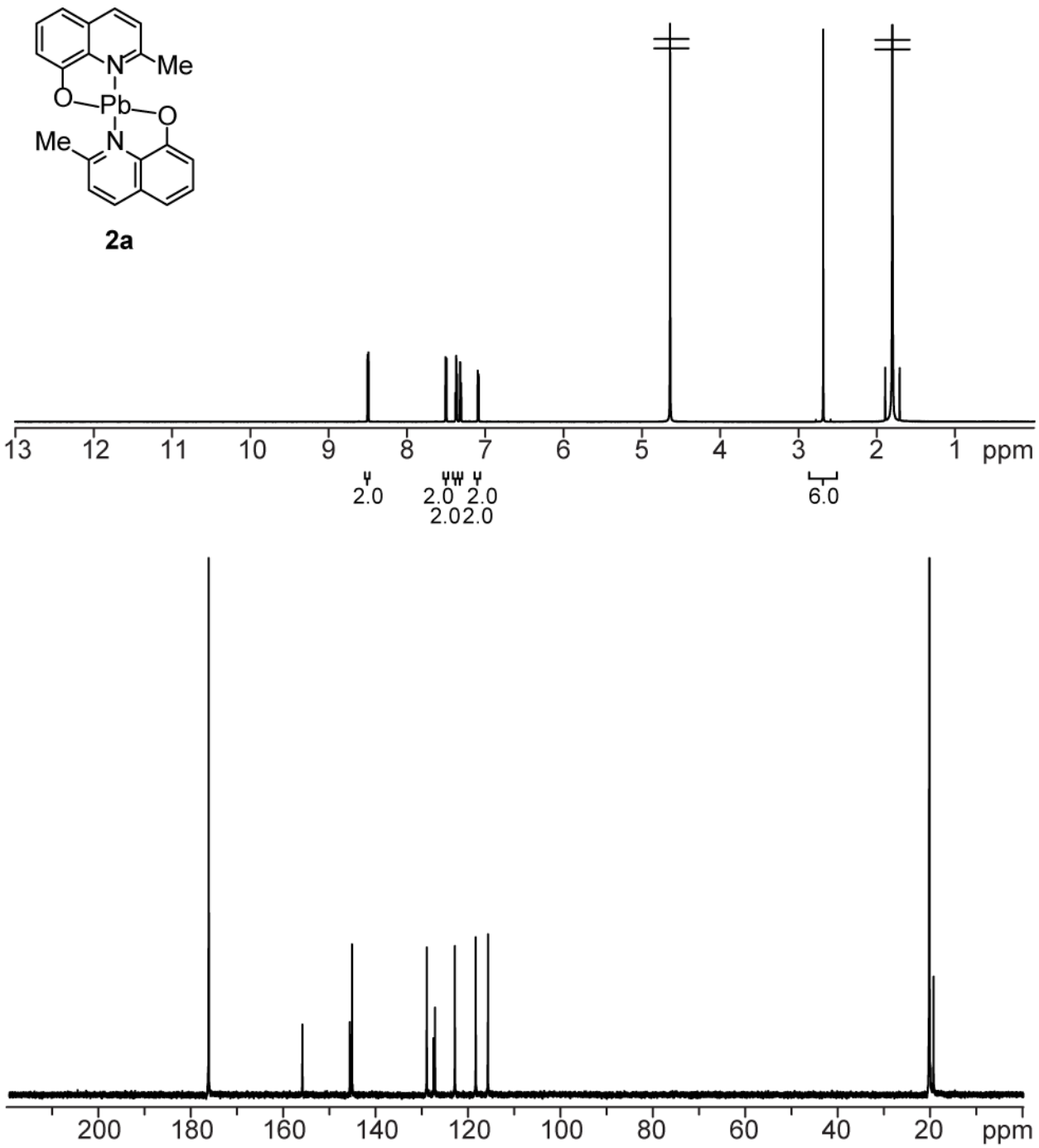

Figure S3-5. ^{1}H and ^{13}C NMR spectra of **2a**. ^{1}H NMR (700 MHz, D_2O and DOAc) δ 8.50 (d, *J* = 8 Hz, 2H), 7.50 (d, *J* = 8 Hz, 2H), 7.37 (t, *J* = 8 Hz, 2H), 7.32 (d, *J* = 8 Hz, 2H), 7.09 (d, *J* = 8 Hz, 2H), 2.69 (s, 6H). ^{13}C NMR (176 MHz, $CDCl_3$) δ 156.56, 146.31, 145.82, 129.60, 128.13, 127.80, 123.50, 118.98, 116.33, 19.65.

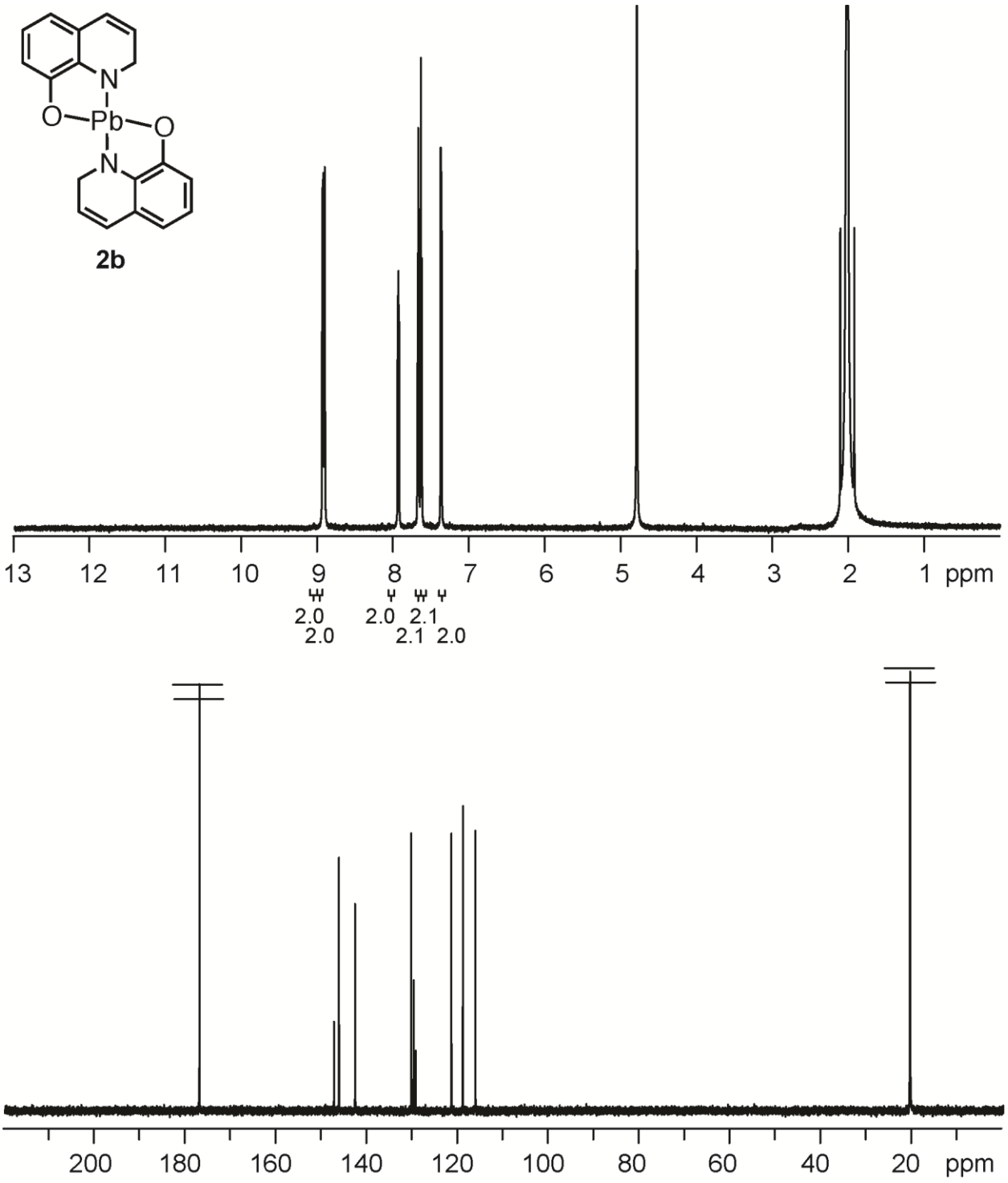

Figure S3-6. ^{1}H and ^{13}C NMR spectra of **2b**. ^{1}H NMR (700 MHz, $CDCl_3$) δ 8.78 (d, J = 8 Hz, 2H), 8.76 (d, J = 5 Hz, 2H), 7.79 (d of d, J = 8 Hz, 5 Hz, 2H), 7.52 (d of d, J = 8 Hz, 8 Hz, 2H), 7.22 (d, J = 7 Hz, 2H). ^{13}C NMR (176 MHz, $CDCl_3$) δ 147.48, 146.36, 142.83, 130.46, 129.92,129.47, 121.64, 119.11, 116.33.

V. Materials Studio Calculations

A. Procedure for Cambridge Structural Database Search

1) A search for Pb-complexes was performed using the Draw tool in CCDC Conquest.

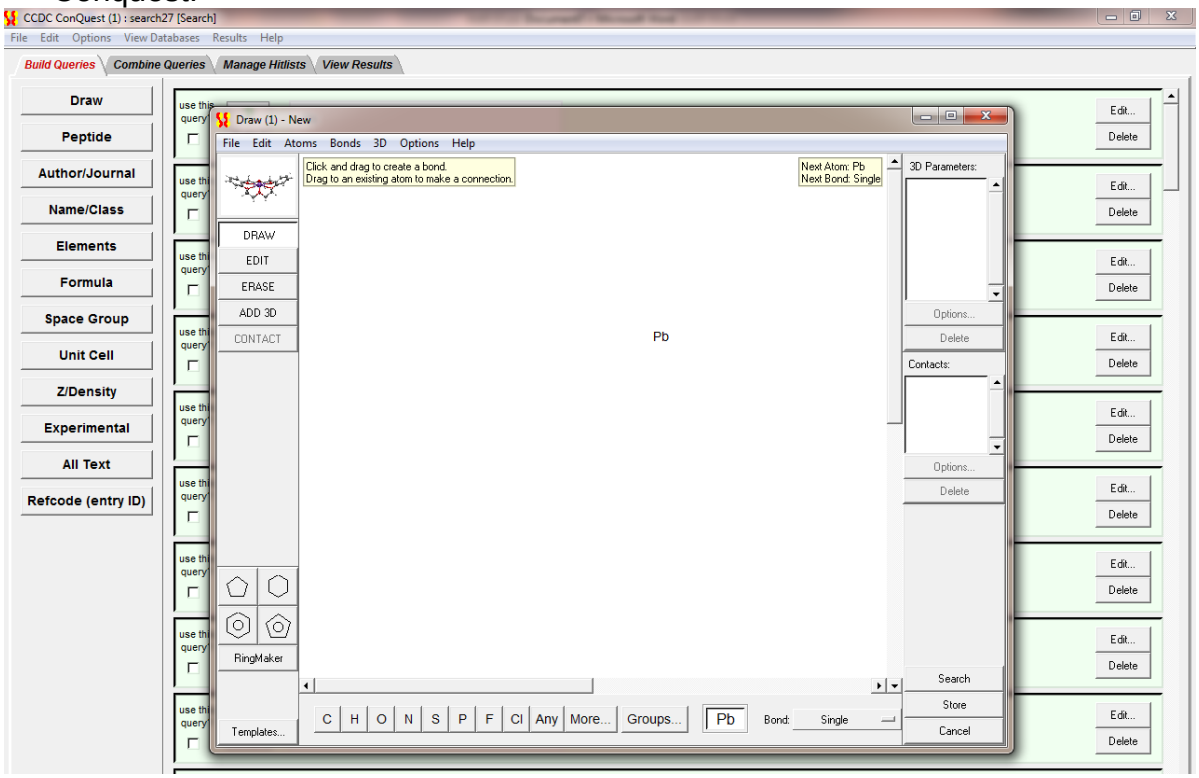

2) Filters were applied to ensure that CIF files obtained were sufficient for morphology prediction calculations.

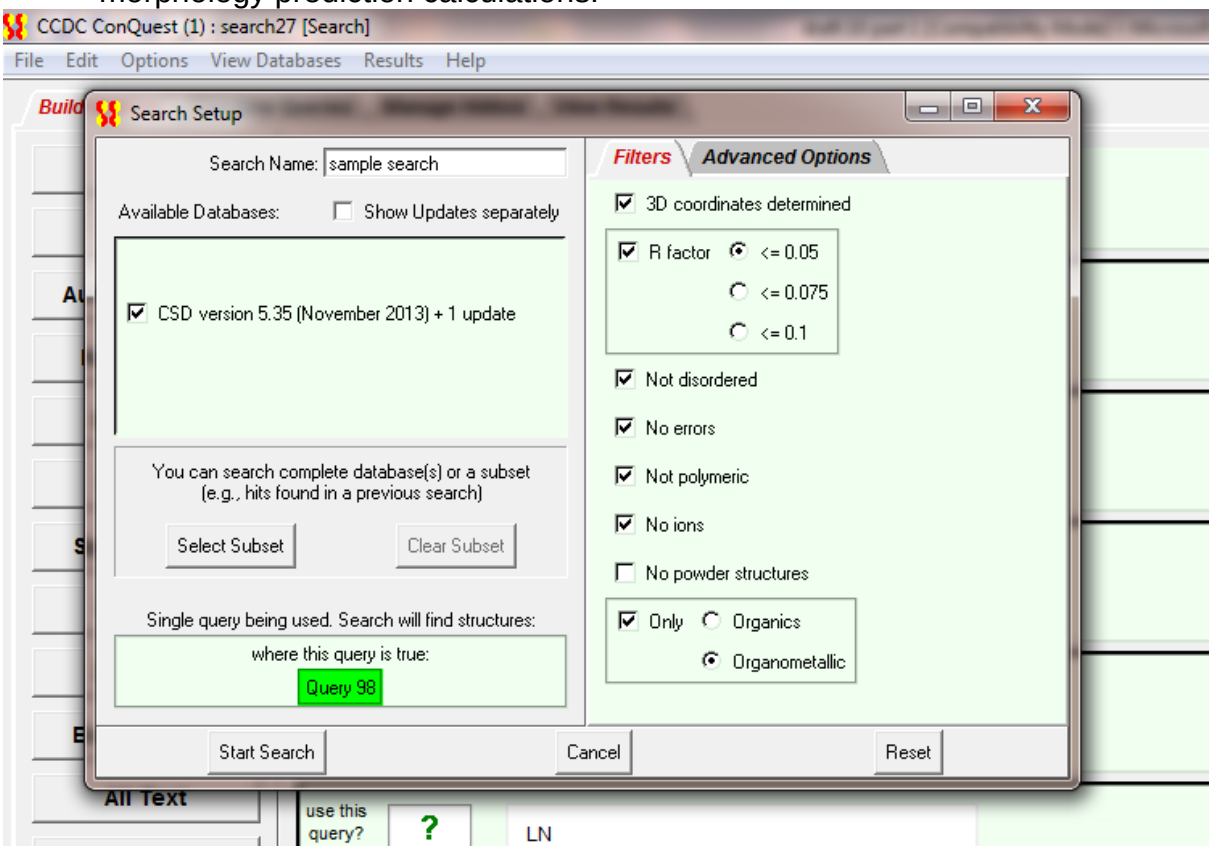

3) Using the Combine Queries in combination with the Draw tool, complexes containing all other metals and metalloids were excluded from the search.

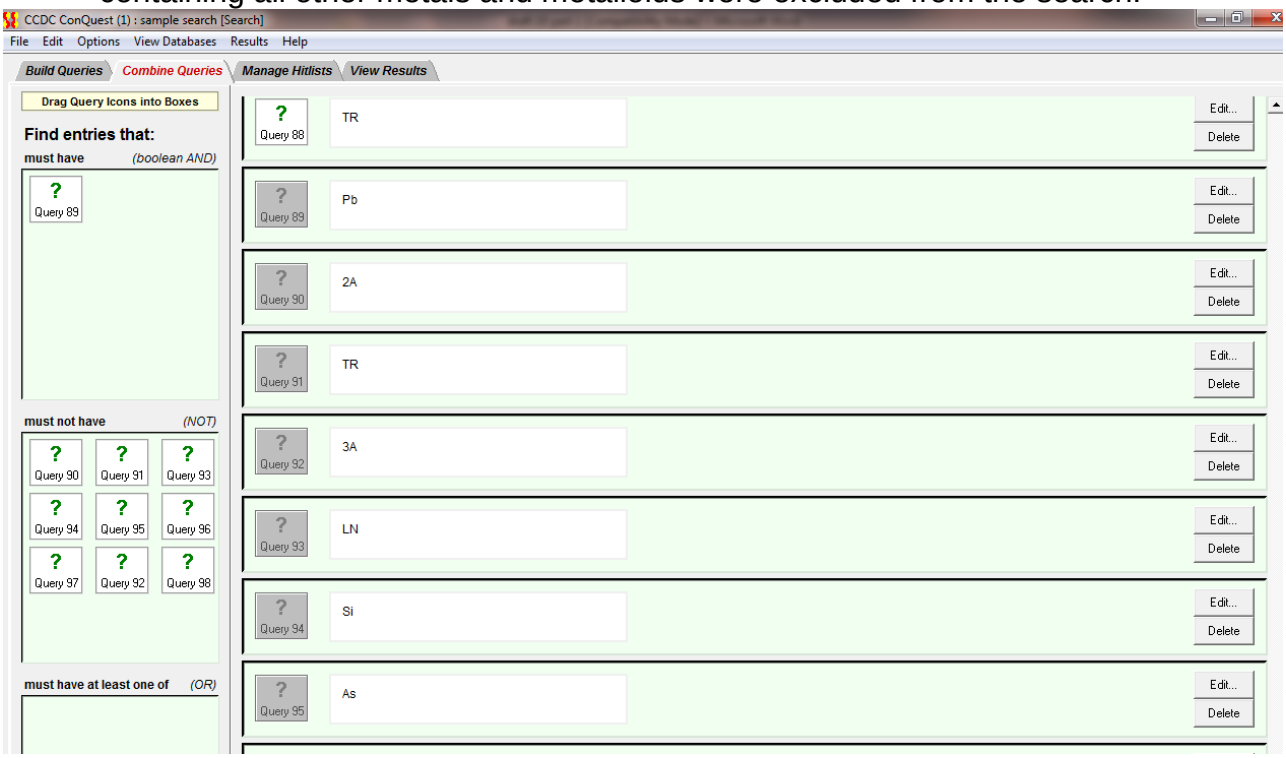

4) Solvate structures were excluded from the search manually.

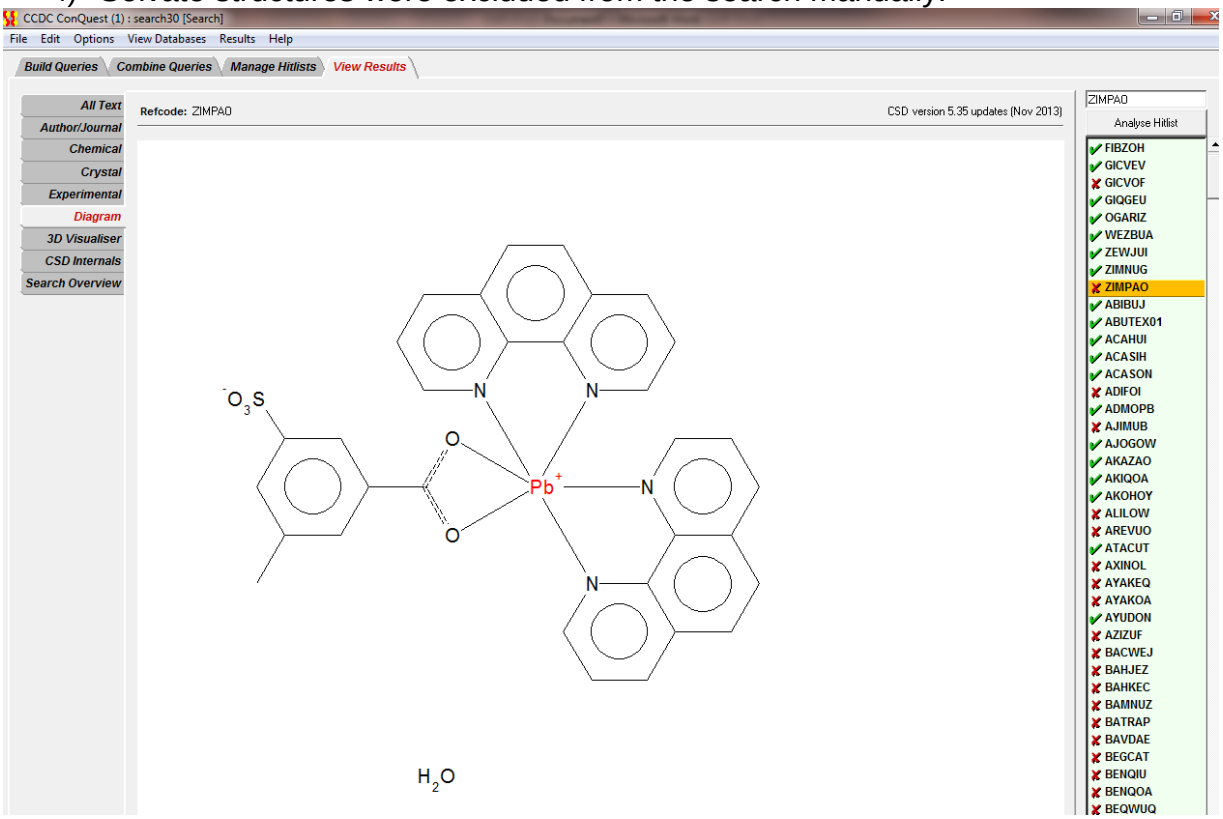

B. Procedure for Morphology Prediction

5) CIF files representing crystal structures obtained from the CSD were opened with Materials Studio using File → Import

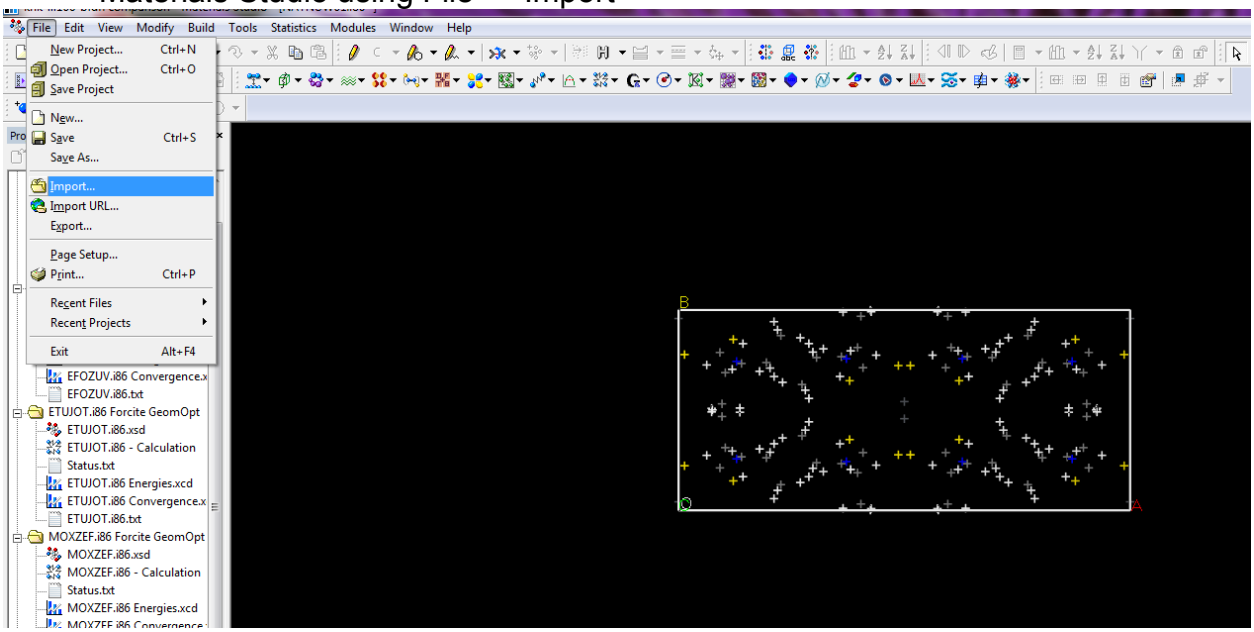

6) Bonds were calculated by the default settings for distance between atoms and the atom type.

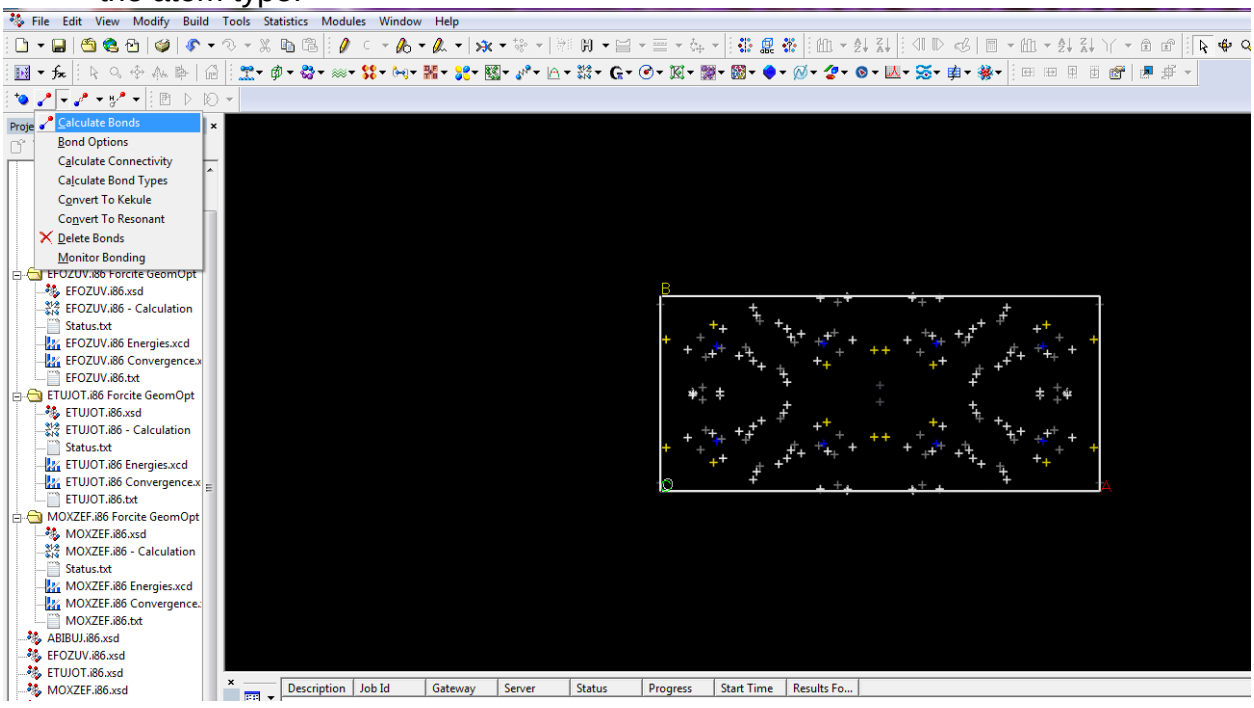

7) Molecules are completed using the Build Crystal tool

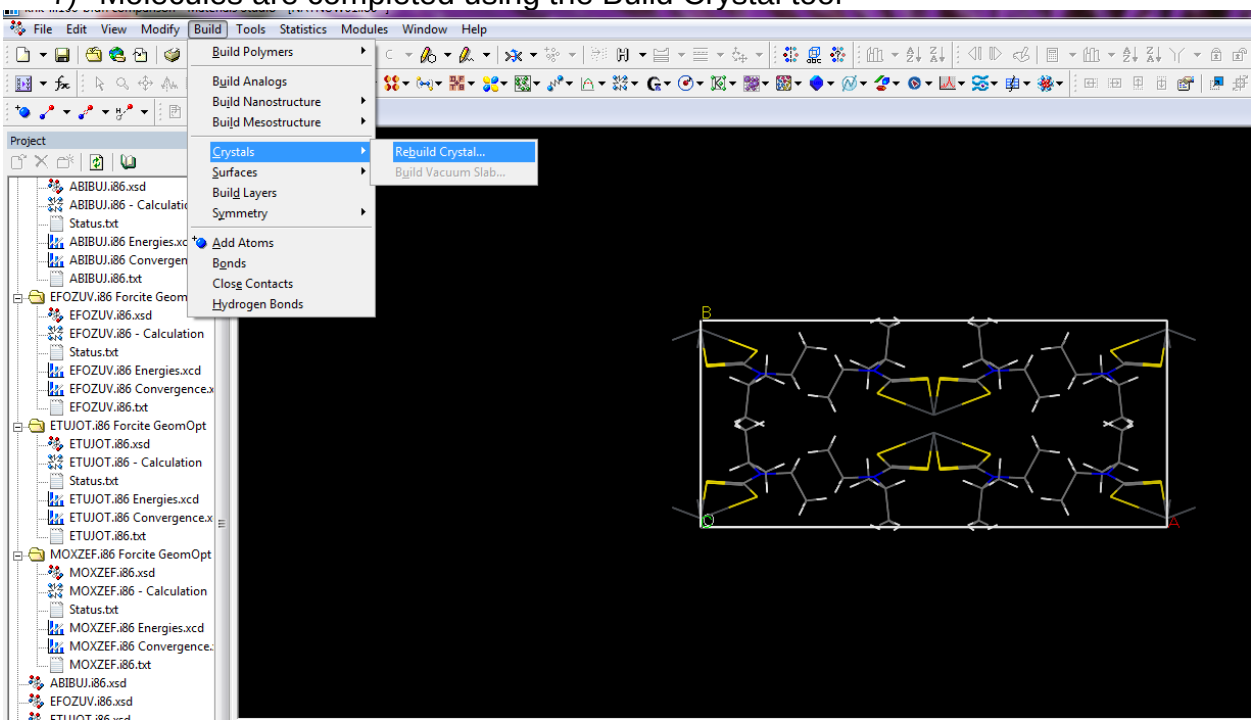

8) Hydrogen atom positions were normalized.

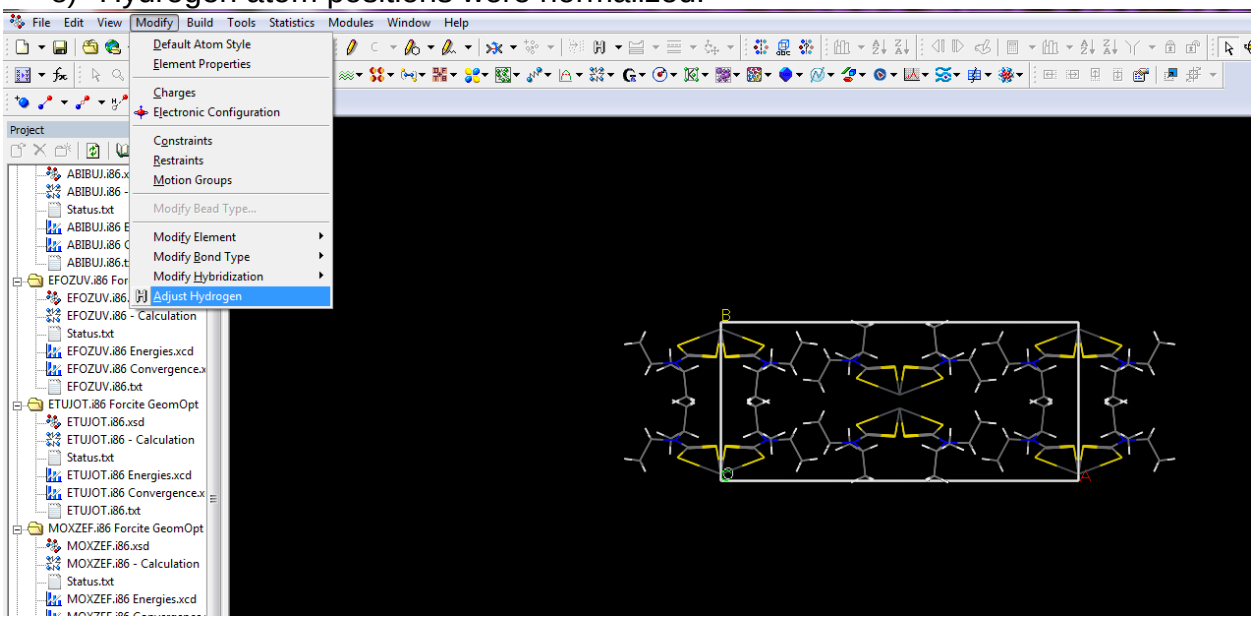

9) Geometry optimization was performed using Forcite. The Forcite module can be accessed by selecting Module→Forcite→Calculation.

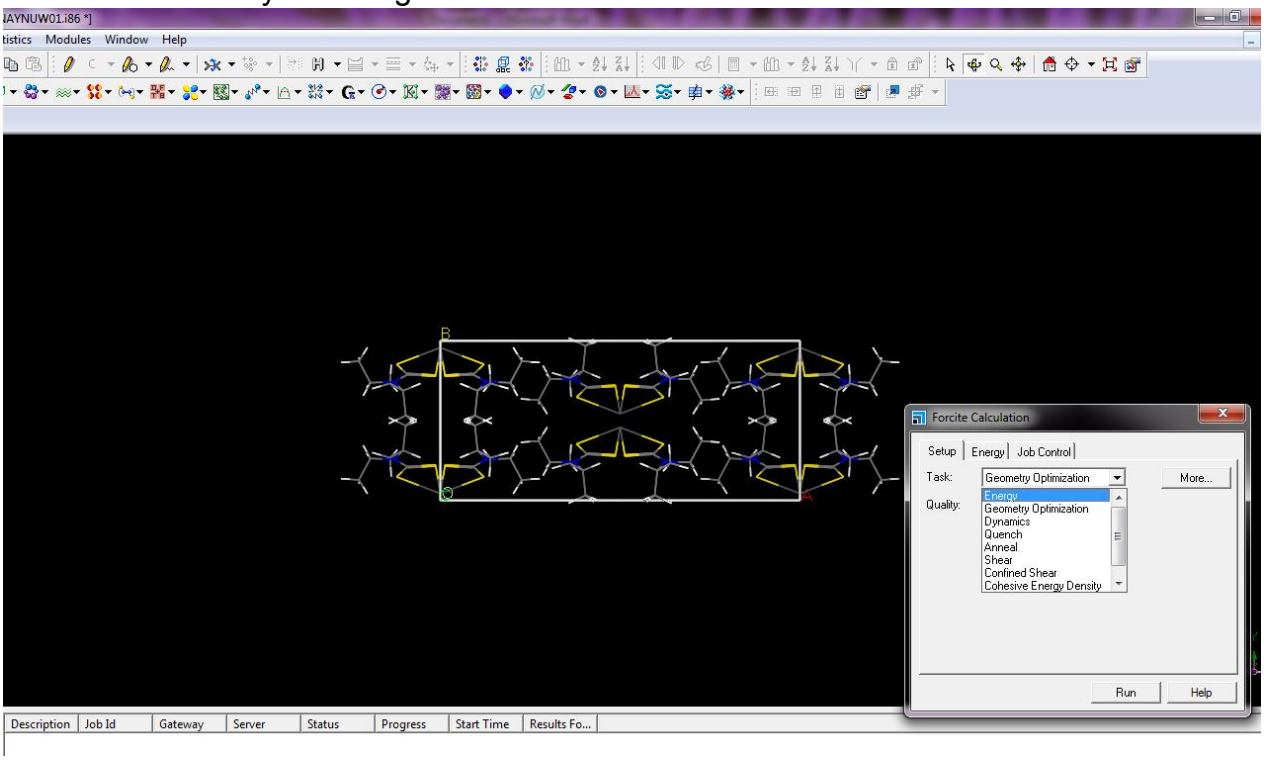

10) If a full, unconstrained geometry optimization is desired, then choosing the “More…” button next to Task menu while Geometry Optimization is selected will open a menu where this option can be selected by checking the box next to optimize cell.

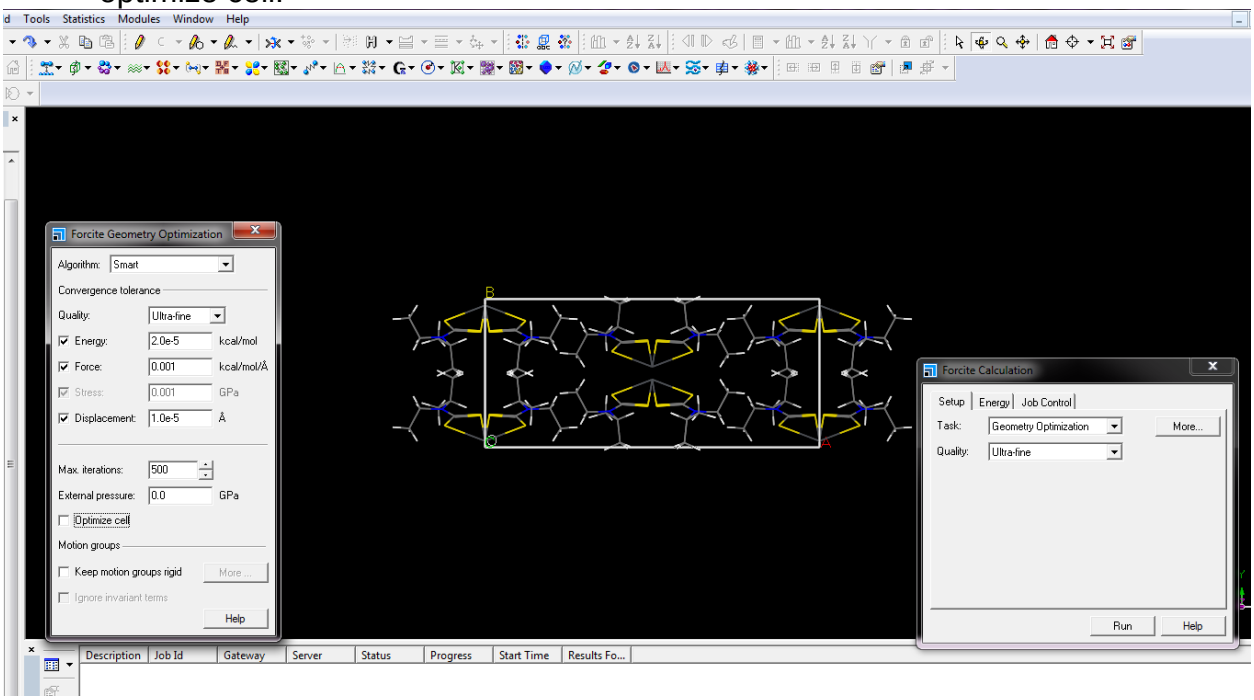

11) The calculation was performed at the ultra-fine quality level with the Universal Force Field (UFF) with charges assigned using QEq and electrostatic and van der Waals summation methods both set at Ewald. Unit cell parameters before and after unconstained optimization can be found in Table S3-1.

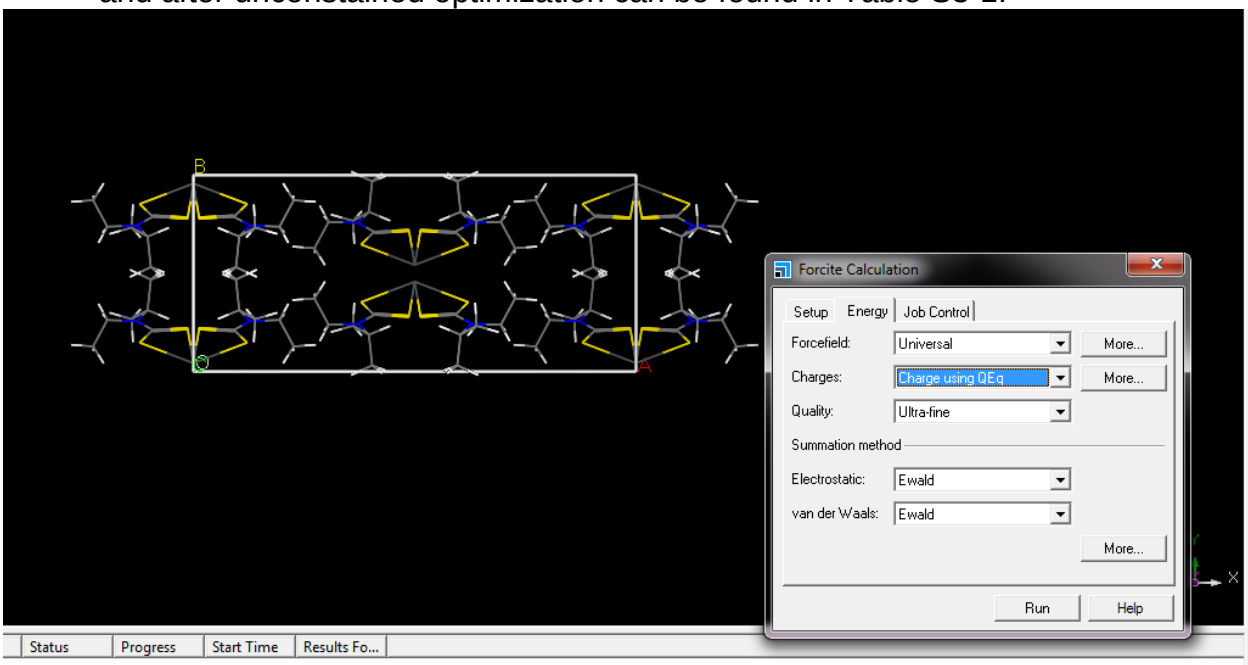

12) Crystal graphs were generated using the Morphology module, Crystal Graph

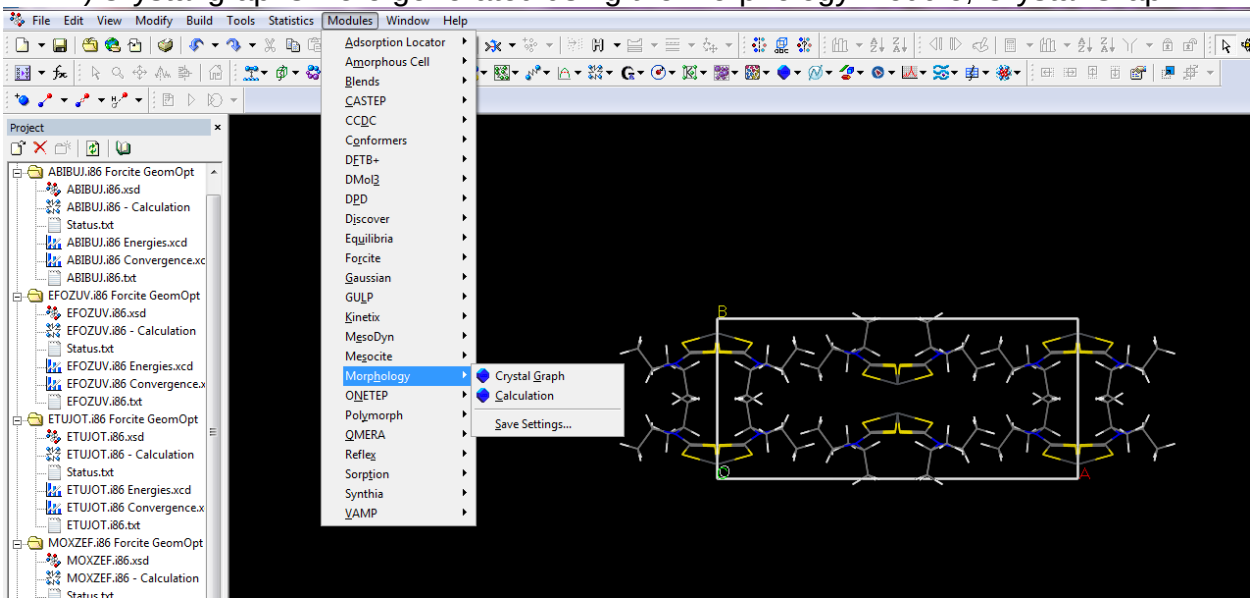

13) The crystal graph was generated using the same force field as the geometry optimization and charge assignment as the geometry optimization (Step 11). The maximum unit cell separation was set to one by one by one (calculation sphere). This can be done by either entering in the numbers or by selecting a “course” quality setting. A minimum energy of interaction filter was set to -0.596 kcal/mol.

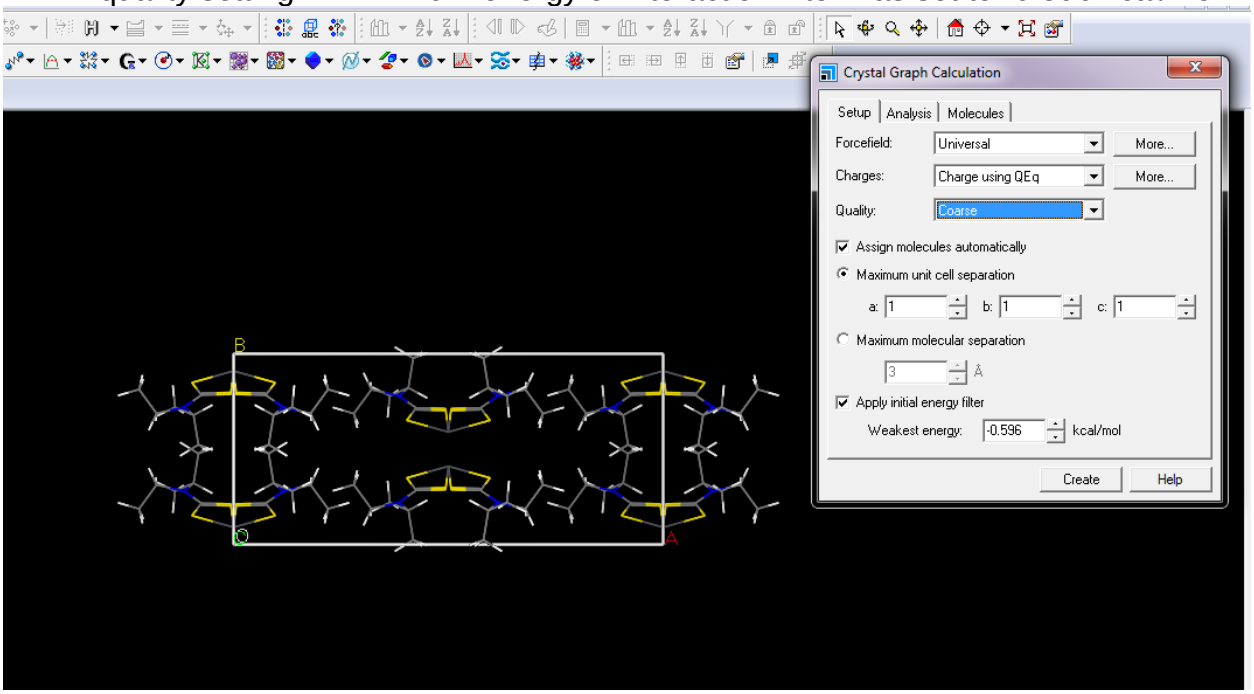

14) Morphologies were predicted by using the Morphology module, accessed by selecting Module→Morphology→Calulation

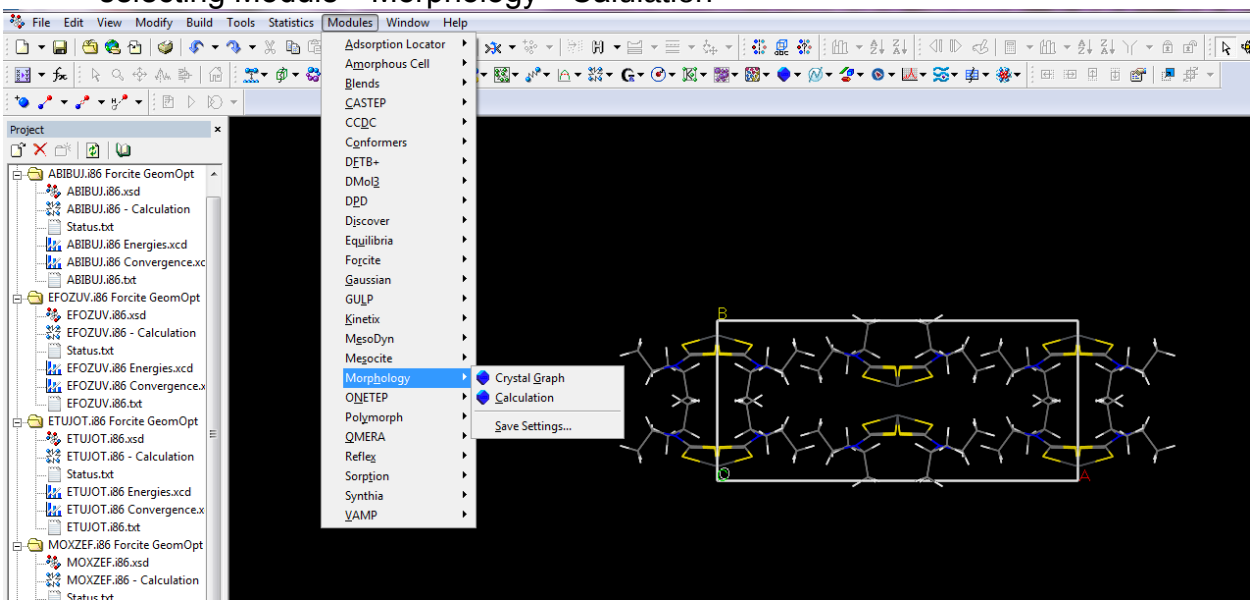

15) Using the crystal graph, the morphology is predicted via the Growth Morphology method.

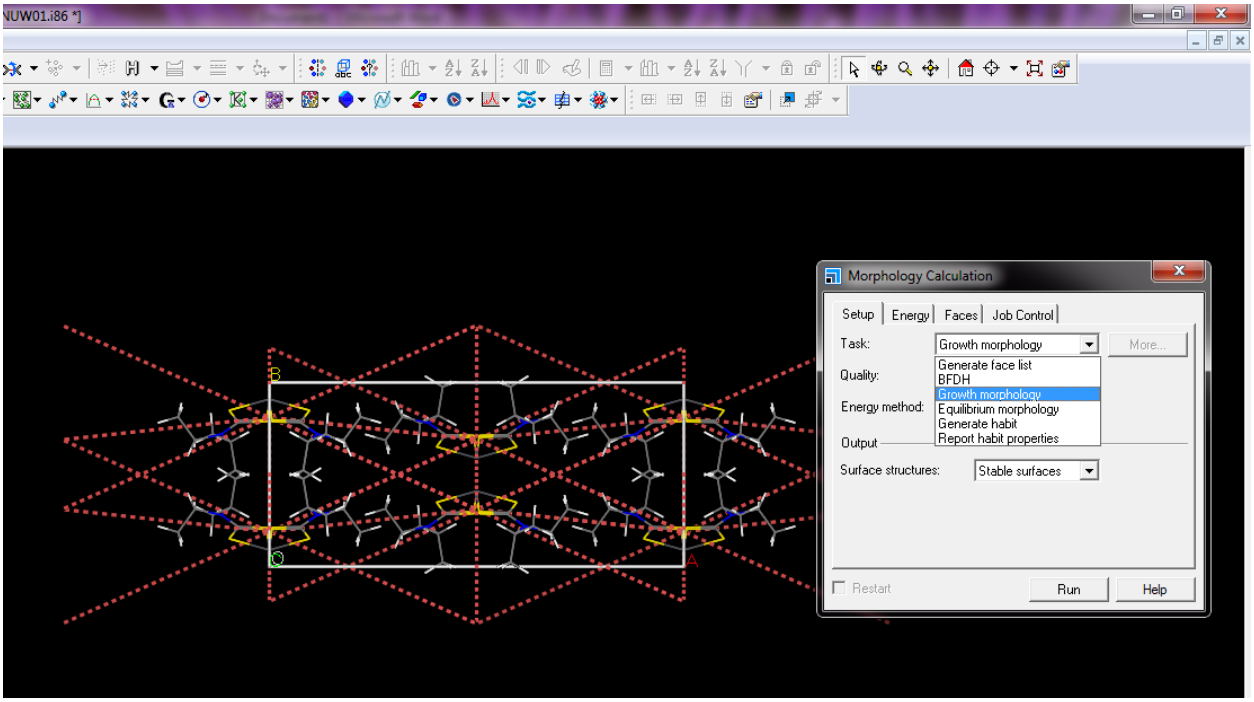

16) The calculation was performed using the Universal forcefield, charges assigned by Qeq, and an ultra-fine quality method. The summation method for electrostatic and van der Waals interactions used were default to the program (Ewald and Atom-based, respectively).

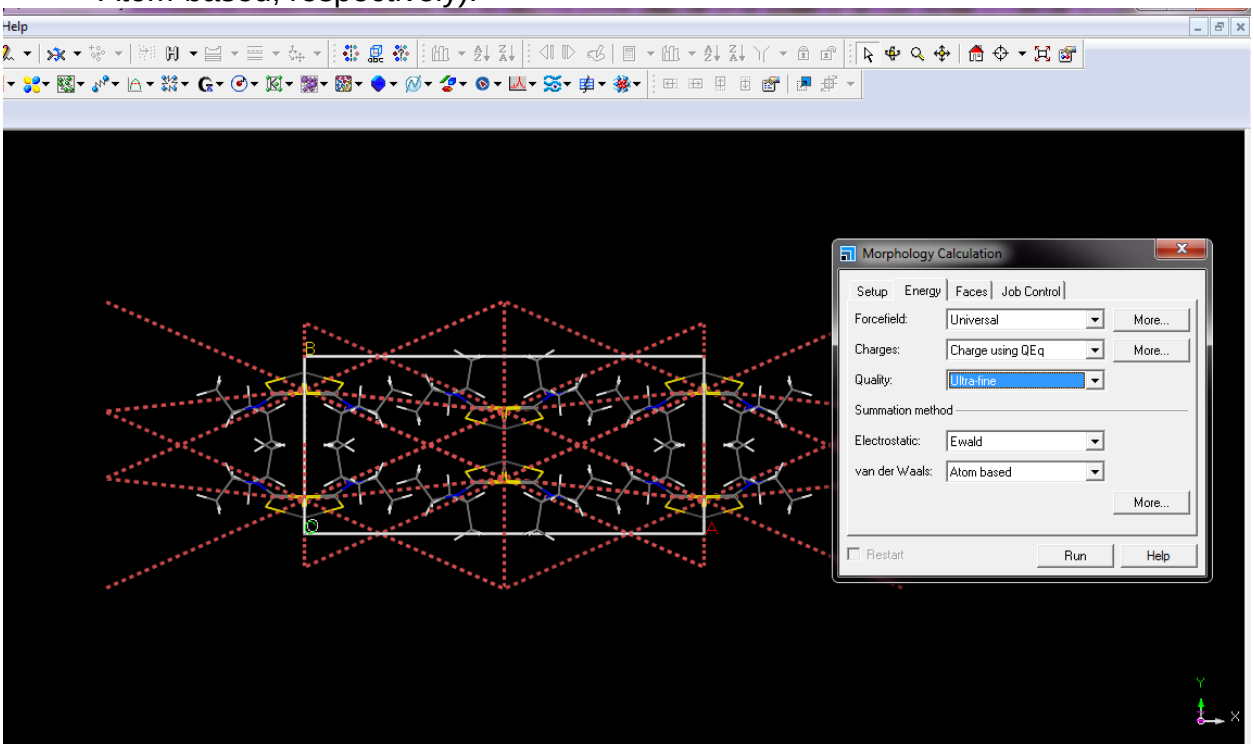

17) Morphology is displayed overlayed on the unit cell with the generated crystal graph.

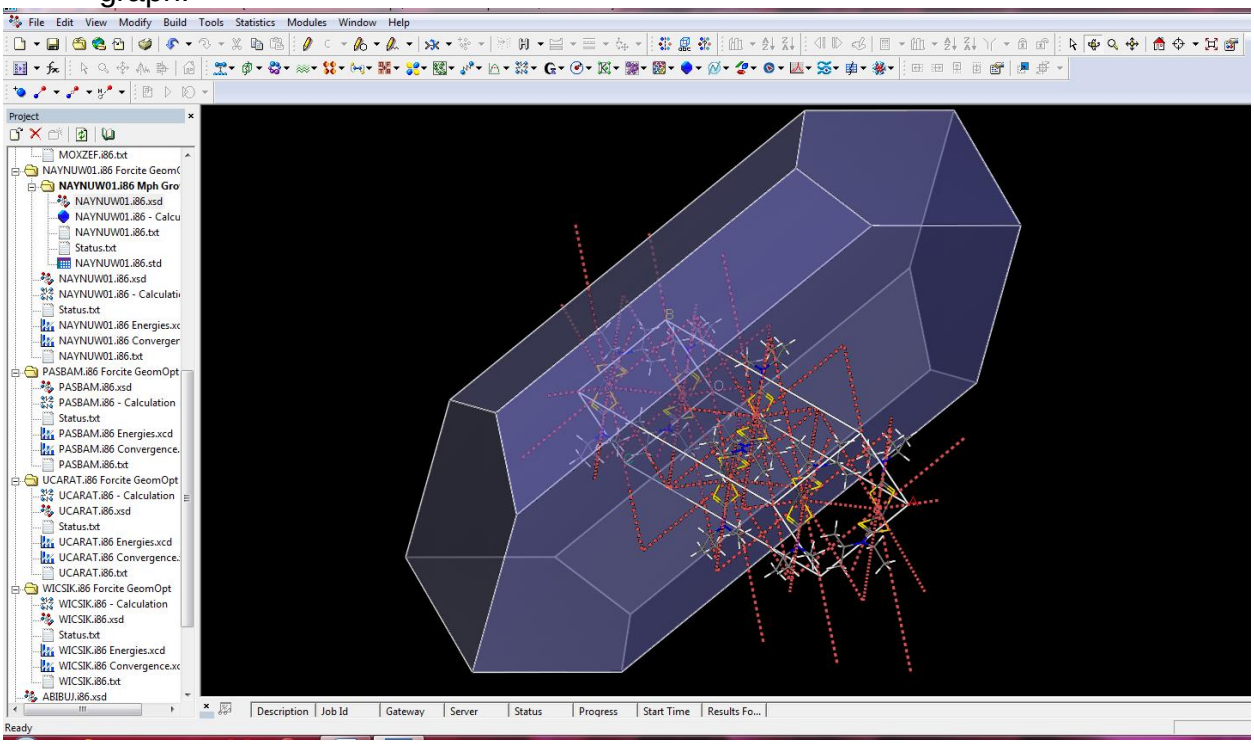

18) Details such as lattice energy and aspect ratio can be found in the .txt output file

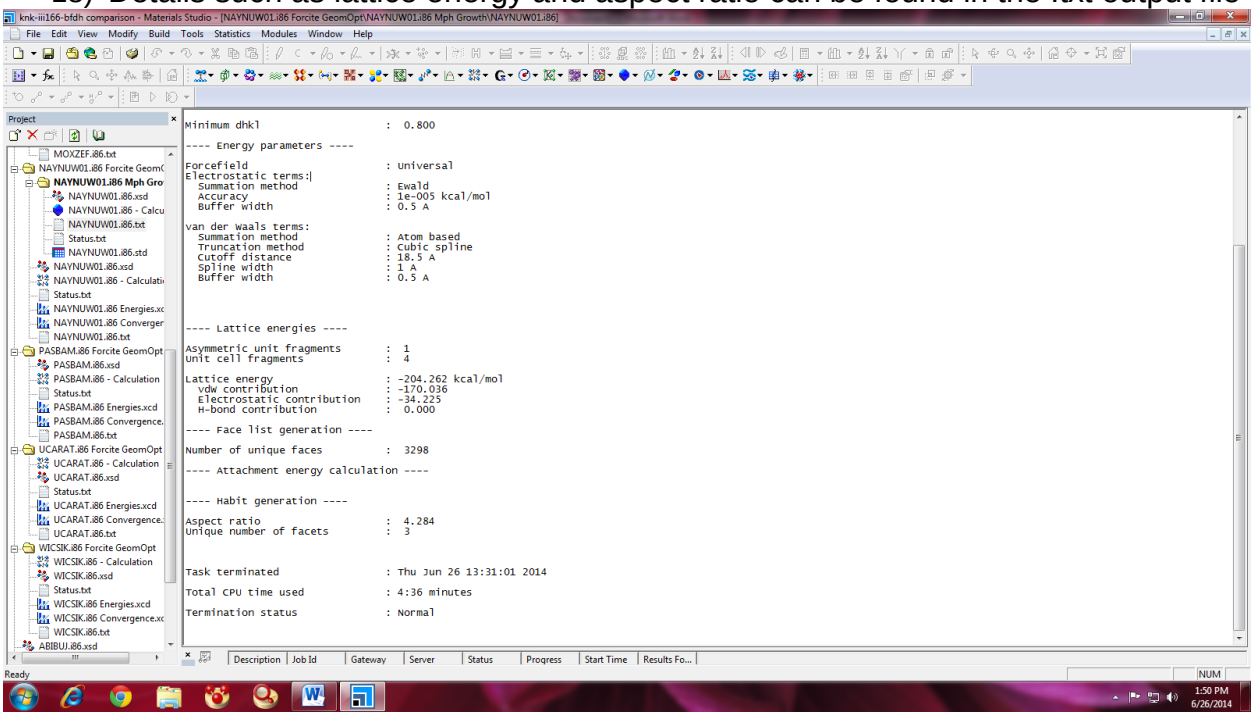

C. Geometry Optimization Data

Table S3-1. Unit cell parameters before and after full, unconstrained Forcite calculations.

	unoptimized lattice parameters						optimized lattice parameters						% change					
Compound	**a (Å)**	**b (Å)**	**c (Å)**	**α (˚)**	**β (˚)**	**γ (˚)**	**a (Å)**	**b (Å)**	**c (Å)**	**α (˚)**	**β (˚)**	**γ (˚)**	**a (Å)**	**b (Å)**	**c (Å)**	**α (˚)**	**β (˚)**	**γ (˚)**
ABIBUJ	10.614	12.278	13.462	95.311	111.434	104.811	14.755	12.753	9.664	86.330	112.110	109.503	39.015	3.869	-28.213	-9.423	0.607	4.477
ABUTEX01	10.079	10.779	11.928	74.665	70.677	85.778	13.405	10.514	9.819	55.656	82.432	90.714	32.994	-2.458	-17.684	-25.459	16.632	5.754
ACAHUI	6.543	13.575	16.172	90.000	97.561	90.000	7.505	12.226	16.783	90.000	112.352	90.000	14.704	-9.935	3.779	0.000	15.161	0.000
ACASIH	19.397	4.131	16.584	90.000	91.865	90.000	18.207	4.621	15.822	90.000	82.710	90.000	-6.135	11.862	-4.595	0.000	-9.966	0.000
ACASON	8.750	31.678	10.775	90.000	90.000	90.000	8.756	31.361	11.771	90.000	90.000	90.000	0.067	-1.001	9.244	0.000	0.000	0.000
AJIMUB	9.666	18.888	18.297	90.000	102.630	90.000	9.706	19.290	17.514	90.000	105.996	90.000	0.414	2.128	-4.279	0.000	3.280	0.000
AJOGOW	8.279	33.881	22.794	90.000	99.642	90.000	8.258	33.986	21.982	90.000	104.680	90.000	-0.251	0.310	-3.562	0.000	5.056	0.000
AKOHOY	9.074	9.499	13.853	85.640	76.127	74.730	7.939	10.269	14.151	93.193	81.122	82.133	-12.508	8.106	2.151	8.819	6.561	9.906
ATACUT	8.672	13.196	28.629	90.000	93.538	90.000	8.671	12.703	27.400	90.000	97.705	90.000	-0.006	-3.733	-4.293	0.000	4.455	0.000
AYUDON	7.299	13.083	23.587	90.000	94.617	90.000	7.694	12.782	22.337	90.000	75.850	90.000	5.415	-2.298	-5.301	0.000	-19.835	0.000
BAHKEC	8.674	9.552	14.297	79.701	82.447	75.025	8.890	9.544	14.575	81.452	71.569	69.444	2.491	-0.086	1.947	2.198	-13.194	-7.438
BAMNUZ	9.632	13.573	18.666	90.000	104.175	90.000	9.135	14.114	20.384	90.000	113.128	90.000	-5.163	3.984	9.202	0.000	8.594	0.000
BAVDAE	9.687	10.422	11.721	90.000	102.570	90.000	10.072	10.132	11.471	90.000	99.825	90.000	3.974	-2.783	-2.133	0.000	-2.676	0.000
BEQWUQ	14.973	9.902	20.581	90.000	109.379	90.000	14.293	10.536	20.433	90.000	107.860	90.000	-4.542	6.398	-0.719	0.000	-1.389	0.000
BOJXOO	8.797	10.005	11.993	66.280	74.318	68.154	8.590	9.910	12.017	69.280	75.979	68.602	-2.358	-0.946	0.199	4.526	2.235	0.657
BOJXUU	12.987	14.107	14.792	90.000	95.445	90.000	13.603	13.032	15.253	90.000	95.876	90.000	4.747	-7.622	3.120	0.000	0.452	0.000
BOSDOD	10.136	11.166	11.314	95.460	116.336	111.668	10.327	14.137	11.542	89.958	120.998	126.543	1.884	26.608	2.012	-5.764	4.007	13.321
BUMMOL	11.600	8.975	6.863	97.790	90.190	101.540	11.054	9.193	7.069	111.566	81.278	98.243	-4.707	2.429	3.002	14.087	-9.881	-3.247
BURPIO	31.345	7.561	22.366	90.000	132.843	90.000	28.264	8.837	21.242	90.000	136.321	90.000	-9.829	16.882	-5.025	0.000	2.618	0.000
CEVLEV	7.272	12.539	16.295	90.000	97.800	90.000	7.246	12.866	16.216	90.000	105.010	90.000	-0.355	2.608	-0.485	0.000	7.372	0.000
CIJQES	10.407	12.034	12.470	89.464	72.864	70.868	10.239	12.206	12.465	83.572	73.182	66.897	-1.614	1.427	-0.040	-6.586	0.436	-5.603
CIJQIW	10.414	12.084	12.468	89.224	72.815	70.638	10.275	12.242	12.490	83.380	72.863	66.682	-1.332	1.308	0.179	-6.550	0.066	-5.600
CIJQIW01	10.361	12.033	12.431	89.330	72.910	70.560	10.267	12.341	12.495	83.032	72.925	66.064	-0.907	2.560	0.515	-7.050	0.021	-6.372
CIJQOC	22.366	11.214	11.602	90.000	101.411	90.000	21.980	11.371	11.556	90.000	102.964	90.000	-1.724	1.396	-0.397	0.000	1.531	0.000
CIQGUE	8.241	23.765	8.341	90.000	112.910	90.000	8.056	24.544	8.176	90.000	111.938	90.000	-2.245	3.278	-1.978	0.000	-0.861	0.000
COCLAI	7.868	20.506	12.874	90.000	93.800	90.000	9.180	19.066	12.116	90.000	87.880	90.000	16.680	-7.022	-5.888	0.000	-6.311	0.000

	unoptimized lattice parameters						optimized lattice parameters						% change					
Compound	a (Å)	b (Å)	c (Å)	α (˚)	β (˚)	γ (˚)	a (Å)	b (Å)	c (Å)	α (˚)	β (˚)	γ (˚)	a (Å)	b (Å)	c (Å)	α (˚)	β (˚)	γ (˚)
DAMTIV	8.624	10.424	11.295	97.154	106.891	109.874	13.820	11.540	12.146	68.609	139.885	130.893	60.250	10.706	7.534	-29.381	30.867	19.130
DAXMAR	18.651	3.313	24.434	90.000	102.340	90.000	18.902	7.634	20.629	90.000	88.591	90.000	1.346	130.405	-15.573	0.000	-13.435	0.000
DOBZID10	14.831	16.722	8.399	90.000	95.270	90.000	25.979	10.844	15.666	90.000	151.688	90.000	75.167	-35.151	86.522	0.000	59.219	0.000
DODMUF	28.939	28.939	14.158	90.000	90.000	90.000	31.593	31.593	13.252	90.000	90.000	90.000	9.170	9.170	-6.400	0.000	0.000	0.000
DUPXAO	9.347	10.643	11.378	106.696	95.343	99.117	8.315	10.856	12.129	98.463	88.802	106.432	-11.041	1.998	6.604	-7.716	-6.860	7.380
DURGON	16.451	7.290	14.188	90.000	108.981	90.000	14.939	8.455	14.739	90.000	110.241	90.000	-9.191	15.989	3.886	0.000	1.156	0.000
DURJEG	7.320	8.307	23.325	90.000	90.397	90.000	9.359	8.364	19.843	90.000	97.218	90.000	27.860	0.692	-14.927	0.000	7.546	0.000
EFOZUV	10.266	12.304	14.844	92.054	103.473	105.561	9.545	13.479	14.831	105.421	107.958	101.508	-7.025	9.552	-0.090	14.521	4.334	-3.839
ERIGES	9.011	10.923	11.920	83.760	87.626	71.601	10.756	12.175	10.616	90.177	99.483	54.424	19.365	11.462	-10.940	7.661	13.531	-23.990
ETUJOT	21.937	7.457	23.238	90.000	90.000	90.000	20.955	7.285	23.188	90.000	90.000	90.000	-4.476	-2.305	-0.215	0.000	0.000	0.000
FAZFIX	26.226	4.585	15.541	90.000	119.667	90.000	24.927	4.243	15.344	90.000	93.605	90.000	-4.952	-7.457	-1.268	0.000	-21.779	0.000
FIHCUV	10.267	22.017	7.451	90.000	92.432	90.000	9.765	27.507	7.264	90.000	98.725	90.000	-4.889	24.935	-2.515	0.000	6.808	0.000
FIMDUB	12.859	13.074	17.064	90.000	105.504	90.000	13.281	12.320	18.866	90.000	113.607	90.000	3.280	-5.764	10.560	0.000	7.680	0.000
FOFCEI	10.569	11.082	17.918	72.784	88.671	85.959	10.459	10.911	18.158	72.294	90.740	85.128	-1.039	-1.543	1.339	-0.673	2.333	-0.967
FOHFEO	35.937	8.337	25.432	90.000	126.076	90.000	38.377	8.618	27.536	90.000	138.411	90.000	6.790	3.371	8.273	0.000	9.784	0.000
FOPJIE	10.240	13.111	17.619	90.000	98.972	90.000	9.831	13.140	18.749	90.000	104.587	90.000	-3.995	0.219	6.412	0.000	5.673	0.000
GAGCIC	17.201	14.170	19.873	90.000	115.644	90.000	16.686	13.075	21.344	90.000	121.852	90.000	-2.995	-7.724	7.404	0.000	5.368	0.000
GAGXES	11.000	18.299	12.894	90.000	107.661	90.000	11.407	23.080	11.898	90.000	125.896	90.000	3.696	26.128	-7.722	0.000	16.937	0.000
GICKUZ	13.923	13.135	12.171	90.000	110.384	90.000	11.898	15.030	12.738	90.000	117.960	90.000	-14.544	14.427	4.659	0.000	6.863	0.000
GIMPUN	12.254	10.833	16.792	90.000	98.471	90.000	12.102	10.146	18.506	90.000	110.793	90.000	-1.240	-6.343	10.207	0.000	12.513	0.000
GODWIG	10.057	11.074	14.553	69.707	73.897	74.244	9.966	10.990	14.826	68.456	70.264	73.177	-0.903	-0.762	1.879	-1.795	-4.916	-1.437
GOJGUI	9.217	11.587	19.103	102.516	97.867	97.715	11.648	11.572	19.079	76.687	111.152	91.375	26.377	-0.129	-0.127	-25.195	13.575	-6.488
GOLMEA	8.258	8.805	9.677	103.976	98.262	108.190	8.178	13.321	9.390	121.433	62.028	129.831	-0.968	51.286	-2.961	16.789	-36.875	20.003
GOLMIE	13.742	18.068	18.611	90.000	90.000	90.000	14.058	14.732	22.969	90.000	90.000	90.000	2.299	-18.464	23.414	0.000	0.000	0.000
GOLMOK	5.305	11.820	17.493	90.000	94.569	90.000	4.797	12.300	23.090	90.000	122.005	90.000	-9.574	4.061	31.997	0.000	29.012	0.000
GOPYIT	18.920	9.647	22.275	90.000	112.592	90.000	24.055	10.084	24.978	90.000	139.233	90.000	27.141	4.526	12.135	0.000	23.662	0.000
GUWCOR	11.234	11.946	13.513	100.361	109.481	100.996	11.234	11.946	13.513	100.361	109.481	100.996	-0.002	0.001	-0.002	0.000	0.000	0.000

Compound	unoptimized lattice parameters						optimized lattice parameters						% change					
	a (Å)	b (Å)	c (Å)	α (˚)	β (˚)	γ (˚)	a (Å)	b (Å)	c (Å)	α (˚)	β (˚)	γ (˚)	a (Å)	b (Å)	c (Å)	α (˚)	β (˚)	γ (˚)
HABGAU	10.160	5.160	18.758	90.000	94.687	90.000	10.604	5.330	16.926	90.000	87.761	90.000	4.370	3.295	-9.766	0.000	-7.315	0.000
HAGSOX	8.198	14.220	17.793	90.000	94.010	90.000	8.691	12.104	21.304	90.000	95.104	90.000	6.014	-14.880	19.732	0.000	1.164	0.000
HEDNIO	11.449	16.113	21.369	90.000	100.327	90.000	11.247	16.934	19.934	90.000	96.093	90.000	-1.762	5.098	-6.714	0.000	-4.220	0.000
HEFHAB	9.017	10.839	12.808	99.480	90.130	97.910	9.658	10.392	12.512	96.782	92.116	98.177	7.109	-4.124	-2.311	-2.712	2.203	0.273
HERHUH	11.226	9.820	12.258	90.000	100.500	90.000	11.601	8.498	12.636	90.000	96.041	90.000	3.340	-13.462	3.084	0.000	-4.437	0.000
HIQHEV	11.054	20.906	11.291	90.000	101.667	90.000	11.197	18.383	12.201	90.000	102.365	90.000	1.295	-12.068	8.064	0.000	0.687	0.000
HOXQOB	15.841	16.146	40.504	90.000	90.000	90.000	15.996	17.016	40.739	90.000	90.000	90.000	0.981	5.387	0.580	0.000	0.000	0.000
HUGVUB	10.439	11.973	12.424	90.450	107.020	108.520	10.655	11.532	13.064	78.686	111.469	104.704	2.069	-3.683	5.151	-13.006	4.157	-3.516
HUGWAI	10.146	31.930	19.622	90.000	99.340	90.000	10.293	31.688	19.524	90.000	100.663	90.000	1.449	-0.758	-0.499	0.000	1.332	0.000
HUGWEM	8.760	11.529	16.702	75.200	82.280	87.860	8.501	11.509	17.478	75.095	80.794	87.639	-2.959	-0.173	4.646	-0.140	-1.806	-0.252
IHEMUE	19.532	11.008	7.219	90.000	112.325	90.000	18.689	12.016	7.699	90.000	119.122	90.000	-4.318	9.154	6.649	0.000	6.051	0.000
IJAYEX	10.689	10.824	24.782	86.171	79.687	69.544	11.378	10.814	23.371	83.113	78.859	68.899	6.442	-0.088	-5.693	-3.549	-1.039	-0.927
IJONEB	7.342	8.400	23.801	90.000	93.733	90.000	8.199	7.968	21.976	90.000	89.925	90.000	11.674	-5.147	-7.667	0.000	-4.063	0.000
ILOBUH	8.278	15.412	11.702	90.000	115.707	90.000	10.465	14.734	11.562	90.000	124.242	90.000	26.419	-4.399	-1.196	0.000	7.376	0.000
IVEFIY	10.368	20.577	12.239	90.000	107.970	90.000	11.888	19.776	10.519	90.000	97.752	90.000	14.660	-3.893	-14.053	0.000	-9.464	0.000
IWOVAR	8.646	10.579	10.793	91.477	111.107	109.929	10.802	11.302	12.030	83.161	136.210	114.090	24.936	6.834	11.457	-9.091	22.594	3.785
JADJIH	9.576	14.151	16.175	104.840	102.260	90.620	8.714	13.934	18.230	116.432	94.878	85.338	-9.002	-1.533	12.705	11.057	-7.219	-5.829
JAWHAR	27.659	16.275	17.166	90.000	121.620	90.000	32.441	15.032	16.468	90.000	127.242	90.000	17.289	-7.637	-4.066	0.000	4.623	0.000
JIBZAV	12.107	11.738	15.540	90.000	111.090	90.000	11.478	11.929	14.897	90.000	108.707	90.000	-5.195	1.627	-4.138	0.000	-2.145	0.000
JITBEU	8.708	10.570	10.963	78.131	79.035	85.183	8.610	10.197	11.668	79.512	86.064	84.819	-1.125	-3.529	6.429	1.768	8.894	-0.427
JUCCEP	8.171	15.499	7.586	90.000	105.808	90.000	8.237	15.274	7.671	90.000	116.570	90.000	0.808	-1.452	1.120	0.000	10.171	0.000
JUCCEP02	8.170	15.480	7.441	90.000	106.652	90.000	7.907	15.519	7.129	90.000	107.570	90.000	-3.219	0.252	-4.198	0.000	0.861	0.000
KAMKAL	27.180	10.662	15.005	90.000	96.234	90.000	27.512	9.790	15.317	90.000	88.443	90.000	1.221	-8.180	2.079	0.000	-8.096	0.000
KEGZAX	18.067	12.518	8.103	90.000	101.930	90.000	17.448	8.122	13.507	90.000	117.988	90.000	-3.426	-35.117	66.691	0.000	15.754	0.000
KEGZEB	7.958	7.445	19.007	90.000	98.740	90.000	5.103	9.202	25.395	90.000	98.090	90.000	-35.876	23.600	33.609	0.000	-0.658	0.000
KILMEX	11.837	11.993	14.611	90.000	97.930	90.000	11.473	12.779	13.441	90.000	99.405	90.000	-3.075	6.554	-8.008	0.000	1.506	0.000
KUJCIB	8.382	9.648	11.427	102.792	105.623	90.303	7.903	8.960	12.127	101.967	105.329	83.500	-5.719	-7.128	6.130	-0.803	-0.278	-7.534
KUJCOH	8.126	12.294	10.685	90.000	110.170	90.000	9.059	14.138	8.469	90.000	124.764	90.000	11.482	14.999	-20.739	0.000	13.247	0.000
KUQFAE	7.856	8.416	9.155	78.524	69.771	82.813	7.181	8.738	9.488	81.426	70.125	89.107	-8.588	3.832	3.637	3.696	0.507	7.600

	unoptimized lattice parameters						optimized lattice parameters						% change					
Compound	a (Å)	b (Å)	c (Å)	α (˚)	β (˚)	γ (˚)	a (Å)	b (Å)	c (Å)	α (˚)	β (˚)	γ (˚)	a (Å)	b (Å)	c (Å)	α (˚)	β (˚)	γ (˚)
KUQFAE01	12.037	5.731	16.327	90.000	90.368	90.000	10.881	5.931	18.889	90.000	76.913	90.000	-9.604	3.490	15.692	0.000	-14.889	0.000
LAJCAC	8.436	10.391	12.075	90.000	103.421	90.000	8.001	10.795	11.009	90.000	96.622	90.000	-5.156	3.891	-8.831	0.000	-6.574	0.000
LERQAB	9.458	16.264	12.652	90.000	9.856	90.000	10.692	12.745	14.089	90.000	105.431	90.000	13.051	-21.637	11.357	0.000	969.714	0.000
LEWPIM	6.814	6.766	22.649	90.000	90.000	90.000	8.834	7.364	17.851	90.000	90.000	90.000	29.645	8.838	-21.184	0.000	0.000	0.000
LIZFUW	10.529	11.398	13.280	73.398	89.522	76.447	9.582	11.228	14.423	71.733	89.983	77.510	-8.994	-1.491	8.607	-2.268	0.515	1.391
LIZGAD	12.431	12.431	21.323	90.000	90.000	90.000	12.356	12.356	21.650	90.000	90.000	90.000	-0.606	-0.606	1.534	0.000	0.000	0.000
MAWNON	14.646	15.501	15.429	90.000	99.583	90.000	12.660	17.708	16.606	90.000	105.783	90.000	-13.560	14.238	7.628	0.000	6.226	0.000
MAWPAB	16.212	14.420	25.146	90.000	92.014	90.000	16.005	13.903	25.521	90.000	89.892	90.000	-1.277	-3.584	1.491	0.000	-2.306	0.000
MIFSIE02	17.709	13.410	12.902	90.000	104.896	90.000	18.157	14.166	12.028	90.000	113.026	90.000	2.531	5.641	-6.777	0.000	7.751	0.000
MONLIK	10.277	17.922	14.368	90.000	92.080	90.000	10.449	18.047	14.189	90.000	90.641	90.000	1.674	0.697	-1.246	0.000	-1.563	0.000
MOXYOO	12.283	10.590	15.260	90.000	95.140	90.000	10.578	11.383	18.217	90.000	92.916	90.000	-13.881	7.488	19.377	0.000	-2.338	0.000
MOXZEF	10.060	11.932	12.059	93.420	91.980	112.880	9.968	12.378	12.701	91.608	88.240	112.213	-0.915	3.738	5.324	-1.940	-4.066	-0.591
MTCBPB	21.073	27.422	4.214	90.000	90.000	90.000	18.536	28.304	4.304	90.000	90.000	90.000	-12.039	3.216	2.136	0.000	0.000	0.000
NADVEV	9.710	11.816	17.999	72.985	88.178	89.040	10.125	11.552	17.841	71.669	84.076	85.525	4.279	-2.233	-0.875	-1.803	-4.652	-3.948
NAKGIP	21.078	42.546	8.388	90.000	90.000	90.000	21.074	43.174	8.283	90.000	90.000	90.000	-0.019	1.476	-1.252	0.000	0.000	0.000
NAPVOR	18.117	10.216	8.654	90.000	112.000	90.000	14.469	8.172	13.598	90.000	111.780	90.000	-20.136	-20.009	57.137	0.000	-0.196	0.000
NAYNUW	22.478	9.718	8.734	90.000	102.620	90.000	22.000	9.193	8.806	90.000	107.091	90.000	-2.127	-5.402	0.824	0.000	4.357	0.000
NAYNUW01	22.478	9.718	8.734	90.000	102.620	90.000	22.011	9.179	8.770	90.000	106.838	90.000	-2.078	-5.546	0.412	0.000	4.110	0.000
NEDVAU	10.100	11.287	11.615	77.868	89.884	84.785	9.576	11.148	12.041	74.788	96.502	88.741	-5.191	-1.233	3.670	-3.955	7.363	4.666
NETVIR	10.986	13.823	14.160	90.000	90.000	90.000	8.276	19.145	14.115	90.000	90.000	90.000	-24.668	38.501	-0.318	0.000	0.000	0.000
NIPFAU	19.685	10.964	36.763	90.000	91.304	90.000	19.466	10.889	37.350	90.000	89.418	90.000	-1.112	-0.680	1.598	0.000	-2.066	0.000
NIXTIX	8.860	9.394	9.783	108.930	98.670	107.870	9.495	9.623	9.037	110.745	97.595	105.368	7.167	2.438	-7.625	1.666	-1.089	-2.319
NOGQOQ	8.314	19.379	21.059	90.000	90.000	90.000	8.327	19.687	20.814	90.000	90.000	90.000	0.156	1.588	-1.164	0.000	0.000	0.000
NOMJUV	11.763	11.763	11.918	90.000	90.000	120.000	10.028	10.028	13.426	90.000	90.000	120.000	-14.753	-14.753	12.653	0.000	0.000	0.000
NONXOE	9.978	9.263	17.363	90.000	97.260	90.000	10.494	8.298	18.698	90.000	94.859	90.000	5.171	-10.420	7.689	0.000	-2.469	0.000
NUFQEL02	10.394	10.776	11.462	90.000	90.000	90.000	9.306	10.933	12.809	90.000	90.000	90.000	-10.466	1.458	11.753	0.000	0.000	0.000
NUNXOK	22.439	4.764	15.714	90.000	101.167	90.000	21.704	6.423	13.431	90.000	97.606	90.000	-3.276	34.835	-14.528	0.000	-3.520	0.000
NUWHUJ	11.608	11.746	12.603	107.979	112.338	100.396	11.476	12.905	12.872	103.118	114.593	113.477	-1.140	9.864	2.135	-4.502	2.007	13.029

	unoptimized lattice parameters						optimized lattice parameters						% change					
Compound	a (Å)	b (Å)	c (Å)	α (˚)	β (˚)	γ (˚)	a (Å)	b (Å)	c (Å)	α (˚)	β (˚)	γ (˚)	a (Å)	b (Å)	c (Å)	α (˚)	β (˚)	γ (˚)
OJAMIW	9.883	16.419	13.971	90.000	131.564	90.000	10.585	14.587	14.860	90.000	136.089	90.000	7.103	-11.157	6.363	0.000	3.439	0.000
OKIMUR	10.114	10.019	17.394	90.000	96.934	90.000	11.969	8.087	18.925	90.000	95.501	90.000	18.342	-19.283	8.803	0.000	-1.478	0.000
OSAKAV	10.483	12.033	8.126	90.000	91.891	90.000	7.378	16.473	8.080	90.000	80.323	90.000	-29.619	36.903	-0.562	0.000	-12.589	0.000
OSAKEZ	13.196	12.445	15.242	90.000	109.177	90.000	13.829	11.224	14.934	90.000	110.511	90.000	4.796	-9.811	-2.020	0.000	1.222	0.000
OXURUV	10.719	12.040	12.130	103.458	108.499	94.887	10.535	11.036	13.030	90.874	115.029	96.734	-1.714	-8.336	7.424	-12.163	6.018	1.947
OZCDPB	8.400	15.082	17.650	90.000	106.330	90.000	8.761	14.496	19.941	90.000	53.339	90.000	4.298	-3.885	12.980	0.000	-49.836	0.000
PAQVIN	9.168	9.588	16.707	90.000	95.410	90.000	13.358	12.469	9.992	90.000	82.140	90.000	45.702	30.048	-40.193	0.000	-13.908	0.000
PASBAM	7.180	10.346	17.712	90.000	90.000	90.000	7.873	13.363	14.308	90.000	90.000	90.000	9.647	29.161	-19.219	0.000	0.000	0.000
PIGWAE	12.331	12.587	15.119	105.315	100.911	108.965	12.579	12.552	14.902	107.919	99.756	106.588	2.010	-0.276	-1.432	2.473	-1.145	-2.181
PILYAK	7.856	8.148	13.788	74.390	82.770	77.210	7.931	8.986	13.197	74.836	73.391	66.589	0.955	10.285	-4.286	0.600	-11.331	-13.756
POGDOE	10.523	8.992	16.672	90.000	104.142	90.000	10.677	8.164	18.618	90.000	106.920	90.000	1.463	-9.210	11.672	0.000	2.668	0.000
PUHYAT	9.551	10.081	13.248	109.865	97.322	90.643	11.149	9.832	12.939	118.252	86.881	90.337	16.731	-2.465	-2.335	7.634	-10.728	-0.338
PUQVON	16.160	8.097	15.378	90.000	110.982	90.000	16.122	7.593	16.507	90.000	110.874	90.000	-0.233	-6.228	7.342	0.000	-0.097	0.000
PUQVUT	27.517	10.674	13.075	90.000	100.837	90.000	27.191	9.635	15.104	90.000	101.365	90.000	-1.185	-9.734	15.518	0.000	0.524	0.000
QAFPIY	14.745	9.539	30.317	90.000	90.000	90.000	14.859	9.191	30.676	90.000	90.000	90.000	0.774	-3.648	1.186	0.000	0.000	0.000
QEYSET	9.662	25.527	11.181	90.000	90.383	90.000	9.382	27.934	10.649	90.000	100.158	90.000	-2.898	9.429	-4.758	0.000	10.815	0.000
QEYSIX	10.437	11.251	12.736	115.124	95.840	92.309	9.535	11.392	12.661	106.736	95.640	81.777	-8.641	1.253	-0.589	-7.286	-0.209	-11.410
QIBSIE	18.820	9.397	16.324	90.000	109.390	90.000	17.843	10.758	15.487	90.000	105.564	90.000	-5.191	14.483	-5.127	0.000	-3.498	0.000
QOKHAZ	9.980	17.863	12.193	90.000	112.510	90.000	9.604	18.305	12.043	90.000	109.736	90.000	-3.768	2.474	-1.230	0.000	-2.466	0.000
QOPJAH	9.295	9.931	16.482	84.867	79.842	66.327	9.237	8.916	19.866	79.178	63.749	66.938	-0.624	-10.221	20.532	-6.703	-20.156	0.921
QUXQAC	19.916	8.017	16.358	90.000	90.000	90.000	20.837	8.067	14.961	90.000	90.000	90.000	4.622	0.620	-8.537	0.000	0.000	0.000
RABKEK	9.332	10.025	11.668	68.410	68.390	68.580	7.824	9.122	12.240	77.150	76.150	69.550	-16.159	-9.007	4.902	12.776	11.347	1.414
RAQFAQ01	5.323	12.293	13.081	90.000	101.551	90.000	5.496	12.921	12.360	90.000	98.132	90.000	3.244	5.109	-5.513	0.000	-3.367	0.000
RAQQOP	10.834	9.023	8.906	80.340	89.400	79.780	10.186	9.373	8.752	91.044	81.269	97.562	-5.981	3.879	-1.729	13.323	-9.095	22.289
RASRAE	14.224	8.882	22.885	90.000	101.470	90.000	14.169	10.257	19.136	90.000	98.348	90.000	-0.387	15.481	-16.382	0.000	-3.077	0.000
SAHRID	13.316	14.179	14.614	90.000	97.539	90.000	13.667	14.014	14.392	90.000	96.919	90.000	2.633	-1.165	-1.522	0.000	-0.636	0.000
SAHSIE	8.043	18.649	27.034	90.000	96.516	90.000	7.869	19.263	26.530	90.000	96.577	90.000	-2.161	3.295	-1.866	0.000	0.063	0.000
SIFKAU	11.873	12.653	13.005	103.320	106.940	115.980	12.686	12.164	11.167	96.738	106.831	108.434	6.847	-3.865	-14.136	-6.370	-0.102	-6.506

	unoptimized lattice parameters						optimized lattice parameters						% change					
Compound	a (Å)	b (Å)	c (Å)	α (˚)	β (˚)	γ (˚)	a (Å)	b (Å)	c (Å)	α (˚)	β (˚)	γ (˚)	a (Å)	b (Å)	c (Å)	α (˚)	β (˚)	γ (˚)
SUCNUZ	10.625	11.864	15.086	77.860	68.210	69.510	10.660	12.823	14.738	73.258	57.854	68.233	0.329	8.083	-2.307	-5.911	-15.183	-1.837
SUXZOB	10.341	10.833	11.418	89.923	72.080	65.273	10.601	10.532	12.661	97.937	58.733	90.451	2.512	-2.776	10.888	8.912	-18.517	38.573
TAMBUF	9.431	10.950	11.609	80.900	84.410	73.360	9.481	11.202	11.995	85.529	92.192	62.185	0.527	2.301	3.325	5.722	9.219	-15.233
TASCIZ	11.032	9.187	25.426	90.000	96.860	90.000	9.638	9.933	26.255	90.000	106.742	90.000	-12.636	8.120	3.260	0.000	10.202	0.000
TATREM	20.640	7.454	22.897	90.000	101.164	90.000	18.397	8.805	20.353	90.000	95.258	90.000	-10.866	18.118	-11.109	0.000	-5.838	0.000
TIWCUX	21.086	10.831	15.899	90.000	118.930	90.000	20.251	11.236	15.948	90.000	118.656	90.000	-3.960	3.739	0.308	0.000	-0.230	0.000
TOJPIR	11.237	10.992	8.139	90.000	97.320	90.000	8.062	13.022	7.658	90.000	76.439	90.000	-28.255	18.468	-5.910	0.000	-21.456	0.000
TOXPEB	9.252	9.742	11.141	75.920	77.040	87.340	9.970	9.803	10.632	82.121	61.905	87.535	7.760	0.626	-4.569	8.168	-19.646	0.223
TUMFAJ	18.544	11.924	20.901	90.000	96.231	90.000	17.297	12.579	22.457	90.000	94.059	90.000	-6.725	5.493	7.445	0.000	-2.257	0.000
UCARAT	9.593	10.899	11.246	99.450	109.678	96.891	9.816	15.701	10.213	104.902	88.892	130.473	2.321	44.066	-9.188	5.482	-18.952	34.660
UDIKOI	7.792	11.332	13.888	66.876	82.502	73.039	9.396	13.510	11.980	67.895	60.576	70.771	20.584	19.219	-13.738	1.524	-26.576	-3.105
ULAVUZ	9.615	11.534	13.272	82.459	79.280	67.369	12.131	11.216	11.846	72.319	86.034	77.593	26.169	-2.757	-10.747	-12.297	8.519	15.176
ULAWAG	7.703	15.995	18.893	90.000	100.919	90.000	7.505	16.947	19.680	90.000	103.165	90.000	-2.574	5.953	4.166	0.000	2.226	0.000
VAMWIP01	17.505	13.383	6.792	90.000	112.250	90.000	13.588	10.356	11.635	90.000	70.566	90.000	-22.376	-22.618	71.315	0.000	-37.135	0.000
VEJNIH	8.049	18.927	31.080	90.000	90.000	90.000	8.650	19.302	27.423	90.000	90.000	90.000	7.467	1.981	-11.766	0.000	0.000	0.000
VEWREU	14.231	10.487	15.814	84.950	144.280	91.890	14.235	10.329	15.839	85.499	145.660	92.182	0.028	-1.507	0.158	0.646	0.956	0.318
VOCHIF	11.047	14.486	32.048	91.300	99.730	101.610	10.978	14.534	32.153	89.413	103.914	96.859	-0.625	0.331	0.328	-2.067	4.195	-4.676
WABQEX	9.278	11.441	12.276	73.820	72.754	68.680	9.975	14.661	20.166	48.055	33.986	61.717	7.517	28.146	64.266	-34.902	-53.286	-10.138
WACCUA	10.909	4.827	15.980	90.000	100.020	90.000	11.570	4.626	16.347	90.000	92.869	90.000	6.059	-4.166	2.297	0.000	-7.150	0.000
WAJQON01	20.457	11.292	8.409	90.000	91.370	90.000	17.174	17.712	9.756	90.000	61.856	90.000	-16.048	56.854	16.019	0.000	-32.302	0.000
WALQIK	8.737	16.261	6.951	90.000	94.824	90.000	8.055	14.478	8.326	90.000	89.383	90.000	-7.806	-10.965	19.781	0.000	-5.738	0.000
WALQOQ	9.027	17.016	7.210	90.000	95.360	90.000	8.105	18.698	7.273	90.000	100.052	90.000	-10.214	9.885	0.874	0.000	4.920	0.000
WAQBIZ	7.720	12.880	14.316	111.051	97.022	98.520	9.658	11.537	13.996	88.643	113.279	117.475	25.104	-10.427	-2.235	-20.178	16.756	19.240
WATSEP	10.180	25.275	9.665	90.000	90.000	90.000	7.396	12.944	14.244	111.125	103.005	98.951	-27.347	-48.787	47.379	23.472	14.450	9.946
WICSIK	10.412	11.884	12.742	89.892	78.783	81.928	10.765	11.718	12.164	90.020	88.388	87.887	3.387	-1.398	-4.538	0.142	12.192	7.273
WILNOV	8.770	9.733	12.857	81.219	81.435	74.993	10.963	7.413	13.924	101.376	75.270	81.233	25.006	-23.836	8.299	24.817	-7.570	8.321
WIMKIN	14.196	10.984	15.590	90.000	116.482	90.000	13.468	12.130	14.590	90.000	113.596	90.000	-5.126	10.432	-6.416	0.000	-2.478	0.000
WITQOF	11.104	12.671	13.124	92.420	109.300	99.480	11.394	12.874	13.843	98.317	114.883	106.096	2.612	1.602	5.479	6.381	5.108	6.651

	unoptimized lattice parameters						optimized lattice parameters						% change					
Compound	a (Å)	b (Å)	c (Å)	α (˚)	β (˚)	γ (˚)	a (Å)	b (Å)	c (Å)	α (˚)	β (˚)	γ (˚)	a (Å)	b (Å)	c (Å)	α (˚)	β (˚)	γ (˚)
WOCYUJ	15.300	23.967	20.180	90.000	99.930	90.000	14.797	24.220	20.072	90.000	97.840	90.000	-3.288	1.056	-0.535	0.000	-2.091	0.000
WUXGAY	15.755	17.460	20.784	90.000	115.010	90.000	17.444	17.996	18.955	90.000	80.248	90.000	10.720	3.069	-8.800	0.000	-30.225	0.000
XAGKEX	7.413	10.923	12.087	98.073	106.450	99.980	8.421	12.828	10.785	99.764	111.874	100.541	13.605	17.440	-10.770	1.724	5.095	0.561
XAGKIB	7.209	12.928	16.536	90.000	115.624	90.000	7.374	12.712	17.593	90.000	121.178	90.000	2.283	-1.671	6.392	0.000	4.804	0.000
XANCOG	11.108	12.614	11.312	99.070	110.680	109.920	12.257	12.483	12.024	103.673	111.657	114.609	10.344	-1.039	6.294	4.646	0.883	4.266
XIJFOL	16.857	13.390	8.871	90.000	109.191	90.000	18.537	13.243	8.495	90.000	112.584	90.000	9.966	-1.094	-4.234	0.000	3.107	0.000
XIRBUW	13.781	14.517	21.279	90.000	90.000	90.000	13.919	14.352	20.982	90.000	90.000	90.000	1.001	-1.137	-1.396	0.000	0.000	0.000
XIRCEH	28.043	9.858	18.872	90.000	116.997	90.000	29.571	9.476	19.042	90.000	114.079	90.000	5.449	-3.875	0.901	0.000	-2.494	0.000
XISSAT	9.295	13.680	15.390	90.000	98.365	90.000	10.019	12.763	15.193	90.000	86.553	90.000	7.793	-6.700	-1.282	0.000	-12.008	0.000
XOPDUB	8.158	9.070	11.019	68.089	82.769	74.970	8.521	8.554	12.816	58.733	79.806	71.508	4.448	-5.686	16.311	-13.741	-3.580	-4.618
XUZZAU	8.698	12.120	15.115	91.885	98.639	97.444	8.485	11.937	15.280	90.983	95.889	95.286	-2.448	-1.506	1.094	-0.982	-2.788	-2.215
YAGLAT01	9.943	12.229	12.616	112.530	82.570	91.550	8.965	11.803	14.491	112.282	95.787	91.885	-9.836	-3.484	14.862	-0.220	16.007	0.366
YAQWEU	9.284	9.309	11.899	102.136	93.599	108.409	8.350	9.402	12.101	102.988	92.872	97.687	-10.060	1.002	1.698	0.834	-0.777	-9.890
YAZZAB	10.033	10.147	10.431	67.151	62.715	72.064	10.782	9.547	10.338	68.679	62.058	68.014	7.465	-5.913	-0.892	2.275	-1.048	-5.620
YENSIT	11.218	11.680	15.360	93.422	110.575	90.951	11.460	12.048	15.089	103.174	113.826	76.521	2.157	3.151	-1.764	10.439	2.940	-15.866
YORFOA	8.090	11.676	14.803	90.000	121.506	90.000	9.530	11.147	13.843	90.000	113.261	90.000	17.800	-4.531	-6.485	0.000	-6.786	0.000
YUCXAW	11.093	11.266	12.642	109.250	95.430	105.620	11.998	12.263	10.211	101.571	99.496	88.613	8.158	8.850	-19.230	-7.029	4.261	-16.102
ZAXWOK	17.429	8.932	18.443	90.000	112.490	90.000	17.837	8.602	20.069	90.000	119.418	90.000	2.341	-3.695	8.816	0.000	6.159	0.000
ZOXGAU	14.146	18.003	5.372	90.000	90.000	90.000	14.821	18.283	5.277	90.000	90.000	90.000	4.772	1.555	-1.768	0.000	0.000	0.000

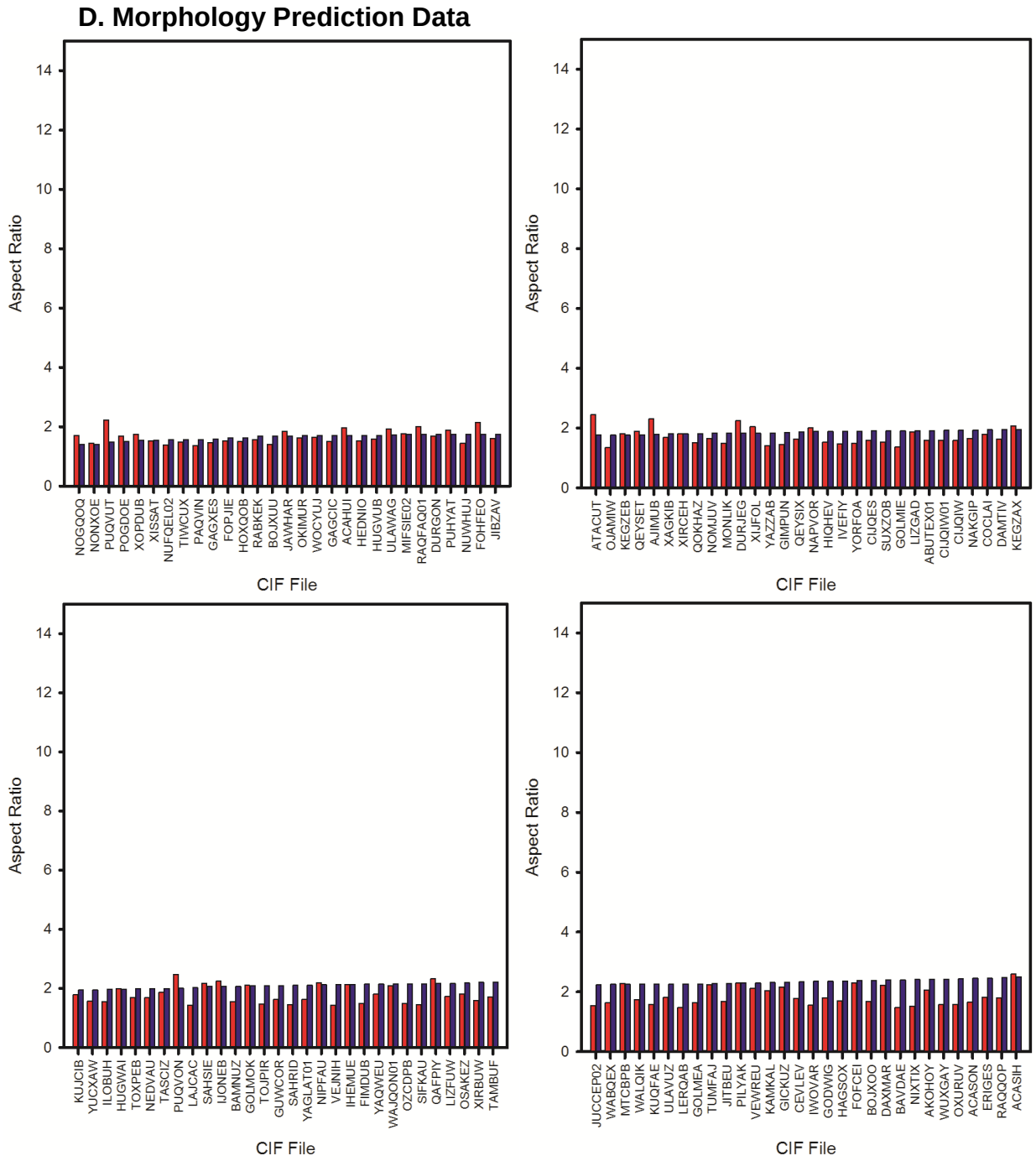

Figure S3-7. Predicted aspect ratios for CIF files included in calculations. BFDH theory values are plotted in red and AE theory values are in blue. Data is reported in Table S3-3.

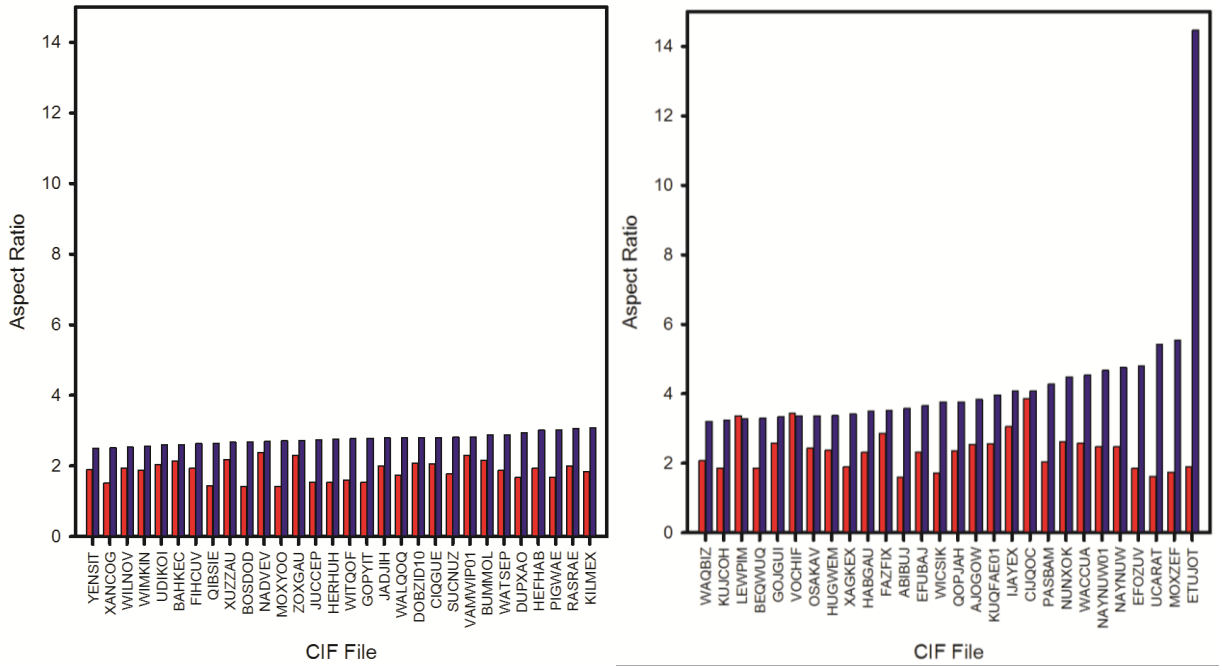

Figure S3-8. Predicted aspect ratios for CIF files included in calculations. BFDH theory values are plotted in red and AE theory values are in blue. Data is reported in Table S3-3.

Table S3-2. Data for interactions present in compounds that showed a 75% or larger change in aspect ratio when calculated by the AE method compared to the BFDH method.

CIF	BFDH AR	AE AR	% Change	Observed Intermolecular Interactions
WACCUA	2.583	4.536	75.610	H-bonding, Pb-π
DUPXAO	1.674	2.949	76.165	H-bonding, π-π
BEQWUQ	1.853	3.295	77.820	Pb-S
JUCCEP	1.529	2.733	78.744	van der Waals
PIGWAE	1.684	3.029	79.869	π-π
XAGKEX	1.897	3.426	80.601	H-bonding, π-π
HERHUH	1.53	2.767	80.850	van der Waals
GOPYIT	1.529	2.788	82.341	H-bonding
QIBSIE	1.437	2.639	83.646	aromatic H-O
NAYNUW01	2.471	4.672	89.073	Pb-S
BOSDOD	1.412	2.685	90.156	H-bonding, π-π
MOXYOO	1.427	2.714	90.189	H-bonding, π-π
WICSIK	1.726	3.763	118.019	H-bonding, π-π
ABIBUJ	1.591	3.581	125.079	Pb-π
EFOZUV	1.855	4.796	158.544	Pb-S interaction, π-π
MOXZEF	1.732	5.54	219.861	H-bonding, π-π
UCARAT	1.624	5.413	233.313	halogen bonding
ETUJOT	1.899	7.123	275.092	Pb-O interaction, π-π

Table S3-3. Predict BFDH aspect ratios (BFDH AR), as well as energy of crystallization (Elatt) and attachment energy aspect ratios (AE AR) for all CIF files after a constrained (Const.) and unconstrained (Unconst.) geometry optimization. Also contains predicted AE AR with partial bonding to represent electron delocialization after a unconstrained geometry optimization.

CIF File	BFDH AR	AE AR Const.	E_{latt} Const.	AE AR partial bonds	E_{latt} Unconst.	AE AR Unconst.
NOGQOQ	1.697	1.402	-482.154	1.441	-303.684	1.837
NONXOE	1.446	1.413	-190.608	1.407	-166.069	1.579
PUQVUT	2.220	1.475	-332.123	1.475	-493.292	2.105
POGDOE	1.680	1.495	-194.920	1.468	-109.700	1.686
XOPDUB	1.745	1.535	-100.042	2.021	-88.537	2.244
XISSAT	1.516	1.551	-257.687	1.861	-254.248	1.823
NUFQEL02	1.379	1.557	-158.469	1.557	-169.176	2.304
TIWCUX	1.486	1.560	-344.034	1.751	-323.927	2.230
PAQVIN	1.358	1.570	-2219.252	1.570	-203.691	1.821
GAGXES	1.464	1.582	-197.131	1.582	-202.098	2.041
FOPJIE	1.533	1.613	-526.131	1.504	-797.855	1.422
HOXQOB	1.506	1.626	-5418.562	1.626	-3393.542	1.637
RABKEK	1.569	1.678	-86.882	1.531	-345.434	1.628
BOJXUU	1.399	1.679	-192.095	1.679	-199.840	1.631
JAWHAR	1.845	1.683	-1930.351	1.683	-133.933	1.594
OKIMUR	1.616	1.693	-135.154	1.693	-134.145	failed
WOCYUJ	1.633	1.694	-374.918	1.694	-374.619	1.735
GAGCIC	1.501	1.696	-266.082	1.696	-330.821	1.551
ACAHUI	1.958	1.707	-191.651	1.707	-189.377	1.551
HEDNIO	1.521	1.708	-284.383	1.708	-239.968	1.697
HUGVUB	1.585	1.712	-109.747	1.712	-107.021	1.820
ULAWAG	1.920	1.727	-237.655	1.727	-223.570	2.115
MIFSIE02	1.759	1.734	-732.889	1.734	-12157.167	failed
RAQFAQ01	2.005	1.737	-287.997	1.644	-122.961	2.552
DURGON	1.692	1.739	-225.414	1.740	-246.095	1.686
PUHYAT	1.882	1.744	-114.721	1.727	-137.836	2.073
NUWHUJ	1.436	1.747	-298.696	1.747	-265.002	1.719
FOHFEO	2.134	1.749	-518.689	1.749	-563.542	1.613
JIBZAV	1.611	1.752	-122.446	1.752	-107.583	2.036
ATACUT	2.440	1.759	-352.935	1.759	-391.498	1.759
OJAMIW	1.344	1.759	-237.045	1.754	-146.976	1.950
KEGZEB	1.809	1.764	-116.655	1.764	-372.619	3.204
QEYSET	1.892	1.773	-686.756	1.922	-424.341	1.939
AJIMUB	2.301	1.800	-310.370	1.800	-325.953	1.797
XAGKIB	1.684	1.811	-288.893	1.777	-279.763	1.744
XIRCEH	1.807	1.812	-496.810	1.812	-457.280	1.765
QOKHAZ	1.502	1.813	-214.771	1.826	-482.068	2.672
NOMJUV	1.653	1.828	-133.895	1.828	-206.970	1.397

MONLIK	1.481	1.829	-474.629	1.869	-257.982	2.216

CIF file	BFDH AR	AE AR Const.	E_{latt} Const.	AE AR partial bonds	E_{latt} Unconst.	AE AR Unconst.
DURJEG	2.243	1.830	-115.817	2.020	-131.443	1.529
XIJFOL	2.046	1.831	-225.098	1.868	-231.857	1.909
YAZZAB	1.409	1.836	-92.223	1.836	-101.243	1.733
GIMPUN	1.456	1.852	-311.291	1.801	-340.515	1.607
QEYSIX	1.629	1.878	-408.346	1.875	-339.215	2.052
NAPVOR	2.008	1.880	-251.106	1.891	-202.150	3.863
HIQHEV	1.528	1.881	-254.023	1.956	-282.858	1.897
IVEFIY	1.475	1.890	-118.475	2.032	-127.167	3.237
YORFOA	1.499	1.891	-90.354	1.682	-113.473	1.651
CIJQES	1.590	1.900	-120.079	1.886	-127.792	1.858
SUXZOB	1.536	1.904	-94.673	1.904	-100.071	1.985
GOLMIE	1.377	1.911	-510.610	2.029	-481.787	2.673
LIZGAD	1.867	1.914	-328.793	1.914	-287.505	failed
PASBAM	2.030	1.918	-150.058	3.676	-113.041	2.453
ABUTEX01	1.598	1.920	-399.779	1.920	-531.295	2.158
CIJQIW01	1.590	1.922	-123.930	1.924	-129.173	1.913
CIJQIW	1.588	1.928	-121.617	1.930	-128.831	1.904
NAKGIP	1.657	1.933	-585.933	1.933	-420.760	2.060
COCLAI	1.797	1.943	-331.173	1.803	-332.664	1.727
DAMTIV	1.632	1.946	-281.407	2.231	-184.177	2.769
KEGZAX	2.067	1.947	-186.147	1.947	-129.495	3.263
KUJCIB	1.789	1.953	-218.562	2.464	-142.391	1.932
YUCXAW	1.575	1.953	-234.759	2.377	-287.466	1.771
ILOBUH	1.557	1.966	-190.903	1.965	-218.544	2.216
HUGWAI	1.983	1.980	-472.612	1.980	-468.913	1.918
TOXPEB	1.692	1.986	-484.999	1.986	-546.037	2.418
NEDVAU	1.682	1.990	-215.312	1.990	-276.346	failed
TASCIZ	1.862	1.998	-217.138	1.786	-276.353	1.831
PUQVON	2.470	2.007	-148.271	2.007	-378.816	1.540
LAJCAC	1.425	2.020	-199.592	2.020	-237.695	2.388
SAHSIE	2.167	2.066	-286.836	2.066	-167.918	1.935
IJONEB	2.245	2.073	-138.101	2.073	-140.286	2.236
BAMNUZ	1.558	2.074	-421.629	1.463	-2310.749	1.607
GOLMOK	2.106	2.095	-156.089	2.078	-112.962	2.842
TOJPIR	1.479	2.096	-64.005	1.878	-110.594	1.536
GUWCOR	1.622	2.098	-420.570	2.157	-395.425	2.353
SAHRID	1.451	2.101	-172.397	2.101	-290.183	2.118
YAGLAT01	1.632	2.107	-424.265	2.107	-508.020	2.075
NIPFAU	2.190	2.127	-530.545	2.128	-82.958	2.054

CIF file	BFDH AR	AE AR Const.	E_{latt} Const.	AE AR partial bonds	E_{latt} Unconst.	AE AR Unconst.
VEJNIH	1.432	2.130	-641.187	2.130	-710.524	2.267
IHEMUE	2.129	2.138	-168.430	2.167	-172.409	2.179
FIMDUB	1.492	2.140	-299.211	2.189	-288.900	2.248
YAQWEU	1.810	2.144	-130.934	2.144	-177.966	2.525
WAJQON01	2.096	2.152	-388.375	2.152	-779.668	2.106
OZCDPB	1.497	2.152	-148.090	2.152	-1850.427	1.419
SIFKAU	1.461	2.159	-207.359	2.049	-230.026	2.670
QAFPIY	2.323	2.161	-472.699	2.137	-805.153	1.928
LIZFUW	1.722	2.161	-137.412	2.161	-329.139	1.976
OSAKEZ	1.809	2.183	-265.192	2.183	-321.300	2.157
XIRBUW	1.591	2.202	-481.014	2.202	-496.120	2.164
TAMBUF	1.704	2.215	-192.221	2.817	-201.535	2.650
JUCCEP02	1.545	2.241	-102.614	2.970	-418.500	2.321
WABQEX	1.633	2.248	-97.892	2.277	-122.094	3.048
MTCBPB	2.275	2.249	-322.139	2.249	-148.545	2.633
WALQIK	1.745	2.251	-115.426	2.251	-138.387	2.402
KUQFAE	1.578	2.253	-68.185	2.317	-142.041	2.908
ULAVUZ	1.818	2.257	-111.134	2.257	-103.431	2.065
LERQAB	1.482	2.266	-215.041	2.309	-158.750	2.214
GOLMEA	1.641	2.267	-69.371	2.218	-88.630	2.253
TUMFAJ	2.230	2.280	-394.713	failed	-368.419	2.328
JITBEU	1.682	2.285	-108.451	2.248	-107.993	2.493
PILYAK	2.293	2.299	-126.801	2.736	-203.513	1.424
VEWREU	2.112	2.302	-144.970	2.368	-150.223	2.333
KAMKAL	2.046	2.312	-390.429	3.508	-229.210	2.531
GICKUZ	2.160	2.325	-186.159	2.432	-199.398	1.763
CEVLEV	1.774	2.331	-174.670	2.318	-174.311	2.229
IWOVAR	1.549	2.356	-166.916	2.408	-190.853	2.474
GODWIG	1.805	2.358	-121.145	2.358	-127.116	2.341
HAGSOX	1.687	2.360	-209.770	2.320	-214.300	2.392
FOFCEI	2.294	2.371	-132.992	2.371	-124.650	3.152
BOJXOO	1.686	2.380	-80.782	2.380	-81.289	2.353
DAXMAR	2.223	2.400	-392.430	2.400	-374.975	1.963
BAVDAE	1.470	2.402	-377.727	2.402	-381.775	2.356
NIXTIX	1.514	2.410	-84.083	2.410	-483.941	1.421
AKOHOY	2.050	2.412	-122.249	2.427	-125.271	2.942
WUXGAY	1.571	2.414	-610.834	2.254	-563.447	2.450
OXURUV	1.581	2.431	-263.830	2.431	-173.837	1.933
ACASON	1.657	2.451	-397.724	2.206	-415.262	2.415

CIF File	BFDH AR	AE AR Const.	E_{latt} Const.	AE AR partial bonds	E_{latt} Unconst.	AE AR Unconst.
ERIGES	1.823	2.456	-104.083	2.680	-124.838	2.976
RAQQOP	1.796	2.485	-112.317	2.485	-383.065	2.756
ACASIH	2.591	2.488	-143.650	2.499	-152.604	2.227
YENSIT	1.896	2.507	-167.440	2.404	-209.408	2.100
XANCOG	1.519	2.515	-176.663	2.090	-202.344	2.329
WILNOV	1.943	2.535	-105.816	2.535	-121.434	2.352
WIMKIN	1.885	2.555	-405.997	2.632	-516.628	2.232
UDIKOI	2.033	2.602	-201.759	2.602	-180.965	1.736
BAHKEC	2.146	2.608	-139.839	2.054	-141.787	2.611
FIHCUV	1.937	2.637	-130.044	2.351	-166.564	3.709
QIBSIE	1.437	2.639	-371.833	2.167	-228.035	1.785
XUZZAU	2.173	2.673	-107.067	2.673	-111.339	2.870
BOSDOD	1.412	2.685	-92.347	3.003	-82.212	4.302
NADVEV	2.388	2.697	-149.321	2.697	-580.084	1.950
MOXYOO	1.427	2.714	-252.396	2.660	-103.877	4.289
ZOXGAU	2.299	2.729	-125.394	2.421	-114.288	2.428
JUCCEP	1.529	2.733	-95.550	3.211	-111.027	2.456
HERHUH	1.530	2.767	103.175	2.141	-124.252	2.174
WITQOF	1.602	2.776	-136.827	2.776	-126.030	2.473
GOPYIT	1.529	2.788	-234.969	2.071	-290.606	1.533
JADJIH	2.005	2.795	-166.916	3.224	-2241.888	1.617
WALQOQ	1.732	2.798	-102.614	2.798	-127.743	4.687
DOBZID10	2.080	2.802	-116.562	2.903	-273.313	2.275
CIQGUE	2.060	2.808	-168.869	2.808	-175.653	2.816
SUCNUZ	1.781	2.811	-152.337	3.214	-150.991	2.235
VAMWIP01	2.290	2.821	-186.848	2.821	-187.002	1.904
BUMMOL	2.150	2.880	-71.538	2.860	-82.970	2.879
WATSEP	1.871	2.882	-247.983	2.882	-263.765	3.125
DUPXAO	1.674	2.949	-130.479	2.973	-123.941	2.377
HEFHAB	1.934	3.021	-118.299	3.021	-122.937	2.705
PIGWAE	1.684	3.029	-115.757	3.029	-136.878	2.041
RASRAE	2.004	3.061	-277.786	2.167	-175.503	2.108
KILMEX	1.832	3.082	-333.810	3.082	-222.635	2.414
WAQBIZ	2.081	3.210	-85.117	2.659	-104.233	2.499
KUJCOH	1.864	3.244	-125.533	1.744	-66.845	2.376
LEWPIM	3.365	3.272	-117.723	3.343	-142.890	2.500
BEQWUQ	1.853	3.295	-262.680	3.294	-271.292	3.100
GOJGUI	2.586	3.348	-179.926	3.561	-151.196	2.953
VOCHIF	3.433	3.355	-404.253	3.355	-411.606	3.261

CIF File	BFDH AR	AE AR Const.	E_{latt} Const.	AE AR partial bonds	E_{latt} Unconst.	AE AR Unconst.
OSAKAV	2.431	3.368	-89.056	4.394	-306.807	2.408
HUGWEM	2.371	3.370	-115.731	3.370	-117.517	3.958
XAGKEX	1.897	3.426	-85.648	3.682	-90.758	2.090
HABGAU	2.316	3.507	-121.372	3.507	-121.979	3.236
FAZFIX	2.852	3.531	-225.078	3.589	-246.291	2.716
ABIBUJ	1.591	3.581	-126.746	3.146	-129.210	2.942
EFUBAJ	2.316	3.659	-508.622	3.125	-482.513	3.544
WICSIK	1.726	3.763	-164.158	2.757	-159.558	2.853
QOPJAH	2.350	3.764	-450.979	2.965	-270.357	failed
AJOGOW	2.548	3.833	-571.539	3.994	-605.029	4.018
KUQFAE01	2.560	3.967	-118.822	3.796	-255.343	2.071
IJAYEX	3.051	4.080	-232.048	4.080	-167.652	1.737
CIJQOC	3.863	4.088	-237.837	4.081	-242.610	3.969
NUNXOK	2.621	4.489	-199.211	4.581	-303.684	1.837
WACCUA	2.583	4.536	-88.713	4.536	-94.876	5.623
NAYNUW01	2.471	4.672	-183.969	4.672	-248.886	1.980
NAYNUW	2.471	4.760	-184.952	4.706	-203.595	3.912
EFOZUV	1.855	4.796	-121.356	4.483	-131.247	3.622
UCARAT	1.624	5.413	-210.518	2.362	-186.152	2.372
MOXZEF	1.732	5.540	-92.778	5.481	-399.845	1.944
ETUJOT	1.899	7.123	-322.391	26.804	-409.279	8.864
ZAXWOK	1.404	failed†	-224.969	failed†	-227.978	failed†
NETVIR	1.443	failed†	-303.724	failed†	-524.161	2.118
MAWNON	1.583	failed†	-297.911	failed†	-552.56	failed
DODMUF	1.614	failed†	-3516.158	failed†		
QUXQAC	1.635	failed†	-245.176	1.891	-116.469	2.812
MAWPAB	1.753	failed†	-515.599	failed†	-755.287	1.71
TATREM	1.921	failed†	-416.802	failed†	-458.744	failed†
BURPIO	1.954	failed†	-399.174	failed†	-493.66	failed†
AYUDON	1.957	failed†	-190.572	1.961	-238.234	1.842

†Calculations fail when a morphology is predicted to be unstable.

E. Top 5% Aspect Ratio Data

Table S3-4 Predicted aspect ratios and lattice energies for the highest 5% of predicted aspect ratios, sorted smallest to largest. Normalized E_{latt} is the energy per molecule in the unit cell.

CIF File	AE AR	E_{latt} (kcal/mol)	# of unique faces	Normalized E_{latt} (kcal/mol)	E_{attach} smallest face (kcal/mol)	E_{attach} largest face (kcal/mol)
AJOGOW	3.833	-571.539	3	-190.513	-125.997	-71.703
KUQFAE01	3.967	-118.822	3	-39.607	-84.308	-24.667
IJAYEX	4.080	-232.048	6	-38.675	-30.657	-95.579
CIJQOC	4.088	-237.837	3	-79.279	-99.244	-42.581
NUNXOK	4.489	-199.211	5	-39.842	-149.674	-35.186
WACCUA	4.536	-88.713	5	-17.743	-67.643	-16.099
NAYNUW01	4.672	-183.969	3	-61.323	-105.712	-32.65
EFOZUV	4.796	-121.356	5	-24.271	-73.338	-16.416
MOXZEF	5.54	-92.778	4	-23.195	-83.589	-15.809
ETUJOT	7.125	-322.391	5	-64.478	-281.629	-27.367

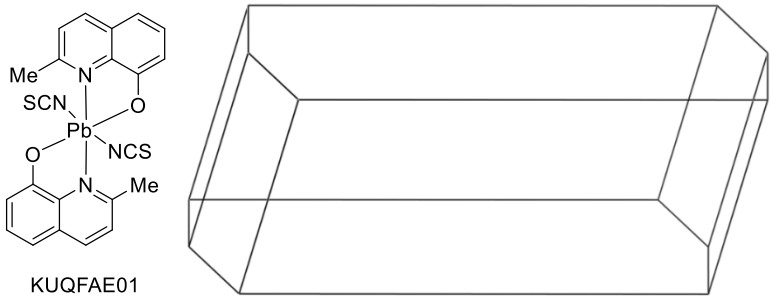

Figure S3-9. Molecular diagram and predicted morphology for KUQFAE01.[5]

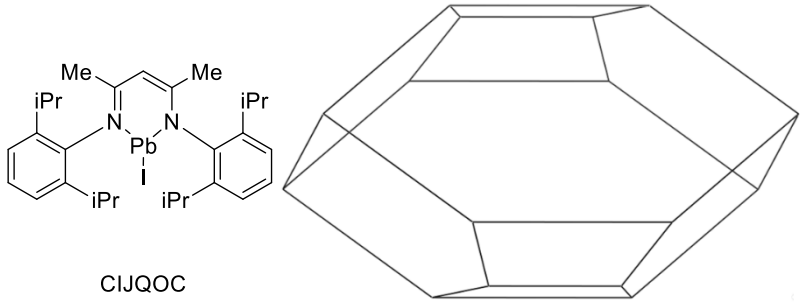

Figure S3-10. Molecular diagram and predicted morphology for CIJQOC.[6]

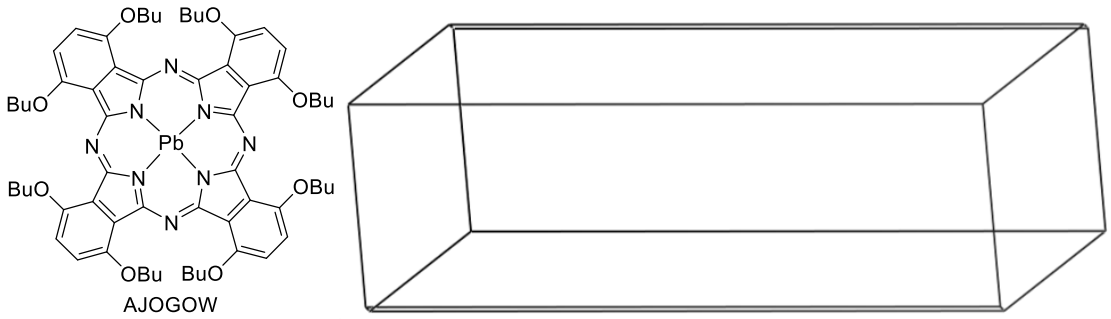

Figure S3-11. Molecular diagram and predicted morphology for AJOGOW.[7]

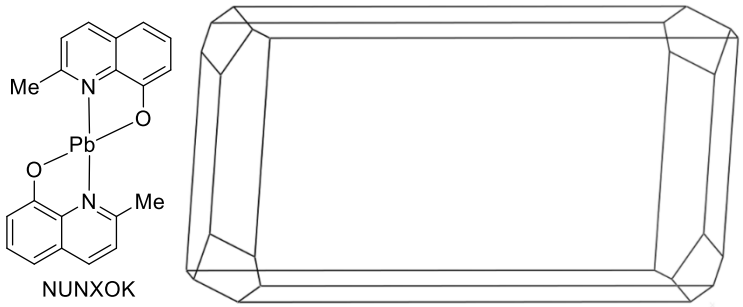

Figure S3-12. Molecular diagram and predicted morphology for NUNXOK.[3]

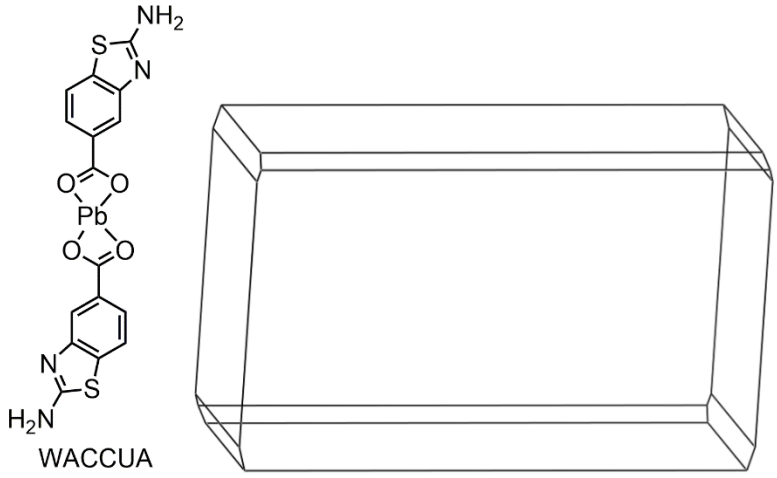

Figure S3-13. Molecular diagram and predicted morphology for WACCUA.[8]

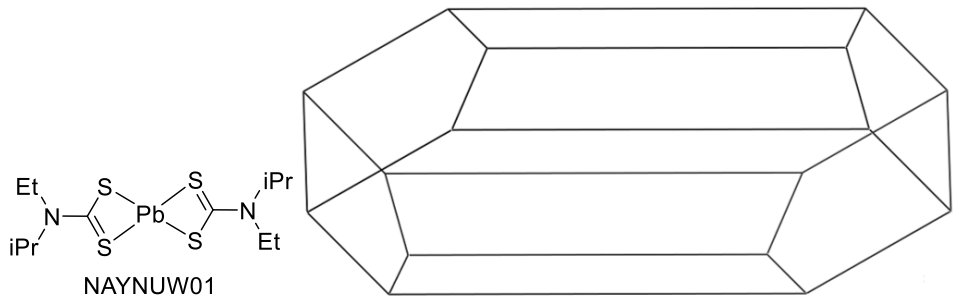

Figure S3-14. Molecular diagram and predicted morphology for NAYNUW01.[1,2]

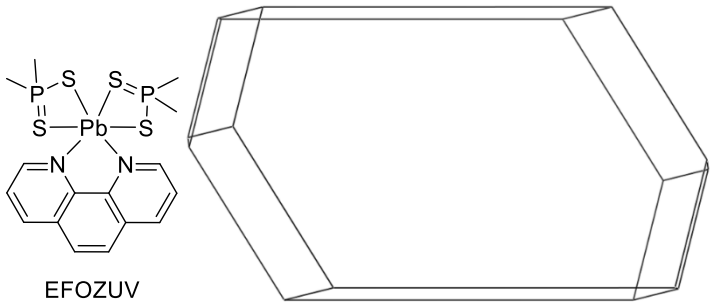

Figure S3-15. Molecular diagram and predicted morphology for EFOZUV.[9]

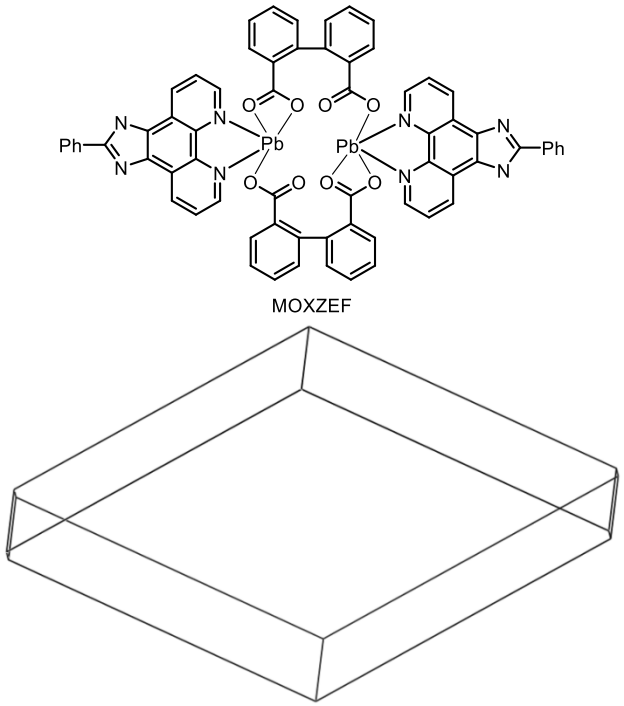

Figure S3-16. Molecular diagram and predicted morphology for MOXZEF.[10]

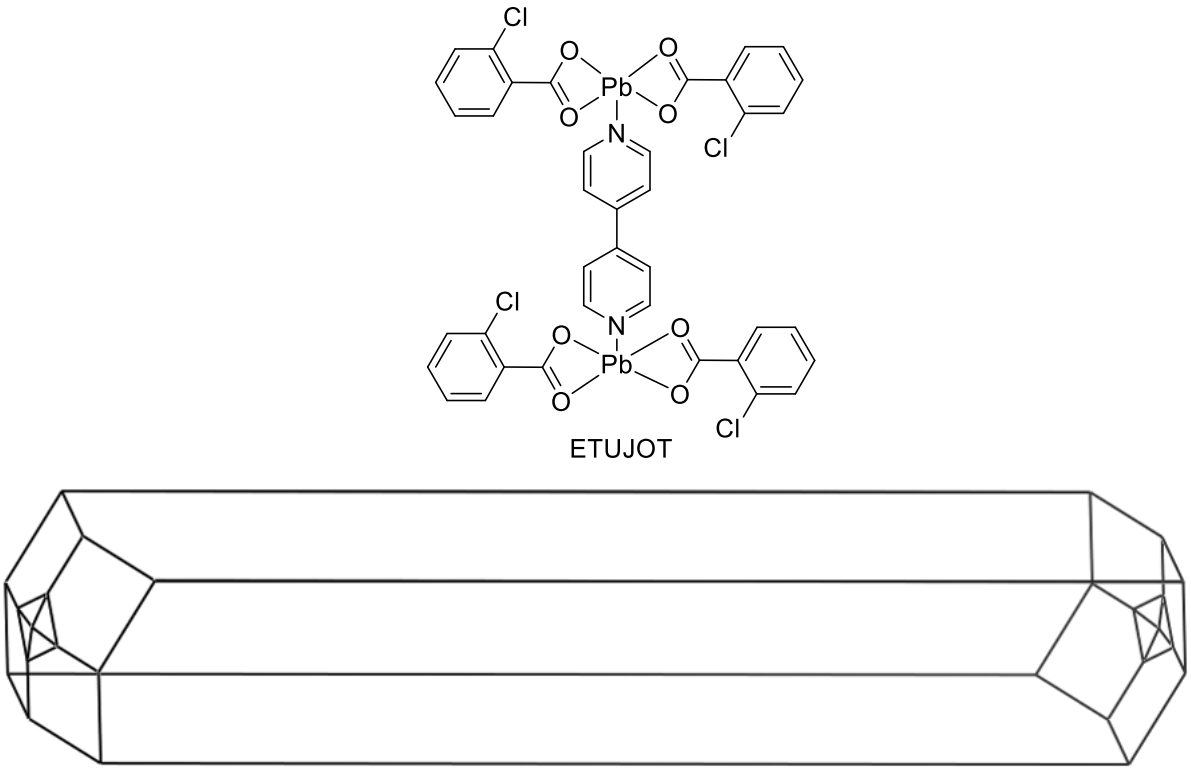

Figure S3-17. Molecular diagram and predicted morphology for ETUJOT.[11]

F. Resonance Structure Effect on Morphology Prediction

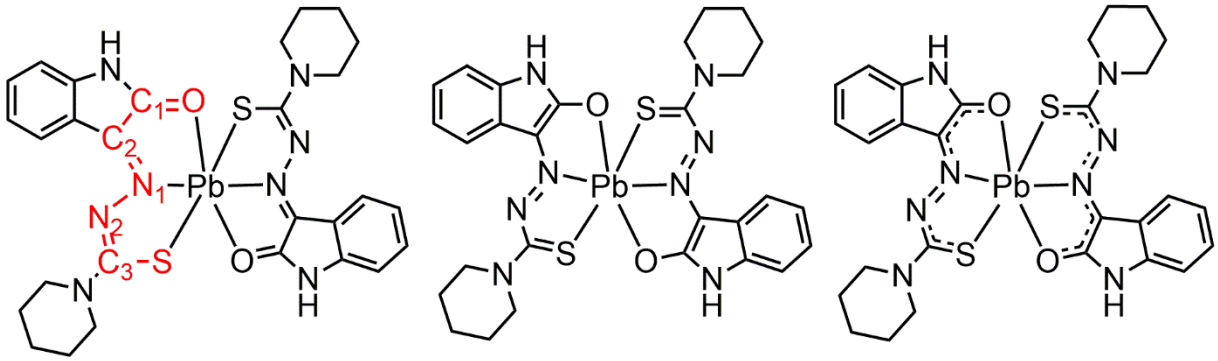

Figure S3-18. Resonance structures of **3**[12] used in morphology calculations. Structures **3** I, **3** II, and **3** III were used to predict morphologies in **Figure S3-19**.

Table S3-5. Bond length data and predicted aspect ratios for structures unoptimized 1a (from CIF file), and optimized $\mathbf{3}_{i}$, $\mathbf{3}_{ii}$, and $\mathbf{3}_{iii}$.

3	O-C_1 (Å)	C_1-C_2 (Å)	C_2-N_1 (Å)	N_1-N_2 (Å)	N_2-C_3 (Å)	C_3-S (Å)	Aspect Ratio
Unoptimized	1.211	1.488	1.300	1.347	1.355	1.726	n/a
$\mathbf{3}_{i}$	1.218	1.429	1.279	1.391	1.289	1.806	3.619
$\mathbf{3}_{ii}$	1.393	1.362	1.403	1.269	1.419	1.429	3.607
$\mathbf{3}_{iii}$	1.273	1.352	1.324	1.318	1.339	1.491	2.505

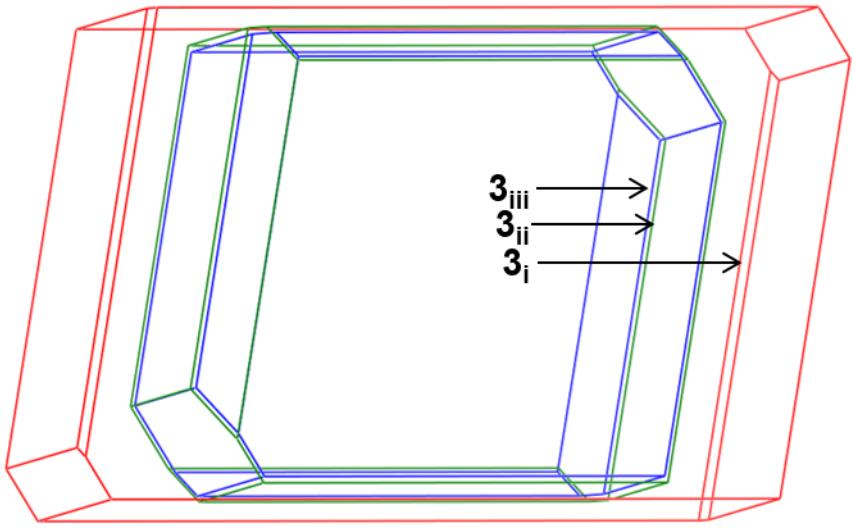

Figure S3-19. Predicted morphologies for resonance structures $\mathbf{3}_{i}$ (red), $\mathbf{3}_{ii}$ (green), and $\mathbf{3}_{iii}$ (blue).

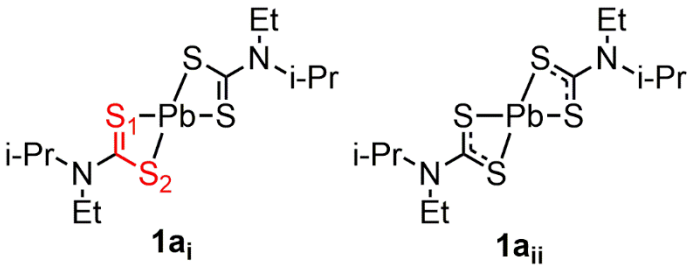

Figure S3-20. Resonance structures for **1a** used in morphology calculations. Resonance structures **1a**$_{i}$ and **1a**$_{ii}$ correspond to predict morphologies in **Figure S3-21**.

Table S3-6. Bond length data and predicted aspect ratios for unoptimized **1a** (from CIF file), and optimized **1a**$_{i}$ and **1a**$_{ii}$.

	S1-C (Å)	C-S$_2$ (Å)	Aspect Ratio
Unoptimized	1.720	1.728	n/a
1a$_{i}$	1.507	1.506	4.672
1a$_{ii}$	1.507	1.506	4.672

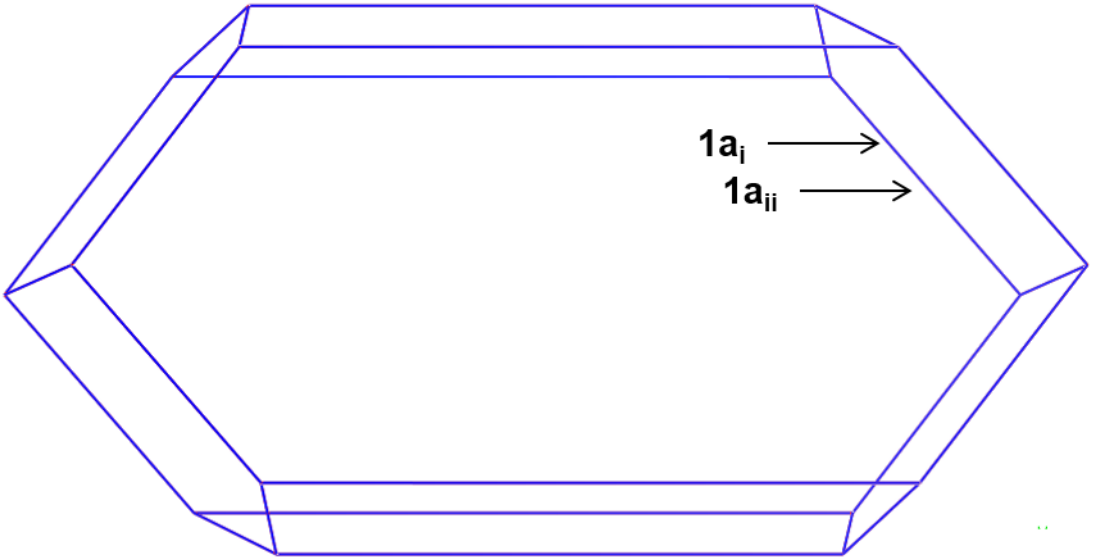

Figure S3-21. Predicted morphologies for resonance structures **1a** I (red) and **1a** II (blue). Note: predicted morphologies overlay perfectly.

V. Gel Experiments

Procedure for determining cgc for 1d. The cgc was determined by adding a known amount of **1d** (~1–10 mg) into an 8 mL vial containing 1 mL of solvent. The vial was capped, heated to dissolve the solid, and allowed to cool with approximately 20 s of sonication in a H_2O bath (near ambient temperature). If the resulting gel was stable to inversion, then 0.1 mL of solvent was added and the procedure was repeated until the gel was no longer stable to inversion. If no gel formed initially, then additional compound was added and the procedure was repeated until the solubility limit at the boiling point of the solvent was reached.

Procedure for triggering gelation for 2b and cgc determination. A known amount of **2b** was weighed out and placed in an 8 mL vial with 0.5 mL of EtOH. Then, 50 µL of HOAc was added and the vial was shaken to dissolve. Next, 1 mL of 1M NaOH was added in 0.1 mL increments. Finally, the vial was capped and heated to dissolve, then allowed to cool with ~30 s of sonication in a H_2O bath (near ambient temperature). The cgc of **2b** was determined by decreasing the amount weighed out until gelation no longer occurred.

Table S3-7. Cgcs for gelators **1d** and **2b** in various solvent conditions.

compound	acetone	ethyl acetate	basic H_2O/EtOH
1d	1.99 ± 0.00 mM	1.46 ± 0.01 mM	precip.
2b	precip.	precip.	13.9 ± 0.3

VI. Rheological Data

General Procedure – Rheological measurements were taken on an AR2000ex rheometer (TA Instruments) with a 25 mm serrated parallel plate. A gel was loaded onto the plate. The gap was then fixed at 300 μm for **1d** and 500 μm for **2b**. A solvent trap was used to limit solvent evaporation. After 30 min, the sample was pre-sheared under a stress of 0.1 Pa for 30 s before conducting the frequency sweep and oscillating stress sweep experiments. All measurements were repeated an average of 5 times to verify reproducibility. The frequency sweep experiment was performed under 0.1 Pa stress with a frequency range from 0.628 to 628 rad/s (i.e., 0.1 Hz–100 Hz). The oscillating stress sweep experiment was performed at 1 Hz, with a stress range from 0.03 to 150 Pa.

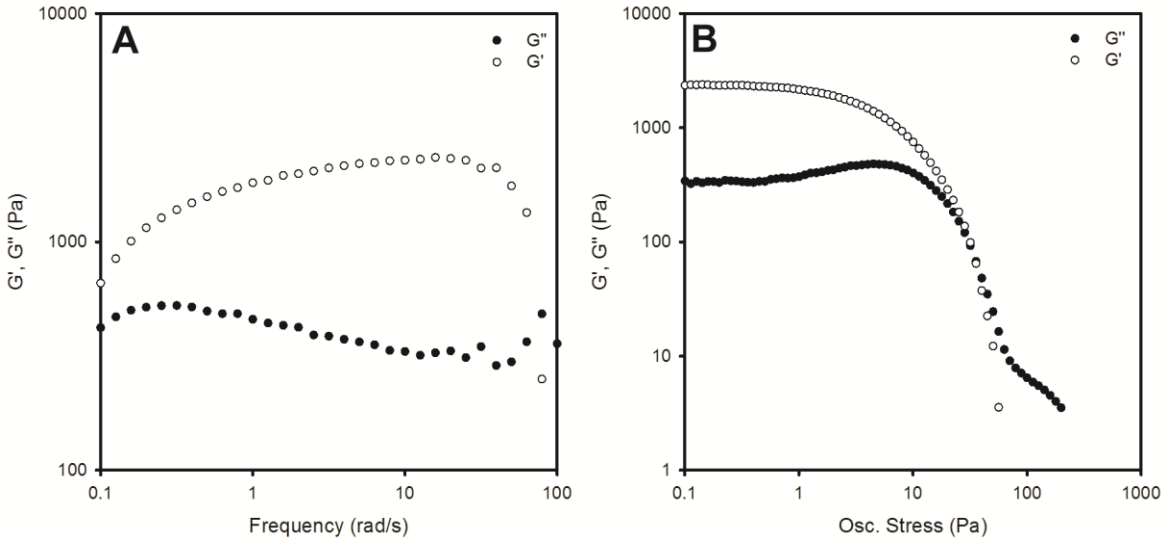

Figure S3-22. (A) Frequency sweep and (B) oscillating stress sweep of a gel of **1d** (7.18 mM in EtOAc).

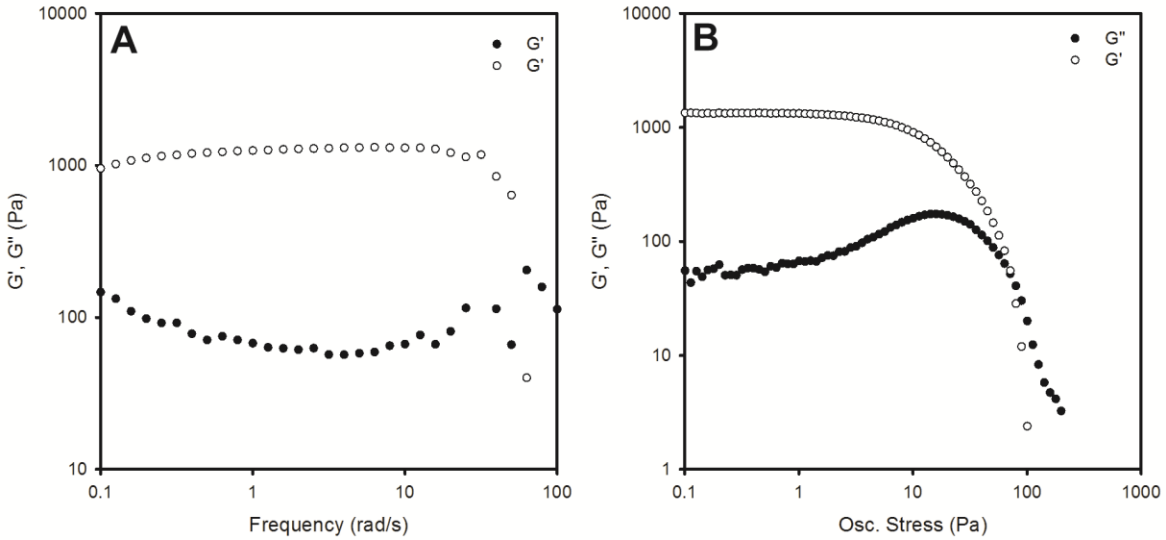

Figure S3-23. A) Frequency sweep and B) oscillating stress sweep of a gel of **2b** (13.9 mM in H_2O/EtOH solution at pH 12).

VII. Scanning Electron Microscopy Images

General Procedure –. A wet gel sample of **1d** and **2b** were mounted with copper tape onto a stainless steel SEM holder and dried under vacuum. Samples were sputter-coated with Au for 30 s to reduce charge build-up during imaging. All gels were imaged using the high vacuum mode on a Hitachi S3200N SEM using a 15-kV accelerating voltage. The images were digitally recorded.

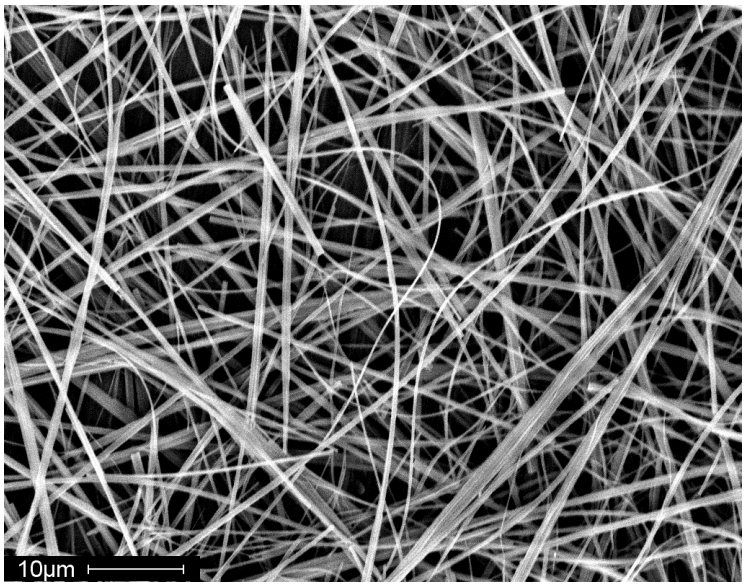

Figure S3-24. SEM image of **1a** (2.7 mM) in acetone.

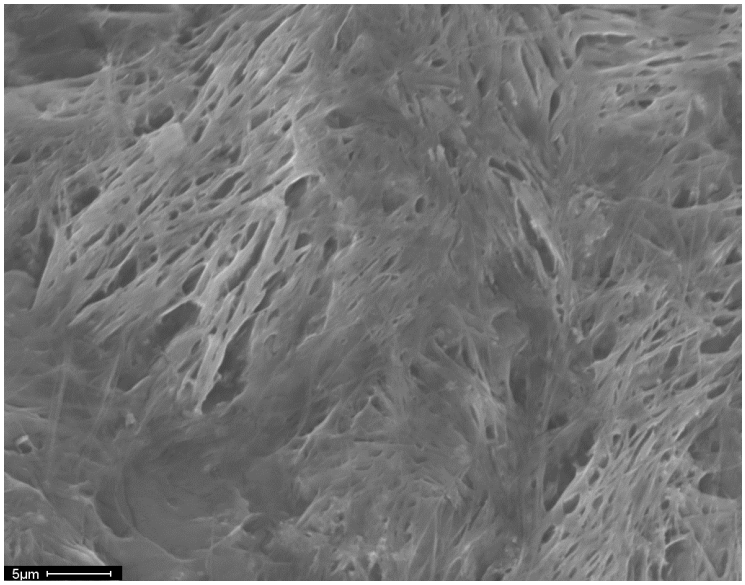

Figure S3-25. SEM image of **2b** (13.9 mM) in basic H_2O/EtOH solution (pH 12).

VIII. References

[1] Trindade, T.; O'Brien, P.; Zhang, X.-M.; Motevalli, M. *J. Mater. Chem.* **1997**, *7*, 1011–1016.

[2] Ng, S. W. *Acta Cryst.* **1999**, *C55*, IUC9900091.

[3] Mohammadneshad, G.; Ghanbarpour, A. R.; Amini, M. M.; Ng, S. W. *Acta Cryst.* **2010**, E*66*, m529.

[4] Accelrys Software Inc., Discovery Studio Modeling Environment, Release 4.0, San Diego: Accelrys Software Inc., 2013.

[5] Mohammadnezhad, G.; Amini, M. M.; Langer, V. *Acta Cryst Sect. C* **2010**, *C66*, m44–m47.

[6] Chen, M.; Fulton, J. R.; Hitchcock, P. B.; Johnstone, N. C.; Lappert, M. F.; Protchenko, A. V. *Dalton Trans.* **2007**, 2770–2778.

[7] Gao, Y.; Chen, Y.; Li, R.; Bian, Y.; Li, X.; Jiang, J. *Chem. Eur. J.* **2009**, *15*, 13241–13252.

[8] Zheng, K.-K.; Fang, X.; Yu, H.-Y.; Ke, H.; Wang, J.-D. *Acta Cryst.* **2010**, *E66*, m1700–m1701.

[9] Klevtsova, R. F.; Sankova, E. A.; Kokina, T. E.; Glinskaya, L. A.; Larionov, S. V. *J. Struct. Chem.* **2008**, *49*, 117–124.

[10] Yang, J.; Ma, J.-F.; Liu, Y.-Y.; Ma, J.-C.; Batten, S. R. *Cryst. Growth Des.* **2009**, *9*, 1894–1911.

[11] Feng, T.-J. *Acta Cryst.* **2011**, *E67*, m935.

[12] Labisbal, E.; Sousa, A.; Castineiras, A.; Garcia-Vasques, A.; Romero, J.; West, D. X. *Polyhedron* **2000**, *19*, 1255–1262.